

# Nanoscale modelling of ionic transport in the porous C-S-H network

Présentée le 17 octobre 2022

Faculté des sciences et techniques de l'ingénieur  
Laboratoire des matériaux de construction  
Programme doctoral en science et génie des matériaux

pour l'obtention du grade de Docteur ès Sciences

par

**Khalil FERJAOUI**

Acceptée sur proposition du jury

Prof. A. Mortensen, président du jury  
Prof. K. Scrivener, F. J. M. Georget, directeurs de thèse  
Prof. M. Predota, rapporteur  
Dr G. Kosakowski, rapporteur  
Prof. M. Ceriotti, rapporteur



To my parents

“... all models are approximations. Essentially, all models are wrong...  
The practical question is how wrong do they have to be to not be useful.”

— George E.P. Box





# Acknowledgements

Firstly, I would like to express my sincere gratitude to Prof. Karen Scrivener, my thesis supervisor, who gave me the opportunity to join the LMC team and be part of this very unique lab. This thesis was part of the ERICA consortium funded by the European Union under the Horizon 2020 – Marie Skłodowska-Curie – Innovative Training Network (ITN) programme. All my thanks to the programme for the funding and the support. Many thanks also to the members of the jury for their time and feedback.

Doing a PhD can be a very lonely journey at times... And while I remain deeply grateful for the introspective experience (both personal and intellectual) that I went through during the thesis, I always felt that I could count on the support and help of my co-supervisors. I owe a debt of gratitude to Fabien for his insight, valuable advice and all the fruitful discussions throughout the last four years. Also a big thank you to Prof. Paul Bowen for his guidance and for organizing all those interesting workshops.

Being part of the ERICA project was a great opportunity to travel all over the continent but mainly to meet a group of great people which made this special journey even more so. A special thought to all the ESRs: Alex, Maya, Rémi, Miryea, Nabor, Monisha, Magda, Anastasia, Petr, Ors, Arifah and, last but not least, Masood.

I feel particularly honored and so privileged for being a member of the LMC family. Thanks to all the PhD students, postdocs and staff (the rookies and the veterans) for the conversations, the laughter, the kindness and all the memories shared! My gratitude to Mira and Marie-Alix (for the good humor and all the logistic help), Andrea (for all the funny/crazy moments), Diana (for the salsa classes), Wiola (for the raclette/cinema evenings), Silas (for the Tuesday aperos), the kind Shiyu, François, Elise, Solène, Emmanuelle, Jean, John, Mahsa, Qiao, Mai, Jinfeng, William, Yu Yan, Gabi, Anna, Ziga, Bea, Hisham and to all those who might have slipped my mind, thank you!

My deep appreciation for those with whom I had the chance to share more personal time. A special thought for Sarra (the foody) and Yosra (the princess) for all those moments we spent talking, laughing or travelling together... I look forward to sharing many more adventures in the future. To the irreplaceable Thai band: thanks to Franco for his dark humour and all the embarrassing moments, Fabien (again) for being my daddou and Erng for the good food, the kindness and the memorable trip to the “Land of White Elephants”.

The LMC would not also be as fabulous without Lionel and Maude. A big thank you to Lionel for his help, energy, joy and unique sense of humor and to Maude for being the guardian angel of the lab.

Prior to the pandemic and the era of telecommuting, I had the great pleasure of sharing my office with a duo of trouble makers that fast became very good friends of mine. Thanks to Julien for your unique IT skills, the veggies, the hikes, the games, the SF conversations and Alex for your bloody humor, the financial advices and all the great evenings that we spent in your cosy hobbit hole in Epesses.

All my love and gratitude to Joy, Léon and Oscar (and all the colocs: Mursal, Francesco, Ahmed...) for being a second family here in Lausanne. I took immense pleasure sharing your lives for the last 3

years and half. Thank you for the precious moments spent together; sharing a good meal, playing social games or discussing music, life, love... Our shared summer stay in Champéry shall remain one of my favorite memories.

During my stay in Lausanne, I have also had the pleasure of meeting many interesting people which I am happy to call friends. To all the international homies; Mathilde (aka lapinou), Xisca, Sheila, Patricia, Purva and Elena, I am thankful for our adventures, the trips, the hilarious situations and I wish for many more to come. To my local swiss friends: Laetitia, Marie, Sacha, Sam, Jon, Olia... Thanks for all those Wednesday apéros (which I have been missing lately...) and all the pleasant moments.

Finally, I would like to thank my family for their unwavering support and unconditional love. I dedicate this thesis to my parents; Hallouma Hemadi and Tahar Ferjaoui, to whom I owe everything, and to my little brother Khaled.

Lausanne, le 19/09/2022

# Abstract

To reduce the CO<sub>2</sub> footprint of construction materials, concrete producers blend their cement with Supplementary Cementitious Materials (SCMs). SCMs such as fly ash or blast furnace slag are mostly the byproducts of other industries. And while SCMs are chosen to match the properties of the common Ordinary Portland cement (OPC), their addition to the cement recipe may alter the chemistry of the system. These changes can potentially lead to different mechanical and transport properties of the cement-based structure which may, in turn, affect its long-term resistance to harmful external agents. Therefore, understanding the relationship between cement's microstructure and the degradation mechanisms is key for optimizing the design of new cementitious materials

In this context, chloride attack is the most common reason for steel rebars to corrode especially when exposed to external chloride (seawater, deicer salts...). At low w/c ratios (typically <0.4), it was found that the majority of the saturated pores, which contribute to ionic transport, are interhydrate and C-S-H (calcium-silicate-hydrate) gel pores of 10nm size and below. The C-S-H gel, which constitutes over 50% of the cement paste, is a complex nearly amorphous material characterized by a high specific surface area. In contact with the highly alkaline (pH>13) pore solution, the C-S-H surface develops a negative surface charge density. Electrostatic interactions between the surface and the ions in the pore solution result in a redistribution of the ionic species in two layers of charge at the interface of the solid i.e. the Electrical double layer (EDL). In nanoscopic pores, the EDL is dominated by atomic phenomena which are thought to interfere with the mobility of ions and chloride in particular.

In order to understand and quantify the surface effects and their influence on ionic transport, we firstly propose an atomistic model of the EDL formation based on the use of the Metropolis Monte Carlo algorithm. This model is used to compute the ionic distributions and electrochemical potentials of electrolytes at equilibrium in nanoscopic pores. These quantities constitute the main driving forces of ionic transport at the pore scale. The microstructure parameters including the surface charge density of C-S-H, the ionic strength (and pH) of the pore solution and the pore size are equally investigated and their effect on chloride's behavior quantified. Among the other parameters, the model also provides quantitative information on the effect of calcium ions which are thought to play a major role in the binding of chloride on C-S-H.

The next step consists in using the calculated atomic scale properties of the EDL in order to resolve the transport problem at the pore scale and compute microscopic diffusivities of chloride. This is achieved by using the molecular computations from the Monte Carlo (MC) engine in order to implement a modified version of the classical Poisson-Boltzmann system. The method is compared to the classical Finite element analysis of the Poisson-Nernst-Planck (PNP) equations and the data are discussed in the light of established experimental results in the literature.

**Keywords:** Cement, chloride ingress, C-S-H, electrical double layer, atomic simulation, ionic transport



# Résumé

En vue de réduire l'empreinte  $\text{CO}_2$  des matériaux de construction, les producteurs de béton mélangent leur ciment avec des matériaux cimentaires de substitution (SCM). Ces matériaux, tels que les cendres volantes ou le laitier de haut fourneau, sont pour la plupart des sous-produits d'autres industries. Bien que ces matériaux de substitution soient choisis pour correspondre aux propriétés du ciment Portland (OPC), leur ajout à la recette du ciment peut modifier la chimie du système. Ces changements peuvent éventuellement conduire à des propriétés mécaniques et/ou de transports différents de la structure qui peuvent, à leur tour, affecter sa résistance à long terme aux agents externes nuisibles. Il est donc essentiel de comprendre la relation entre la microstructure de la pâte de ciment et les mécanismes de dégradation afin d'optimiser la conception de nouveaux matériaux cimentaires.

Dans ce contexte, la dégradation du béton par les chlorures est probablement la cause la plus courante de corrosion des barres d'armature en acier, en particulier lorsqu'elles sont exposées à des chlorures externes (eau de mer, sels de déverglaçage...). Pour de faibles rapports eau/ciment (typiquement  $e/c < 0,4$ ), il a été constaté que la majorité des pores saturés, qui contribuent au transport ionique, sont les pores du gel de C-S-H (silicate de calcium hydraté) dont la taille reste de l'ordre des 10 nm et moins. Le gel de C-S-H, qui constitue plus de 50% de la pâte de ciment, est un matériau complexe nanocristallin caractérisé par une surface spécifique élevée. En contact avec la solution de pores hautement alcaline ( $\text{pH} > 13$ ), la surface du C-S-H développe une densité de charge de surface négative. Les interactions électrostatiques entre la surface et les ions de la solution des pores entraînent une redistribution des espèces ioniques selon deux couches de charge à l'interface du solide, d'où la formation de la double couche électrique (EDL). Dans les pores nanoscopiques, la double couche est dominée par des phénomènes atomiques dont on pense qu'ils interfèrent avec la mobilité des ions, en général, et celle des ions chlorure en particulier.

Afin de comprendre et de quantifier les effets de surface et leur influence sur le transport ionique, nous proposons tout d'abord un modèle moléculaire de la formation de l'EDL basé sur l'utilisation de l'algorithme de Metropolis-Hastings (Monte Carlo). Ce modèle est utilisé pour calculer les distributions ioniques et les potentiels électrochimiques des électrolytes à l'équilibre dans les pores nanoscopiques. Ces quantités constituent les principales forces motrices du transport ionique à l'échelle du pore. Les paramètres de microstructure incluant la densité de charge de surface du C-S-H, la force ionique (et le pH) de la solution de pore et la taille du pore sont également étudiés et leur effet sur le comportement du chlorure quantifié. Parmi les autres paramètres, le modèle fournit également des informations quantitatives sur l'effet des ions calcium qui sont généralement supposés jouer un rôle majeur dans la fixation du chlorure sur les C-S-H.

L'étape suivante consiste à utiliser les propriétés calculées à l'échelle atomique de l'EDL afin de résoudre le problème de transport à l'échelle du pore et de calculer les diffusivités microscopiques du chlorure. Ceci est réalisé en utilisant les calculs moléculaires de l'algorithme de Monte Carlo (MC) afin d'implémenter une version modifiée de l'équation classique de Poisson-Boltzmann. La méthode est comparée à l'analyse classique par éléments finis du système d'équations de Poisson-Nernst-Planck (PNP). Les prédictions du modèle sont, finalement, discutées à la lumière des résultats expérimentaux établis dans la littérature.

**Mots clés:** Ciment, dégradation par les chlorures, C-S-H, double couche électrique, modélisation moléculaire, transport ionique.

# Table of contents

Acknowledgements .....	5
Abstract.....	7
Résumé .....	9
Table of contents .....	11
List of figures .....	15
List of tables .....	21
Glossary.....	23
Chapter 1 Introduction.....	27
I. Context.....	29
II. Chloride attack.....	29
A. Brief introduction to cement chemistry .....	29
B. Statement of the problem and objectives.....	30
III. Structure of the thesis .....	31
IV. References .....	33
Chapter 2 Literature review.....	35
I. Chloride ingress : A major threat to reinforced concrete.....	37
II. Binding mechanisms of chloride in cementitious materials .....	39
A. The chemical binding .....	39
B. The physical binding .....	40
III. Standard approach for the quantification of chloride ingress.....	40
A. Empirical modelling of chloride ingress and limitations.....	40
B. Characterisation of blended systems: Need for a fundamental understanding of the small scales.....	43
IV. The microstructure of cement paste: A key parameter in the study of ionic transport.....	43
A. Pore structure .....	44
B. Pore solution.....	46
C. C-S-H .....	48
V. Ionic adsorption/diffusion at the atomic scale .....	54
A. Surface charging of C-S-H .....	54
B. The classical theory of the electrical double layer (EDL) .....	54
C. The necessity of atomistic models.....	56
VI. Conclusion.....	59
VII. References .....	60

Chapter 3 Computational methods .....	69
I. Force Fields .....	71
A. Interatomic potentials .....	71
B. Long range interactions .....	72
II. Molecular Dynamics.....	74
A. The algorithm.....	74
B. Thermostats .....	76
C. Application case: Relaxation of a Lennard-Jones fluid between pushing walls .....	77
III. Free energy calculations .....	78
A. The chemical potential .....	78
B. The Widom insertion algorithm.....	80
C. Application case: Excess chemical potential of a non-homogeneous LJ liquid .....	80
D. Extension to electrolytic fluids.....	81
IV. Metropolis Monte Carlo .....	82
A. Principle .....	82
B. The Grand Canonical Monte Carlo (GCMC) .....	84
V. Finite element method .....	86
A. Principle .....	86
B. The variational formulation: Case of the Poisson-Nernst-Planck (PNP) equations.....	86
VI. References .....	89
Chapter 4 Modelling the formation of electrical double layers around C-S-H surfaces in Na-systems ....	91
I. Limitations of the classical theory: The atomistic modelling of the EDL .....	93
A. The Poisson-Boltzmann equation .....	93
B. The study of the EDL: A multi-parameter problem .....	94
C. Computational validation: Zeta potential ( $\zeta$ ) at a C-S-H surface with Ca/Si <1 .....	108
II. Electrical double layers in slit pores.....	112
A. Effect of the pore size .....	112
B. Interactions at the surface: Influence of $\sigma_{\text{C-S-H}}$ .....	116
C. Effect of the concentration.....	118
D. Explicit OH <sup>-</sup> in simulation boxes.....	119
III. Summary .....	121
IV. References .....	122
Chapter 5 Insight on the EDL formation in Ca-containing systems.....	125
I. Choice of the C-S-H surface .....	127
A. A more realistic surface charge density.....	127
B. Zeta potential calculation: Titration of a C-S-H suspension in a Ca(OH) <sub>2</sub> solution .....	127



II.	Modelling the pore solution in cement paste.....	130
III.	Calcium adsorbed surfaces in C-S-H.....	131
A.	Effect of calcium adsorption in slit pores .....	131
B.	The pore size effect.....	137
C.	Case of the full calcium occupancy of the ionized C-S-H surface (Ca-Si occupancy ratio equal to 100%) .....	140
IV.	Conclusions .....	143
V.	Appendix A: Multi-parameter study of the EDL in Ca-containing environments .....	145
A.	Effect of the ionization degree .....	145
B.	Effect of pH decrease.....	148
VI.	References .....	150
Chapter 6 Diffusion of chloride ions in the nanoscopic C-S-H gel pores .....		153
I.	Introduction .....	155
A.	Definition of the nanoscopic transport problem and objectives.....	155
B.	Choice of the resolution method .....	156
II.	The governing equations of ionic transport in saturated cement paste .....	157
A.	Case of an ideal solution: The classical Poisson-Nernst-Planck (PNP) equations.....	158
B.	Extension to non-ideal electrolytes: the modified Poisson-Boltzmann (MPB) .....	160
III.	Results and discussion .....	163
A.	Transport in symmetric monovalent electrolytes .....	163
B.	Transport in a more realistic model of the cement paste .....	170
IV.	Summary .....	178
V.	References .....	179
Chapter 7 Summary and Outlook .....		181
I.	Physical binding of chloride: The electrical double layer.....	183
A.	Methodology .....	183
B.	Contribution.....	183
C.	Outlook .....	185
II.	Diffusion of chloride in the nanoporous C-S-H gel .....	187
A.	Contribution.....	187
B.	Outlook .....	187
III.	Closing words.....	188
IV.	References .....	189
Curriculum vitae .....		192



# List of figures

Fig.1.1. Proportions of hydration products in a mature paste [Taylor1997, ScrivCourse] .....	30
Fig.2.1. Protective passivation layer around embedded steel rebars in concrete.....	37
Fig.2.2. Corrosion of a steel rebar in contact with pore solution.....	38
Fig.2.3. Chloride profile for OPC and blended systems with different SCMs: CClay=Calcined Clay, LS=Limestone, FA=Fly Ash; after 1 year exposure to a 0.5 M NaCl solution. Taken from [Sui2019(2)]	41
Fig.2.4. Relationship between the apparent diffusion coefficient and porosity, critical pore size of different blended systems: CClay=Calcined Clay, LS=Limestone, FA=Fly Ash. Taken from [Sui2019(2)] .....	42
Fig.2.5. Cumulative <b>(a)</b> and derivative <b>(b)</b> curve of the pore structure from MIP measurements on Portland cement paste samples (w/c = 0.4). Taken from [Berod2015] .....	45
Fig.2.6. Evolution of the different NMR signal fractions with hydration time (w/c = 0.40). Blue circles are free water, becoming interhydrate water (empty black circles) beyond 2 days of hydration. The estimated error is $\pm 2\%$ . Taken from [Muller2014, p.56].....	46
Fig.2.7. Evolution of the apparent diffusion coefficient with respect to the alkali content in the pore solution. Taken from [Sui2019(2)].....	47
Fig.2.8. The layered structure of tobermorite is composed of a calcium plane (red dots) bordered by two silicate planes (blue chains) and separated by the interlayer space containing water molecules, hydroxyl groups and some calcium ions. The silicate planes are composed of silicate chains with a specific three-unit repetition ("dreierketten"): two silicate tetrahedra, noted as $Q^2$ , are coordinated by calcium planes (red dots) whereas the third silicate (called the bridging tetrahedron and noted as $Q^{2p}$ or $Q^{2i}$ ) is not. The end-chain tetrahedra are noted $Q^1$ . The tetrahedra linking two silicate chains in the interlayer space are noted $Q^3$ whereas the sites $Q^2$ next to $Q^3$ are named $Q^{2v}$ . The calcium ions belonging to the main plane are noted $Ca^{MP}$ whereas those in the interlayer are noted $Ca^L$ . Taken from [Brun2004].....	49
Fig.2.9. A proposed atomic structure of C-S-H with a stoichiometry $(CaO)_{1.75}(SiO_2)_{1.0}(H_2O)_{1.86}$ with percentages of $Q^1 = 78.3\%$ , $Q^{2b} = 7.25\%$ and $Q^{2p} = 14.5\%$ . Atomic color code used are calcium - turquoise, silicon - dark blue, oxygen - red, hydroxyl oxygen - purple, hydrogen - white. Taken from [KunhiPhd2018].....	50
Fig.2.10. <b>(a)</b> Transmission electron micrograph and <b>(b)</b> schematic diagram showing an inner/outer product interface region in a paste hydrated for 3 months (w/c = 0.4 at 20 °C) (Taken from [Rich1993]) <b>(c)</b> SEM polished section of a w/c = 0.7 paste at 28 days. Sections of C-S-H "needles" are observed (points) in different areas, in particular in the bottom right. Etch pits are visible on the anhydrous white core. Taken from [Ouzia2019].....	51
Fig.2.11. <b>(A)</b> Packing of globules showing small gel pores (SGP) (Taken from [Jennings2008]) <b>(B)</b> Configuration of the coarse-grained C-S-H model, after equilibration, where three featured structures can be found (Taken from [Yu2016]) <b>(C)</b> Example of structures generated with the sheet growth algorithm using different growth parameters. Taken from [Etzold2014] .....	53

Fig.2.12. Schematic of the main EDL models <b>(a)</b> Helmholtz model <b>(b)</b> Gouy-Chapman model.....	55
<b>(c)</b> Grahame model. Taken from [Fried2008].....	55
Fig.3.1. <b>(a)</b> Cross section of the infinite simulation cell in the direction <b>x</b> and <b>y</b> and <b>(b)</b> Representation of the mean charge density perpendicular to the charged walls as a set of infinite and equally spaced walls each having a different but uniform surface charge density. Taken from [Torrie1980] .....	73
Fig.3.2. Density profile as function of the position in a confined LJ liquid with a particle number <i>N</i> equal to <b>(a)</b> 720 and <b>(b)</b> 920; Adapted from [Perego2018] .....	78
Fig.3.3. Schematic of the insertion moves performed at each step of the Widom algorithm. In green, we represent an accepted virtual move. In red, the move is rejected due to the overlapping with particles of the system. ....	80
Fig.3.4. Evolution of the excess chemical potential as function of the simulation time. Results are presented in the cases of <b>(a)</b> a low density Lennard-Jones liquid with <i>N</i> =720 and <b>(b)</b> a higher density configuration with <i>N</i> =920. In blue are presented the predictions of the Widom algorithm used in this work with 27000 particle insertions each 500 iterations. In red and orange, the computations achieved with Well-Tempered (WT) Metadynamics using, respectively, 512 (Meta I) and 64 (Meta II) particle insertions each 500 time steps. Adapted from [Perego2018] .....	81
Fig.4.1. Schematic of the implemented Gouy-Chapman-Stern model of EDL formation in a single-wall solution under different conditions: <b>(a)</b> A moderately concentrated monovalent NaCl salt in contact with a highly charged surface <b>(b)</b> A highly concentrated solution (NaCl) at the edge of a moderately charged surface and <b>(c)</b> The effect of calcium divalence (at moderate concentration) on the electric properties of the EDL. The solvent (water) is implicit but ions are explicitly described. The considered ionic species are, respectively, sodium Na <sup>+</sup> (red), chloride Cl <sup>-</sup> (blue) and calcium Ca <sup>2+</sup> (green). ....	95
Fig.4.2. Simulated (GCMC) surface charge density, $\sigma$ vs pH for a bulk solution containing either 2 mM calcium (solid lines) or 2mM sodium (dotted lines) for increasing surface site density: 0.8 (no symbols), 2.8 (empty circles), and 4.8 sites.nm <sup>-2</sup> (filled circles). Taken from [Lab2011] .....	97
Fig.4.3. Ionic distribution of ions in a NaCl 0.01M salt in contact with surfaces with different surface charge densities respectively -0.48 and -2.4 e.nm <sup>-2</sup> . Plot <b>(a)</b> presents distributions of Na <sup>+</sup> and Cl <sup>-</sup> from PB resolution. Plot <b>(b)</b> presents a comparison between Na <sup>+</sup> distributions from PB and from MC calculations.....	99
Fig.4.4. Ionic distributions in a NaCl 0.1M for <b>(a)</b> $\sigma_{C-S-H} = -0.24$ e.nm <sup>-2</sup> and <b>(b)</b> $\sigma_{C-S-H} = -2.4$ e.nm <sup>-2</sup> according to Poisson-Boltzmann (PB) computations and Monte Carlo (MC) simulations where <i>x</i> =0 represents the OHP. ....	100
Fig.4.5. Charge densities <b>(a)</b> and potential profiles <b>(b)</b> in a NaCl 0.1M solution with $\sigma_{C-S-H} = -0.24$ and -2.4 e.nm <sup>-2</sup> according to Poisson-Boltzmann (PB) computations and Monte Carlo (MC) simulations. ....	101
Fig.4.6. Evolution of the Debye length $\lambda_D$ <b>(a)</b> and the potential drop in the DL <b>(b)</b> for a 0.1M NaCl solution as a function of the absolute value of the surface charge density $\sigma_{C-S-H}$ for MC and PB computations .....	102
Fig.4.7. Ionic distributions in a NaCl around a surface with $\sigma_{C-S-H} = -0.24$ e.nm <sup>-2</sup> at concentrations of <b>(a)</b> 0.01M and <b>(b)</b> 1M.....	104
Fig.4.8. Evolution of <b>(a)</b> the Debye length $\lambda_D$ and <b>(b)</b> the potential drop in the DL for a 0.1M NaCl solution as a function of the concentration for MC and PB computations .....	105

Fig.4.9. Comparison between ionic distributions <b>(a)</b> and electric potential profiles <b>(b)</b> in a $\text{CaCl}_2$ 0.05M and NaCl 0.1M electrolytes at a C-S-H surface of $\sigma_{\text{C-S-H}} = -2.4 \text{ e.nm}^{-2}$ for MC calculations. ....	107
Fig.4.10. Comparison between chloride distributions <b>(a)</b> and electric potential profiles <b>(b)</b> in a $\text{CaCl}_2$ 0.05M and NaCl 0.1M electrolytes at a C-S-H surface of $\sigma_{\text{C-S-H}} = -2.4 \text{ e.nm}^{-2}$ for MC and PB calculations. ....	108
Fig.4.11. <b>(a)</b> Simulated ionization fraction, $\alpha$ , versus pH for various bulk conditions: dotted line and squares $\text{Ca(OH)}_2$ salt solution; dotted line and filled circles NaOH salt solution. The ideal curve (solid line) is given for comparison <b>(b)</b> Comparison between experimental (points) and simulated (line) net increase of the ionization fraction ( $\Delta\alpha$ ) as a function of the pH for C-S-H nano-particles dispersed in solution containing a low bulk calcium concentration (below 20 mM). Taken from [Lab2011]. ....	109
Fig.4.12. <b>(a)</b> Electric potential around C-S-H surfaces at different concentrations of $\text{Ca(OH)}_2$ <b>(b)</b> a focus on the first 6 Å with two zeta planes: 3.4 Å (blue) and 6 Å (red) and <b>(c)</b> the evolution of the Zeta potential as function of the concentration. Adapted from [Lab2011]. ....	110
Fig.4.13. Ionic distributions <b>(a)</b> and effective charge densities <b>(b)</b> as function of the normalized distance from the pore center in a NaCl 0.1M electrolyte within pores of various diameters $L_x$ . ....	113
Fig.4.14. <b>(a)</b> Effective charge distribution, <b>(b)</b> the electric field and <b>(c)</b> the electrochemical potential computed from MC data in pores of sizes 4 nm (blue), 8 nm (red) and 16 nm (yellow) for a NaCl 0.1M solution and $\sigma_{\text{C-S-H}} = -0.24 \text{ e.nm}^{-2}$ ....	115
Fig.4.15. <b>(a)</b> Average potential as function of the pore size and <b>(b)</b> evolution of the potential value at the surface ( $\psi_o$ ), the OHP ( $\psi^D$ ) and the center ( $\psi^C$ ) plane in pores of 4, 8 and 16 nm of size. ....	117
Fig.4.16. <b>(a)</b> Electrochemical potentials as function of the position in a 4 nm pore and <b>(b)</b> the evolution of the potential average as function of the pore size for NaCl solutions of 0.1M (dark blue) and 0.5M (light blue) ....	118
Fig.4.17 Ionic distributions in pores of <b>(a)</b> 12 nm and <b>(b)</b> 4 nm [For simplicity, only distributions at pH values of 13 and 13.5 are shown]. ....	119
Fig.4.18. <b>(a)</b> Electrochemical potentials as function of the position in a 4nm pore and <b>(b)</b> the evolution of the potential average as function of the pore size for NaCl+NaOH solutions of pH 13 (triangles), 13.3 (Circles) and 13.5 (dotted lines) ....	120
Fig.5.1. Electric potential around C-S-H with $\sigma_{\text{C-S-H}} = -1.2 \text{ e.nm}^{-2}$ at different concentrations of $\text{Ca(OH)}_2$ ....	128
Fig.5.2. Schematic of the C-S-H silicate chains with two ways to define calcium adsorption on the C-S-H surface. In the surface (1), $\text{Ca}^{2+}$ (green balls) are adsorbed in the Stern layer and the surface is defined by the silicate chains with the silanols ionization dependent on pH. In the definition (2) of the surface, the $\text{Ca}^{2+}$ ions are incorporated in the structure. Image inspired from [Viallis2000] ....	129
Fig.5.3. Schematic of the $\text{Ca}^{2+}$ charge replacement ratio at values of 0%, 25% and 50% ....	132
Fig.5.4. Evolution of <b>(a)</b> the anionic distribution and <b>(b)</b> the electrochemical potential in the 12nm pore at different charge replacement ratios of 0%, 50%, 65% and 100% ....	133
Fig.5.5. Evolution of <b>(a)</b> the Ca occupancy of the available ionized sites and <b>(b)</b> the $\text{Ca}^{2+}$ distributions in the pore of as function of the charge replacement ratio. ....	134

Fig.5.6. Evolution of zeta potential of the surface and the potential average in the 12 nm pore as function of the charge replacement ratio.....	135
Fig.5.7. Evolution of <b>(a)</b> the $\text{Na}^+$ distributions and <b>(b)</b> the electrostatic potential in a 12 nm pore for charge replacement ratios of 25% and 50%.....	136
Fig.5.8. Evolution of <b>(a)</b> the Ca occupancy of the available ionized sites and <b>(b)</b> the $\text{Ca}^{2+}$ distributions in 4nm pore at charge replacement ratios of 0%, 50% and 65%. The red area denotes the interval of $\text{Ca}^{2+}$ concentration where the reversal of charge happens. ....	137
Fig.5.9. Chloride distribution profiles in pores of <b>(a)</b> 8nm and <b>(b)</b> 4nm of diameter. The charge replacement ratios are varied through the whole range with values at 0%, 50% and 100%. ....	138
Fig.5.10. Evolution of the potential average as function of the replacement ratio in pores of 4, 8 and 12nm of size .....	139
Fig.5.11. Schematic of a fully calcium-covered C-S-H surface. Two adsorption mechanism are suggested: <b>(a)</b> Each ionized site $\text{Si-O}^-$ is occupied by a $\text{Ca}^{2+}$ ion (Type I) <b>(b)</b> Each pair of ionized sites ( $2\text{Si-O}^-$ ) can attract either $2\text{Ca}^{2+}$ (Type I) or $1\text{Ca}^{2+}$ (Type II).....	140
Fig.5.12. Chloride distribution profiles around C-S-H surfaces of charge densities $+0.6$ and $+1.2 \text{ e.nm}^{-2}$ in pores of 4 and 12 nm size.....	141
Fig.5.13. <b>(a)</b> Electrochemical potentials as function of the position in a 12nm pore and <b>(b)</b> evolution of the potential average as function of the pore size. The surface charge densities are $+0.6$ and $+1.2 \text{ e.nm}^{-2}$ representing, respectively, the high (Fig.5.11.(a)) and low (Fig.5.11.(b)) Ca-Si occupancy cases. ....	142
Fig.A.1. Evolution of <b>(a)</b> the anionic distribution and <b>(b)</b> the $\text{Ca}^{2+}$ distribution in a 12 nm pore with surface charge density of $-0.48 \text{ e.nm}^{-2}$ at charge replacement ratios of 25%, 50%, 65% and 100%. .	146
Fig.A.2. <b>(a)</b> Evolution of the Ca-Si occupancy as function of the replacement ratio at $\sigma_{\text{C-S-H}}$ equal to $-0.48 \text{ e.nm}^{-2}$ and <b>(b)</b> Comparison of the evolution of the potential average as function of the charge replacement ratio with $\sigma_{\text{C-S-H}}$ varying between $-0.48$ and $-1.2 \text{ e.nm}^{-2}$ . Results are presented for pores of 4, 8 and 12 nm.....	147
Fig.A.3. <b>(a)</b> Evolution of the Ca occupancy of the available ionized sites as function of the replacement ratio in pores of 12 and 4 nm pore at pH equal to 12.7 and 13. <b>(b)</b> $\text{Ca}^{2+}$ distribution in pores of 12 and 4 nm at charge replacement ratios of 50 and 65% for pH=12.7.....	148
Fig.A.4. Evolution of the potential average as function of the charge replacement ratio in pores of 4, 8 and 12 nm at pH equal to 12.7 and 13 .....	149
Fig.6.1.Capture of the finite element mesh of the pore space used for the simulation of the electrical double layer formation in a slit pore with a focus on different regions of the domain. ....	160
Fig.6.2. Evolution of the average $x$ -component of ionic fluxes (diffusive, electrophoretic (migration) and total) of sodium $\text{Na}^+$ and chloride $\text{Cl}^-$ in a 0.1M NaCl pore solution as function of the pore size around C-S-H surfaces of charge densities $\sigma_{\text{C-S-H}}$ equal to <b>(a)</b> $-0.24$ and <b>(b)</b> $-0.48 \text{ e.nm}^{-2}$ . ....	164
Fig.6.3. Normalized diffusivity of <b>(a)</b> sodium $\text{Na}^+$ and <b>(b)</b> chloride $\text{Cl}^-$ in a 0.1M NaCl pore solution as function of the pore size around C-S-H surfaces of charge densities $\sigma_{\text{C-S-H}}$ equal to $-0.12$ , $-0.48$ and $-0.96 \text{ e.nm}^{-2}$ . PNP calculations represent results for the ideal case and MPB computations account for non-ideality of the solution. ....	165

Fig.6.4. Normalized diffusivity of <b>(a)</b> sodium $\text{Na}^+$ and <b>(b)</b> chloride $\text{Cl}^-$ as function of the pore size in NaCl solutions of concentrations 0.1M, 0.3M and 0.5M around C-S-H surfaces of charge density equal to $-0.24 \text{ e.nm}^{-2}$ . PNP calculations represent results for the ideal case and MPB computations account for non-ideality of the solution. ....	167
Fig.6.5. Normalized diffusivity of <b>(a)</b> sodium $\text{Na}^+$ and <b>(b)</b> chloride $\text{Cl}^-$ as function of the pore size in NaCl solutions of pH values at 13, 13.3 and 13.5 around C-S-H surfaces of charge density equal to $-0.24 \text{ e.nm}^{-2}$ . PNP calculations represent results for the ideal case and MPB computations account for non-ideality of the solution. ....	168
Fig.6.6. Normalized diffusivity of <b>(a)</b> sodium $\text{Na}^+$ and <b>(b)</b> chloride $\text{Cl}^-$ as function of the pore size. The pore solution is modeled as a {NaCl 98mM + $\text{CaCl}_2$ 1mM + NaOH 0.1M} with a pH of 13. The surface charge density of C-S-H ( $\sigma_{\text{C-S-H}}$ ) is set at $-1.2 \text{ e.nm}^{-2}$ . PNP calculations represent results for the ideal case and MPB computations account for non-ideality of the solution at charge replacement ratios of 0, 25 and 50%. ....	171
Fig.6.7. Normalized diffusivity of <b>(a)</b> sodium $\text{Na}^+$ and <b>(b)</b> chloride $\text{Cl}^-$ as function of the pore size. The pore solution is modeled as a {NaCl 98mM + $\text{CaCl}_2$ 1mM + NaOH 0.1M} with a pH of 13. The effect of the surface charge density of C-S-H ( $\sigma_{\text{C-S-H}}$ ) is investigated and varied between $-0.48$ and $-1.2 \text{ e.nm}^{-2}$ . MPB computations account for non-ideality of the solution at charge replacement ratios of 0%, 25% and 50%. ....	172
Fig.6.8. Normalized diffusivity of <b>(a)</b> sodium $\text{Na}^+$ and <b>(b)</b> chloride $\text{Cl}^-$ as function of the pore size. The pore solution is modeled as a {NaCl + $\text{CaCl}_2$ + NaOH}. The effect of pH is investigated and, hence, varied between 12.7 and 13. The surface charge density of C-S-H ( $\sigma_{\text{C-S-H}}$ ) is set at $-1.2 \text{ e.nm}^{-2}$ . MPB computations account for non-ideality of the solution at charge replacement ratios of 0, 25 and 50%. ....	174
Fig.6.9. Normalized diffusivity of <b>(a)</b> sodium $\text{Na}^+$ and <b>(b)</b> chloride $\text{Cl}^-$ as function of the pore size. The pore solution is modeled as a {NaCl 98mM + $\text{CaCl}_2$ 1mM + NaOH 0.1M}. Due to the high $\text{Ca}^{2+}$ adsorption, we consider two positive surface charge densities: $+0.6$ and $1.2 \text{ e.nm}^{-2}$ . MPB computations account for the non-ideality of the solution. ....	175
Fig.6.10. <b>(a)</b> Porosity distribution of PC and LC3-50 (with increasing kaolinite content) paste samples after 6-month exposure to water or 2M NaCl solution and <b>(b)</b> Correlation between the bound chloride, the critical pore entry radius with the apparent chloride diffusion coefficient. Taken from [Maraghechi2018] .....	177
Fig.7.1. <b>(a)</b> Representation of the simulation setup and the considered Quartz surface of charge density $-0.12 \text{ C/m}^2$ where the green line defines the zero plane. <b>(b)</b> Ionic distributions of sodium ( $\text{Na}^+$ ) and strontium ( $\text{Sr}^{2+}$ ) ions, respectively, in NaCl 0.38M and $\text{SrCl}_2$ 0.38L solutions. MD results from the paper are compared to GCMC predictions from the present work. Adapted from [Kroutil2015]. ....	186





# List of tables

Table.2.1. Concentrations of different species present in the pore solution of a PC paste (w/c = 0.4) at 69 days of hydration. Measurements have been obtained through pore solution extraction at pressures going from 60 MPa up to 330 MPa. Taken from [Loth2010].....	46
Table.3.1. Non bond parameters for the studied ionic species .....	72
Table.3.2. Bond parameters for the oxygen and hydrogen atoms of the hydroxide ion [CHARMM] ..	72
Table.4.1. Simulation box for $\text{Ca}(\text{OH})_2$ in contact with C-S-H surface at different values of the pH...	109
Table.5.1. Concentration of ionic species in the pore solution model at different values of the pH .	131
Table.5.2. Simulation box for a pore solution modeled as {NaOH 0.1M + NaCl 98mM + $\text{CaCl}_2$ 1mM} in a 12nm-pore with C-S-H surfaces neutralized with $\text{Na}^+$ and $\text{Ca}^{2+}$ ions at various replacement ratios. The surface charge density is set at $\sigma_{\text{C-S-H}} = -1.2 \text{ e.nm}^{-2}$ .....	133
Table.A.1. Simulation box for a pore solution modeled as {NaOH 0.1M + NaCl 98mM + $\text{CaCl}_2$ 1mM} in a 12nm-pore with C-S-H surfaces neutralized with $\text{Na}^+$ and $\text{Ca}^{2+}$ ions at various replacement ratios. The surface charge density is set at $\sigma_{\text{C-S-H}} = -0.48 \text{ e.nm}^{-2}$ .....	145
Table.6.1. Ionic diffusion coefficients in water at infinite dilution at 25°C [Lide1994] .....	162



# Glossary

## Cement shorthand notation

C: CaO (CalciumOxide)  
S: SiO<sub>2</sub> (Silicon dioxide)  
A: Al<sub>2</sub>O<sub>3</sub> (Aluminium oxide)  
F: Fe<sub>2</sub>O<sub>3</sub> (Iron oxide)  
H: H<sub>2</sub>O (Water)

## Abbreviation of materials and phases

OPC: Ordinary Portland cement  
PC: Plain cement  
SCM: Supplementary cementitious materials  
LC3: Limestone calcined clay cement  
C-S-H: Calcium silicate hydrate  
Ip C-S-H: Inner product C-S-H  
Op C-S-H: Outer product C-S-H  
C-A-S-H: Calcium aluminate silicate hydrate  
CH: Calcium hydroxide (portlandite)  
AFm: Aluminate ferrite mono  
AFt: Aluminate ferrite tri  
LDH: Layered double hydroxide

## Abbreviations of techniques

TGA: Thermogravimetric analysis  
XRD: X-Ray diffraction  
NMR: Nuclear Magnetic Resonance  
MIP: Mercury intrusion porosimetry  
SEM: Scanning electron microscopy  
TEM: Transmission electron microscopy  
EDS: Energy dispersive X-Ray spectroscopy  
EXAFS: Extended X-ray absorption fine structure

## Miscellaneous abbreviations

RH: Relative humidity  
pH: Potential of hydrogen  
BC: Boundary condition  
w/c: Water to cement ratio (in mass)  
Ca/Si: Calcium to silicon ratio  
Ca-Si: Calcium occupancy ratio of ionized silanol sites  
EDL: Electrical double layer  
DL: Diffuse layer  
SL: Stern layer  
OHP: Outer Helmholtz plan  
IHP: Inner Helmholtz plan  
GC: Gouy-Chapman  
GCS: Gouy-Chapman-Stern

PB: Poisson-Boltzmann  
FF: Force field  
MD: Molecular dynamics  
NH: Nosé-Hoover  
SVR: Stochastic velocity rescaling  
MC: Monte Carlo  
GCMC: Grand Canonical Monte Carlo  
FEM: Finite element method  
PNP: Poisson-Nernst-Planck  
PDE: Partial differential equation  
SSD: Silanols site density  
MCL: Mean chain length  
LJ: Lennard-Jones  
PME: Particle mesh ewald  
FMM: Fast Multipole Method  
PPM: Parts per million  
LAMMPS: Large-scale Atomic/Molecular Massively Parallel Simulator  
REV: Representative element of volume  
REA: Representative element area





# Chapter 1 Introduction

Due to the growing necessity of developing more sustainable construction materials, the construction industry is presently undergoing deep changes. This chapter aims to put the present thesis into context of the key research issues in the field of cement chemistry. The main focus of this work is presented along with the objectives to achieve. Lastly, the structure of the thesis is explained.

Chapter 1 Introduction.....	27
I.    Context.....	29
II.   Chloride attack.....	29
A.   Brief introduction to cement chemistry .....	29
B.   Statement of the problem and objectives.....	30
III.  Structure of the thesis .....	31
IV.  References .....	33





## I. Context

Concrete is a composite made of aggregates, cement, water and air. It is also the most widespread construction material. Producing cement requires CO<sub>2</sub>-intensive industrial processes such as the calcination of raw materials and high-temperature phase formation. In practice, concrete remains a relatively good material in terms of greenhouse gases emission. It is, however, the most produced material in the world [Ashby2012] and the second most used resource after water. Worldwide, it is the production of over 30 billion tons of cementitious materials per year that makes the cement industry responsible of 6 to 8% of the world CO<sub>2</sub> emissions [IPCC2014, And2018] i.e. half of the contribution of the transportation sector. Given the population and economic growth of many developing countries such as China or India, the need for construction materials is most likely to rise dramatically.

As concrete is practically irreplaceable on a global scale, many manufacturers have worked to improve the energy efficiency of the cement production by modifying their cement mixes to reduce CO<sub>2</sub> production. To achieve this, concrete producers replace part of the Ordinary Portland Cement (OPC) with Supplementary Cementitious Materials (SCMs) which are usually byproducts of other industrial processes. Among these materials, we count limestone, calcined clay, the residual fly ash from the coal combustion or condensed silica fume; a byproduct of the semiconductor industry...

Although the manufacture of blended systems is eco-friendlier than OPC, these cements can only be used if they comply with the expected performance standards. SCMs are, in fact, likely to alter the chemistry of the cementitious systems which may eventually lead to different long-term mechanical and transport properties [Wilson2022]. Given the wide range of possible SCMs to use, the experimental testing of each formulation under different conditions is not possible. Models can, however, provide insight and help refine our choices to the most promising formulations. In this context, chloride ingress is the most common problem for the long-term durability of reinforced concrete. Understanding and predicting the mechanisms of chloride diffusion in cement paste is a vital issue for optimizing the design of new cementitious materials.

## II. Chloride attack

### A. Brief introduction to cement chemistry

The most common type of cement is Ordinary Portland Cement (OPC). It is a multicomponent system which contains, in its anhydrous (no water) form, 4 types of minerals: alite (C<sub>3</sub>S), belite (C<sub>2</sub>S), calcium aluminate (C<sub>3</sub>A) and a calcium aluminoferrite phase (C<sub>4</sub>AF)<sup>\*†</sup>. The reaction of non-hydrated cement with water is termed, in cement chemistry, hydration [Taylor1997]. And when mixed with water, the hydration reaction leads to mainly four products: C-S-H, Portlandite (Ca(OH)<sub>2</sub>), AFm and AFt phases.

---

<sup>\*</sup> A stands for Al<sub>2</sub>O<sub>3</sub>, C for CaO, F for Fe<sub>2</sub>O<sub>3</sub>, S for SiO<sub>2</sub> and H for H<sub>2</sub>O

<sup>†</sup> Ferrite can also be written as C<sub>2</sub>(A/F) as it is a solid solution where the A/F ratio is variable.

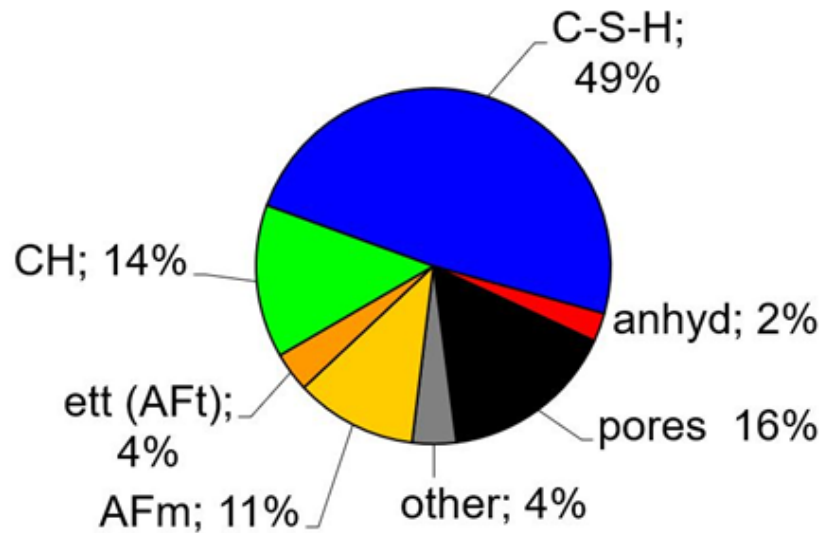


Fig.1.1. Proportions of hydration products in a mature paste [Taylor1997, ScrivCourse]

Calcium silicate hydrate is the main reaction product (Fig.1.1). It is usually abbreviated to C-S-H, the dashes indicating that there is no strict stoichiometry i.e. the ratio  $\text{SiO}_2/\text{CaO}$  is variable. C-S-H is also the main percolating phase in cement paste [Bentz1991]. It means that all macroscopic properties, including ionic transport and mechanical strength, are tightly linked to the properties of C-S-H.

## B. Statement of the problem and objectives

In reinforced concrete made structures, concrete is usually what provides a physical and chemical protection to the reinforcing steel bars. The chemical environment in cement paste is usually characterized by a high alkalinity that provides steel with a protective film on its surface, hence, improving its resistance to corrosion. Nonetheless, when chloride concentration at the rebars surface reaches a threshold, chloride ions act as catalysts to corrosion by breaking down the protective layer on the steel. The corrosion of the reinforcement bars greatly damages the cement-based structure by inducing cracks in the concrete and reducing its mechanical properties which can eventually cause the whole structure to fail [Broom2003].

For the purposes of developing more sustainable cement formulations without over-engineering, it is necessary to be able to predict the resistivity of reinforced concrete to chloride attack. Building consistent transport models is critical for the optimization of a cement recipe which would fulfill both strength and durability requirements. Nonetheless, chloride ingress mechanisms are not fully understood for both OPC and blended systems [Sui2019]. In fact, the transport of chloride in the pore network of cementitious materials is a complex process which is mainly affected by three underlying parameters:

- i. The chemical reactivity between the solid phases and the pore solution
- ii. The morphology of the porous network in the percolating phases.
- iii. The influence of the C-S-H surface on the ionic mobility

Although there remains a lot to do on all three subjects, experimental techniques and thermodynamic models have provided cement scientists with some idea on the contribution of points (i) and (ii). However, we are still in the dark when it comes to identifying the mechanisms

behind the interactions between the surfaces and the ions in the solution or whether these effects are of any significance. As most of the interfacial phenomena take place at the atomic level, experimental investigation becomes too intricate to extract data at such small scales and the governing phenomena too complex for the mean field models to predict.

As the main percolating phase, C-S-H is expected to play a prime role in transport properties. The study of the structure of C-S-H through  $^{29}\text{Si}$  NMR spectroscopy [Lipp1982, Cong1996, Brun2004] showed that C-S-H is a construction of calcium planes bordered on each side by silicate chains. Within the high pH cement environment, it was found the silanol groups ( $\text{Si-OH}$ ) present at the surface tend to engage in acid-base reaction which resulted in their deprotonation and the development of negative charges ( $\text{Si-O}^-$ ). In this context, the theory of the electrical double layer, firstly discovered by Helmholtz [Helm1879] and then developed by Gouy [Gouy1910], Chapman [Chap1913], Stern [Ste1924], Grahame [Gra1947] and others, would ascribe the interactions between chloride and C-S-H to electrostatic correlations between the ions present in the pore solution and the ionized C-S-H surface. We usually speak of the “physical binding” of chloride. The specificity of physical binding is that the ion is assumed to adsorb on the surface of solid phases without actually getting trapped in covalent bonds. Therefore, a relevant question would be: Since the “physically bound” chloride are not chemically bound which means they are still part of the pore solution, does the physical binding stop or at least delay the chloride ingress?

In order to answer this question, it is important to downscale to the atomic level where the fundamental interactions arise. Therefore, the object of this thesis is twofold:

- To present a consistent atomistic model that correctly predicts the forming of the EDL in agreement with measurements of the electric potential in C-S-H suspensions
- To quantify the influence of these surface effects on the mobility of ions at the pore scale, and specifically on the diffusion of chloride as the main species of interest.

### III. Structure of the thesis

**Chapter 2** is a literature review on chloride ingress in cementitious materials. It summarizes our current understanding of the microstructure of cement paste which plays a vital part on chloride diffusion. The existing empirical and theoretical models to describe the mechanisms of chloride transport are also discussed.

**Chapter 3** presents an overview of the computational methods (Monte Carlo, molecular dynamics...) that were implemented or used through the whole thesis.

**Chapter 4** focuses on the development of an atomistic model of the electrical double layer (EDL) formation in a monovalent solution. The limitations of the classical Poisson-Boltzmann theory are first discussed. Atomistic results obtained by Monte Carlo calculations are then validated with published experimental and numerical results. Finally, the model is extended to the case of an EDL forming in a slit pore.

**Chapter 5** aims to extend the model developed in chapter 4 to the case of a more realistic pore solution model where the presence of calcium ions is considered and its effect discussed.

**Chapter 6** presents the resolution of the equations of ionic transport at the scale of nanopores in the C-S-H gel. The microscopic diffusivities of ions, in particular of chloride, are quantified. Finally, the

significance of the surface effects in the context of cement resistance to chloride attack is discussed in the light of established experimental results in the literature

**Chapter 7** is the conclusion of the thesis. It summarizes the main findings from this work and discusses the possible ways to explore the remaining open questions on the subject.

## IV. References

- [And2018] Andrew, Robbie M. "Global CO<sub>2</sub> emissions from cement production." *Earth System Science Data* 10.1 (2018): 195-217.
- [Ashby2012] Ashby, Michael F. *Materials and the environment: eco-informed material choice*. Elsevier, 2012.
- [Brun2004] Brunet, F., et al. "Application of <sup>29</sup>Si homonuclear and <sup>1</sup>H–<sup>29</sup>Si heteronuclear NMR correlation to structural studies of calcium silicate hydrates." *The Journal of Physical Chemistry B* 108.40 (2004): 15494-15502.
- [Broom2003] Broomfield, John. *Corrosion of steel in concrete: understanding, investigation and repair*. Crc Press, 2003.
- [Bentz1991] Bentz, Dale P., and Edward J. Garboczi. "Percolation of phases in a three-dimensional cement paste microstructural model." *Cement and concrete research* 21.2-3 (1991): 325-344.
- [Cong1996] Cong, Xiandong, and R. James Kirkpatrick. "<sup>29</sup>Si and <sup>17</sup>O NMR investigation of the structure of some crystalline calcium silicate hydrates." *Advanced Cement Based Materials* 3.3-4 (1996): 133-143.
- [Chap1913] Chapman, David Leonard. "LI. A contribution to the theory of electrocapillarity." *The London, Edinburgh, and Dublin philosophical magazine and journal of science* 25.148 (1913): 475-481.
- [Gra1947] Grahame, David C. "The electrical double layer and the theory of electrocapillarity." *Chemical reviews* 41.3 (1947): 441-501.
- [Gouy1910] Gouy, M. J. J. P. T. A. "Sur la constitution de la charge électrique à la surface d'un électrolyte." *J. Phys. Theor. Appl.* 9.1 (1910): 457-468.
- [Helm1879] Helmholtz, H. von. "Studien über electrische Grenzschichten." *Annalen der Physik* 243.7 (1879): 337-382.
- [IPCC2014] IPCC, A. "IPCC Fifth Assessment Report—Synthesis Report." (2014).
- [Lipp1982] Lippmaa, E., et al. "A high resolution <sup>29</sup>Si NMR study of the hydration of tricalciumsilicate." *Cement and Concrete Research* 12.5 (1982): 597-602.
- [ScrivCourse] Material for lecture MSE-322 "Building materials + Laboratory work" by Karen Scrivener, Undergraduate level, EPFL, 2022
- [Sui2019] Sui, Shiyu, et al. "Towards a generic approach to durability: Factors affecting chloride transport in binary and ternary cementitious materials." *Cement and Concrete Research* 124 (2019): 105783.
- [Ste1924] Stern, Otto. "Zur theorie der elektrolytischen doppelschicht." *Zeitschrift für Elektrochemie und angewandte physikalische Chemie* 30.21-22 (1924): 508-516.
- [Taylor1997] Taylor, Harry FW. *Cement chemistry*. Vol. 2. London: Thomas Telford, 1997.
- [Wilson2022] Wilson, William, et al. "Insights on chemical and physical chloride binding in blended cement pastes." *Cement and Concrete Research* 156 (2022): 106747.



# Chapter 2 Literature review

This chapter is an overview of the current state of the art understanding of chloride ingress in cementitious materials. It starts with presenting the degradation mechanisms resulting from chloride attack. Secondly, the chloride binding capacity of concrete is discussed by introducing the two main binding mechanisms responsible of mitigating chloride ingress. Then follows an account of the empirical models commonly used to quantify the resistance of OPC and blended cements to chlorides exposure. The theoretical and experimental work on the microstructure of cement paste, being a vital factor in the binding and transport properties of concrete, is also reviewed. Finally, in the optic of developing more insightful models, our current understanding of the atomic-scale phenomena is summarized.

Chapter 2 Literature review.....	35
I. Chloride ingress : A major threat to reinforced concrete.....	37
II. Binding mechanisms of chloride in cementitious materials.....	39
A. The chemical binding .....	39
B. The physical binding .....	40
III. Standard approach for the quantification of chloride ingress.....	40
A. Empirical modelling of chloride ingress and limitations.....	40
B. Characterisation of blended systems: Need for a fundamental understanding of the small scales.....	43
IV. The microstructure of cement paste: A key parameter in the study of ionic transport.....	43
A. Pore structure .....	44
B. Pore solution.....	46
C. C-S-H .....	48
i) Atomistic modelling of C-S-H .....	48
ii) Morphology and microstructure models of C-S-H.....	50
V. Ionic adsorption/diffusion at the atomic scale .....	54
A. Surface charging of C-S-H .....	54
B. The classical theory of the electrical double layer (EDL) .....	54
C. The necessity of atomistic models.....	56
i) Limitations of the classical theory .....	56
ii) Experimental investigation of surface properties: The Zeta potential ( $\zeta$ ) .....	57
iii) Modelling of ionic transport at the atomic scale .....	58
VI. Conclusion.....	59
VII. References .....	60





## I. Chloride ingress : A major threat to reinforced concrete

Reinforced concrete is a composite material made of a concrete matrix in which are embedded steel reinforcing bars (rebars). It has not only high resistance to compressive stresses but also good performance in tension mainly due to the presence of the steel reinforcement. For this reason, reinforced concrete is a very reliable construction material that is extensively used in buildings, bridges and more. These structures are often exposed to aggressive environments that can deteriorate the mechanical performances of the concrete and ultimately threaten the integrity of the whole structure.

Steel is a thermodynamically unstable metal that, like most metals, is prone to corrosion in presence of water or oxygen under normal atmospheric conditions. Concrete is, however, an alkaline environment with pHs between 12.5 to 13.8 [Loth2010, Sui2019(2)]. At high pH, a thermodynamically stable oxide layer forms on the steel (Fig.2.1). It is called steel passivation. This protective passivity layer does not actually stop corrosion but significantly slows down its progress. The corrosion rate of passive steel in concrete is approximately  $0.1 \mu\text{m}$  per year. Without the passive film, the steel would corrode at rates at least 1000 times higher [Glass1997].

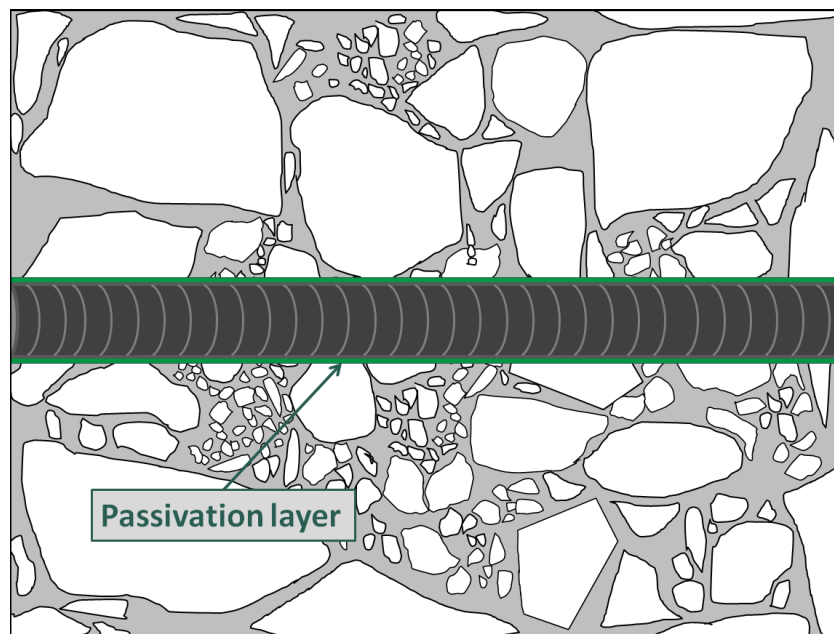
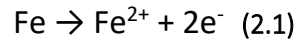


Fig.2.1. Protective passivation layer around embedded steel rebars in concrete

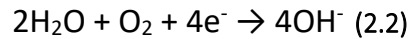
Exposure to chloride is the primary cause of premature corrosion of reinforcement rebars. This can be caused, for example, by de-icing salts or when in contact with sea water in marine environments. Verbeck [Verb1975] described chloride ions as “a specific and unique destroyer”. The mechanisms by which chloride promotes corrosion remain only partly understood but here is a brief description of the corrosion phenomenon [Nev1995].

Corrosion is an electrochemical process involving the flow of charges (electrons and ions). In reinforced concrete, the rebar may have many separate areas at different electrical potentials which creates anodic and cathodic regions. Pore solution acts as the electrolyte, and the metallic connection is provided by the rebar itself. At active sites on the bar, called anodes, iron atoms lose

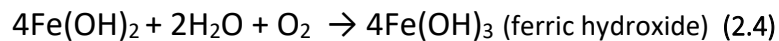
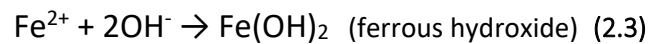
electrons and pass into the surrounding electrolyte as ferrous ions  $\text{Fe}^{2+}$ . This process is called the anodic reaction and can be written as follows:



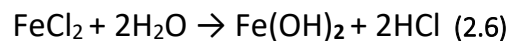
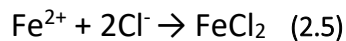
The free electrons remain in the metal and flow to sites called cathodes, where they combine with water and oxygen in the concrete to form hydroxyl ions  $\text{OH}^-$ . The reaction at the cathode is called a cathodic reaction or a reduction reaction and it can be written as follows:



To maintain electrical neutrality, the ferrous ions migrate through the pore solution to these cathodic sites where they combine to form ferric hydroxides which is converted by further oxidation to rust:



But for the corrosion to be actually initiated, the passive layer has to be penetrated. The action of chloride ions is to break down this protective film which they do by converting the steel into an anode and the passivated surface into the cathode:



The previous reactions translate into a drop in the pH. Chloride ions continue to regenerate since they only form iron chloride at an intermediate stage (2.5) but eventually revert back to their ionic form (2.6).

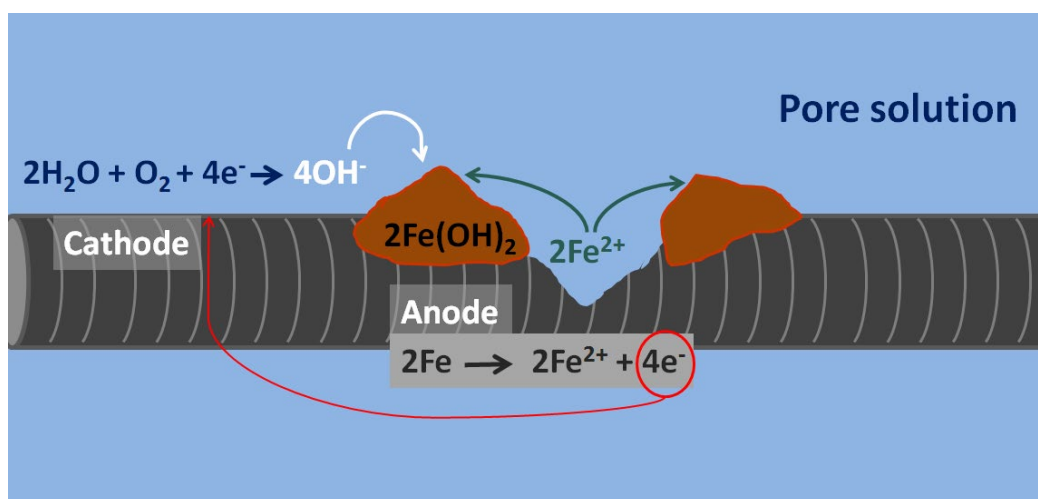


Fig. 2.2. Corrosion of a steel rebar in contact with pore solution

It is important though to mention that chloride corrosion initiates only when a certain minimum concentration of chloride reaches the steel surface. Fixing a threshold is not obvious as it depends on a multitude of parameters (presence of chloride in the original mix, non uniform distribution of chloride in the paste, etc) that are not yet fully understood [Glass1997]. Moreover, a number of chlorides can find themselves chemically bound, adsorb on hydrates surfaces or even be incorporated in some of the cement hydration products. So it is not the total amount of chloride present in the system that matters but rather the so-called free chlorides\*.

The usually mentioned consequence of steel corrosion is the volume increase of the corrosion products that leads to internal stress within the hardened concrete causing cracking and spalling. A second effect is the reduction of the steel cross-section due to the progress of the corrosion reaction which ultimately reduces the load-carrying capacity of the rebars [Nev1995].

## II. Binding mechanisms of chloride in cementitious materials

As previously mentioned, cementitious systems have the capacity to trap chloride ions by so-called binding mechanisms. Chloride binding has an important effect on the initiation of steel corrosion. By decreasing the amount of free ions, binding chloride does not only reduce the rate at which chloride ions diffuse through concrete but it also decreases the amount of mobile chlorides accumulating at the steel surface. Binding mechanisms of chloride in cementitious materials are twofold: chemical and physical.

### A. The chemical binding

Cement hydration results in many products among which are AFm (aluminate ferrite mono) and hydrotalcite phases [Bernard2022]. These hydration products classify as layered double hydroxides (LDHs). They are a class of ionic solids and their general formula is  $[M^{2+}_{1-x}N^{3+}_x(OH^-)_2]^{x+} [(A^{n-})_{x/n}] \cdot mH_2O$  where  $[M^{2+}_{1-x}N^{3+}_x(OH^-)_2]^{x+}$  are the main double layers and  $[(A^{n-})_{x/n}]$  is the intercalated anion (or anions with total charge x-).

In the case of AFm, a representative formula is  $[(Ca^{2+})_2(Al^{3+}, Fe^{3+})(OH^-)_6]^{+1} \cdot A^{-1} \cdot mH_2O$  where a third of the divalent cations  $Ca^{2+}$  [ $M^{2+}_{1-x}$  in the general formula] have been replaced by trivalent  $Al^{3+}$  or  $Fe^{3+}$  cations. It results in a positively charged layers that is compensated by an intercalated anion  $[(A^{n-})_{x/n}]$  such as  $SO_4^{2-}$  or  $Cl^-$  in the interlayer. Thanks to their structure, AFms efficiently bind chloride by forming stable products [Dam1994] such as Friedel's salt [Bir1998] and Kuzel's salt. Through this chemical binding, AFms permanently trap ions and act as a sink for chloride ions hence retarding their diffusion. Estimating the amount of chemically bound chlorides in the AFm phases is challenging but possible through various experimental methods. The two main techniques that are usually applied are TGA and XRD-Rietveld analyses.

---

\* The amount of free chlorides is usually estimated from the total porosity by assuming that, at equilibrium, the chloride concentration in the pore solution is equal to the concentration in the exposure solution [Wilson2022]

## B. The physical binding

Experimental work on chemically bound chloride has shed some light on the contribution of Friedel's salt and the amount and location of chlorides in AFm phases. It has also proved that a non-negligible proportion of the bound chloride (non free chloride) resides in other hydrates and principally C-S-H as it is the main hydration product. This is the so-called physically bound chloride. It can be calculated by (i) subtracting free chlorides (obtained by isopropanol extraction) and chemically bound chlorides from the total chloride (measured by titrating the ground samples) or (ii) measured with EDS point analysis to identify the composition of C-S-H.

The panel of techniques used to measure physically bound chloride is limited and results are usually quite approximate. It is assumed that the physical binding occurs through the adsorption of chlorides on the C-S-H surface. The electrical double layer (EDL) theory, which describes the interaction between ions in the pore solution with the C-S-H interface, predicts that chlorides reside in the diffuse layer. It is an area where chlorides are under the electrostatic influence of the surface without forming actual chemical bounds. Thus, it is reasonable to assume that physically bound chloride enjoy some degree mobility which allow them to eventually diffuse. However, many questions arise about the residency time of adsorbed chlorides and to what extent does the physical binding affect chlorides ingress in cementitious materials.

In order to push our understanding of chlorides adsorption but not only, cement scientists have spent over 60 years investigating the complex structure of C-S-H. But to properly understand the forces in action between C-S-H's interface and the pore solution, it has become clear that we have to go down to the microscopic scale where the mechanisms operating are less well understood. A lot of promising work has been achieved during the last couple decades but many areas of the domain remain poorly understood.

*The physical binding of chloride, which is the main subject of the present thesis, will be discussed in more detail in **section V** after the introduction of some key concepts in **section IV** about the microstructure properties of cement paste and the prominent role that C-S-H plays.*

## III. Standard approach for the quantification of chloride ingress

### A. Empirical modelling of chloride ingress and limitations

In order to study and quantify the transport of chloride in hydrated cement, the conditions of sea water immersion are simulated in the laboratory. One way to do this consists in conducting bulk diffusion experiments [ASTM]. This experiment consists in leaving mortar or concrete in a known NaCl solution for a certain period of time (6 months to a few years). After drilling, powder grinding and finally chloride titration of samples obtained at different depths, profile of total chloride content can be plotted as a function of depth. Such work has recently been conducted on a variety of blended systems by Sui et al. [Sui2019] with results represented in Fig.2.3.

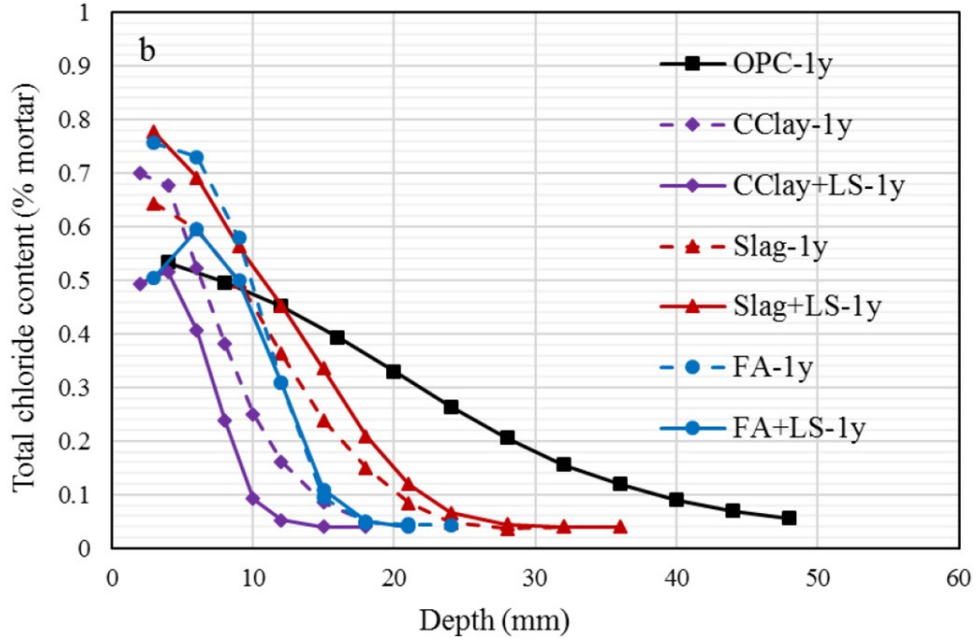


Fig.2.3. Chloride profile for OPC and blended systems with different SCMs: CClay=Calcined Clay, LS=Limestone, FA=Fly Ash; after 1 year exposure to a 0.5 M NaCl solution. Taken from [Sui2019(2)]

Given the profiles on Fig.2.3, it seems that we can, through observation, rank the resistivity of the different systems to the chloride ingress. Nonetheless, before any qualitative predictions, a main question remains: how can we quantitatively classify these systems?

A first empirical modelling approach would rely on the fact that the chloride content curves (Fig.2.3.) look like diffusion profiles. Therefore, a way to quantify the transport is to fit experimental data on a diffusion equation such as the macroscopic Fick's second law of diffusion [Chatterji1995]:

$$\frac{\partial C}{\partial t} = D_a \frac{\partial^2 C}{\partial x^2} \quad (2.7)$$

If we fix the boundary conditions (BC) to (2.7) and we assume a constant and homogeneous diffusion coefficient  $D_a$  [ $\text{m}^2\text{s}^{-1}$ ], the partial differential equation can be solved analytically, and the solution is the following:

$$C(x, t) = C_{BC} \operatorname{erfc} \left( \frac{x}{2\sqrt{D_a t}} \right) \quad (2.8)$$

Hence, the apparent diffusion coefficients  $D_a$  are back calculated for each of the systems by fitting the solution (2.8) to the different chloride profiles in Fig.2.3. The computed apparent diffusion coefficient does not, however, represent the real diffusion of physical species. It could be interpreted as the diffusion of the penetration depth. Moreover, due its oversimplified representation (i.e. important processes not considered), Fick's law actually amalgamates matter diffusion and binding mechanisms of chemical species with solid phases.

For a more physical interpretation, Sui et al. [Sui2019(2)] tried to connect transport to microstructure by looking at the relation between the apparent diffusion coefficient and the pore structure parameters; total porosity and critical pore diameter (Fig.2.4):

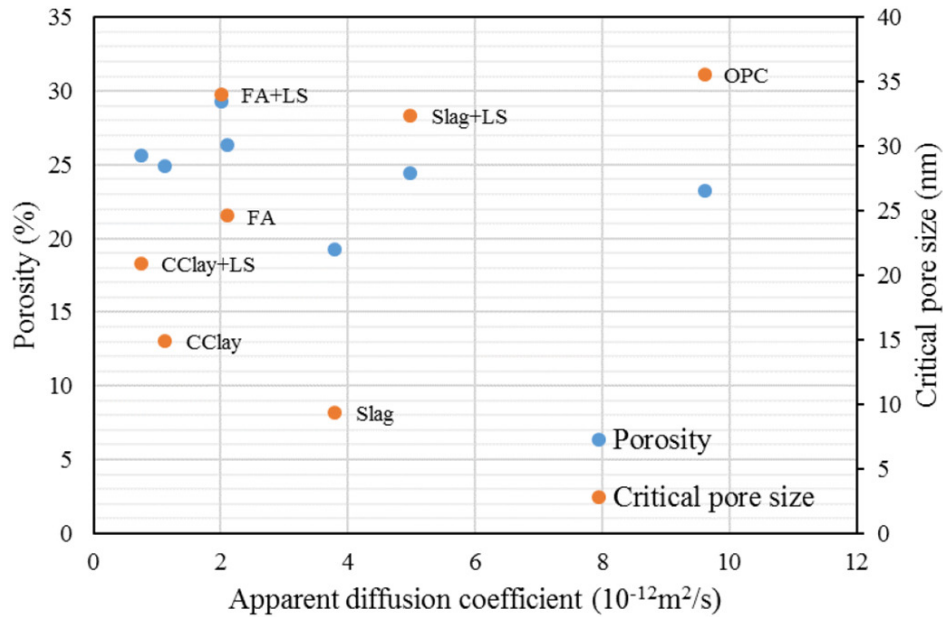


Fig.2.4. Relationship between the apparent diffusion coefficient and porosity, critical pore size of different blended systems: CClay=Calcined Clay, LS=Limestone, FA=Fly Ash. Taken from [Sui2019(2)]

Looking at the Fig.2.4, it seems there is no clear correlation between  $D_a$  and porosity. This may, in fact, indicate that  $D_a$  does not have a consistent physical meaning or rather imply that the use of the porosity parameter is ill-defined. In reality, the apparent diffusion coefficient englobes a multitude of parameters including the contribution of binding, porosity (total porosity, pore classes...), pore solution properties such as pH and even the water saturation degree of the paste... And while the hypothesis  $D_a = f(\text{Porosity})$  usually does make sense once studying simple PC systems, it is not very helpful in the investigation of blended systems. In order to classify inherently different systems and ultimately being able to determine the best cement formulations, it is important to decouple the various parameters lumped in  $D_a$  and measure separately the contribution of each variable.

Another modelling alternative is to use reactive transport models [Huet2010, Jens2015, Georg2017, Tran2018] where chloride content evolves (i) through the contribution of the mass transport and (ii) a “retardation” term which plays the role of a sink/source term representing the binding processes i.e. both chemical binding and adsorption on solid phases:

$$\frac{\partial [Cl^-]}{\partial t} = -\nabla \cdot (D_e \nabla [Cl^-]) - \frac{\partial s_{Cl-}([Cl^-])}{\partial t} \quad (2.9)$$

Where  $[Cl^-]$  in  $[\text{mol L}^{-1}]$  is the concentration of chloride in the solution as function of time,  $s_{Cl-}[Cl^-]$  in  $[\text{mol L}^{-1}]$  is the chloride bound in solid phases and  $D_e$  in  $[\text{m}^2 \text{s}^{-1}]$  is the effective diffusion coefficient.

In this context, migration tests under moderate electric potential difference [Cast1999, Yang2003, Yang2006, Yuan2009, Wilson2021] are conducted as an “accelerated” alternative to the bulk diffusion experiment and result into the measure of the flux [ $\text{mol m}^{-2} \text{s}^{-1}$ ] as a function of time. The chloride effective diffusion coefficient is therefore back calculated by resolving the diffusion equation (2.9). This approach has obviously the merit of de-convoluting mass transport and chemical reaction. However, results are usually qualitative and the computation of diffusion coefficients remains quite far from accurate quantitative predictions. In fact, such a complex model requires a lot of parameters (initial composition, initial porosity...). Moreover, for reactive transport models, these parameters are functions of the advancement of the chemical reactions. Thus, the calibration and validation of the model requires a large set of consistent experimental data [Georg2017].

## B. Characterisation of blended systems: Need for a fundamental understanding of the small scales

Measuring transport properties (typically ionic diffusion coefficients) is usually long and uncertain [Mcgrath1999, Yang2005, Stanish2001]. And even when experimental data are thoroughly obtained, most of the used models are not predictive and often interpretation dependent, since they essentially rely on fitting. In the case of blended systems, the application of standard transport models, such as previously discussed, provides very little insight on the mechanisms that are at the origin of ionic adsorption. In fact, the incorporation of different SCMs in the cement recipe usually results in deep alterations of the chemical processes that control the formation of cement paste’s microstructure and its features at different scales. So in order to understand the change in the macroscopic properties for a wide range of blended cements, the understanding of the chemo-physical processes at smaller scales is necessary.

Since ionic diffusion, specifically of chloride, is what we are interested in, the interactions of ions in the solution and with their environment (solid phases and mainly C-S-H) cannot be neglected. Fundamental understanding of atomistic phenomena and proper quantification of their effects on diffusion of ions is important. In order to compare with experimental data, bridging such nanoscopic contributions to the bigger scales is necessary. However, consistent transport models at different scales are generally missing in cement science.

## IV. The microstructure of cement paste: A key parameter in the study of ionic transport

Concrete is a constantly changing material (not in thermodynamic equilibrium) gradually shifting towards a (meta-) stable state. A simple proof of this statement lies in all the possible deterioration mechanisms that can touch concrete-made structures. Exposure to an aggressive chemical environment, such as seawater, can generate corrosion of rebars induced by chloride ingress or the disintegration of concrete due to sulfate attack. Destructive weathering factors, such as freezing and thawing, can cause expansion of the paste in saturated concrete and cracking. Therefore, concrete constantly reacts to its environment.

Hydrates also continue to form with time i.e. the microstructure of cement paste “never” stops evolving. This equally applies to the transport properties which are microstructure dependent



[Neith2010]. It means that ionic effective diffusivities are function of porosity, pore size distribution, pore classes which in turn are function of w/c, the hydration degree, initial particle size distribution... Hence, a representative model of the microstructure of cement paste is critical for the understanding and the prediction of ionic transport. And among all the microstructure variables, ionic transport (and specifically chloride's) requires an even deeper understanding of three system-dependent parameters: (i) The structure of C-S-H, which as the major phase of cement paste, greatly influences transport properties, (ii) pore structure which depicts the size distribution of pores at different ages of the cement paste and (iii) the pore solution that contains chloride but also other species that can strongly affect the mobility of all ions and the surface properties of the hydrates.

## A. Pore structure

Porosity is one, if not the most, important feature of the microstructure of cement paste. It affects major properties such as mechanical strength and permeability. And not only does the total porosity influence mechanical and transport properties of cement paste, but so does the structure (size, shape, connectivity...) of these pores. It has been shown for example that keeping a constant total porosity while changing pore structure through processing ends up in a change of the material's properties [Lange1991]. Pore structure is, however, challenging to assess experimentally since direct measurements are particularly difficult to perform and can easily alter the original structure. For this matter, indirect methods such as Mercury intrusion porosimetry (MIP) or Nitrogen adsorption method have been used instead to characterize pore structure. However, the interpretation of data obtained through such techniques usually relies on making assumptions on the geometry of pores that prove to be rather rough and non-representative. To faithfully represent the microstructure of cement paste, previous methods have been accompanied with other characterization techniques such as SEM (Scanning Electron Microscopy) or NMR (Nuclear magnetic resonance) to get a more accurate description of the pore structure [Prom2009, Gallucci2007]. <sup>1</sup>H NMR experiments, on the other hand, provide information on the location and the exchange of water between the different pores [McDon2005, Valori2013].

Thanks to these observation techniques, it has been established that cement paste has a hierarchical pore structure. In fact, it is possible to classify pores accordingly to their size as it follows:

- Air voids: 10  $\mu\text{m}$  to 1mm
- Capillary pores: 50 nm to 10  $\mu\text{m}$
- Inter hydrate pores: ~8-20 nm
- Gel pores: 1 to 10 nm

Berodier et al. [Berod2015] used MIP measurements to track down the evolution of the pore structure in PC and blended systems. MIP curves of the PC paste at different ages (Fig.2.5.) show basically that the volume and the critical radius of pores penetrated by mercury decrease as a function of the curing time. As the sample ages, hydrates fill the space and the porosity refines. The maximum pore entry radius went from sizes up to 100nm, at 1 day age, down to a population dominated by pores below 10nm of diameter after 14 days and beyond.



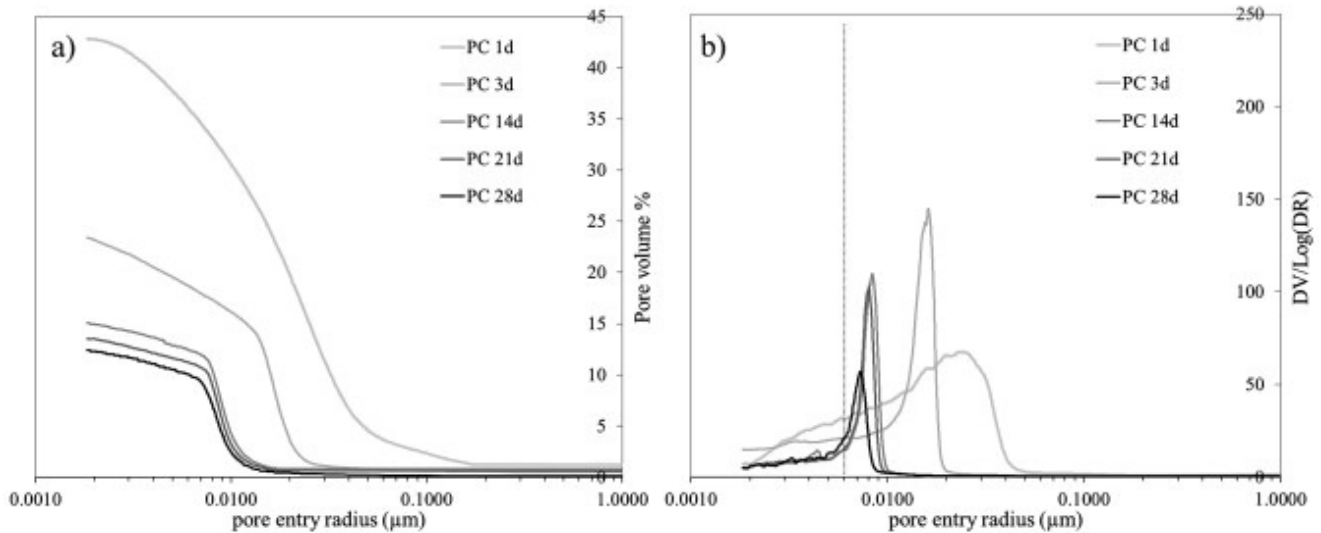


Fig.2.5. Cumulative (a) and derivative (b) curve of the pore structure from MIP measurements on Portland cement paste samples (w/c = 0.4). Taken from [Berod2015]

Nonetheless, pore structure information is more than merely identifying the pore size distribution of a cement paste sample. As we are interested in chloride diffusion, it is equally important to investigate the location of water in the pores as diffusion of ions only occurs through saturated pores. In this regard,  $^1\text{H}$  NMR is the ideal tool to probe water molecules. It is a non-invasive technique (for example no drying necessary) that provides detailed data on the state of water in pores of various sizes.

In their paper [Muller2013], Muller et al. performed  $^1\text{H}$  NMR measurements on a cement paste with w/c = 0.4 and showed the evolution of the NMR signal of different water populations as function of the hydration time. In sum, Fig.2.6 shows that the signal corresponding to capillary water (in big pores) drops with time (especially the first 48h) while the signal attributed the C-S-H gel pore water firstly increases and then reaches a plateau signal (also after 48h). In simple words, as the hydration reaction is going on, water is basically filling up the smaller pores. Beyond the structural data, these measurements actually provide evidence that, in cement pastes of low w/c ratios ( $\sim 0.4$ ), C-S-H is the main percolating phase. In fact, the C-S-H gel porosity substitutes to the capillary pore network (which dominates at higher w/c ratios  $\sim 0.7$ ) to become the major pathway for water and ions to diffuse. Quantifying the effect of the pore size ( $<10\text{nm}$ ) on ionic mobility is, therefore, of vital importance to understand chloride diffusion.

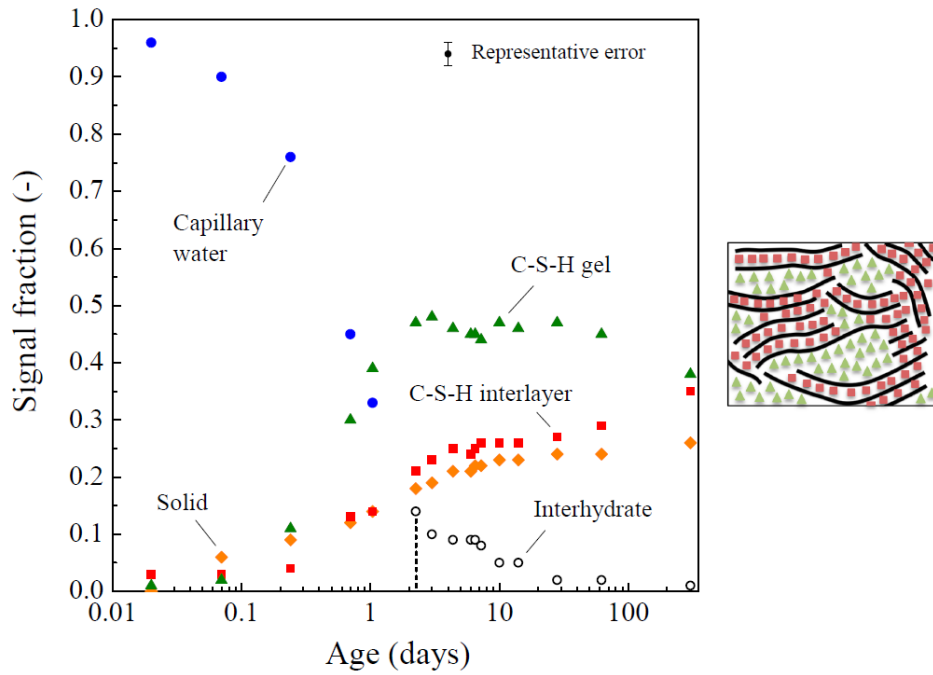


Fig.2.6. Evolution of the different NMR signal fractions with hydration time ( $w/c = 0.40$ ). Blue circles are free water, becoming interhydrate water (empty black circles) beyond 2 days of hydration. The estimated error is  $\pm 2\%$ . Taken from [Muller2014, p.56]

## B. Pore solution

Pore solution may be simply defined as the electrolytic alkaline solution that resides within the saturated pores in the cement paste. It is characterized by a pH ranging from 13 to 13.8 due to the presence of alkali, mainly sodium and potassium. Given the low concentration of  $\text{Ca}^{2+}$  (usually a few mmols), calcium doesn't contribute much to the alkalinity. However, portlandite ( $\text{Ca}(\text{OH})_2$ ) that forms during hydration plays the role of an alkali reserve and buffers pH at approximately 12.6. An example of the composition of the pore solution in a PC paste ( $w/c = 0.4$ ) at 69 days of hydration is presented in Tab.2.1.

Pressure (MPa)	Li (mM)	Na (mM)	K (mM)	Ca (mM)	Sr (mM)	Al (mM)	Si (mM)	S (mM)	OH (mM) <sup>a</sup>	pH	C.B. <sup>b</sup> (%)
60 – 120	0.69	46	450	1.8	0.046	0.09	0.21	8.2	490	13.6	0
120 – 150	0.69	49	480	2.0	0.050	0.09	0.21	9.2	490	13.6	5
150 – 180	0.69	49	480	2.0	0.050	0.09	0.23	10	490	13.6	5
180 – 270	0.69	50	490	2.0	0.050	0.09	0.24	12	490	13.6	7
270 – 330	0.63	50	480	1.9	0.050	0.09	0.26	13	500	13.6	1

Table.2.1. Concentrations of different species present in the pore solution of a PC paste ( $w/c = 0.4$ ) at 69 days of hydration. Measurements have been obtained through pore solution extraction at pressures going from 60 MPa up to 330 MPa. Taken from [Loth2010]

<sup>a</sup> The values of  $\text{OH}^-$  refer to free concentrations, all other values represent total concentrations.

<sup>b</sup> The charge balance error C.B. gives the surplus of cations (cations – anions), relative to the total charge caused theoretically by cations (i.e.  $[\text{Na}^+] + [\text{K}^+] + 2[\text{Ca}^{2+}]$ ).

As part of the same underlying chemical transformations, the pore structure, along with the pore solution, evolves through time. Its composition also greatly depends on the system so that trends that have been established for PC might radically change once SCMs are added [Voll2016]. Hence, the study of the pore solution in blended systems and its evolution are essential, given that it may strongly impact the system's durability, in general, and its resistivity to chloride ingress in our particular case. The correlation between ionic diffusion and pore solution remains poorly understood though and is, up to this day, an ongoing subject of research [Nguy2006, Elaknes2009, Barbarulo2000, Tang1999]. Nonetheless, despite the limited understanding that experimental work and macroscopic models provide, it was possible to unravel some features of the strong link between ionic transport and pore solution.

Sui et al. [Sui2019(2)] compared the apparent diffusion coefficient to the content of alkali in the solutions as another parameter of the microstructure:

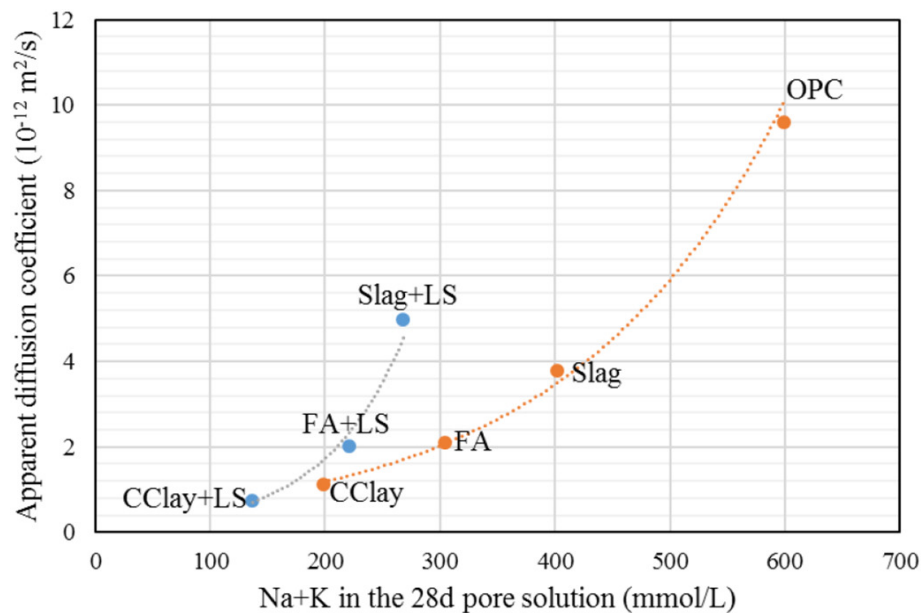


Fig.2.7. Evolution of the apparent diffusion coefficient with respect to the alkali content in the pore solution. Taken from [Sui2019(2)]

In Fig.2.7, we do observe the increase of the apparent diffusion coefficient with the alkali content. However, the phenomena explaining such a trend are not obvious. To unravel all the mechanisms, it would require a more fundamental understanding of how the alkali content interacts with chloride and its environment. In spite of the multitude of parameters in action, three main phenomena seem to dominate: the conservation of electroneutrality, the non-ideality of the solution and the surface effects.

Due to their specific radii and valences, ions normally have different effective diffusion coefficients. According to the local conservation of electroneutrality, faster ions are slowed down while slower counterions are accelerated. The Nernst-Planck equation is commonly used to model such an effect [Zhang1996]. Still, the complexity of the pore solution [Yone1988, Sare2002, Goni1990] generally makes it difficult to predict the extent of these effects on chloride diffusion.

Secondly, cement paste's pore solution is a strongly non ideal electrolyte. As a result, the driving forces of diffusion are the gradients of chemical potential, which account for finite ionic size, and no more simplify to the usual concentration gradient [Barbarulo2000]. In most cementitious systems, the pore solution has an ionic strength typically around 0.5M (mol/L) (example in a PC paste in Tab.2.1). In this range of high concentrations and high pH, most mean field models fail [Beth2022]. Therefore, to understand the effects of ionic strength in these systems, further studies on the microscopic scale are needed.

As for surface effects, C-S-H has a high specific surface area ( $\sim 200\text{-}300\text{ m}^2\text{g}^{-1}$ ) [Kantro1959, Brun1973]. This literally means that a large part of the pore solution is in contact with C-S-H. The composition of the solution could influence the surface properties [Viallis2001]. For example, the presence of alkali may affect the adsorption of chloride [DeWeerd2015]. However, the influence of the surface and its effect on chlorides or alkalis is still not fully understood.

## C. C-S-H

Calcium Silicate Hydrate, also called C-S-H, is usually known as the main product of the hydration reaction of cement. It is also important to remind, given that transport is the main focus here, that C-S-H is also the main percolating phase. In other words, understanding the mechanisms of chloride diffusion and quantifying it within the C-S-H phase would allow us to transpose that knowledge to all cementitious systems where C-S-H is the dominant phase.

An extensive amount of experimental work has been conducted through the years in order to determine the C-S-H atomistic structure. X-Ray diffraction analysis has showed that C-S-H is a poorly crystalline mineral that displays some degree of order [Ren2009(1), Ren2009(2), Skin2010] thus the use of the terminology “nanocrystalline”. Moreover, C-S-H has a variable stoichiometry with a chemical composition that may possibly vary within the same unique sample. Through X-ray spectroscopy (EDS), It was possible to characterize it by the Ca/Si (or CaO/SiO<sub>2</sub>) ratio which, according to [Rich1993], varies from 1.2 to 2.2 which translates into an average value of  $\langle \text{Ca/Si} \rangle = 1.75$ . <sup>29</sup>Si NMR spectroscopy became later on the tool of predilection to study the arrangement of silicate in C-S-H [Lipp1982, Cong1996, Brun2004] making it possible to locate and distinguish the different Si n-mers (Q<sup>n</sup>) such as the Si monomers (Q<sup>0</sup>), the end chain Si (Q<sup>1</sup>) or the connecting Si (Q<sup>2</sup>). It was eventually these observations on the silicate chain lengths which lead to assume that “the chains are formed of dimers which are linked with bridging Si tetrahedral” what is also known as the “dreierketten” structure.

### i) Atomistic modelling of C-S-H

Since 1952, the C-S-H structure has been approached by the tobermorite [Bernal1952]. More specifically, 14 Å tobermorite ( $\text{Ca}_5\text{Si}_6\text{O}_{16}(\text{OH})_2 \cdot 7\text{H}_2\text{O}$ ) is a layer-structured calcium-silicate crystal that contains water in its interlayer spaces. It is characterized by a Ca/Si ratio of 0.83, an interlayer distance of 14 Å and molar water content of 42 % [Bonac2005] and, similarly to C-S-H, it presents a “dreierketten” structure (Fig.2.8.)

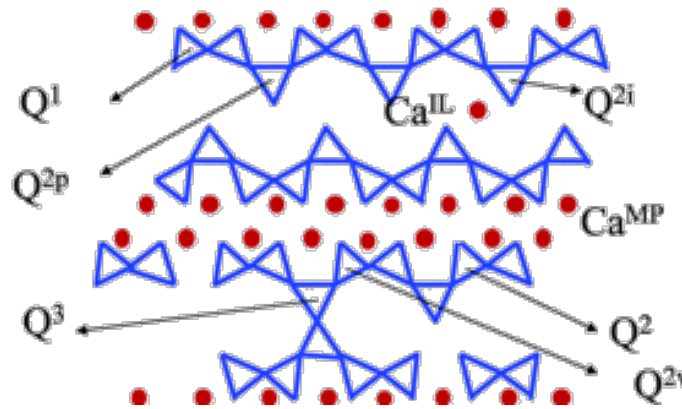


Fig.2.8. The layered structure of tobermorite is composed of a calcium plane (red dots) bordered by two silicate planes (blue chains) and separated by the interlayer space containing water molecules, hydroxyl groups and some calcium ions. The silicate planes are composed of silicate chains with a specific three-unit repetition (“dreierketten”): two silicate tetrahedra, noted as  $Q^2$ , are coordinated by calcium planes (red dots) whereas the third silicate (called the bridging tetrahedron and noted as  $Q^{2p}$  or  $Q^{2i}$ ) is not. The end-chain tetrahedra are noted  $Q^1$ . The tetrahedra linking two silicate chains in the interlayer space are noted  $Q^3$  whereas the sites  $Q^2$  next to  $Q^3$  are named  $Q^{2v}$ . The calcium ions belonging to the main plane are noted  $Ca^{MP}$  whereas those in the interlayer are noted  $Ca^{IL}$ . Taken from [Brun2004]

Further studies have then showed that for C-S-H samples with Ca/Si ratios higher than 1.0, structure was closer to a jennite-like crystal [Kirk1997]. Jennite, which chemical formula writes as  $Ca_9Si_6O_{18}(OH)_6 \cdot 8H_2O$  [Bonac2004], also displays an infinite linear “dreierketten” silicate chains but with a Ca/Si ratio of 1.5 and a molar water content of 42 %. On the same way, C-S-H has been approached by many other sheet-like minerals such as jaffeite, metajennite or other minerals [Rich2008].

Most experimental evidence seems to indicate that, for C-S-H structures with low Ca/Si ratios typically below 1.5, the 14 Å tobermorite would be the closest model structure [Kirk1997, Rich2004]. On the other hand, for higher Ca/Si ratios ( $> 1.5$ ), most opinions split between some that would (i) stand by 14 Å tobermorite as a good enough model that covers the wide range of C-S-H structures [Non2004, Rich2004] and others that (ii) would rather consider a model that mixes tobermorite and jennite structures as a better representation [Tay1986]. Later, it was found that the jennite theory was no longer tenable [Kumar2017]. More recently, it has been suggested that C-S-H conforms to a 14 Å tobermorite structure with a significant amount of defects and a low degree of silicon polymerization. From there, more questions have risen essentially about the homogeneity of C-S-H at the nanometric scale and, hence, about the distribution of these defects. Kunhi et al. [Kunhi2018] suggested an atomistic model of “a defective, nanocrystalline tobermorite structure with missing bridging silicate tetrahedra, leading to a decreased silicate chain length, and deprotonated silanol groups, the charge of which is compensated by additional calcium ions in the water-interlayer and with additional Ca-OH groups” (Fig.2.9.).

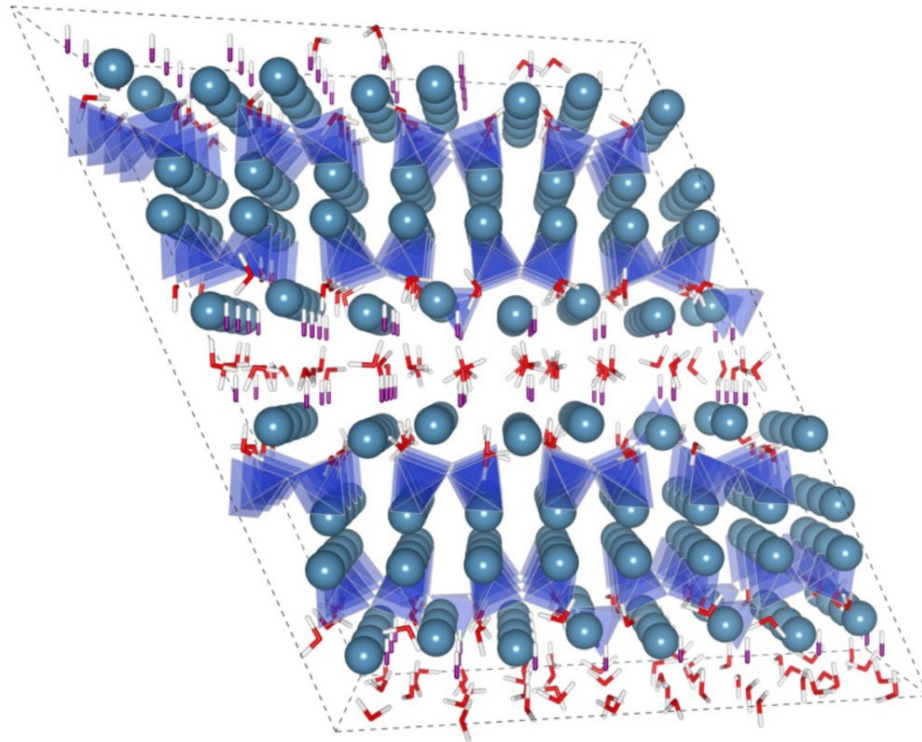


Fig.2.9. A proposed atomic structure of C-S-H with a stoichiometry  $(CaO)_{1.75}(SiO_2)_{1.0}(H_2O)_{1.86}$  with percentages of  $Q^1 = 78.3\%$ ,  $Q^{2b} = 7.25\%$  and  $Q^{2p} = 14.5\%$ . Atomic color code used are calcium - turquoise, silicon - dark blue, oxygen – red, hydroxyl oxygen – purple, hydrogen - white. Taken from [KunhiPhd2018]

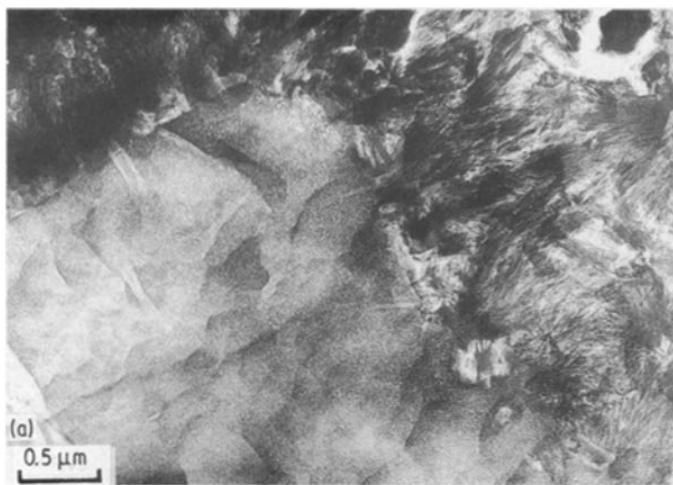
Despite the fact that most models have been developed considering only synthetic C-S-H, huge advances in the understanding of the structure of C-(A)-S-H have been accomplished during the last 80 years or so. However, there still is a lot to do. One of the main challenges that modelers are facing is the need to incorporate more ions such as aluminum, sodium and potassium in the existing models in order to approach the actual C-(A)-S-H structure that develops upon the hydration of blended cements for instance. Another critical issue, which immediately relates to our study of ionic transport, is the lack of consistent surface models. In fact, C-S-H has a high surface area and it is almost certain that all the significant interactions with the pore solution (water molecules and ionic species) are happening at this interface. Most elaborate models [Kunhi2018] are now able to create realistic bulk constructions of C-S-H. However, defects at the surface are often randomly distributed [Andro2017].

## ii) Morphology and microstructure models of C-S-H

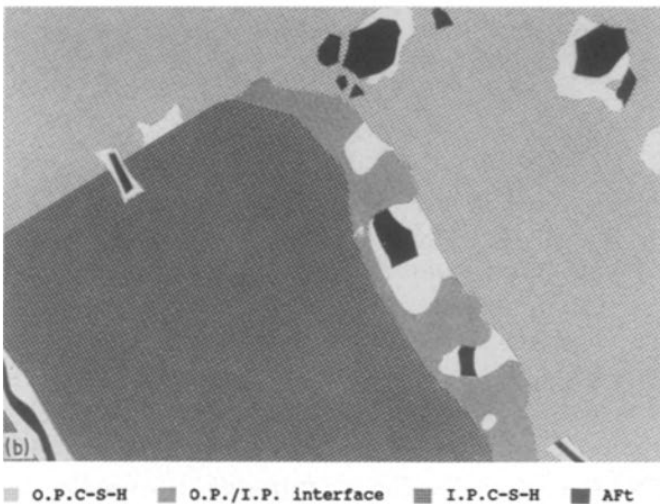
During the hydration of alite ( $C_3S$ ), portlandite (CH) forms along with two morphologically distinct C-S-H gels [Grosv1986(1), Grosv1986(2)]. We distinguish between calcium silicate hydrates as being either "inner" (Ip) or "outer" (Op) product. The Ip C-S-H forms within the boundary of the original cement grain before hydration while the Op C-S-H is usually observed in the water-filled space in the originally unhydrated microstructure.



Transmission electron micrographs obtained by Richardson et al. [Rich1993] have showed that the morphology of the outer product (Op) varies, inter alia, as a function of the space constraint. In large pore spaces, Op C-S-H shows a fibrillar and directional aspect reaching up to 100nm of diameter, while in smaller spaces, although exhibiting a directional character, it adapts its shape to the limited available space. Through the last decades, cement researchers have tried to faithfully describe the Op C-S-H morphology, relying on imaging techniques, taking into account a multitude of parameters: time and rate of formation, space availability, Ca/Si ratio, degree of polymerization... Different wordings have been used, covering a wide range of shapes, from fibrous particles, rolled sheets [Bernal1952, Diam1976], thin flakes, crumpled foils or tapered needles [Jennings1981, Scriv1984] to foil-like [Rich1999] and even, more recently, directly as needles [Ouzia2019] (Fig.2.10.).



(a)



(b)



(c)

Fig.2.10. (a) Transmission electron micrograph and (b) schematic diagram showing an inner/outer product interface region in a paste hydrated for 3 months ( $w/c = 0.4$  at  $20\text{ }^{\circ}\text{C}$ ) (Taken from [Rich1993]) (c) SEM polished section of a  $w/c = 0.7$  paste at 28 days. Sections of C-S-H “needles” are observed (points) in different areas, in particular in the bottom right. Etch pits are visible on the anhydrous white core. Taken from [Ouzia2019]

On the other hand, Ip C-S-H is commonly observed as a compact, fine-scaled and homogeneous phase [Rich1993, Rich2004]. In SEM images, Ip C-S-H is often characterized by lighter shades of grey compared to the Op C-S-H which appears darker due to its lower density. In fact, the porosity in Ip C-S-H is typically more refined than Op C-S-H with sizes around 10nm and below.

Relying on the previously mentioned experimental observations, many microstructural models have been developed to provide a complete spatial representation of the C-S-H at the microscopic scale (1-100nm scale). Among the first microstructural representations, there is the Feldman and Sereda model [Feld70] where the authors favored a sheet-like morphology of C-S-H that accounted for its layered atomistic structure and aligned with experimental data on the irreversible changes upon drying and rewetting of cement samples. Johnson and Jennings [Jennings1986] first presented the idea of modelling cement hydration as nucleation and growth of spherical particles in three-dimensional space. Bishnoi et al. [Bish2009] developed a "space filling" growth model implemented in the open-source modelling platform "μic" (pronounced Mike as in MICrostructure). The software also managed to remedy limitations of other models on the number of particles handled. Nonetheless, many of the microstructural models at the time did not match with SEM observations of the needle-like or foil-like shape of C-S-H. They also failed to correctly reproduce the C-S-H nanoporosity which was a key feature in the very high specific surface area of the hydrate. In the context of transport, Patel et al. [Patel2018] showed that, in the absence of micro-cracks, the gel/inter-hydrates porosities form the main pathway for ions to diffuse. Therefore, more C-S-H models accounting for the nano-porosity have been developed: Colloidal models [Jennings2000, Jennings2008, Ioan2016], disk packing models [Yu2016] or sheet-based models [Etzold2014] (Fig.2.11.).



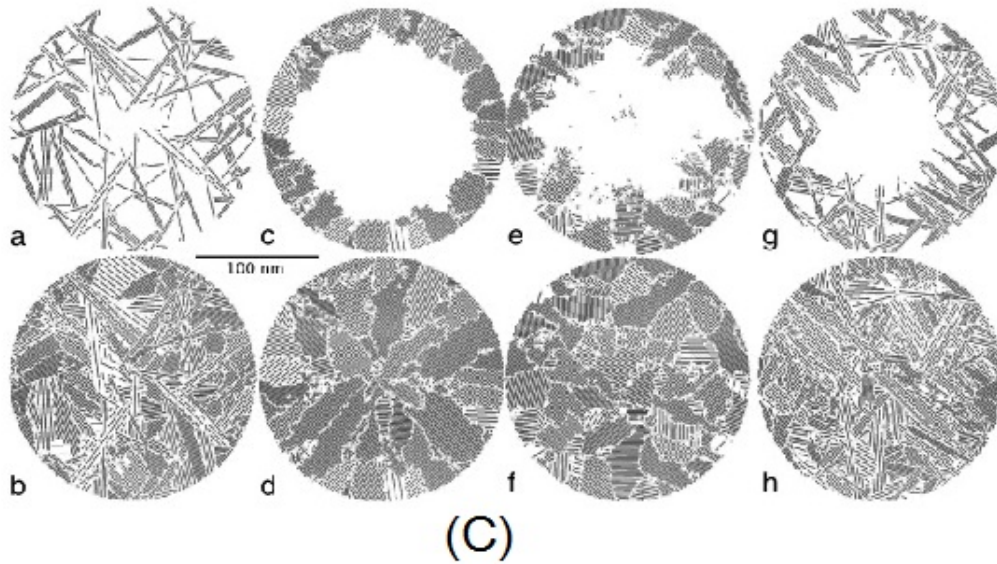
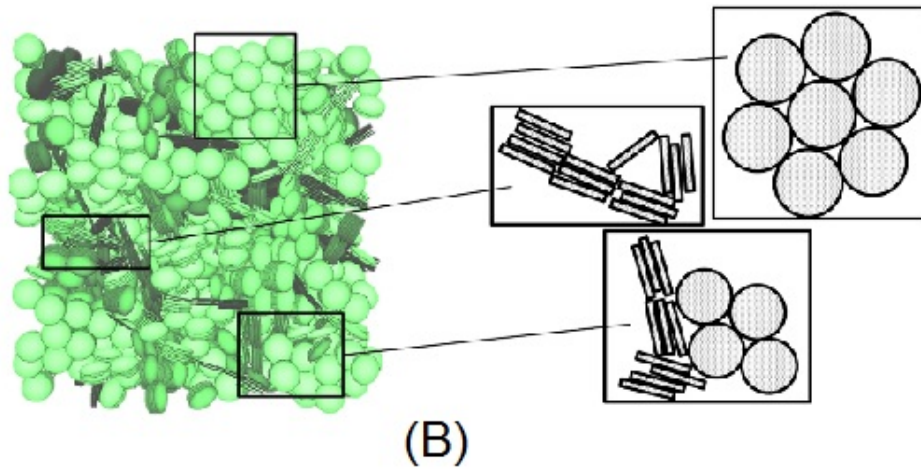
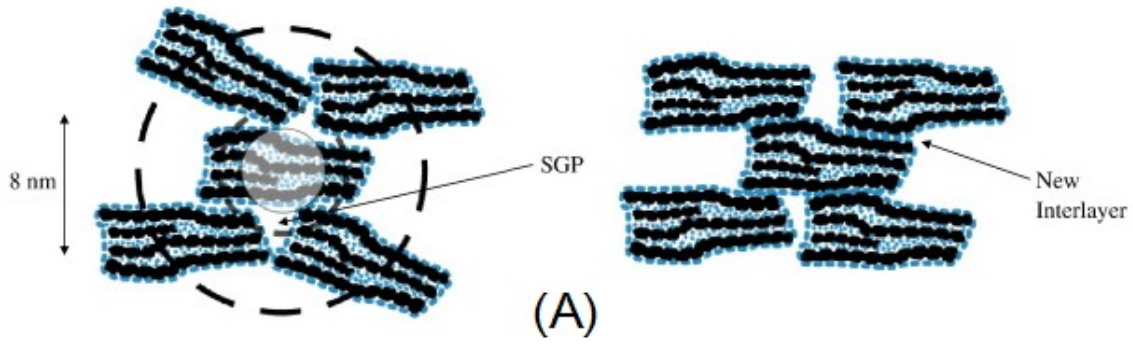
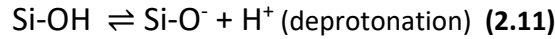
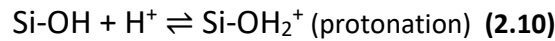


Fig.2.11. (A) Packing of globules showing small gel pores (SGP) (Taken from [Jennings2008]) (B) Configuration of the coarse-grained C-S-H model, after equilibration, where three featured structures can be found (Taken from [Yu2016]) (C) Example of structures generated with the sheet growth algorithm using different growth parameters. Taken from [Etzold2014]

## V. Ionic adsorption/diffusion at the atomic scale

### A. Surface charging of C-S-H

As most minerals, C-S-H develops a charge at its surface when put in contact with an electrolytic solution. The stoichiometry and structure of these C-S-H surfaces is thought to be a strong function of the synthesis path as well as the composition of the pore solution at equilibrium [Non2004]. Once in contact with water, the surface  $(\text{SiO}_4)^{4-}$  sites are hydroxylated [Dam1995] and C-S-H surface develops a silanol (Si-OH) surface density. These silanol (Si-OH) groups can, more or less, ionize depending on the pH value of the solution through acid-base reactions which can be summarized by the following equations:



As C-S-H dissolves for values of  $\text{pH} < 10$  and since pore solution has usually pH values above 12.5 (typically between 13 and 13.8), the deprotonation (2.11) of silanol groups of the C-S-H occurs. Moreover, the degree of deprotonation of the surface goes up as pH increases, thus charging negatively the surface of the C-S-H [Lab2006, Lab2011, Chu2014].

### B. The classical theory of the electrical double layer (EDL)

In 1853, Helmholtz [Helm1853] was the first to discover the forming of a layered structure which forms around a charged solid surface when it interacts with a liquid. Due to the excess charge at the surface, the mobile ions distribute inhomogeneously around the surface. In proportion to the charge at the surface, ions with opposite charges (counterions) accumulate near the interface to neutralise the surface charge while ions with the same charge (co-ions) are depleted in this region due to ion-ion correlations and Columbian repulsion from the surface. It is the cumulative result of all these phenomena that lead to the formation of the electrical double layer (EDL) around the C-S-H.

The first model of a double layer has been suggested by Helmholtz [Helm1879] studying a metal in contact with an electrolyte and was built on the assumption that a compact layer of ions existed at the interface of the charged metal (Fig. 2.12.(a)). Based on the dielectric constant of the electrolyte ( $\epsilon_H$ ) and the thickness of the double layer  $d$ , this early model projected a constant differential capacitance  $C_H = \frac{\epsilon_H}{d}$  independent of charge density. This theory, however, did not account, for instance, for the dispersion/diffusion of ions due to their thermal energy. To remedy the shortcomings of Helmholtz's approach, the Gouy [Gouy1910] and Chapman [Chap1913] model features a diffuse layer (DL) where (i) the potential is obtained by resolving the Poisson equation and in which (ii) the accumulating ions extend to some distance from the solid surface according to the Boltzmann distribution (Fig. 2.12.(b)). The usual system of equations for a multi-species system writes as the following:

$$\begin{cases} \Delta\Psi = -\frac{\rho}{\epsilon_0\epsilon_r} \\ \rho = eN_A \sum_i z_i C_{b,i} \exp\left(\frac{-z_i e \Psi}{k_B T}\right) \end{cases} \quad (2.12)$$

Where  $\epsilon_0$  is the permittivity of free space [ $\text{C V}^{-1} \text{m}^{-1}$ ],  $\epsilon$  is the dielectric constant of the solution [-],  $\rho$  the charge distribution [ $\text{C m}^{-3}$ ],  $e$  is the elementary electrostatic charge [ $\text{C}$ ],  $N_A$  is Avogadro's number [ $\text{mol}^{-1}$ ],  $z_i$  the valence of the species  $i$  [-],  $C_{b,i}$  is the concentration in the bulk pore solution of the species  $i$  [ $\text{mol m}^{-3}$ ] and  $k_B$  is the Boltzmann constant [ $\text{J K}^{-1}$ ].

In consecutive developments, Stern [Ste1924] proposed to combine the compact layer of Helmholtz and the diffuse layer of Gouy-Chapman and Grahame [Gra1947] improved the model by introducing the concept of “specific adsorption”. In this paradigm, two planes are often associated with the compact layer of the Helmholtz model. Firstly, there is the inner Helmholtz plane (IHP) that goes across the centers of ions that have been “specifically” adsorbed. The second plane, known as the outer Helmholtz plane (OHP), runs through the centers of the hydrated ions in contact with the surface. The electric potentials associated with the IHP and OHP are often denoted, respectively, as  $\psi_1$  and  $\psi_2$  (Fig.2.12.(c)). Beyond of the OHP, the diffuse layer forms.

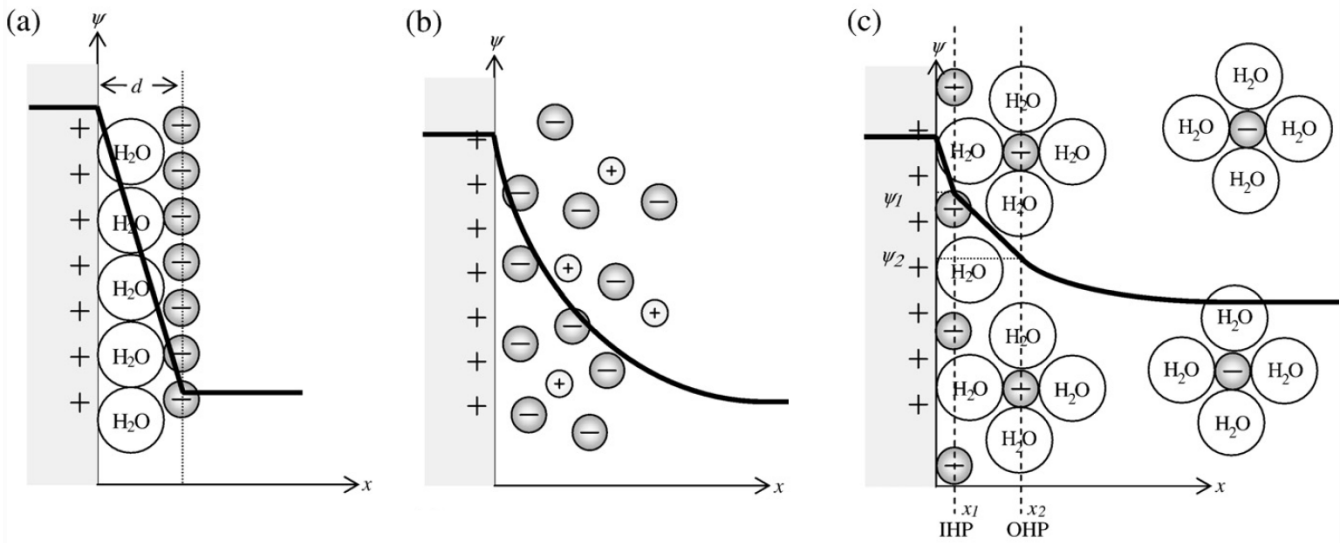


Fig.2.12. Schematic of the main EDL models **(a)** Helmholtz model **(b)** Gouy-Chapman model **(c)** Grahame model. Taken from [Fried2008]

In 1955 and 1963, Parsons [Pars1955] and Bockris [Bock1963] have, respectively, taken into account the effect of the solvent in their research. As the solvent molecules reach high concentrations in the confined electrolytes (e.g. around 55.5 M for water), it became clear that the interaction of dipoles (in dipolar solvents like water) with a charged surface were too noticeable to be neglected. As a consequence, Parsons showed, in the case of metal surfaces, that the dielectric constant of the solvent in the compact area of adsorbed molecules is much lower compared to the outer diffuse layer.

In most EDL applications [Abdi2022, Sarno2020, Alt2018], electrolytes are confined within pores or structures which sizes are, at most, a couple orders of magnitude of the actual size of ions. Transport in cementitious materials being no exception, it is the EDLs forming within the gel pores that are primarily assumed to be responsible of the decrease of chloride diffusivity by at least an order of magnitude (compared to diffusion in free water) so that chloride appears as “permanently” physically bound [Fried2008, Maraghechi2018].

The classical theory, often used to describe the forming of the EDL, is widely based on the Gouy-Chapman model and described by the Poisson-Boltzmann formalism (2.12). This approach anticipates that the EDL properties (for e.g. the ionic distributions or the mean electric potential) are expressed as functions of a decaying exponential term  $\exp(-\kappa_D z)$  where  $z$  is the distance from the surface and  $\kappa_D$  is a decay constant. The referential potential is usually taken as null in the bulk solution.

The inverse of the decay constant is usually referred to as the screening length and more commonly known as the Debye length denoted by  $\kappa_D^{-1}$ . It is a system-dependent distance that assesses the range over which the perturbation due to a double layer extends. Mathematically speaking, the Debye length represents the distance at which the electric potential drops by a factor of  $\frac{1}{e}$ . In the classical Gouy-Chapman theory, the screening length is given by the formula

$$\kappa_D^{-1} = \left( \frac{\epsilon_0 \epsilon_r k_B T}{e^2 \sum_{i=1}^N z_i^2 C_{b,i}} \right)^{1/2} \quad (2.13)$$

## C. The necessity of atomistic models

### i) Limitations of the classical theory

The validity of the classical theory has been well established in the simple case of monovalent electrolytes at relatively low concentrations ( $<0.5$  M) [Torrie1982]. Nonetheless, one common mistake consists in mistaking the screening length with the effective thickness of the electrical double layer. A number of studies [Chatterji1992, Koho2000, Tad2002, Elaknes2009(2)] imply that the Debye length may not adequately capture the decay length in multivalent and/or asymmetric electrolytes. Torrie and Valleau [Torrie1982] have also showed how, in the presence of divalent counterions, the classical theory overestimates the surface potential even at relatively low surface charges ( $<30 \mu\text{C}\cdot\text{cm}^{-2}$  or  $1.9 \text{ e}\cdot\text{nm}^{-2}$ ). In practice, it is actually a compromising hypothesis to solely assume the existence of monovalent counterions. For example, the physical binding of chloride in cement paste is supposedly happening thanks to the charge reversal due to the accumulation of calcium cations  $\text{Ca}^{2+}$  [Viallis2001] on the negatively charged C-S-H.

From a modelling standpoint, the main challenge to every EDL model is ultimately to find out what the charge density function looks like. In that light, some of the assumptions, upon which relies the mean field Poisson-Boltzmann theory, have to be revisited:

- (i) Ions are depicted as point charges i.e. steric effects of non ideality, such as effect of ionic radii, are not accounted for.
- (ii) All ion-ion correlations such as short range interactions (e.g. the attractive dispersion force or the exclusion volumetric effects) are neglected

- (iii) Non-continuum effects, such as the interaction of solvent molecules with the surface or the ions, are overridden.

In contrast to the classical theory, molecular modeling techniques account for ion-size, ion-ion and ion-solvent interactions which provide better insights into the EDL structure within nanostructures. In molecular dynamics (MD) (*ref. chapter 3 section II*), the dynamics of the whole system is simulated and the charge density function is derived as a function of particle positions, contrarily to the Boltzmann distribution that uses particles potential energy to describe the distribution.

Given the lack of atomistic models of the C-S-H surface, the Grand Canonical Monte Carlo (GCMC) is sometimes preferred to Molecular dynamics as a better compromise between accuracy and complexity. After convergence, the Monte Carlo algorithm reaches an equilibrated distribution  $C_i^{GCMC}$  of the different present species. These ionic density functions are plugged in the Poisson equation, the resolution of which delivers the electrostatic potentials nearby the C-S-H surface in a steady-state configuration:

$$\begin{cases} \Psi^{GCMC}(x) = -\frac{1}{\epsilon_0 \epsilon} \int_x^\infty (t-x) \rho(t) dt \\ \rho = e N_A \sum_i z_i C_i^{GCMC} \end{cases} \quad (2.14)$$

Equation (2.14) can also prove useful for having a theoretical estimate of the Zeta potential ( $\zeta$ ).

#### ii) Experimental investigation of surface properties: The Zeta potential ( $\zeta$ )

In a given suspension of particles, the Zeta potential is a characteristic value of the electric potential that basically estimates the potential difference between the dispersion medium (beyond the diffuse layer) and the stern layer of attached particles to the charged surface. Zeta potential measurements are probably the most common way to experimentally characterize the properties of the electrical double layer in a colloidal dispersion. To perform these measurements, instrumentation techniques usually rely on the assessment of the occurring electrokinetic phenomena. The motion of particles under influence of electric field observed in 1807 by Reuss [Reuss1807] was at the origin of the development of Zeta potential measurements by electrophoresis. It consists in applying a constant electric field  $E$  across the suspension and measure the resulting velocity of the particles  $V_p$ . The ratio between the velocity  $V_p$  and the applied electric field  $E$  is called electrophoretic mobility and writes  $\mu_e = \frac{V_p}{E}$ . In 1903, Smoluchowski [Smol1903] developed an electrokinetic theory that allowed the calculation of the Zeta potential knowing the electrophoretic mobility. The well-known Smoluchowski relation writes as:

$$\zeta = \frac{\mu_e \eta}{\epsilon_r \epsilon_0} \quad (2.15)$$

where  $\eta$  is the dynamic viscosity of the solvent,  $\epsilon_r$  the relative dielectric constant of the solvent and  $\epsilon_0$  the permittivity of free space. This value of  $\zeta$  is supposedly measured at the shear plane also called zeta plane or slipping plane. The precise position of the zeta plane remains, however, unknown. But



it is usually assumed to be at a distance of two to three water molecule diameters, so up to 6 Å, from the surface.

Despite the limited validity of the equation (2.15), where for e.g. the Debye length is typically assumed negligible compared to the particle size, the theory of Smoluchowski has contributed through the last century to gain invaluable insight into the study of electrokinetic phenomena. Applications obviously include the study of surface properties of C-S-H. In their paper, Viallis-Terrisse et al. [Viallis2001] investigated the interaction between alkaline cations and calcium silicate hydrates in the optics of proposing a consistent C-S-H surface complexation model.

Besides electrophoresis, other experimental techniques have been developed; namely the widely used acoustophoresis. More generally, electroacoustic techniques rely on different electrokinetic effects (then electrophoresis) such as the colloid vibration current: it is the fact that under the influence of ultrasounds, particles in motion generate an electric current. In the context of studying the effect of the aluminum uptake on C-S-H, Barzgar et al. [Barz2020] used an acoustophoresis electroacoustic method that computes the zeta potential from the frequency-dependent “dynamic mobility” introduced by O'Brien [OBri1990].

### iii) Modelling of ionic transport at the atomic scale

For the resolution of the transport problem, the implementation of the mean field theory is usually preferred to the costly atomic simulations (MD, Brownian dynamics...). However, molecular modelling techniques can still be employed in order to consider non-continuum effects in classical ionic transport equations. In a recent work, Yang et al. [Yang2019] have coupled Monte Carlo simulations to define a more general form of the Poisson-Nernst-Planck (PNP) equations where steric effects are considered. In the case of a non-ideal electrolyte, as it is the case of the pore solution in cement paste, the authors define the driving forces of ionic diffusion as three: (i) the matter diffusion term, as in most Fickian processes, written as the gradient of ionic concentrations  $\nabla C_i$ , (ii) the non-uniform profile of the electric potential or migration term expressed as  $\nabla \Psi$  and (iii) the contribution of previously mentioned steric effects of non-ideality computed by the excess part of the chemical potential and its gradient  $\nabla \mu_i^{\text{ex}}$ . The modified PNP is ultimately written as:

$$\begin{cases} \frac{\partial C_i}{\partial t} + \nabla \cdot \mathbf{J}_i = 0 \\ \mathbf{J}_i = -D_{i,0} \nabla C_i - D_{i,0} \frac{z_i e C_i}{k_B T} \nabla \Psi - D_{i,0} \frac{C_i}{k_B T} \nabla \mu_i^{\text{ex}} \end{cases} \quad (2.16)$$

Where  $\mathbf{J}_i$ ,  $C_i$ ,  $D_{i,0}$  and  $z_i$  denote the diffusion flux [mol m<sup>-2</sup> s<sup>-1</sup>], the aqueous concentration [mol m<sup>-3</sup>], diffusion coefficient in free water [m<sup>2</sup> s<sup>-1</sup>] and valence of the i<sup>th</sup> species, respectively.  $t$  represents the time [s],  $e$  the absolute charge of electron [C],  $k_B$  the Boltzmann constant [J K<sup>-1</sup>] and  $T$  the absolute temperature [K].

The resolution of the equation with lattice Boltzmann led the authors to the conclusion that EDL surface effects were quite negligible. The upscaling of the transport equation by defining an REV showed that it was rather the geometrical effects due to the tortuosity of the pore network that were delaying chloride diffusion. In the literature, this work stands out as one of the few attempts to link the different scales in order to explain the mechanisms of chloride ingress. However, a few

limitations arise. In fact, the authors have considered Fick's law as the homogenized transport equation while we know that diffusion processes in cement paste are anomalous. Although predictions provided some insight on the geometrical effects, results can only be considered qualitatively. The presence of calcium in the pore solution was also not discussed as we know that, unlike sodium or potassium, calcium has a very low solubility and is more likely to be absent in solution especially at high pHs.

Relying on the same simplistic assumptions (on calcium content), Zhou et al. [Zhou2018] used molecular dynamics simulations to simulate chloride adsorption in nanopores of 11 Å tobermorite. Results in the paper have shown the increase of the adsorption and residency time of chloride with high calcium concentration. Still from a molecular perspective, Kalinichev et al. were among the first that conducted an exhaustive study on the behavior of ions at interfaces (mainly portlandite and tobermorite 9Å) [Kalinichev2002]. In their work, the authors identified different types of "adsorption" where some ions were more or less "incorporated" within the structure of the solid surface (inner-sphere occupancy) and others remained separated from the solid by one molecular layer (outer-sphere) or more (in the Diffuse layer).

## VI. Conclusion

In reality, the EDL formation in cementitious materials remains partially understood and not a widely spread subject in the community despite its importance. Due to the challenging experimental investigation of surface effects at the smallest scales, Zeta potential measurement is the most popular way to characterize C-S-H surfaces. However, surface potentials in suspensions are most likely to differ from potentials within confined pores due the pore size effect. Also, the lack of consistent surface models of C-S-H (when  $\text{Ca/Si} > 1$ ) consists of one of the main impediments to the development of more realistic EDL models. It stays, nonetheless, crucial to pursue a better understanding of the very atomic features that tune the macroscopic properties of our materials. And the main objective of the present work is to provide a multi-parameter study of the EDL effects which we believe is missing in the current state of the art.

## VII. References

- [Abdi2022] Abdi, Arastoo, et al. "Smart water injection." *Chemical Methods* (2022): 313-356
- [Alt2018] Alt-Epping, Peter, et al. "Incorporating electrical double layers into reactive-transport simulations of processes in clays by using the Nernst-Planck equation: A benchmark revisited." *Applied geochemistry* 89 (2018): 1-10.
- [Andro2017] Androniuk, Iuliia, et al. "Adsorption of gluconate and uranyl on CSH phases: Combination of wet chemistry experiments and molecular dynamics simulations for the binary systems." *Physics and Chemistry of the Earth, Parts A/B/C* 99 (2017): 194-203.
- [ASTM] <https://www.astm.org/Standards/C1556.htm>
- [Bernard2022] Bernard, Ellina, et al. "Stability of hydrotalcite (Mg-Al layered double hydroxide) in presence of different anions." *Cement and Concrete Research* 152 (2022): 106674.
- [Beth2022] Bethke, Craig M. *Geochemical and biogeochemical reaction modeling*. Cambridge university press, 2022.
- [Barz2020] Barzgar, Sonya, et al. "The effect of sodium hydroxide on Al uptake by calcium silicate hydrates (CSH)." *Journal of Colloid and Interface Science* 572 (2020): 246-256.
- [Berod2015] Berodier, E., and Karen Scrivener. "Evolution of pore structure in blended systems." *Cement and Concrete Research* 73 (2015): 25-35.
- [Bish2009] Bishnoi, Shashank, and Karen L. Scrivener. "µic: A new platform for modelling the hydration of cements." *Cement and concrete research* 39.4 (2009): 266-274.
- [Bonac2005] Bonaccorsi, E. "The crystal structure of tobermorite 14A (Plombierite), a CSH phase/E. Bonaccorsi, S. Merlino, A. Kampf." *J. Am. Ceram. Soc* 88 (2005): 505-512.
- [Bonac2004] Bonaccorsi, Elena, Stefano Merlino, and H. F. W. Taylor. "The crystal structure of jennite, Ca<sub>9</sub>Si<sub>6</sub>O<sub>18</sub> (OH) 6· 8H<sub>2</sub>O." *Cement and Concrete Research* 34.9 (2004): 1481-1488.
- [Brun2004] Brunet, F., et al. "Application of <sup>29</sup>Si homonuclear and <sup>1</sup>H- <sup>29</sup>Si heteronuclear NMR correlation to structural studies of calcium silicate hydrates." *The Journal of Physical Chemistry B* 108.40 (2004): 15494-15502.
- [Barbarulo2000] Barbarulo, R., et al. "Dimensional analysis of ionic transport problems in hydrated cement systems: Part 1. Theoretical considerations." *Cement and concrete research* 30.12 (2000): 1955-1960.
- [Bir1998] Birnin-Yauri, U. A., & Glasser, F. P. (1998). Friedel's salt, Ca<sub>2</sub>Al (OH) 6 (Cl, OH)· 2H<sub>2</sub>O: its solid solutions and their role in chloride binding. *Cement and Concrete Research*, 28(12), 1713-1723.
- [Brun1973] Brunauer, Stephen, et al. "Hardened portland cement pastes of low porosity: VII. Further remarks about early hydration. Composition and surface area of tobermorite gel. Summary." *Cement and Concrete Research* 3.3 (1973): 279-293.
- [Bock1963] Bockris, JO'M. *STUDIES OF THE FUNDAMENTAL CHEMISTRY PROPERTIES AND BEHAVIOR OF FUEL CELLS*. PENNSYLVANIA UNIV PHILADELPHIA, 1963.



[Bernal1952] Bernal, J. D. "The structures of cement hydration compounds." *Proc. 3rd Int. Symp. Chem. Cem., London: Cement and Concrete Association*. 1952.

[Chu2014] Churakov, Sergey V., et al. "Intrinsic acidity of surface sites in calcium silicate hydrates and its implication to their electrokinetic properties." *The journal of physical chemistry C* 118.22 (2014): 11752-11762.

[Cast1999] Castellote, Marta, C. Andrade, and C. Alonso. "Chloride-binding isotherms in concrete submitted to non-steady-state migration experiments." *Cement and Concrete Research* 29.11 (1999): 1799-1806.

[Cong1996] Cong, Xiandong, and R. James Kirkpatrick. "<sup>29</sup>Si and <sup>17</sup>O NMR investigation of the structure of some crystalline calcium silicate hydrates." *Advanced Cement Based Materials* 3.3-4 (1996): 133-143.

[Chatterji1995] Chatterji, S. "On the applicability of Fick's second law to chloride ion migration through Portland cement concrete." *Cement and Concrete Research* 25.2 (1995): 299-303.

[Chatterji1992] Chatterji, Susanta, and M. Kawamura. "Electrical double layer, ion transport and reactions in hardened cement paste." *Cement and Concrete Research* 22.5 (1992): 774-782.

[Chap1913] Chapman, David Leonard. "LI. A contribution to the theory of electrocapillarity." *The London, Edinburgh, and Dublin philosophical magazine and journal of science* 25.148 (1913): 475-481

[DeWeerd2015] De Weerd, Klaartje, et al. "Impact of the associated cation on chloride binding of Portland cement paste." *Cement and Concrete Research* 68 (2015): 196-202.

[Dam1995] Damidot, D., and F. P. Glasser. "Thermodynamic investigation of the CaO—Al<sub>2</sub>O<sub>3</sub>—CaSO<sub>4</sub>—CaCO<sub>3</sub>—H<sub>2</sub>O closed system at 25 °C and the influence of Na<sub>2</sub>O." *Advances in cement research* 7.27 (1995): 129-134.

[Dam1994] DAMIDOT, Denis, STRONACH, S., KINDNESS, A., et al. Thermodynamic investigation of the CaO—Al<sub>2</sub>O<sub>3</sub>—CaCO<sub>3</sub>—H<sub>2</sub>O closed system at 25° C and the influence of Na<sub>2</sub>O. *Cement and Concrete Research*, 1994, vol. 24, no 3, p. 563-572.

[Etzold2014] Etzold, Merlin A., Peter J. McDonald, and Alexander F. Routh. "Growth of sheets in 3D confinements—a model for the C—S—H meso structure." *Cement and Concrete Research* 63 (2014): 137-142.

[Elaknes2009] Elakneswaran, Y., T. Nawa, and K. Kurumisawa. "Influence of surface charge on ingress of chloride ion in hardened pastes." *Materials and Structures* 42.1 (2009): 83-93.

[Elaknes2009(2)] Elakneswaran, Y., T. Nawa, and K. Kurumisawa. "Electrokinetic potential of hydrated cement in relation to adsorption of chlorides." *Cement and Concrete Research* 39.4 (2009): 340-344.

[Fried2008] Friedmann, Hubert, Ouali Amiri, and Abdelkarim Aït-Mokhtar. "Physical modeling of the electrical double layer effects on multispecies ions transport in cement-based materials." *Cement and Concrete Research* 38.12 (2008): 1394-1400.

[Feld70] Feldman, R. F., and P. J. Sereda. "A new model for hydrated Portland cement and its practical implications." *Engineering Journal* 53.8-9 (1970): 53-59.

[Georg2017] Georget, Fabien. *A Reactive Transport Simulator for Cement Pastes*. Diss. Princeton University, 2017.

[Galluci2007] Gallucci, E., et al. "3D experimental investigation of the microstructure of cement pastes using synchrotron X-ray microtomography ( $\mu$ CT)." *Cement and Concrete Research* 37.3 (2007): 360-368.

[Glass1997] Glass, G. K., & Buenfeld, N. R. (1997). The presentation of the chloride threshold level for corrosion of steel in concrete. *Corrosion science*, 39(5), 1001-1013.

[Goni1990] Goni, S., and C. Andrade. "Synthetic concrete pore solution chemistry and rebar corrosion rate in the presence of chlorides." *Cement and Concrete Research* 20.4 (1990): 525-539.

[Grovi1986(1)] Groves, G. W., P. J. Le Sueur, and W. Sinclair. "Transmission Electron Microscopy and Microanalytical Studies of Ion-Beam-Thinned Sections of Tricalcium Silicate Paste." *Journal of the American Ceramic Society* 69.4 (1986): 353-356.

[Grovi1986(2)] Groves, Geoffrey W. "TEM studies of cement hydration." *MRS Online Proceedings Library (OPL)* 85 (1986).

[Gra1947] Grahame, David C. "The electrical double layer and the theory of electrocapillarity." *Chemical reviews* 41.3 (1947): 441-501.

[Gouy1910] Gouy, M. J. J. P. T. A. "Sur la constitution de la charge électrique à la surface d'un électrolyte." *J. Phys. Theor. Appl.* 9.1 (1910): 457-468.

[Hem2020] Hemstad, Petter, Alisa Machner, and Klaartje De Weerd. "The effect of artificial leaching with HCl on chloride binding in ordinary Portland cement paste." *Cement and Concrete Research* 130 (2020): 105976.

[Huet2010] Huet, Bruno M., Jean H. Prevost, and George W. Scherer. "Quantitative reactive transport modeling of Portland cement in CO<sub>2</sub>-saturated water." *International Journal of Greenhouse Gas Control* 4.3 (2010): 561-574.

[Helm1879] Helmholtz, H. von. "Studien über electrische Grenzschichten." *Annalen der Physik* 243.7 (1879): 337-382.

[Helm1853] Helmholtz, H. von. "Ueber einige Gesetze der Vertheilung elektrischer Ströme in körperlichen Leitern, mit Anwendung auf die thierisch-electrischen Versuche (Schluss.)." *Annalen der Physik* 165.7 (1853): 353-377.

[Ioan2016] Ioannidou, Katerina, et al. "Mesoscale texture of cement hydrates." *Proceedings of the National Academy of Sciences* 113.8 (2016): 2029-2034.

[Jens2015] Jensen, Mads Mønster, et al. "Use of a multi-species reactive transport model to simulate chloride ingress in mortar exposed to NaCl solution or sea-water." *Computational Materials Science* 105 (2015): 75-82.

[Jennings2008] Jennings, Hamlin M. "Refinements to colloid model of CSH in cement: CM-II." *Cement and Concrete Research* 38.3 (2008): 275-289.

[Jennings2000] Jennings, Hamlin M. "A model for the microstructure of calcium silicate hydrate in cement paste." *Cement and concrete research* 30.1 (2000): 101-116.

[Jennings1986] Jennings, Hamlin M., and Steven K. Johnson. "Simulation of microstructure development during the hydration of a cement compound." *Journal of the American Ceramic Society* 69.11 (1986): 790-795.

[Jennings1981] Jennings, H. M., B. J. Dalgleish, and PrL Pratt. "Morphological development of hydrating tricalcium silicate as examined by electron microscopy techniques." *Journal of the American Ceramic Society* 64.10 (1981): 567-572.

[KunhiPhd2018] Kunhi Mohamed, Aslam. *Atomistic Simulations of The Structure of Calcium Silicate Hydrates: Interlayer Positions, Water Content And A General Structural Brick Model*. No. THESIS. EPFL, 2018.

[Kunhi2018] Mohamed, Aslam Kunhi, et al. "An atomistic building block description of CSH-Towards a realistic CSH model." *Cement and Concrete Research* 107 (2018): 221-235.

[Kumar2017] Kumar, Abhishek, et al. "The atomic-level structure of cementitious calcium silicate hydrate." *The Journal of Physical Chemistry C* 121.32 (2017): 17188-17196.

[Kalinichev2002] Kalinichev, Andrey G., and R. James Kirkpatrick. "Molecular dynamics modeling of chloride binding to the surfaces of calcium hydroxide, hydrated calcium aluminate, and calcium silicate phases." *Chemistry of Materials* 14.8 (2002): 3539-3549.

[Koho2000] Kohonen, Mika M., Marilyn E. Karaman, and Richard M. Pashley. "Debye length in multivalent electrolyte solutions." *Langmuir* 16.13 (2000): 5749-5753.

[Kirk1997] Kirkpatrick, R. James, et al. "Raman spectroscopy of CSH, tobermorite, and jennite." *Advanced Cement Based Materials* 5.3-4 (1997): 93-99.

[Kantro1959] Kantro, D. L., Stephen Brunauer, and C. H. Weise. "The ball-mill hydration of tricalcium silicate at room temperature." *Journal of Colloid science* 14.4 (1959): 363-376.

[Lab2011] Labbez, Christophe, et al. "CSH/solution interface: Experimental and Monte Carlo studies." *Cement and Concrete research* 41.2 (2011): 161-168.

[Loth2010] Lothenbach, Barbara. "Thermodynamic equilibrium calculations in cementitious systems." *Materials and Structures* 43.10 (2010): 1413-1433.

[Lab2006] Labbez, Christophe, et al. "Surface charge density and electrokinetic potential of highly charged minerals: experiments and Monte Carlo simulations on calcium silicate hydrate." *The Journal of Physical Chemistry B* 110.18 (2006): 9219-9230.

[Lange1991] Lange, David Albert. *Relationship between microstructure, fracture surfaces and material properties of portland cement*. Diss. Northwestern University, 1991.

[Lipp1982] Lippmaa, E., et al. "A high resolution  $^{29}\text{Si}$  NMR study of the hydration of tricalciumsilicate." *Cement and Concrete Research* 12.5 (1982): 597-602.

[Maraghechi2018] Maraghechi, Hamed, et al. "Performance of Limestone Calcined Clay Cement (LC3) with various kaolinite contents with respect to chloride transport." *Materials and structures* 51.5 (2018): 1-17.

- [Muller2014] Muller, Arnaud Charles Albert. *Characterization of porosity & CSH in cement pastes by  $^1\text{H}$  NMR*. No. THESIS. EPFL, 2014.
- [Muller2013] Muller, Arnaud CA, et al. "Densification of C–S–H measured by  $^1\text{H}$  NMR relaxometry." *The Journal of Physical Chemistry C* 117.1 (2013): 403-412.
- [McDon2005] McDonald, P. J., et al. "Surface relaxation and chemical exchange in hydrating cement pastes: a two-dimensional NMR relaxation study." *Physical Review E* 72.1 (2005): 011409.
- [Mcgrath1999] McGrath, Patrick F., and R. Doug Hooton. "Re-evaluation of the AASHTO T259 90-day salt ponding test." *Cement and Concrete Research* 29.8 (1999): 1239-1248.
- [Neith2010] Neithalath, Narayanan, and Jitendra Jain. "Relating rapid chloride transport parameters of concretes to microstructural features extracted from electrical impedance." *Cement and Concrete Research* 40.7 (2010): 1041-1051..
- [Nguy2006] Nguyen, T. Q., V. Baroghel-Bouny, and P. Dangla. "Prediction of chloride ingress into saturated concrete on the basis of a multi-species model by numerical calculations." *Computers and Concrete* 3.6 (2006): 401-422.
- [Non2004] Nonat, André. "The structure and stoichiometry of CSH." *Cement and concrete research* 34.9 (2004): 1521-1528.
- [Nev1995] Neville, A. (1995). Chloride attack of reinforced concrete: an overview. *Materials and Structures*, 28(2), 63-70.
- [Ouzia2019] Ouzia, Alexandre, and Karen Scrivener. "The needle model: a new model for the main hydration peak of alite." *Cement and Concrete Research* 115 (2019): 339-360.
- [OBri1990] O'Brien, Richard W. "Electroacoustic studies of moderately concentrated colloidal suspensions." *Faraday Discussions of the Chemical Society* 90 (1990): 301-312.
- [Patel2018] Patel, Ravi A., et al. "Effective diffusivity of cement pastes from virtual microstructures: Role of gel porosity and capillary pore percolation." *Construction and Building Materials* 165 (2018): 833-845.
- [Prom2009] Promentilla, Michael Angelo B., et al. "Quantification of tortuosity in hardened cement pastes using synchrotron-based X-ray computed microtomography." *Cement and Concrete Research* 39.6 (2009): 548-557.
- [Pars1955] Parsons, Roger. "The specific adsorption of ions at the metal-electrolyte interphase." *Transactions of the Faraday Society* 51 (1955): 1518-1529.
- [Ren2009(1)] Renaudin, Guillaume, et al. "Structural characterization of C–S–H and C–A–S–H samples—part I: long-range order investigated by Rietveld analyses." *Journal of Solid State Chemistry* 182.12 (2009): 3312-3319.
- [Ren2009(2)] Renaudin, Guillaume, et al. "Structural characterization of C–S–H and C–A–S–H samples—Part II: Local environment investigated by spectroscopic analyses." *Journal of Solid state chemistry* 182.12 (2009): 3320-3329.
- [Rich2008] Richardson, Ian G. "The calcium silicate hydrates." *Cement and concrete research* 38.2 (2008): 137-158.

[Rich2004] Richardson, I. G. "Tobermorite/jennite-and tobermorite/calcium hydroxide-based models for the structure of CSH: applicability to hardened pastes of tricalcium silicate,  $\beta$ -dicalcium silicate, Portland cement, and blends of Portland cement with blast-furnace slag, metakaolin, or silica fume." *Cement and concrete research* 34.9 (2004): 1733-1777.

[Rich1999] Richardson, Ian G. "The nature of CSH in hardened cements." *cement and concrete research* 29.8 (1999): 1131-1147.

[Rich1993] Richardson, I. G., and G. W. Groves. "Microstructure and microanalysis of hardened ordinary Portland cement pastes." *Journal of Materials science* 28.1 (1993): 265-277.

[Reuss1807] Reuss, Ferdinand Friedrich. "Sur un nouvel effet de l'électricité galvanique." *Mem. Soc. Imp. Natur. Moscou* 2 (1809): 327-337.

[Sarno2020] Sarno, Maria. "Nanotechnology in energy storage: The supercapacitors." *Studies in Surface Science and Catalysis*. Vol. 179. Elsevier, 2020. 431-458.

[Sui2019] Sui, Shiyu, et al. "Quantification methods for chloride binding in Portland cement and limestone systems." *Cement and Concrete Research* 125 (2019): 105864.

[Sui2019(2)] Sui, Shiyu, et al. "Towards a generic approach to durability: Factors affecting chloride transport in binary and ternary cementitious materials." *Cement and Concrete Research* 124 (2019): 105783.

[Shi2017] Shi, Zhenguo, et al. "Friedel's salt profiles from thermogravimetric analysis and thermodynamic modelling of Portland cement-based mortars exposed to sodium chloride solution." *Cement and Concrete Composites* 78 (2017): 73-83.

[Skin2010] Skinner, L. B., et al. "Nanostructure of calcium silicate hydrates in cements." *Physical review letters* 104.19 (2010): 195502.

[Sare2002] Saremi, M., and E. Mahallati. "A study on chloride-induced depassivation of mild steel in simulated concrete pore solution." *Cement and concrete research* 32.12 (2002): 1915-1921.

[Stanish2001] Stanish, K. D., R. Doug Hooton, and Michael DA Thomas. "Testing the chloride penetration resistance of concrete: a literature review." (2001).

[Scriv1984] Scrivener, Karen Louise. *The development of microstructure during the hydration of Portland cement*. Diss. Imperial College London (University of London), 1984.

[Ste1924] Stern, Otto. "Zur theorie der elektrolytischen doppelschicht." *Zeitschrift für Elektrochemie und angewandte physikalische Chemie* 30.21-22 (1924): 508-516.

[Smol1903] Smoluchowski, M. "Przyczynek do teoryi endosmozy elektrycznej i niektórych zjawisk pokrewnych." *Bull Acad Sci Cracovie* (1903).

[Tran2018] Tran, Van Quan, Anthony Soive, and Véronique Baroghel-Bouny. "Modelisation of chloride reactive transport in concrete including thermodynamic equilibrium, kinetic control and surface complexation." *Cement and Concrete Research* 110 (2018): 70-85.

[Tad2002] Tadmor, Rafael, et al. "Debye length and double-layer forces in polyelectrolyte solutions." *Macromolecules* 35.6 (2002): 2380-2388.

- [Tang1999] Tang, Luping. "Concentration dependence of diffusion and migration of chloride ions: Part 2. Experimental evaluations." *Cement and Concrete Research* 29.9 (1999): 1469-1474.
- [Tay1986] Taylor, Harry FW. "Proposed structure for calcium silicate hydrate gel." *Journal of the American Ceramic Society* 69.6 (1986): 464-467.
- [Torrie1982] Torrie, G. M., and J. P. Valteau. "Electrical double layers. 4. Limitations of the Gouy-Chapman theory." *The Journal of Physical Chemistry* 86.16 (1982): 3251-3257.
- [Voll2016] Vollpracht, Anya, et al. "The pore solution of blended cements: a review." *Materials and Structures* 49.8 (2016): 3341-3367.
- [Valori2013] Valori, Andrea, Peter J. McDonald, and Karen L. Scrivener. "The morphology of C–S–H: Lessons from 1H nuclear magnetic resonance relaxometry." *Cement and Concrete Research* 49 (2013): 65-81.
- [Viallis2001] Viallis-Terrisse, Hélène, André Nonat, and Jean-Claude Petit. "Zeta-potential study of calcium silicate hydrates interacting with alkaline cations." *Journal of colloid and interface science* 244.1 (2001): 58-65..
- [Verb1975] Verbeck, G. J. (1975). Mechanisms of corrosion of steel in concrete. Special Publication, 49, 21-38.
- [Wilson2022] Wilson, William, et al. "Insights on chemical and physical chloride binding in blended cement pastes." *Cement and Concrete Research* 156 (2022): 106747.
- [Wilson2021] Wilson, William, Fabien Georget, and Karen Scrivener. "Unravelling chloride transport/microstructure relationships for blended-cement pastes with the mini-migration method." *Cement and Concrete Research* 140 (2021): 106264.
- [Yang2019] Yang, Yuankai, et al. "Multiscale modeling of ion diffusion in cement paste: electrical double layer effects." *Cement and Concrete Composites* 96 (2019): 55-65.
- [Yu2016] Yu, Zechuan, Ao Zhou, and Denvind Lau. "Mesoscopic packing of disk-like building blocks in calcium silicate hydrate." *Scientific reports* 6.1 (2016): 1-8.
- [Yuan2009] Yuan, Qiang, et al. "Chloride binding of cement-based materials subjected to external chloride environment—a review." *Construction and building materials* 23.1 (2009): 1-13.
- [Yang2006] Yang, Chung-Chia. "On the relationship between pore structure and chloride diffusivity from accelerated chloride migration test in cement-based materials." *Cement and Concrete Research* 36.7 (2006): 1304-1311.
- [Yang2005] Yang, Chung-Chia. "A comparison of transport properties for concrete using the ponding test and the accelerated chloride migration test." *Materials and structures* 38.3 (2005): 313-320.
- [Yang2003] Yang, Chung-Chia, and S. W. Cho. "An electrochemical method for accelerated chloride migration test of diffusion coefficient in cement-based materials." *Materials Chemistry and Physics* 81.1 (2003): 116-125.
- [Yone1988] Yonezawa, T., V. Ashworth, and R. P. M. Procter. "Pore solution composition and chloride effects on the corrosion of steel in concrete." *Corrosion* 44.7 (1988): 489-499.

[Zhou2018] Zhou, Yang, et al. "Experimental and molecular dynamics studies on the transport and adsorption of chloride ions in the nano-pores of calcium silicate phase: the influence of calcium to silicate ratios." *Microporous and Mesoporous Materials* 255 (2018): 23-35.

[Zhang1996] Zhang, Tiewei, and Odd E. GjØrv. "Diffusion behavior of chloride ions in concrete." *Cement and Concrete Research* 26.6 (1996): 907-917.





# Chapter 3 Computational methods

This chapter summarizes the computational methods used throughout the thesis. Firstly, the different elements of the employed force field are briefly depicted. Then comes the description of each one of the implemented atomic modeling techniques including Molecular dynamics, the Widom insertion method and the Metropolis Monte Carlo. The principle and mathematical framework of each method are presented and their pertinence in this work discussed. Finally, we recall the main outlines of the Finite element method as the tool to choice to resolve partial different equations, and in particular the equations of ionic transport.

Chapter 3 Computational methods .....	69
I.    Force Fields .....	71
A.    Interatomic potentials .....	71
B.    Long range interactions .....	72
II.   Molecular Dynamics.....	74
A.    The algorithm.....	74
B.    Thermostats .....	76
i) The Nosé-Hoover thermostat .....	76
ii) The velocity rescaling thermostat.....	76
C.    Application case: Relaxation of a Lennard-Jones fluid between pushing walls .....	77
III.  Free energy calculations .....	78
A.    The chemical potential .....	78
B.    The Widom insertion algorithm.....	80
C.    Application case: Excess chemical potential of a non-homogeneous LJ liquid .....	80
D.    Extension to electrolytic fluids.....	81
IV.  Metropolis Monte Carlo .....	82
A.    Principle .....	82
B.    The Grand Canonical Monte Carlo (GCMC) .....	84
V.    Finite element method .....	86
A.    Principle .....	86
B.    The variational formulation: Case of the Poisson-Nernst-Planck (PNP) equations.....	86
i) Weak form of the Nernst-Planck equations .....	87
ii) Weak form of the Poisson equation .....	88
VI.  References .....	89



## I. Force Fields

Within the framework of molecular modelling, the simulated systems are typically composed of atoms in interaction with their environment. To best estimate these particle-particle correlations, computational methods such as classical molecular dynamics or Monte Carlo algorithms rely on force fields (FF). A force field usually consists in a set of analytical functions, using empirical parameters, that represent the interatomic potentials from which derive the acting forces that, ultimately, determine the energy landscape of the atomistic system.

The interactions between atoms can be of various forms depending on the nature of the system of interest. Atoms can be, in fact, part of a given molecule within a solid bulk or rather acquire a charge and take an aqueous form to interact with other ions or molecules. A general formulation of the configurational potential energy of a system made of  $N$  atoms is

$$U_{\text{Tot}}(\mathbf{x}_1, \mathbf{x}_2, \dots, \mathbf{x}_N) = \sum_{i,j} U_{\text{pair}}(\mathbf{x}_i, \mathbf{x}_j) + \sum_{ij} U_{\text{bond}}(\mathbf{x}_i, \mathbf{x}_j) + \sum_{ijk} U_{\text{angle}}(\mathbf{x}_i, \mathbf{x}_j, \mathbf{x}_k) \\ + \sum_{ijkl} U_{\text{dihedral}}(\mathbf{x}_i, \mathbf{x}_j, \mathbf{x}_k, \mathbf{x}_l) + \sum_i U_{\text{constraint}}(\mathbf{x}_i) \quad (3.1)$$

where  $U_{\text{pair}}$  usually refers to the nonbonding interactions between atomic pairs. The terms  $U_{\text{bond}}$ ,  $U_{\text{angle}}$  and  $U_{\text{dihedral}}$  represent, respectively, interactions between bonded pairs, triplets forming an angle and quadruplets of atoms. The last term  $U_{\text{constraint}}$  accounts for possible constraints on the atoms of the system such as ions interacting with a charged wall.

### A. Interatomic potentials

In the context of studying electrolytes, ionic species are usually correlated through pairwise interactions which express as the following sum

$$U_{\text{pair}}(\mathbf{x}_i, \mathbf{x}_j) = U_{\text{Coulomb}}(\mathbf{x}_i, \mathbf{x}_j) + U_{\text{LJ}}(\mathbf{x}_i, \mathbf{x}_j) \quad (3.2)$$

where  $U_{\text{Coulomb}}$  is the electrostatic potential between two charges  $q_i$  and  $q_j$  separated by a distance  $d_{ij}$ :

$$U_{\text{Coulomb}}(\mathbf{x}_i, \mathbf{x}_j) = \frac{1}{4\pi\epsilon} \frac{q_i q_j}{d_{ij}} \quad (3.3)$$

and  $U_{\text{LJ}}$  the Lennard-Jones potential accounting for the Van der Waals repulsion-attraction forces

$$U_{\text{LJ}}(\mathbf{x}_i, \mathbf{x}_j) = 4\epsilon_{ij} \left[ \left( \frac{\sigma_{ij}}{d_{ij}} \right)^{12} - \left( \frac{\sigma_{ij}}{d_{ij}} \right)^6 \right] \quad (3.4)$$

With  $\epsilon_{ij}$  the potential well and  $\sigma_{ij}$  the zero-crossing distance of the potential.

As pH is among the important parameters within the study of alkaline solutions, hydroxide ions will be considered in this work. Hydroxide is a diatomic anion where oxygen and hydrogen form a covalent bond which can be modeled by a harmonic potential

$$U_{bond}(\mathbf{x}_i, \mathbf{x}_j) = K_{ij}(l_{ij} - l_{0,ij})^2 \quad (3.5)$$

Where  $K$  is the force constant (including the factor  $\frac{1}{2}$ ),  $l_{ij}$  the bond length and  $l_{0,ij}$  the bond length at rest (no forces applied).

The interaction parameters used in this thesis are mostly based on the CLAYFF force field that was developed for the simulation of clays phases, hydrated minerals and their interfaces with aqueous solutions. All the implemented values for the pairwise interactions ((3.3) and (3.4)) along with the bond parameters for the harmonic potential ((3.5)) are summarized in the tables below:

Species	Symbol	Charge (e)	$\epsilon$ (eV)	$\sigma$ (Å)	Reference
Hydroxide hydrogen	Ho	+0.35	0	0	[Vacha2007]
Hydroxide oxygen	Oh	-1.35	0.006488	3.840	[Vacha2007]
Aqueous sodium ion	Na <sup>+</sup>	+1	0.005641671	2.6378	[Cygan2004]
Aqueous calcium ion	Ca <sup>2+</sup>	+2	0.004336412	2.872	[Cygan2004]
Aqueous chloride ion	Cl <sup>-</sup>	-1	0.004340748	4.4	[Cygan2004]

Table.3.1. Non bond parameters for the studied ionic species

Bond stretch		$K_{ij}$ (eV/Å <sup>2</sup> )	$l_{0,ij}$ (Å)
Species i	Species j		
Oh	Ho	23.6493	0.97

Table.3.2. Bond parameters for the oxygen and hydrogen atoms of the hydroxide ion [CHARMM]

## B. Long range interactions

In the context of studying the formation of electrical double layers in confined electrolytes, the accurate calculation of ionic distribution around charged surfaces is needed. In this regard, the long range interactions are expected to yield a non negligible effect that will greatly affect distributions at equilibrium. However, the computation of these forces becomes quite challenging when the periodicity of the simulation box in all directions is not respected. In the specific case of ionic fluids within slit pores, Torrie and Valleau [Torrie1980] explain that the Ewald summation, which is the usually employed method to efficiently assess long range interactions, cannot be used due to the

non-periodicity of the system. The authors provide an alternative approach based on the nearest images convention. In order to determine the ionic distribution at a charged interface, Torrie and Valleau used the Monte Carlo method in the grand canonical ensemble (*ref. section IV*). The slit pore was modeled as a rectangular cuboid with period conditions applied in parallel to the two hard walls (in the  $x$  and  $y$  directions) that constraint the box in the direction  $z$  of its width (Fig.3.1.(a))

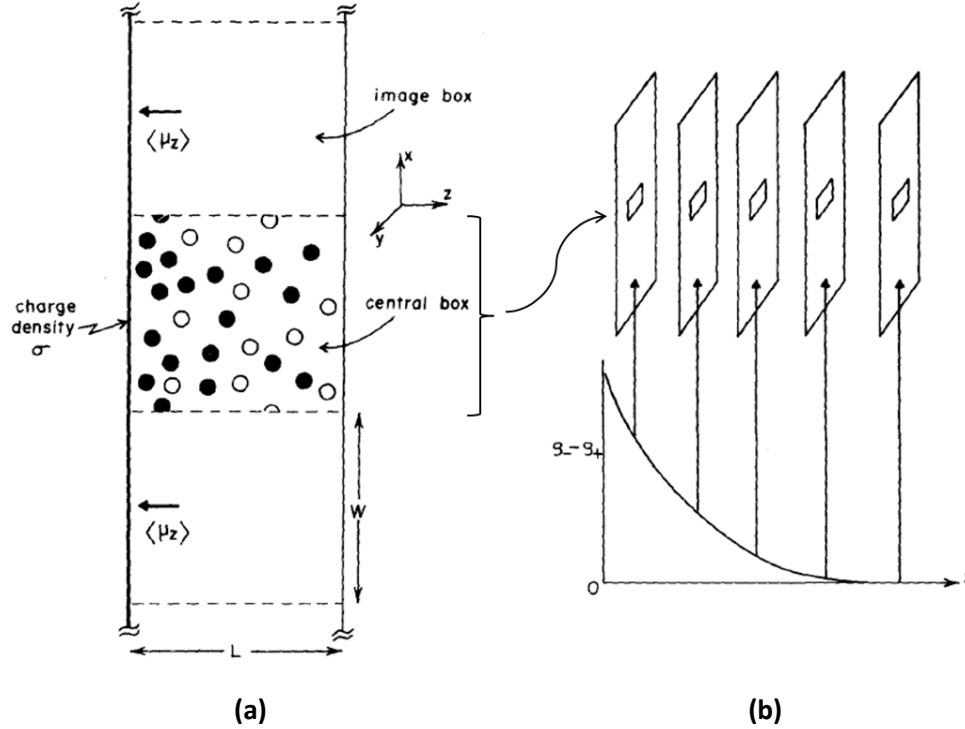


Fig.3.1. (a) Cross section of the infinite simulation cell in the direction  $x$  and  $y$  and (b) Representation of the mean charge density perpendicular to the charged walls as a set of infinite and equally spaced walls each having a different but uniform surface charge density. Taken from [Torrie1980]

Firstly, the pairwise interactions  $U_{pair}$  are computed for all the ionic pairs present in the central box. Secondly, the mean charge distribution in the central box is computed over a number of configurations until equilibration. The averaged distribution obtained is approximated by a set of infinite, equally separated and uniformly charged planes. The long range correlations  $U_{LR}$  are, then, computed through ions interacting with all the planes. However, as the short range electrostatic potentials  $U_{SR}$  between ions in the central box have already been included in the term  $U_{pair}$ , this redundant part is subtracted from  $U_{LR}$  hence the holes at the center of the sheets in Fig.3.1.(b). Finally, the overall potential of the system can be written as it follows

$$U_{Tot} = \sum_{i,j \leq i-1} U_{pair}(\mathbf{x}_i, \mathbf{x}_j) + U_{LR} - U_{SR} \quad (3.6)$$

where the long range term  $U_{LR}$  is the sum of the interactions between all the charges  $q_i$  and the electric potential  $U_p$  of the planes such as

$$U_{LR} = \sum_{i,p} q_i U_p(\mathbf{x}_i) \quad (3.7)$$

And the short range electrostatic interactions  $U_{SR}$  in the central box express as

$$U_{SR} = \sum_{i,h} q_i U_h(\mathbf{x}_i) \quad (3.8)$$

where  $U_h$  represents the electric potential of the rectangular holes.

Further details on the computations based on the paper of Torrie and Valleau [Torrie1980] can be found in [Galmarini2013]. The method has been implemented in LAMMPS [Plimpton1995] by Sandra Galmarini in the context of her thesis at EPFL.

## II. Molecular Dynamics

Molecular dynamics (MD) is a computational simulation technique that relies on the resolution of Newton's equation of motions [Newton1833] to describe the evolution of the dynamics of a system of  $N$  interacting particles. The second law of Newton writes as

$$m_i \frac{d^2 \mathbf{x}_i(t)}{dt^2} = \mathbf{F}_i \quad (3.9)$$

where  $t$  is the time,  $m_i$ ,  $\mathbf{x}_i$  the mass and the position vector of the particle  $i$  and  $\mathbf{F}_i$  the exerted forces. In this work, we chose to conduct MD computations using the LAMMPS software [Plimpton1995].

### A. The algorithm

The algorithm of any Molecular Dynamics simulation is based on a number of operations that can be summarized as it follows:

**Step 1:** Definition of the input parameters such as the temperature  $T$  of the system, the number of particles  $N$ , the volume  $V$  or the density. An important parameter to set is the time step ( $\Delta t$ ). For a good sampling of the particles trajectories, the time step has to be chosen according to the fastest moving particle in the system. In cementitious systems, the hydrogen atom, being the lightest particle, is assumed not to exceed a distance of 1/50 of a typical inter-atomic distance ( $d_{O-H} \sim 1\text{\AA}$ ) at each step [Aschauer2008]. At  $T=300$  K, a reasonable time step is 0.7 fs [Galmarini2013].

**Step 2:** The initialization of the system. This usually refers to the assignment of initial positions and velocities to the particles. One of the important criteria for an acceptable initial configuration is to avoid any overlapping between the positioned particles. This can be achieved by placing the particles on a lattice. Another option, in case of a random insertion of the atoms, is to perform a pre-equilibration energy minimization run in order to relax the system i.e. find its minimum configurational energy.

**Step 3:** The computation of the acting forces on each particle. For a conservative system, the force vector can be rewritten as gradients of the inter-atomic potential  $U_i$  (*ref. section I.A*)

$$\mathbf{F}_i = -\nabla_{\mathbf{x}_i} U_i \quad (3.10)$$

This step is usually the most expensive in terms of computational time especially in dense systems where long-range interactions are of significant importance. To reduce the complexity of the algorithm from the usual  $O(N^2)$ , numerical techniques such as the Particle mesh Ewald (PME) method [Ewald1921] or the Fast Multipole Method (FMM) [Green1987] are necessary.

**Step 4:** Once the forces computed at an instant  $t$ , the equations of motions are numerically integrated to move the system toward its new state at  $t+\Delta t$ . Many algorithms have been developed to do this. Among these, we chose to use the velocity Verlet algorithm [Swope1982] which derives from the classical Verlet integration [Verlet1967]. In this method, the particles coordinates are updated by using positions and velocities computed at equal instants:

$$\mathbf{x}_i(t + \Delta t) = \mathbf{x}_i(t) + \mathbf{v}_i(t)\Delta t + \frac{\mathbf{F}_i(t)}{2m_i} \Delta t^2 \quad (3.11)$$

Then, the new velocities are computed using the previously updated positions and the ensuing new forces that derive from those:

$$\mathbf{v}_i(t + \Delta t) = \mathbf{v}_i(t) + \frac{\mathbf{F}_i(t+\Delta t) + \mathbf{F}_i(t)}{2m_i} \Delta t \quad (3.12)$$

This integration scheme offers the possibility of directly computing the total energy of the system (kinetic and potential energies) at each time step.

**Step 5:** Finally, the previous step is repeated until reaching equilibrium i.e. when the properties of the system no longer vary with time.

In a configuration where the integration of the equations of motion is performed under conserved total energy ( $E$ ), volume ( $V$ ) and number of particles ( $N$ ), it is said that the MD simulation is conducted in the microcanonical ensemble (NVE). It is possible, however, to run simulations in other thermodynamic ensembles. Two ensembles are of particular interest in this work: The canonical

ensemble (NVT) and the Grand Canonical ensemble ( $\mu$ VT). The latter will be further detailed in the section on the Monte Carlo algorithm (*ref. section IV*). In the next paragraph, we focus on the definition of Molecular dynamics at constant temperature i.e. in the NVT ensemble.

## B. Thermostats

As it is the case for real experiments, it is possible to virtually put our simulated system in contact with a large heat bath in order to keep the temperature constant i.e. this is thermostating. The idea behind this procedure is to control the velocity of the particles in the system. There are many methods to achieve this but we will only present the two techniques that have been tested and used in this work: The Nosé-Hoover thermostat [Nose1984] and the stochastic velocity rescaling thermostat [Bussi2007].

### i) The Nosé-Hoover thermostat

In the Nosé-Hoover thermostat, the particles velocity is controlled through the introduction of a friction term  $\gamma(t)$  that varies with time. The equations of motion are, hence, modified and rewrite as it follows

$$\begin{cases} \frac{d\mathbf{x}_i(t)}{dt} = \mathbf{v}_i(t) \\ \frac{d\mathbf{v}_i(t)}{dt} = \frac{\mathbf{F}_i(t)}{m_i} - \gamma(t)\mathbf{v}_i(t) \\ \frac{d\gamma(t)}{dt} = \frac{1}{\tau_d^2} \frac{T(t) - T_0}{T_0} \end{cases} \quad (3.13)$$

Where  $\tau_d$  is the damping time that controls the rapidity at which the temperature is pushed back to the target value  $T_0$ . For a good functioning of the thermostat, the time parameter  $\tau_d$  has to be carefully chosen in order to avoid large fluctuations of the temperature ( $\tau_d$  too small) or an excessively long equilibration time ( $\tau_d$  too big). In LAMMPS, it is advised to set  $\tau_d$  equal to  $100\Delta t$ . Further details on the implementation of the thermostat can be found in the LAMMPS manual [LAMMPS2022].

### ii) The velocity rescaling thermostat

The velocity rescaling thermostat is among the first methods that have been designed to prohibit any temperature changes in the simulated system [Wood1971]. It consists in preventing any temperature fluctuations by multiplying the particles velocities, at a predetermined frequency, by a factor  $\alpha$ :

$$\alpha = \sqrt{\frac{T_0}{T(t)}} \quad (3.14)$$

where  $T(t)$  is the temperature as calculated from the velocities at a given instant  $t$  and  $T_0$  the targeted temperature. Although very intuitive, the use of a constant factor for all particles was found to yield some discrepancies in small systems or where the observables of interest rather depend on



fluctuations and not averages. To adjust these limitations, Bussi et al. extended the validity of the method by using properly chosen random rescaling factors [Bussi2007] hence the “stochastic” velocity rescaling thermostat.

### C. Application case: Relaxation of a Lennard-Jones fluid between pushing walls

In order to ensure the proper setting of the MD engine for the upcoming simulations in the present thesis, we validate our methodology with results from [Perego2018].

In the considered test case, the aim is to simulate the relaxation of a Lennard-Jones (LJ) fluid under the constraint of pushing walls. In line with the simulation set up in the paper, we consider two density values of the fluid; of a low density configuration with a number of particles  $N$  equal to 720 and a high density case with  $N=920$ . All the fluid quantities are expressed in LJ units i.e. distance  $x^*$  is expressed in function of  $\sigma$  [ $x^* = \frac{x}{\sigma}$ ], energies in  $\varepsilon$  [ $E^* = \frac{E}{\varepsilon}$ ] (ref. section I.A), reduced temperature  $T^*$  writes as  $\frac{Tk_B}{\varepsilon}$  and the reduced time  $t^* = t \sqrt{\frac{\varepsilon}{m\sigma^2}}$ . Particle-particle interactions are defined via a LJ potential truncated and shifted at a cutoff distance equal to 2.5. The temperature is set at  $T^*= 0.7$ . For the simulation box, we consider a cell of dimensions with walls defined in the  $x$  and  $y$  directions with a size of  $10 \times 10$ . The walls are separated in the  $z$  dimension with a distance  $L_z^*=11.762$ . Periodic boundary conditions are imposed along the walls. Each wall interacts with the atoms in the box with an LJ potential denoted  $U(z)$  shifted to 0 at  $z^* = L_z^*$  with  $\varepsilon_w^* = 1$  and  $\sigma_w^* = 1$ . The overall potential of the walls writes as:

$$U_{walls}(z^*) = U(z^*) + U(L_z^* - z^*) \quad (3.15)$$

For a time step equal to  $10^{-3}$ , the system reaches equilibrium after  $10^9$  steps in the NVT ensemble. In [Perego2018], the authors chose to use the Velocity rescaling thermostat. We compare the paper results with MD simulations on LAMMPS with both the Nosé-Hover and the stochastic velocity rescaling scheme from [Bussi2007].

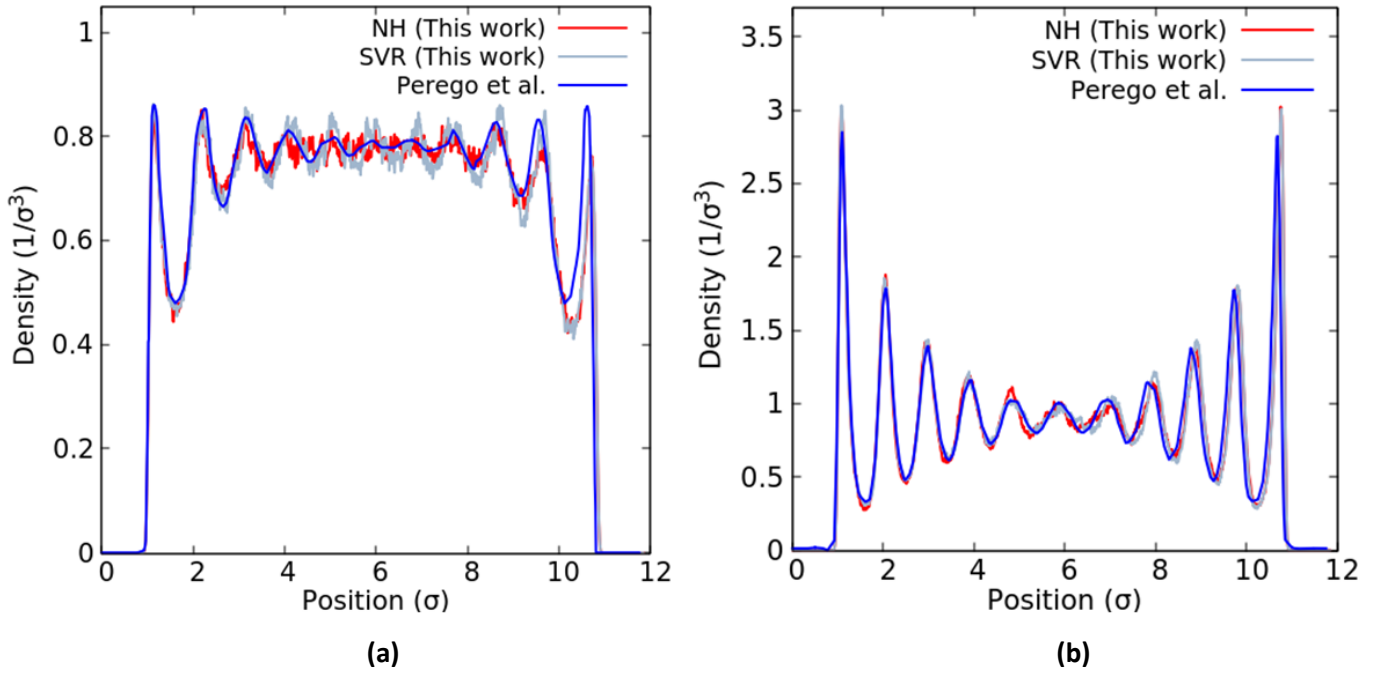


Fig.3.2. Density profile as function of the position in a confined LJ liquid with a particle number  $N$  equal to **(a)** 720 and **(b)** 920; Adapted from [Perego2018]

In Fig.3.2.(a), one can see, on the reference curve (blue), that the walls induce a non-homogeneous distribution. Oscillations appear through the box and tend to amortize at the center. Our simulations manage to reproduce the effect induced by the confining walls. At a higher density, the predictions in Fig.3.2.(b) show the same features than the lower density case with more pronounced oscillations at the sides and a good agreement with the paper's calculations. Although this remains a relatively simple test case, two main steps were determining in ensuring a good relaxation of the system: (i) a good choice of the time step with a sufficiently long simulation time and (b) the necessity of pre-minimization run on the system prior to the main equilibration (production) run.

### III. Free energy calculations

#### A. The chemical potential

In the context of studying the forming of EDLs within saturated pores, we examine non-ideal systems where the present ionic species display various size-ratios (asymmetric electrolytes) and interact with different potentials. Quantifying these effects comes down to calculating the chemical potential of the pore solution. The chemical potential of a species is defined as the change in free energy upon adding a particle of this given species to the system. In the simple case of a one-component system, the chemical potential of the species writes as the derivative of the Helmholtz free energy  $F$  with respect to the number  $N$  of particles

$$\mu = \left( \frac{\partial F}{\partial N} \right)_{V,T} \approx F(N+1, V, T) - F(N, V, T) \quad (3.16)$$

The Helmholtz free energy  $F$  of the  $N$ -particle system expresses as

$$F(N, V, T) = -\beta^{-1} \ln(Z_N) \quad (3.17)$$

Where  $\beta = 1/(k_B T)$  is the inverse thermal energy and  $Z_N$  the configurational partition function of the system in three dimensions, at constant volume  $V$  and temperature  $T$ , given by

$$Z_N = \frac{V^N}{\Lambda^{3N} N!} \int \exp[-\beta U_N(\mathbf{x}^N)] d\mathbf{x}^N \quad (3.18)$$

with  $\Lambda$  the thermal Broglie wavelength,  $U_N$  the potential energy at  $N$  particles and  $\mathbf{x}^N$  the atomic coordinates. One can then rewrite the chemical potential in (3.16) as the sum of an ideal part and an excess part:

$$\mu = \mu_{\text{id}} + \mu_{\text{ex}} \quad (3.19)$$

The ideal contribution depicts the solution as a system with non-interacting particles. It takes into account the effect pressure for gases or density and mass for liquids:

$$\mu_{\text{id}} = -\beta^{-1} \ln\left(\frac{V/\Lambda^3}{N+1}\right) \quad (3.20)$$

The excess term, which is the non-trivial part, accounts for the inter-atomic interactions between the different species. It expresses as

$$\mu_{\text{ex}} = -\beta^{-1} \ln\left[\frac{\int \exp[-\beta U_{N+1}(\mathbf{x}^{N+1})] d\mathbf{x}^{N+1}}{\int \exp[-\beta U_N(\mathbf{x}^N)] d\mathbf{x}^N}\right] = -\beta^{-1} \ln\langle \exp[-\beta \Delta U^+] \rangle_N \quad (3.21)$$

where  $\langle \cdot \rangle_N$  denotes the average over the configuration space of  $N$ -particle systems in the canonical ensemble and  $\Delta U^+$  is the energy shift due to the insertion of a  $(N+1)^{\text{th}}$  particle in the  $N$ -particle system. In order to compute the  $\Delta U^+$  term, we use the so called Widom insertion method.

## B. The Widom insertion algorithm

The Widom insertion method is a statistical algorithm derived by B. Widom in 1963 [Widom1963] for the calculation of the excess chemical potential of a species in a mixture. It consists in operating fictitious insertion moves at random positions and, thus, computing the insertion energy  $\Delta U^*$ . The operation is repeated and the term  $\langle \exp[-\beta \Delta U^*] \rangle$  in (3.21) is obtained by averaging upon a sufficiently large number of insertions.

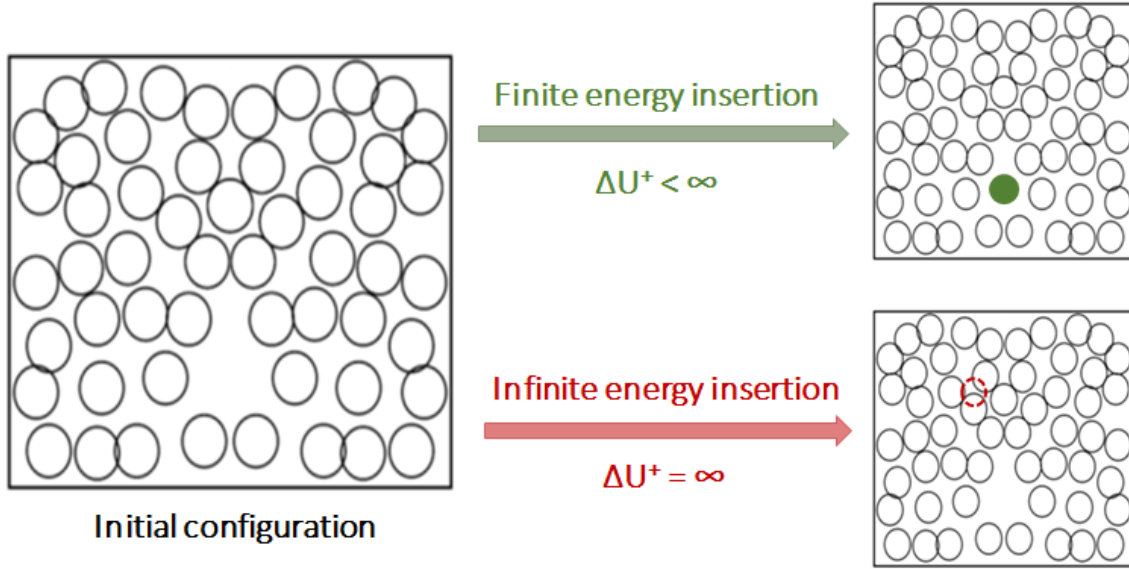


Fig.3.3. Schematic of the insertion moves performed at each step of the Widom algorithm. In green, we represent an accepted virtual move. In red, the move is rejected due to the overlapping with particles of the system.

The Widom method is also known for being a computationally efficient method that carries excellent results in the case of low to moderately high densities (few molars). Although highly alkaline, the pore solution in cement paste has a pH usually of the order of 13.6 [Loth2010] and an overall ionic strength typically below 1M. This qualifies the Widom insertion algorithm as a good tool to compute excess chemical potential of ionic species in cement systems

In this thesis, all simulations were conducted with the implemented Widom algorithm in the LAMMPS distribution. The paper of Perego et al. 2018 [Perego2018] has been used as a reference for the validation step.

## C. Application case: Excess chemical potential of a non-homogeneous LJ liquid

This section is actually the continuation of the MD relaxation simulations in section II.C. After having ensured the equilibration of a Lennard-Jones (LJ) liquid constrained in a slit pore between two pushing walls, we aim at computing the average excess chemical potential of the system. As previously mentioned (section II.C), two configurations of the fluid are considered i.e. Low and high density cases with a total number of atoms equal to, respectively, 720 and 920 LJ particles. The Widom algorithm is run in each case for a total of  $5 \cdot 10^5$  iterations with 27000 particle insertions each 500 iterations. The reference simulations in the article were carried out using Well-Tempered Metadynamics which is a highly accurate sampling technique, well suited for highly concentrated

systems. The Metadynamics simulations were conducted twice by changing the number of insertion trials from 512 (denoted Metadynamics I) down to 64 (denoted Metadynamics II) each 500 timestep. The comparison of the methods is presented in Fig.3.4.

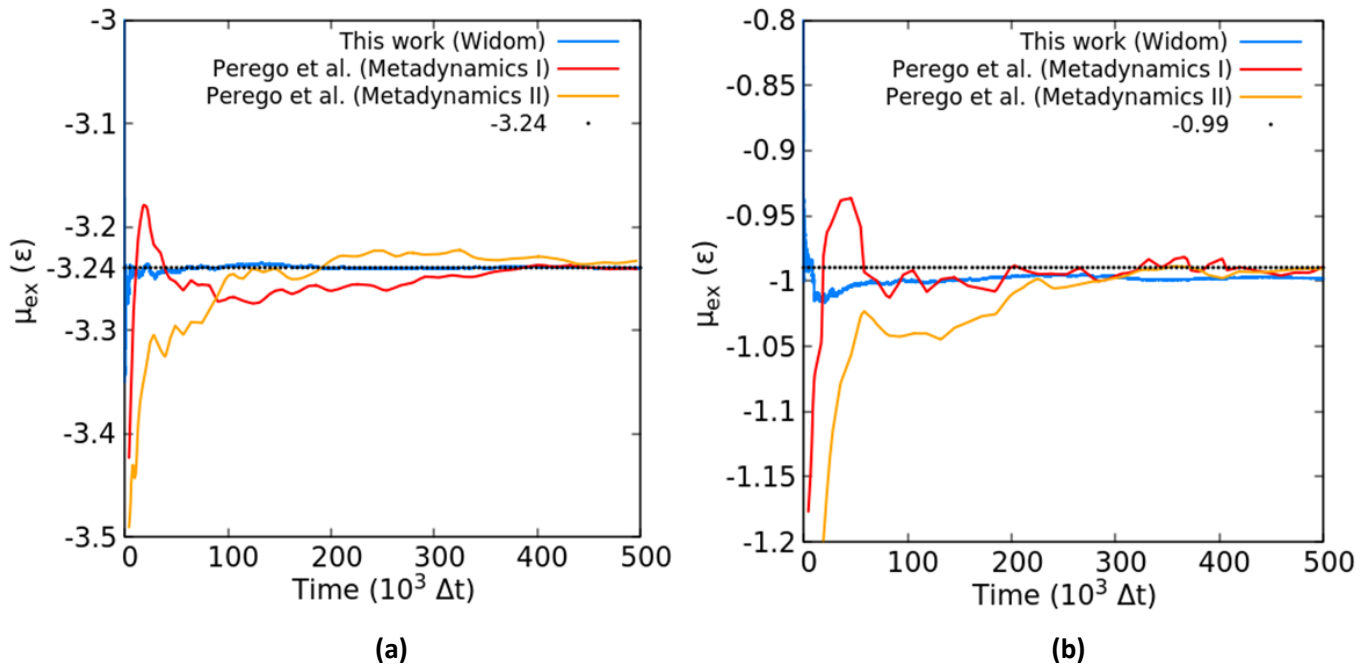


Fig.3.4. Evolution of the excess chemical potential as function of the simulation time. Results are presented in the cases of **(a)** a low density Lennard-Jones liquid with  $N=720$  and **(b)** a higher density configuration with  $N=920$ . In blue are presented the predictions of the Widom algorithm used in this work with 27000 particle insertions each 500 iterations. In red and orange, the computations achieved with Well-Tempered (WT) Metadynamics using, respectively, 512 (Meta I) and 64 (Meta II) particle insertions each 500 time steps. Adapted from [Perego2018]

Considering the low density case in Fig.3.4.(a), one can see that the convergence of the Widom method is very efficient. On the other hand, the enhanced sampling of the Metadynamics ensures that all the local minima are visited before reaching the final value of -3.24 (in  $\epsilon$  units). In this case, the predictions of the Widom scheme are in very good agreement with the paper results with an error below 0.2%. For the higher density fluid (Fig.3.4.(b)), the Widom convergence is slowed down but remains faster than its homologue. Additionally, due to the higher amount of rejected moves the deviation between the two techniques is higher (i.e. 1% error) mainly due to the poorer sampling of our method. So if the Widom method provides us with a very powerful tool, it is, in reality, limited to the case of moderately dense systems.

#### D. Extension to electrolytic fluids

As Widom's method relies on insertion moves, it appears obvious that inserting a single ion in the system will unbalance the total charge and violate electroneutrality. In order to compensate the inserted charge, Sloth et al. introduced a background charge which neutralizes the charge of the inserted ion [Sloth1990]. This translates into adding a correction term to the equation (3.21). The expression of  $\mu_{ex}$  becomes:

$$\beta\mu_{ex}^i = -\beta \frac{q_i(q_i+2) \sum_j N_j q_j^K}{32\pi\epsilon L} - \ln\langle \exp[-\beta\Delta U^+] \rangle \quad (3.22)$$

where  $K = 2[6\ln(2 + \sqrt{3}) - \pi]$ ,  $q_i$  designates the charge of the inserted species,  $N_j$  is the number of particles of the present species  $j$  (including  $i$ ) and  $L$  the side length of the cubic box. Further details on the mathematical development are available in [Sloth1990].

## IV. Metropolis Monte Carlo

### A. Principle

The Monte Carlo (MC) methods are a family of computational algorithms that use randomness as a main ingredient. In 1949, N. Metropolis and U. Stanislaw [Metropolis1949] were the first to introduce the method in detail. Since then, the MC algorithm has been intensively used in statistical physics for the computation of integrals that represent the average values of certain properties of interest in a physical system.

If we were, for example, to compute the integral  $I_f$  of a function  $f(x)$  between  $a$  and  $b$ , the most intuitive way would be to compute the average of the function  $f(x)$  in a large number  $N$  of uniformly distributed  $x$  values such as

$$I_f = \int_a^b f(x)dx = \lim_{N \rightarrow +\infty} \frac{b-a}{N} \sum_{i=1}^N f(x_i) = \lim_{N \rightarrow +\infty} \langle f(x_i) \rangle \quad (3.23)$$

For a limited number  $N$  of evaluation points, the accuracy of the integral can actually be significantly improved if the sampling points were chosen according to a non-uniform distribution  $\lambda(x)$  that provides a better sampling of regions where the integral is more important i.e. the importance sampling. In this case, the integral can be rewritten as

$$I_f = \int_a^b \lambda(x) \frac{f(x)}{\lambda(x)} dx = \lim_{N \rightarrow +\infty} \langle \frac{f(x_i)}{\lambda(x_i)} \rangle \quad (3.24)$$

In statistical physics, the objective is usually to compute the average value of an observable  $A$  that follows a Boltzmann distribution. The integral is calculated on the integrity of the phase space and writes as

$$\langle A \rangle = \int \Gamma(\mathbf{x}) A(\mathbf{x}) d\mathbf{x} = \lim_{N \rightarrow +\infty} \langle A(\mathbf{x}_i) \rangle \quad (3.25)$$

Where  $\mathbf{x}_i$  are the sampling configurations and  $\Gamma(\mathbf{x})$  the probability density function defined as

$$\Gamma(\mathbf{x}) = \frac{\exp[-\beta U(\mathbf{x})]}{Z} \quad (3.26)$$

with  $Z$  the partition function:

$$Z = \int \exp[-\beta U(\mathbf{x})] d\mathbf{x} \quad (3.27)$$

But how can we generate the  $\mathbf{x}_i$  sampling configurations in order to compute  $\langle A \rangle$ ?

Unlike MD calculations where the successive states of the system are derived from the temporal resolution of Newton's equation, the Metropolis Monte Carlo relies on the construction of a Markov chain for the sample generation. A Markov chain consists in a finite set of  $N$  states where the probability of each state  $\mathbf{x}_i$  only depends from the previous state  $\mathbf{x}_{i-1}$ . The order of succession of the states does not have necessary a physical meaning. It is then possible to define a transition matrix  $\Pi$  that describes the probability  $\Pi_{ij}$  of moving from a configuration  $\mathbf{x}_i$  to a configuration  $\mathbf{x}_j$ . Although we do not know the elements of the matrix, we do know the limit distribution of the Markov chain. It is a vector  $\Gamma$  which elements are

$$\Gamma_i = \Gamma(\mathbf{x}_i) = \frac{\exp[-\beta U(\mathbf{x}_i)]}{Z} \quad (3.28)$$

As a distribution of probabilities, the transition matrix has to be stochastic i.e.

$$\sum_{j=1}^N \Pi_{ij} = 1 \quad (3.29)$$

Assuming that we do not want to destroy equilibrium once reached, we have to be able to reach any state  $\mathbf{x}_i$  from any other state  $\mathbf{x}_j$  i.e. the matrix is ergodic. To achieve ergodicity, we usually ensure a stronger condition which is the condition of micro-reversibility (or the detailed balance) that can be written as

$$\Gamma_i \Pi_{ij} = \Gamma_j \Pi_{ji} \quad (3.30)$$

Now, the probability of passage  $\Pi_{ij}$  is the result of two steps. First, a random displacement is performed with a trial probability  $\theta_{ij}$  which defines a trial matrix  $\theta$ . Secondly, the move has to be

either accepted or rejected. The acceptance probability is noted  $\alpha_{ij}$ . In sum, the transition probability can be rewritten as the product of the trial and the acceptance probabilities:

$$\Pi_{ij} = \theta_{ij}\alpha_{ij} \quad (3.31)$$

By choosing the matrix  $\theta$  symmetric ( $\theta_{ij} = \theta_{ji}$ ), the detailed balance condition (3.30) provides a direct relation between the probabilities  $\alpha_{ij}$  and the probability vector  $\Gamma$ :

$$\frac{\alpha_{ij}}{\alpha_{ji}} = \frac{\Gamma_j}{\Gamma_i} = \frac{\exp[-\beta U(\mathbf{x}_j)]}{\exp[-\beta U(\mathbf{x}_i)]} = \exp[-\beta (U(\mathbf{x}_j) - U(\mathbf{x}_i))] \quad (3.32)$$

Interestingly, the relation is independent of  $Z$ .

Finally, the acceptance probabilities are defined by Metropolis as it follows:

$$\alpha_{ij} = \min(1, \exp[-\beta (U(\mathbf{x}_j) - U(\mathbf{x}_i))]) \quad (3.33)$$

For most adsorption studies, the grand canonical ensemble is the natural statistical ensemble to use.

## B. The Grand Canonical Monte Carlo (GCMC)

In the grand canonical ensemble, the temperature  $T$ , volume  $V$  and chemical potential  $\mu$  are fixed. During the simulation, only the number of particles is allowed to fluctuate. In the equivalent experimental setup, the system is put in contact with a reservoir and it is said to have reached equilibrium on the condition that its temperature and chemical potential relax to the ones of the reservoir. For our study of ionic adsorption on charged surfaces, we used the GCMC class implemented in LAMMPS. The algorithm of the Grand Canonical Monte Carlo applied to electrolytes has been inspired from the work of Valteau et al. [Valteau1980].

**Step 1:** Set the values of the temperature  $T$ , volume  $V$  and chemical potential  $\mu$ . The latter is separately computed using the previously discussed Widom insertion method. Other parameters such as total number of iterations  $N_{MC}$  or the acceptance ratio of the Monte Carlo moves can be chosen at this point.

**Step 2:** Generate an initial configuration with  $N_0$  number of particles in respect with the electro-neutrality of the system. As the initial configuration is randomly set, it is usually an energetically improbable distribution. An energy minimization run or an NVT simulation may prevent any overlapping of the atoms prior to the actual production run.



**Step 3:** Run the Metropolis algorithm for a number  $N_{MC}$  of iteration steps. Given a random number between 0 and 1, trial moves are performed. In a grand canonical simulation, acceptable trial moves are:

- *Displacement of particles:* An ion is selected randomly and translated by a displacement vector. The move is accepted with a probability

$$acc(\mathbf{s} \rightarrow \mathbf{s}') = \min(1, \exp\{-\beta[U(\mathbf{s}') - U(\mathbf{s})]\}) \quad (3.34)$$

Where  $\mathbf{s}$  and  $\mathbf{s}'$  are respectively the old and new positions,  $\beta = \frac{1}{k_B T}$  and  $U$  the configurational energy of the system.

- *Insertion and removal of particles:* An electroneutral set of  $\nu$  ions ( $\nu_+$  cations and  $\nu_-$  anions) is randomly selected and either added or deleted in a single. In a trial addition, each of the  $\nu$  particles, is inserted anywhere in the box with equal probability. The creation of the set of  $\nu$  ions is accepted with probability

$$acc(N \rightarrow N + \nu) = \min[1, \frac{(N_s)^\nu}{\Lambda_+^{3\nu_+} \Lambda_-^{3\nu_-}} \frac{(N_i^+)! (N_i^-)!}{(N_j^+)! (N_j^-)!} \exp\{\beta\mu - \beta(U_j - U_i)\}] \quad (3.35)$$

Considering that the simulation box is discretized into an  $N_s$  number of available discrete sites,  $\mu = \nu_+ \mu_+ + \nu_- \mu_-$  the chemical potential of the electrolyte,  $\Lambda_\pm = \frac{h}{\sqrt{2\pi m_\pm k_B T}}$ ,  $U_j$  is the configurational energy of the state  $j$  where there is a total of  $N_j = N_i + \nu$  particles (with  $N_j^+ = N_i^+ + \nu_+$  and  $N_j^- = N_i^- + \nu_-$ ) and  $U_i$  is the energy of the configuration before any additions. In a deletion trial, a set of  $\nu$  ions is deleted. The move is accepted with probability

$$acc(N \rightarrow N - \nu) = \min[1, \frac{\Lambda_+^{3\nu_+} \Lambda_-^{3\nu_-}}{(N_s)^\nu} \frac{(N_j^+)! (N_j^-)!}{(N_i^+)! (N_i^-)!} \exp\{-\beta\mu + \beta(U_j - U_i)\}] \quad (3.36)$$

**Step 4:** Algorithm stops and ionic distributions at equilibrium are reached.

## V. Finite element method

### A. Principle

The Finite element method (FEM) is a mathematical method for the numerical resolution of partial differential equations. The FEM relies on the idea of subdividing the problem system into a discrete set of smaller pieces (or subdomains) called finite elements. To achieve this, the domain is discretized via a mesh formed by elements which are, in turn, comprised of nodes. Approximations are introduced over each element of the space domain to approach the behavior of the unknown functions.

The finite element analysis of a given problem usually decomposes into 4 main steps:

**Step 1:** Definition of the variational formulation also known as the weak form of the boundary value problem

**Step 2:** The definition of a discretization method which consists in choosing the shape of the finite elements (rectangles, triangles...) and the base of reference functions (Lagrange or Hermite polynomial functions)

**Step 3:** At this point, the partial differential equation has been converted into a matrix form problem. A numerical resolution algorithm is necessary to reverse the matrices and obtain the solution vectors. The choice usually comes down to either direct methods (such as the LU factorization) or iterative solvers (such as Newton's method) that gradually converge toward the solution and offer the possibility to adjust the convergence tolerance [Demmel1997, Golub2013].

**Step 4:** Finally, the post-processing procedure for the error estimation and the extraction of the converged solution.

In this thesis, the FEM method was used for the resolution of the Poisson-Nernst-Planck (PNP) equations in the context of studying ionic diffusion in nanoscopic pores (*ref. chapter 6 section II.A.*). The numerical analysis was carried out using COMSOL Multiphysics® [COMSOL]. The full development of the FEM theory is a heavy subject which deviates from the scope and the objectives of this work. We will, however, present the variational formulation for the resolution of the PNP system as it is the basic step for the finite element resolution of the transport problem. Only the spatial discretization is developed here.

### B. The variational formulation: Case of the Poisson-Nernst-Planck (PNP) equations

In order to derive the weak formulation, one usually starts from the "strong" formulation which is the usual closed-form partial differential equation. In the case of a monovalent solution, the PNP system writes as the combination of the Nernst-Planck (NP) equations for cations (+) and anions (-):

$$\frac{\partial C_i}{\partial t} - D \Delta C_i - \alpha_i \nabla \cdot (C_i \nabla \Psi) = 0 \text{ where } i = \{+, -\} \quad (3.37)$$

And Gauss's law of electrostatics (for a monovalent salt)

$$-\Delta\Psi - \beta(\mathcal{C}_+ - \mathcal{C}_-) = 0 \quad (3.38)$$

Where the physical constants are defined as it follows

$$\begin{cases} \alpha_+ = -\alpha_- = D \frac{e}{k_B T} \\ \beta = \frac{e N_A}{\epsilon} \end{cases} \quad (3.39)$$

For the Nernst-Planck equation (3.37), the no-flux condition is applied at the boundaries to insure the insulation of the system i.e.

$$-D \frac{\partial \mathcal{C}_i}{\partial n} - \alpha_i \mathcal{C}_i \frac{\partial \Psi}{\partial n} = 0 \quad (3.40)$$

The choice for the boundary conditions for the Poisson equation can, however, vary from Dirichlet ( $\Psi = \text{constant}$ ) to Neumann conditions ( $\frac{\partial \Psi}{\partial n} = \text{constant}$  where  $n$  denotes the normal direction) depending on the experiment we want to mimic.

#### i) Weak form of the Nernst-Planck equations

The weak form of the Nernst-Planck equation is obtained by operating the scalar product between the equations (3.37) and test functions  $v_i$  with  $i=\{+,-\}$  defined in the space domain  $\Omega$ :

$$\int_{\Omega} \left[ \frac{\partial \mathcal{C}_i}{\partial t} - D \Delta \mathcal{C}_i - \alpha_i \nabla \cdot (\mathcal{C}_i \nabla \Psi) \right] v_i d\mathbf{x} = 0 \quad (3.41)$$

Firstly, the divergence term ( $\nabla \cdot$ ) is expanded which brings a second lagrangian operator ( $\Delta$ ) applied to the electric potential function  $\Psi$ :

$$\int_{\Omega} \frac{\partial \mathcal{C}_i}{\partial t} v_i d\mathbf{x} - D \int_{\Omega} \Delta \mathcal{C}_i v_i d\mathbf{x} - \alpha_i \int_{\Omega} \nabla \mathcal{C}_i \nabla \Psi v_i d\mathbf{x} - \alpha_i \int_{\Omega} \mathcal{C}_i \Delta \Psi v_i d\mathbf{x} = 0 \quad (3.42)$$

By using Green's first identity on the colored terms in (3.42), each volume integral separates in two terms, one of them being a surface integral over the boundary  $\partial\Omega$  of the domain:

$$\begin{aligned} \int_{\Omega} \frac{\partial \mathcal{C}_i}{\partial t} v_i d\mathbf{x} + D \int_{\Omega} \nabla \mathcal{C}_i \nabla v_i d\mathbf{x} - \alpha_i \int_{\Omega} \nabla \mathcal{C}_i \nabla \Psi v_i d\mathbf{x} + \alpha_i \int_{\Omega} \nabla (\mathcal{C}_i v_i) \nabla \Psi d\mathbf{x} \\ - D \int_{\partial\Omega} \frac{\partial \mathcal{C}_i}{\partial n} v_i d\mathbf{s} - \alpha_i \int_{\partial\Omega} \frac{\partial \Psi}{\partial n} \mathcal{C}_i v_i d\mathbf{s} = 0 \quad (3.43) \end{aligned}$$

Given the no-flux boundary condition (3.40), the sum of the surface integrals is zero. The remaining non-linear term is further expanded as

$$\alpha_i \int_{\Omega} \nabla (\mathcal{C}_i v_i) \nabla \Psi d\mathbf{x} = \alpha_i \int_{\Omega} \nabla \mathcal{C}_i \nabla \Psi v_i d\mathbf{x} + \alpha_i \int_{\Omega} \mathcal{C}_i (\nabla \Psi \cdot \nabla v_i) d\mathbf{x} \quad (3.44)$$

And the final variational formulation of the NP equations is:

$$\int_{\Omega} \frac{\partial \mathcal{C}_i}{\partial t} v_i d\mathbf{x} + D \int_{\Omega} \nabla \mathcal{C}_i \nabla v_i d\mathbf{x} + \alpha_i \int_{\Omega} \mathcal{C}_i (\nabla \Psi \cdot \nabla v_i) d\mathbf{x} = 0 \quad (3.45)$$

## ii) Weak form of the Poisson equation

In a very similar manner, the weak form of the Poisson equation is obtained by using a different test function  $w$  as it follows:

$$- \int_{\Omega} \Delta \Psi w d\mathbf{x} - \int_{\Omega} \beta (\mathcal{C}_+ - \mathcal{C}_-) w d\mathbf{x} = 0 \quad (3.46)$$

The Green identity is used to expand the Lagrangian term and make the surface integral term appear:

$$\int_{\Omega} \nabla \Psi \nabla w d\mathbf{x} - \int_{\Omega} \beta (\mathcal{C}_+ - \mathcal{C}_-) w d\mathbf{x} - \int_{\partial\Omega} \frac{\partial \Psi}{\partial n} w d\mathbf{s} = 0 \quad (3.47)$$

Depending on the fixed boundary conditions, the last term yields different values. In the case where the boundaries are electrically insulated ( $\frac{\partial \psi}{\partial n} = 0$ ), the last term cancels out and the weak form is simplified.

## VI. References

- [Aschauer2008] Aschauer, Ulrich. *Atomistic simulation in powder technology*. No. THESIS. EPFL, 2008.
- [Bussi2007] Bussi, Giovanni, Davide Donadio, and Michele Parrinello. "Canonical sampling through velocity rescaling." *The Journal of chemical physics* 126.1 (2007): 014101.
- [Cygan2004] Cygan, Randall T., Jian-Jie Liang, and Andrey G. Kalinichev. "Molecular models of hydroxide, oxyhydroxide, and clay phases and the development of a general force field." *The Journal of Physical Chemistry B* 108.4 (2004): 1255-1266.
- [COMSOL] COMSOL Multiphysics® v.6.0. [www.comsol.com](http://www.comsol.com). COMSOL AB, Stockholm, Sweden.
- [CHARMM] [https://charmm-gui.org/?doc=open\\_toppar&filename=toppar\\_water\\_ions.str](https://charmm-gui.org/?doc=open_toppar&filename=toppar_water_ions.str)
- [Demmel1997] Demmel, James W. *Applied numerical linear algebra*. Society for Industrial and Applied Mathematics, 1997.
- [Ewald1921] Ewald, Paul P. "Die Berechnung optischer und elektrostatischer Gitterpotentiale." *Annalen der physik* 369.3 (1921): 253-287.
- [Galmarini2013] Galmarini, Sandra Caroline. *Atomistic simulation of cementitious systems*. No. THESIS. EPFL, 2013.
- [Golub2013] Golub, Gene H., and Charles F. Van Loan. *Matrix computations*. JHU press, 2013.
- [Green1987] Greengard, Leslie, and Vladimir Rokhlin. "A fast algorithm for particle simulations." *Journal of computational physics* 73.2 (1987): 325-348.
- [LAMMPS2022] <https://docs.lammps.org/Manual.html>
- [Loth2010] Lothenbach, Barbara. "Thermodynamic equilibrium calculations in cementitious systems." *Materials and Structures* 43.10 (2010): 1413-1433.
- [Metropolis1949] Metropolis, Nicholas, and Stanislaw Ulam. "The monte carlo method." *Journal of the American statistical association* 44.247 (1949): 335-341.
- [Nose1984] Nosé, Shūichi. "A molecular dynamics method for simulations in the canonical ensemble." *Molecular physics* 52.2 (1984): 255-268.
- [Newton1833] Newton, Isaac. *Philosophiae naturalis principia mathematica*. Vol. 1. G. Brookman, 1833.
- [Perego2018] Perego, Claudio, Omar Valsson, and Michele Parrinello. "Chemical potential calculations in non-homogeneous liquids." *The Journal of Chemical Physics* 149.7 (2018): 072305.
- [Plimpton1995] Plimpton, Steve. "Fast parallel algorithms for short-range molecular dynamics." *Journal of computational physics* 117.1 (1995): 1-19.
- [Swope1982] Swope, William C., et al. "A computer simulation method for the calculation of equilibrium constants for the formation of physical clusters of molecules: Application to small water clusters." *The Journal of chemical physics* 76.1 (1982): 637-649.

[Torrie1980] Torrie, G. M., and J. P. Valleau. "Electrical double layers. I. Monte Carlo study of a uniformly charged surface." *The Journal of Chemical Physics* 73.11 (1980): 5807-5816.

[Vacha2007] Vácha, Robert, et al. "Autoionization at the surface of neat water: is the top layer pH neutral, basic, or acidic?." *Physical Chemistry Chemical Physics* 9.34 (2007): 4736-4747.

[Valleau1980] Valleau, John P., and L. Kenneth Cohen. "Primitive model electrolytes. I. Grand canonical Monte Carlo computations." *The Journal of chemical physics* 72.11 (1980): 5935-5941.

[Verlet1967] Verlet, Loup. "Computer" experiments" on classical fluids. I. Thermodynamical properties of Lennard-Jones molecules." *Physical review* 159.1 (1967): 98.

[Wood1971] Woodcock, L-V\_. "Isothermal molecular dynamics calculations for liquid salts." *Chemical Physics Letters* 10.3 (1971): 257-261.

[Widom1963] Widom, Ben. "Some topics in the theory of fluids." *The Journal of Chemical Physics* 39.11 (1963): 2808-2812.

# Chapter 4 Modelling the formation of electrical double layers around C-S-H surfaces in Na-systems

In this chapter, the ionic distributions at a Calcium Silicate Hydrate-solution interface are computed in monovalent electrolytic systems using the Metropolis Monte Carlo algorithm in the Grand Canonical ensemble (GCMC).

In the first section, the GCMC computations are compared to the Poisson-Boltzmann resolution within the validity scope of the classical Gouy-Chapman theory. The limitations of the classical approach are, thereafter, demonstrated as the assumptions of the mean field theory break down. The study is conducted on electrical double layers (EDL) forming at a single wall solution configuration. The electrostatic of the EDL are firstly determined with respect to the properties of the C-S-H surface, namely its surface charge density. Then, the effect of the ionic strength of the solution is assessed upon varying the molarity of the solution and the valence of the present ionic species. Finally, the model is validated with some published work on the topic

The second section of the chapter aims to extend the model to the case of slit pores to better approach the real problem of EDLs forming in C-S-H gel pores. To the previously mentioned parameters, the effect of the pore size and the solution alkalinity are included in the study.

Chapter 4 Modelling the formation of electrical double layers around C-S-H surfaces in Na-systems ....	91
I.    Limitations of the classical theory: The atomistic modelling of the EDL .....	93
A.    The Poisson-Boltzmann equation .....	93
B.    The study of the EDL: A multi-parameter problem .....	94
i) Effect of the surface charge density .....	96
•    Choice of the C-S-H surface charge density.....	96
•    Results and discussion .....	97
ii) Effect of the concentration .....	103
•    Results and discussion .....	103
•    Concluding remarks and implications for cementitious systems .....	105
iii) Effect of multivalent ions: The case of $\text{Ca}^{2+}$ .....	106
C.    Computational validation: Zeta potential ( $\zeta$ ) at a C-S-H surface with $\text{Ca/Si} < 1$ .....	108
II.    Electrical double layers in slit pores.....	112
A.    Effect of the pore size .....	112
i) Numerical results .....	112
ii) About slit pores in cement paste .....	116

B.	Interactions at the surface: Influence of $\sigma_{\text{C-S-H}}$ .....	116
C.	Effect of the concentration.....	118
D.	Explicit $\text{OH}^-$ in simulation boxes.....	119
III.	Summary .....	121
IV.	References .....	122



# I. Limitations of the classical theory: The atomistic modelling of the EDL

## A. The Poisson-Boltzmann equation

Models of the electrical double layer have been a subject of research, for over a century, since the first developments of Helmholtz in 1853 until now (*ref. chapter 2 section V.B*). And despite all the advances, the combination of the Gouy–Chapman model and the Stern layer model is still considered to be reasonable. The Gouy–Chapman–Stern (GCS) model is usually referenced at as the “classical theory” as opposed to the atomistic models. Its mathematical background relies on the Poisson-Boltzmann (PB) system [[Fix1979](#), [Vall1982](#), [Outh1983](#), [Old2008](#), [Lopez2011](#)] which is a non-linear equation that results from combining Gauss’s law for conservation of charge (also known as the Poisson equation) and the Boltzmann equation. The distribution of ions around a charged surface following Boltzmann statistics is an important result that offers a simple formalism to describe the formation of the electrical double layer. However, it is also important to understand that the Boltzmann distribution of ions is actually the particular solution of the Nernst-Planck equations **(4.1)** under steady-state conditions:

$$\mathbf{J}_i = -D_{i,0} \nabla C_i - D_{i,0} \frac{z_i e C_i}{k_B T} \nabla \Psi \quad (4.1)$$

For steady-state conditions, the ionic fluxes  $\mathbf{J}_i$  are null and the Nernst–Planck equation can be solved for the ion concentrations  $C_i$  in terms of the bulk molarity  $C_{b,i}$  and the electric potential  $\psi$ :

$$C_i = C_{b,i} \exp\left(\frac{-z_i e \Psi}{k_B T}\right) \quad (4.2)$$

Hence, the Poisson-Boltzmann equation rewrites as:

$$\Delta \Psi = -\frac{\rho}{\epsilon_0 \epsilon_r} \text{ where } \rho = e N_A \sum_i z_i C_{b,i} \exp\left(\frac{-z_i e \Psi}{k_B T}\right) \quad (4.3)$$

In the case of a symmetric z:z electrolyte, the partial differential equation can be analytically solved and the solution  $\psi$ , in one-dimension, expresses in function of x the direction normal to the surface as:

$$\Psi(x) = 2 \frac{k_B T}{e z} \ln\left(\frac{1 + \exp(-x \kappa_D) \tanh\left(\frac{e z \Psi_{\text{OHP}}}{4 k_B T}\right)}{1 - \exp(-x \kappa_D) \tanh\left(\frac{e z \Psi_{\text{OHP}}}{4 k_B T}\right)}\right) \quad (4.4)$$

$\psi^{OHP}$  represents here the potential at the closest approach plane or the outer Helmholtz plane (*ref. chapter 2 section V.B*). In the development of his kinetic theory of the electrical double layer, Grahame introduced in 1947 [Gra1947] the relation between the electric potential  $\psi^{OHP}$  and the “stored” amount of charge surface the diffuse layer (DL) expressed as charge density per unit of surface  $\sigma^d$ :

$$\sigma^d = \sqrt{8\epsilon_r\epsilon_0 C_b N_A k_B T} \sinh \frac{e z \psi^{OHP}}{2 k_B T} \quad (4.5)$$

The parameter  $1/\kappa_D$  in (4.4) represents the Debye length which writes as:

$$\kappa_D^{-1} = \left( \frac{\epsilon_0 \epsilon_r k_B T}{e^2 \sum_{i=1}^N z_i^2 C_{b,i}} \right)^{1/2} \quad (4.6)$$

The mathematical formalism of the classical theory is very practical but its validity remains limited. As we approach to the surface at distances below the outer Helmholtz plane, the inherent assumptions (*ref. chapter 2 section V.B*) upon which the founding equation (4.3) rests break down. As a consequence, the PB resolution can only be used for the description of the liquid beyond the OHP, namely the diffuse layer and the bulk area of the solution.

## B. The study of the EDL: A multi-parameter problem

The characterization of the diffuse double layers in real cementitious systems is a complex task. As cement-based materials evolve in time, the properties of their hydrates and the composition of the pore solution can accordingly vary due to inner chemical processes or as a response to external factors. In the study of chloride ingress, the physical binding of chloride within the diffuse layer is expected to change as a function of these parameters which can be fairly summarized by the three following factors:

- (i) The surface properties of the hydrates (mainly C-S-H)
- (ii) The ionic strength of the solution (concentration, valence, pH...)
- (iii) The pore network (pore size distribution, tortuosity, connectivity...)

All these factors are highly coupled and system-dependent. However, in order to assess the relevance of each variable, we will conduct simulations by varying one parameter at a time while reasonably attenuating the effect of the others. As a first approach, we will study a single wall solution where the EDL is modeled around a C-S-H wall surrounded by an infinite supernatant (electrolyte). Hence, the pore size effects (related to point (iii) above) will be dismissed, in this section, and further developed in section II which rather focuses on slit pores.

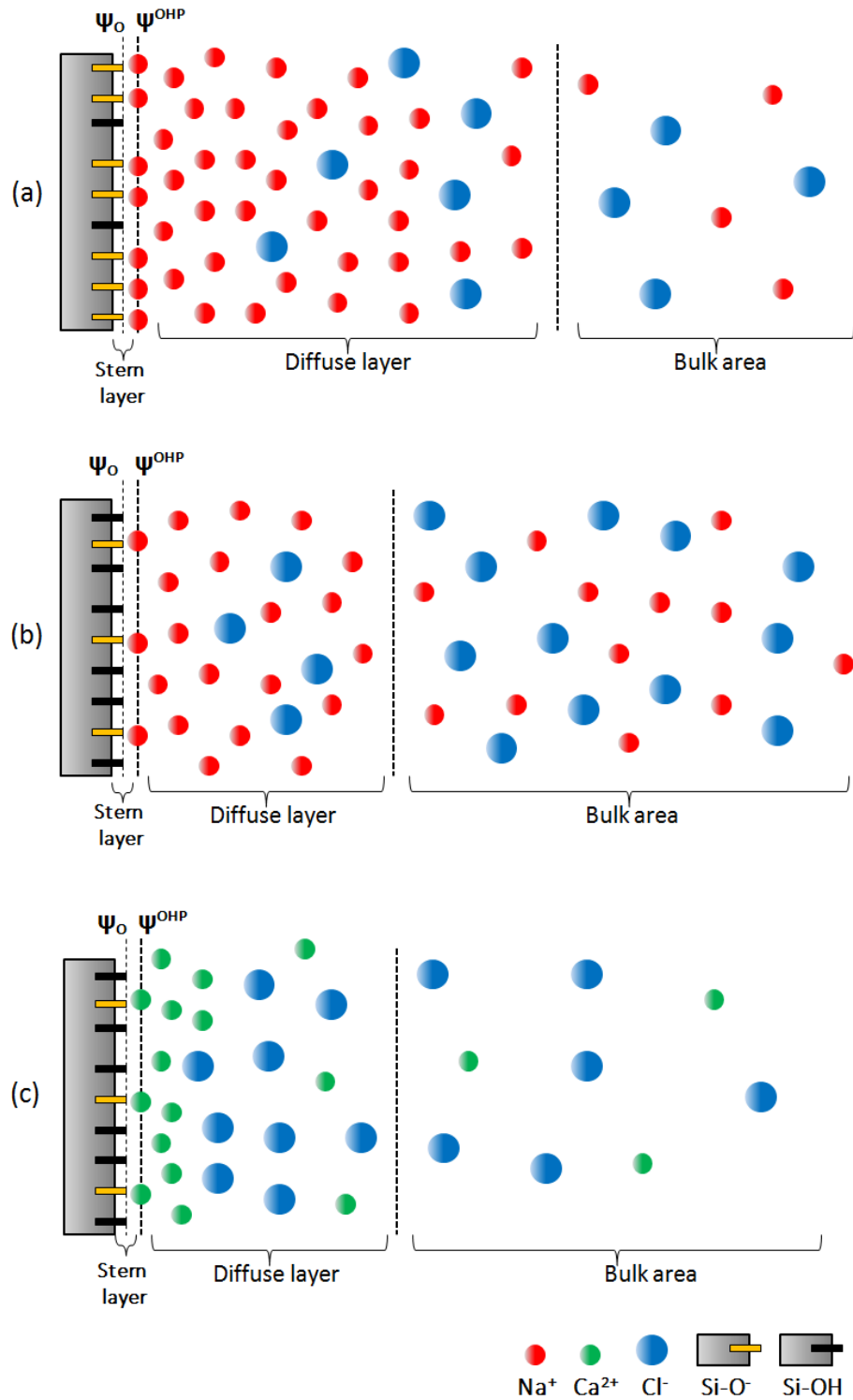


**Fig.4.1.** Schematic of the implemented Gouy-Chapman-Stern model of EDL formation in a single-wall solution under different conditions: **(a)** A moderately concentrated monovalent NaCl salt in contact with a highly charged surface **(b)** A highly concentrated solution (NaCl) at the edge of a moderately charged surface and **(c)** The effect of calcium divalence (at moderate concentration) on the electric properties of the EDL. The solvent (water) is implicit but ions are explicitly described. The considered ionic species are, respectively, sodium  $\text{Na}^+$  (red), chloride  $\text{Cl}^-$  (blue) and calcium  $\text{Ca}^{2+}$  (green).

As represented in the above schematic of the simulations flow, we first measure the effect of the surface charge density on the ionic distributions and other properties of the EDL (Fig.4.1.(a)). Later, it is the ionic concentration that is enhanced at a moderate surface charge density to study the effect of the molarity increase (Fig.4.1.(b)). Finally, we include the presence of calcium ions (Fig.4.1.(c)) that are assumed to play a prime role in the binding capacity of chloride on C-S-H.

In order to test the classical theory within its claimed validity scope (*ref. section I.A*), we discount the study of the Stern layer and we confound the OHP and the surface/liquid interface i.e. we assume that  $\psi_0 = \psi^{OHP}$  in Fig.4.1. As our anchoring method, the results obtained by classical resolution of the PB will be confronted to Monte Carlo simulations in the Grand Canonical ensemble (GCMC).

#### i) Effect of the surface charge density

Prior to presenting simulation results, we will briefly discuss, in the next paragraph, how we chose to model the C-S-H surface in this study.

- *Choice of the C-S-H surface charge density*

Given its crystalline structure and its C-S-H-like chemical composition, 14 Å tobermorite has been used since 1952 [Bernal1952] as a model for C-S-H. It is characterized by an infinite mean chain length (MCL), a Ca/Si stoichiometric ratio of 0.86 (*ref. chapter 2 section IV.C.(ii)*) and a surface Silanol Site density (SSD) of 4.8 sites.nm<sup>-2</sup>. In actual cementitious materials, the MCL of the C-S-H is not infinite and decreases with a diminishing SSD as the Ca/Si goes up [Puertas2011]. So in order to best represent real cement-based systems, an intensive amount of experimental and modelling work has been conducted on synthetic C-S-H [Lab2006, Lab2011, Chu2014, Haas2015, Harris2022] for the purpose of eventually expanding our understanding to the more complex C-(A)-S-H. In the case of low Ca/Si synthetic C-S-H, Labbez et al. [Lab2011] predict that the proportion of the deprotonated sites (so-called ionization degree denoted  $\alpha$ ) depends on two mains factors: (i) the pH and (ii) the presence of multivalent ions in the pore solution. Unfortunately, given the lack of consistent atomistic models of C-S-H/solution interfaces, no predictive model correlating the ionization degree  $\alpha$  and the pH has been developed for realistic C-S-H surfaces at our knowledge. However, the authors in [Lab2011] managed to estimate the evolution of the surface charge as function of the pH of the solution in the two cases of (i) a NaOH and (ii) a Ca(OH)<sub>2</sub> electrolyte (Fig.4.2.)

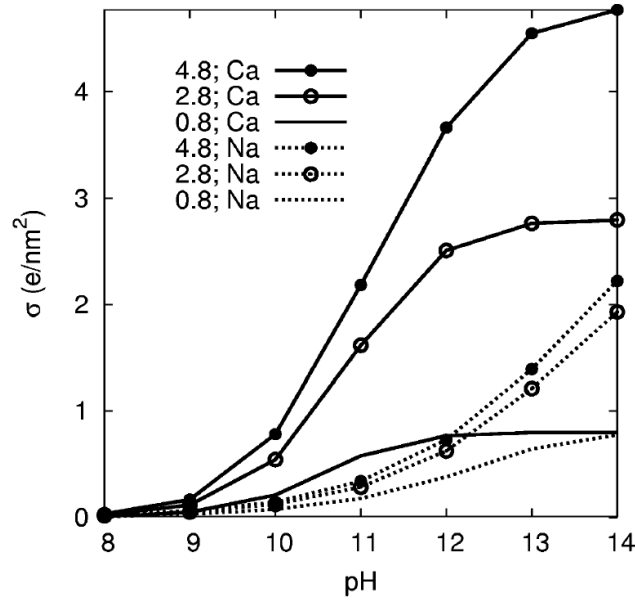


Fig.4.2. Simulated (GCMC) surface charge density,  $\sigma$  vs pH for a bulk solution containing either 2 mM calcium (solid lines) or 2mM sodium (dotted lines) for increasing surface site density: 0.8 (no symbols), 2.8 (empty circles), and 4.8 sites.nm<sup>-2</sup> (filled circles). Taken from [Lab2011]

GCMC simulations have been run for three different values of SSD (0.8; 2.8 and 4.8 sites.nm<sup>-2</sup>) in the optic of covering a reasonable range of C-S-H surfaces with a wide range of Ca/Si ratios. As the study of the C-S-H surfaces stands beyond the scope of this thesis, we will cautiously rely on the data presented in Fig.4.2 as it follows:

- For monovalent systems (NaCl-like) (dotted lines in Fig.4.2.), we will take values of  $\sigma_{C-S-H}$  that range from a lower bound of -0.12 e.nm<sup>-2</sup> ( $\alpha=2.5\%$ ) and upper bound of approximately -2.4 e.nm<sup>-2</sup> ( $\alpha=50\%$ ) for pHs between 10 and 14, where the C-S-H does not dissolve.
- For calcium containing systems, we will consider that surfaces are totally ionized for pH>13 as the ionization degree seems to reach almost 100% independently of the SSD (solid lines in Fig.4.2.)

In all the presented simulations of this chapter, the C-S-H surface is modeled as an implicit plane exclusively characterized by one input parameter: a homogeneous surface charge density  $\sigma_{C-S-H}$ .

## • Results and discussion

The simulated system is a NaCl symmetric and monovalent electrolyte of concentration  $C_{NaCl}$  put in contact with a charged C-S-H surface defined by a surface charge density  $\sigma_{C-S-H}$ . As a first basis of comparison between PB and MC results, we present results for a 0.01M NaCl interacting with two surfaces having different surfaces charge densities (i) -0.48 e.nm<sup>-2</sup> and (ii) -2.4 e.nm<sup>-2</sup>. The first case study (i) is a good example of a system that complies with the validity conditions of the classical theory i.e. low concentrations (< 0.1 M) and low surface charges ( $|\sigma| < 30 \mu C.cm^{-2}$  i.e. 1.9 e.nm<sup>-2</sup>) [Torrie1982]. Conversely, the second example (low concentration, high surface charge) presents a typical case where the mean field theory supposedly fails to capture the atomistic phenomena happening at the surface.

The Monte Carlo simulations rely on the Metropolis algorithm applied in the Grand Canonical ensemble (*ref. chapter 3 section IV.B*). The size of the simulation boxes has been adapted to each case of the concentration  $C_{NaCl}$  and the surface charge density values  $\sigma_{C-S-H}$  such as the box contains a minimum of 1000 particles. For example, in the case of a 0.01M NaCl solution interacting with a surface of  $-0.48 \text{ e.nm}^{-2}$ , the box was a rectangular cuboid of size  $36 \times 36 \times 32 \text{ nm}$  (where 36nm are the dimensions of the walls and 32 nm the width of the box) containing 871  $\text{Na}^+$  and 249  $\text{Cl}^-$  for a total of 1120 particles. Periodic boundary conditions were applied in the direction of the long dimensions of the box (infinite walls). In the direction of the smallest dimension, the system was terminated on one side by a charged wall and on the other side by a hard wall with no surface charge. The charged wall interacts with all species in the box through long range electrostatic potentials covering the whole box space (*ref. chapter 3 section I.B*). The hard wall is a reflective wall that does not allow particles to move outside the box. All ions are modeled explicitly. They interact with each other's through electrostatic and Lennard-Jones potentials (*ref. chapter 3 section I.A*) with a cutoff of  $30 \text{ \AA}$ . The water was only considered implicitly via a dielectric constant of 78.5 (at  $25^\circ\text{C}$ ). The acceptance ratio of the Monte Carlo moves are set to 50% with a number of moves performed equal to the total number of present ions (on average one move per particle each iteration). The volume  $V$  and the temperature  $T$  are fixed (unchanged through the simulation) and the chemical potential  $\mu$  of the reservoir is computed separately with a modified version of the Widom algorithm (*ref. chapter 3 section III.B*). An energy minimization run is performed before the "production" steps to resolve any overlapping of atoms and minimize the configurational energy of the randomly inserted ions. Afterwards,  $10^5$  MC iterations are run and data was collected from the last  $10^4$  iterations. Final ionic distributions are computed after averaging over  $10^3$  configurations.

The final ionic distributions are presented in Fig.4.3. In the PB results shown in Fig.4.3.(a), as a result of electrostatic interactions, sodium cations ( $\text{Na}^+$ ) stick to the negative surface while the chloride anions ( $\text{Cl}^-$ ) are repelled from it. In both cases, it is possible to observe the decaying exponential shape of the  $\text{Na}^+$  curves (respectively increasing for the  $\text{Cl}^-$ ), typical of the Boltzmann distribution. In the high surface charge configuration ( $-2.4 \text{ e.nm}^{-2}$ ), the concentration of the counterions at the surface is higher due to stronger Coulombic interactions between  $\text{Na}^+$  and the ionized silanol sites at the surface. In a respective way, chloride's depletion is stronger for the same reasons. Globally, for different values of  $\sigma_{C-S-H}$ , the curves of a same species split for a distance below 3 nm from the surface. Beyond 3nm, the classical theory predicts that increasing  $\sigma_{C-S-H}$  by fivefold ( $-2.4 = 5 \times -0.48$ ) has basically no effect since all curves in Fig.4.3.(a) seem to reach the bulk concentration of 0.01M simultaneously at around 15nm off the surface. This observation comes with no surprise once we look at the equation (4.6) where the Debye length  $\lambda_D = 1/k_D$  only varies as function of the ionic strength and not of any parameters related to the charged surface.

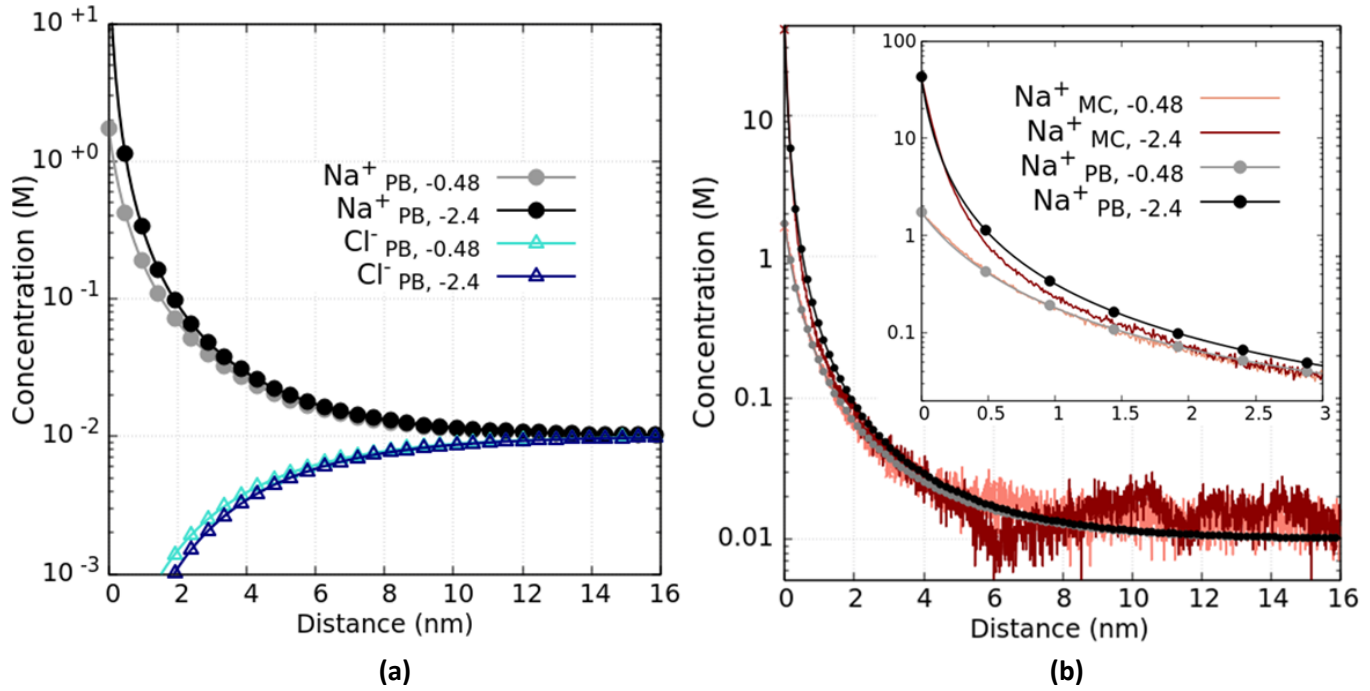


Fig.4.3. Ionic distribution of ions in a NaCl 0.01M salt in contact with surfaces with different surface charge densities respectively  $-0.48$  and  $-2.4 \text{ e.nm}^{-2}$ . Plot (a) presents distributions of  $\text{Na}^+$  and  $\text{Cl}^-$  from PB resolution. Plot (b) presents a comparison between  $\text{Na}^+$  distributions from PB and from MC calculations.

In Fig.4.3.(b), PB results are compared to MC computations. Focusing on the  $\text{Na}^+$  profiles, it is clear that for the low surface charge ( $-0.48 \text{ e.nm}^{-2}$ ), the MC curve (pink) and the PB (grey dots) are quasi superposed which confirms that, for low concentrations low surface charge, non-ideality effects like the ionic size turn out not to be an important consideration. Comparing profiles for the high surface charge ( $\sigma = -2.4 \text{ e.nm}^{-2}$ ), the MC curve (red) splits from the PB solution (black dots) at around  $2 \text{ \AA}$  from the surface with a stronger depletion but equilibrates at  $0.01 \text{ M}$  at roughly the same distance  $\sim 15 \text{ nm}$ . Fluctuations in the MC plot are inherent to the statistical nature of the results and may appear oversized (around  $0.01 \text{ M}$ ) due to the logarithmic scale on the y axis.

Part of understanding the mechanisms behind the shape of the EDLs and their effects, specifically on ionic mobility, is also being able to predict their range of action i.e. their thickness that we will note as  $\Delta_{EDL}$ . As mentioned in *chapter 2 section IV.A*, the main pathway of ionic diffusion in the C-S-H is constituted by gel pores of sizes below  $10 \text{ nm}$ . Therefore, determining the EDL thickness will indicate the extent of its effects within those nanopores.

To better quantify the effect of the surface charge on the thickness of the double layer, more simulations were run at different values of  $\sigma_{C-S-H}$ . The concentration is rather changed to a more representative value of cement paste's pore solution and fixed at  $0.1 \text{ M}$ . To put things in context, the C-S-H surface is described as an implicit tobermorite-like surface ( $4.8 \text{ Si-sites/nm}^2$ ) with different deprotonation degrees  $\alpha$  varying between  $2.5 \%$  and  $50 \%$ , respectively equivalent to  $\sigma_{C-S-H} = -0.12$  and  $-2.4 \text{ e.nm}^{-2}$ , hence covering a wide range of surfaces. Results for ionic distributions around two surfaces of charges  $-0.24$  and  $-2.4 \text{ e.nm}^{-2}$  are presented below:

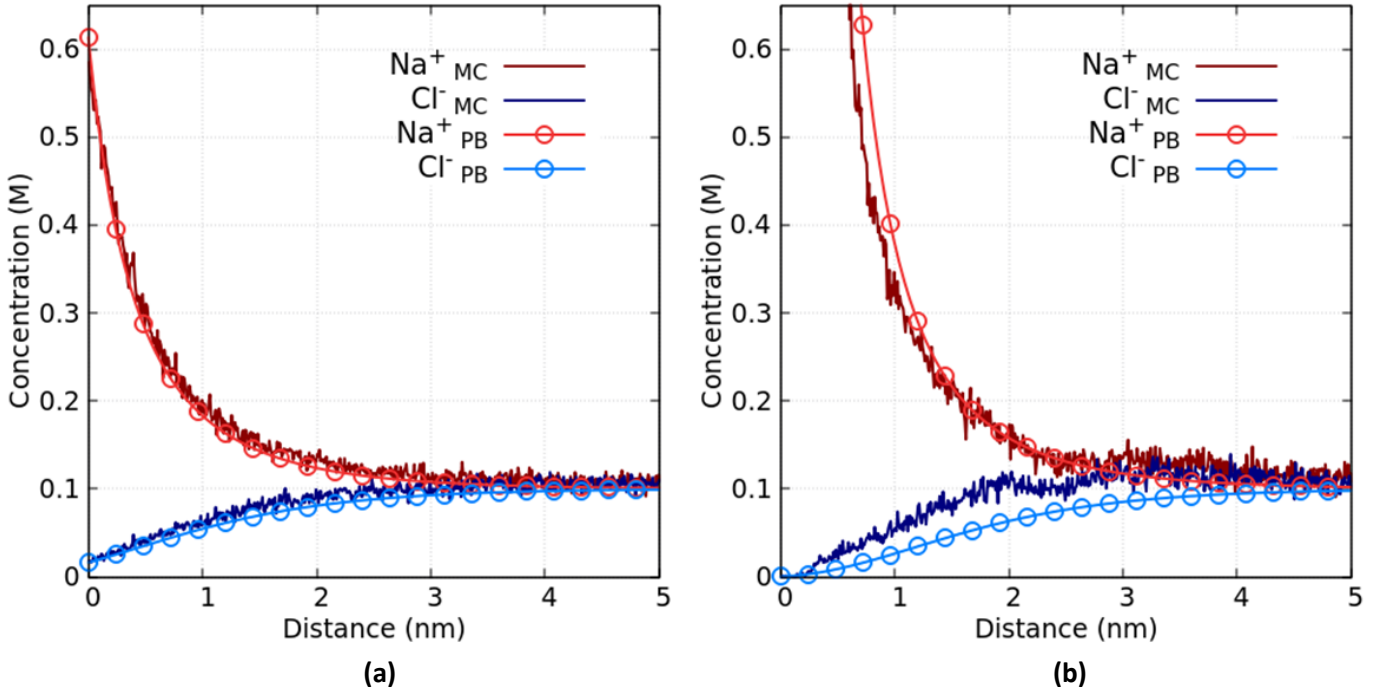


Fig.4.4. Ionic distributions in a NaCl 0.1M for **(a)**  $\sigma_{C-S-H} = -0.24 \text{ e.nm}^{-2}$  and **(b)**  $\sigma_{C-S-H} = -2.4 \text{ e.nm}^{-2}$  according to Poisson-Boltzmann (PB) computations and Monte Carlo (MC) simulations where  $x=0$  represents the OHP.

At low surface charge density (Fig.4.4.(a)), the non-ideality effects at the interface are minor. In this case, the predictions of the classical theory are in good agreement with the atomistic simulations. As  $\sigma_{C-S-H}$  increases in absolute value, the non-continuum effects at the interface dominate and we see a clear deviation<sup>c</sup> in Fig.4.4.(b) between the two methods with a stronger depletion of ions around the surface for the MC computations. Another important feature is that, independently of the surface charge magnitude, the EDL seems to vanish at around 5nm and ionic species retrieve their bulk molarities of 0.1 M. In other terms, the solution in a 5nm-radius gel pore would be completely covered by diffuse layers of the C-S-H walls.

For a better assessment of the electric properties of the solution, the corresponding charge densities (charge per unit of volume) and electrostatic potentials are computed. Using MC data, the electrostatic potential, denoted as  $\psi^{MC}$ , is obtained by integrating the Poisson equation. In our case, where the charged surface interacts with an infinitely wide solution (semi-infinite configuration), the usual integral writes as a convolution:

$$\begin{cases} \Psi^{MC}(x) = -\frac{1}{\epsilon_0 \epsilon} \int_x^\infty (t-x) \rho^{MC}(t) dt \\ \rho^{MC} = e N_A \sum_i z_i C_i^{MC} \end{cases} \quad (4.7)$$

<sup>c</sup> with more than 25% difference in the concentration values at a distance below 1nm from the surface.



Where  $C_i^{MC}$  are the ionic distributions predicted by MC calculations and  $x$  the direction perpendicular to the surface. In (4.7), the boundary condition is set infinitely far from the electrode ( $x \rightarrow \infty$ , where the potential and the electric field are zero). As the contribution of the Stern layer is neglected in the PB equation (4.3), the computation of  $\psi^{MC}$ , as defined in (4.7), is carried away so that, at  $x=0$ , the potential represents the value at the OHP.

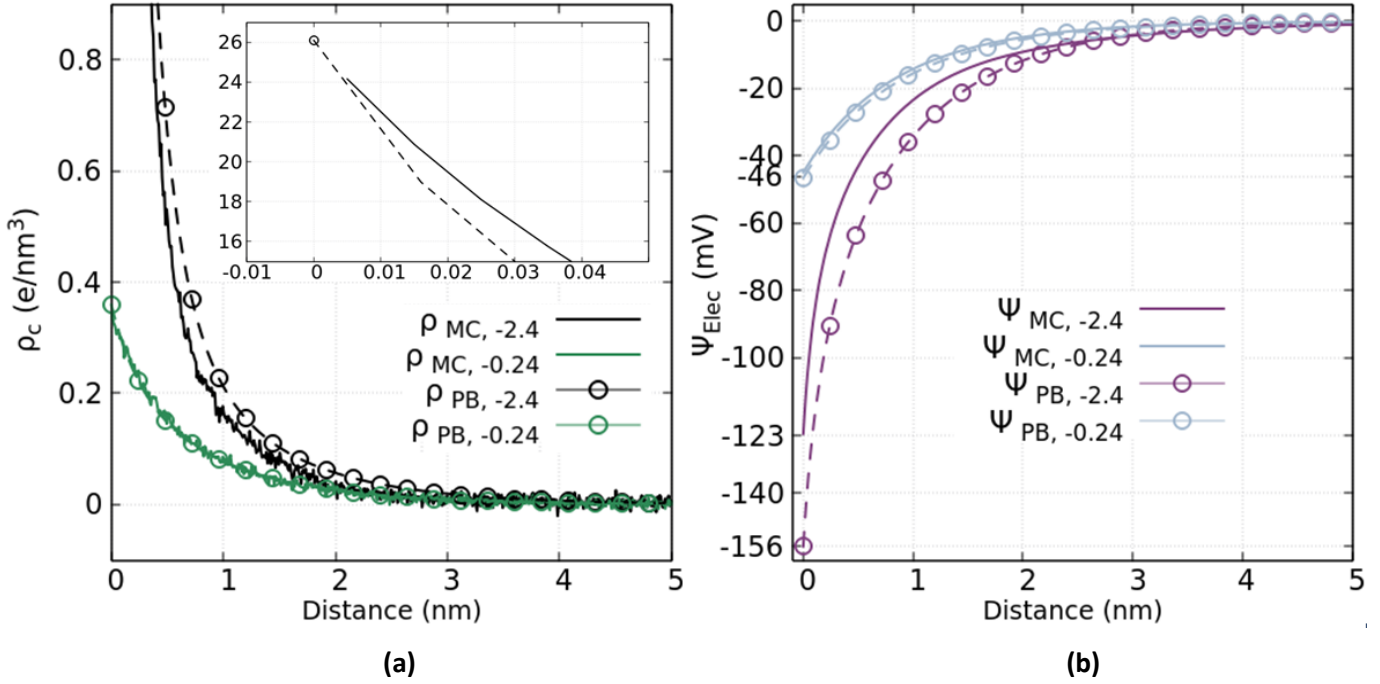


Fig.4.5. Charge densities (a) and potential profiles (b) in a NaCl 0.1M solution with  $\sigma_{C-S-H} = -0.24$  and  $-2.4 \text{ e.nm}^{-2}$  according to Poisson-Boltzmann (PB) computations and Monte Carlo (MC) simulations.

In Fig.4.5.(a), the effective charge density of the closest column of liquid reaches 0.36 and 26 e.nm<sup>-3</sup> for, respectively,  $-0.24 \text{ e.nm}^{-2}$  and  $-2.4 \text{ e.nm}^{-2}$ . These values, which are well predicted by PB, translate the increase of the sodium  $\text{Na}^+$  concentration proportionally to the charge density at the C-S-H surface. Equivalently, as  $\text{Na}^+$  accumulate to compensate the negative charge at the interface, the potential at the OHP increases (less negative). At low surface charge, both methods predict a potential of approximately -46 mV at the OHP (Fig.4.5.(b)). At a higher surface charge, the potential  $\psi^{OHP}$  increases and reaches roughly -156 mV and -123 mV for, respectively, PB and MC simulations. This indicates that, with a lower depletion, the PB solution tends to underestimate the ion-ion correlations at the interface and with it the screening power of counter-ions at a high surface density. Nonetheless, and still in accordance with ionic distributions in Fig.4.4., the charge density and the potential jointly reach zero charge and zero potential at approximately 5nm i.e.  $\Delta_{EDL} = 5 \text{ nm}$ . This suggests that the thickness of the diffuse layer does not change as function of the surface charge density. So in order to more accurately measure the effects of the surface on the diffuse layer, two quantities are computed and studied as function of  $\sigma_{C-S-H}$ .

- 1) The potential  $\psi^{OHP}$  at the OHP
- 2) The screening distance also known as the Debye length  $\lambda_D$ .

Concerning the screening length, the Debye length  $\lambda_D$  is, traditionally, measured as the distance at which the potential  $\psi$  drops by a factor of  $\frac{1}{e}$ :

$$\psi(\lambda_D) = \frac{\psi^{OHP}}{e} \approx 0.37\psi^{OHP} \quad (4.8)$$

This result, which is often mistaken for a definition, is actually obtained from the more general form of  $\psi$  in (4.4) for the case where the  $|\psi^{OHP}| \ll 4\psi_T$  ( $\sim 100$  mV) where  $\psi_T = \frac{k_B T}{z_0 e}$  ( $\sim 25$  mV for a monovalent electrolyte) is the thermal voltage. In other words, the relation (4.8) is only valid for small values of the surface charge density. To give an idea, a surface potential of -10 mV is equivalent to less than 1% of ionized silanols on a tobermorite surface in contact with a monovalent salt of 0.1M.

For the sake of comparison, the Debye length  $\lambda_D$  is computed from MC distributions using the two definitions:

- As defined in equation (4.8) and denoted as  $\lambda_{MC, small}^D$
- As the value of  $\psi$  corresponding to  $x.\kappa_D=1$  in (4.4) and denoted  $\lambda_{MC}^D$

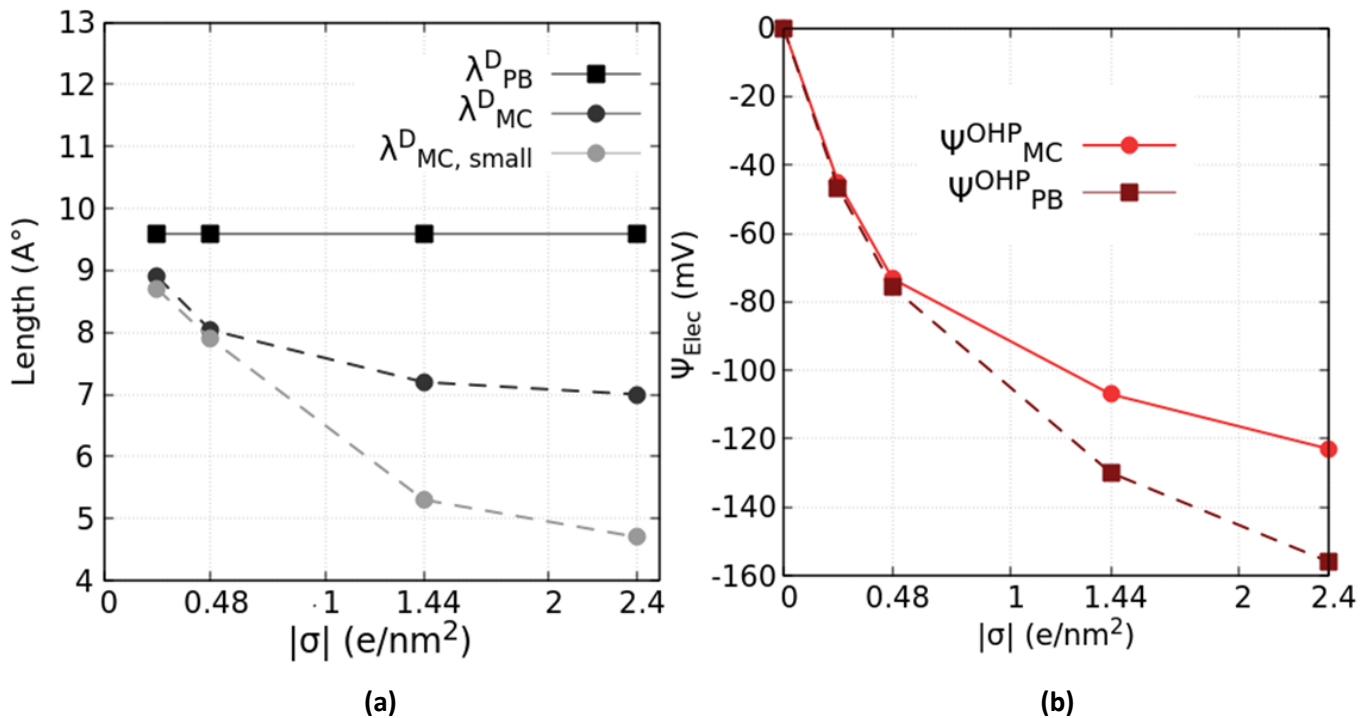


Fig.4.6. Evolution of the Debye length  $\lambda_D$  (a) and the potential drop in the DL (b) for a 0.1M NaCl solution as a function of the absolute value of the surface charge density  $\sigma_{C-S-H}$  for MC and PB computations

As expected, the classical theory does not account for any variations of the screening effect of the counter-ions with respect to the surface charge magnitude. At a constant concentration of 0.1 M, the

Debye length  $\lambda_{PB}^D$ , as computed in (4.6), remains at a constant value of 9.6 Å (Fig.4.6.(a)). On the other hand, the GCMC predicts a clear decay of the screening distance as the surface charge density increases. Although there is a common trend, the way the Debye length is defined seems to result in some discrepancy as the surface charge goes up. For a surface of  $-2.4 \text{ e.nm}^{-2}$ , the calculations with equation (4.4) predicts a value of  $\lambda_{MC}^D = 7 \text{ Å}$  (almost 30% lower than  $\lambda_{PB}^D$ ) against  $\lambda_{MC, small}^D = 4.7 \text{ Å}$  from equation (4.8) i.e. the error is 33%. In reality, using the mean field theory (Poisson equation) to accurately predict the screening effect of ionic charges can only be of approximate precision and even more so at high surface charges. In [Torrie1982], the authors explored the limitations of the classical GC model and have set  $|\sigma| = 1.9 \text{ e.nm}^{-2}$  as a reasonable threshold for the validity of the PB equations at moderately high concentrations ( $\sim 0.2\text{M}$ ). However, the deviation from the Monte Carlo simulation can be explained by a stronger hold of the highly ionized surface over the counter-ions nearby due to stronger short-range Coulombic forces and intermolecular ion-ion pairs correlations (L).

In a more practical way, the predictions of MC and PB remain of the same order of magnitude of 5 to 10 Å. In terms of porosity in C-S-H, a gel pore would typically be of sizes up to 10 nm width which is basically within ten times the Debye length. In effect, the EDL thickness  $\Delta_{EDL}$ , previously estimated to 5nm, appears to be some system-dependent multiple of the screening distance. In agreement with our estimations for a NaCl 0.1M, the authors in [Chatterji1992, Elaknes2009(2)] affirm that the “electrical potential in the double layer vanishes at a distance five times of the Debye length”.

In Fig.4.6.(b), it is the evolution of the potential at the OHP that is plotted as a function of the surface charge density. As the Stern layer is not accounted for with the PB formalism, the  $\psi^{OHP}$  actually represents the drop of the potential through the diffuse layer from the OHP to the bulk area where the potential is null. The general tendency is that as the surface charge density builds up, the OHP potential proportionally increases (more negative) and with it the potential drop through the diffuse layer. At surface charges below  $-0.48$ , the agreement between both solutions is best. At higher values, the underestimated depletion of the effective charge density (Fig.4.5.(a)) results into a slower decrease of the potential from the actual C-S-H interface and, hence, a higher value of  $\psi^{OHP}$ .

The implications on actual cementitious systems of the presently discussed change in the ionization degree are summarized in the next section along with the effect of the solution concentration.

## ii) Effect of the concentration

In this section, we study the influence of the solution density. For this matter, a NaCl solution is considered in interaction with a charged C-S-H wall. In order to mitigate the influence of the surface charge density,  $\sigma_{C-S-H}$  is fixed, in a first step, at a constant value of  $-0.24$  and the molarity is varied from 0.01M to 1M to assess the properties of the EDL for a wide range of pore solution concentrations.

### • Results and discussion

After equilibration, we see that, at a low surface charge density and low concentration (Fig.4.7.(a)), the PB calculations match best with atomistic simulations. As the distance from the charge walls increases, the solution slowly retrieves its bulk concentration of 0.01 M at roughly 15 nm. Conversely, at higher molarity (Fig.4.7.(b)), the PB seems to overestimate  $\text{Na}^+$  and  $\text{Cl}^-$  concentrations

at the OHP. This is due to an exceeding close packing of the point-like ions. By augmenting the bulk concentration by 2 orders of magnitude, the EDL thickness has actually dropped by a factor of 10 with  $\Delta_{EDL} \sim 1.5$  nm.

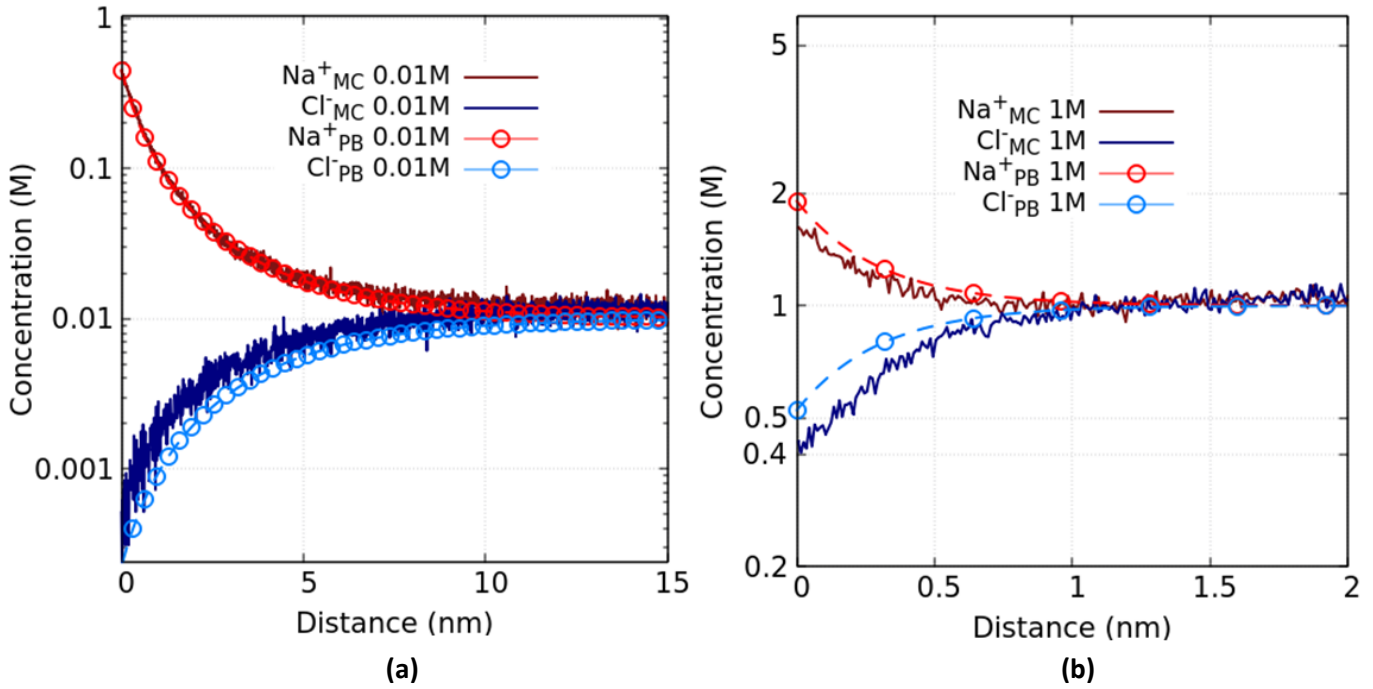


Fig.4.7. Ionic distributions in a NaCl around a surface with  $\sigma_{C-S-H} = -0.24$  e.nm<sup>-2</sup> at concentrations of (a) 0.01M and (b) 1M.

Following the same methodology as the previous part, the charge densities and the ensuing electrostatic potentials were computed. In Fig.4.8. are presented the resulting computations of the Debye length and the OHP potentials as a function of the concentration. The Debye length, in this part, is solely computed by using the equation (4.4) as previously explained and denoted in a similar way as  $\lambda_{MC}^D$ . In this case of a 1:1 electrolyte, the EDL width  $\Delta_{EDL}$  displays a decrease by a factor of nearly 3 as the concentration jumps by 1 order of magnitude (Fig.4.8.(a)). In a very similar manner, the Debye length also decreases monotonically with increasing ionic concentrations due to the effective screening of charges over short distances. For the case of surface charge  $\sigma_{C-S-H} = -0.24$ ,  $\lambda_{MC}^D$  reduces from 27 Å (0.01M) to 9 Å (0.1M) and finally 2.7 Å (1M). In terms of the potential drops between the OHP and the bulk, the increase of the concentration systematically results into a higher screening of the surface and consequently a less negative “apparent” charge at the OHP (Fig.4.8.(b)). As expected, at low surface charge where steric effects at the interface can be omitted, the Poisson-Boltzmann successfully matches Monte Carlo results even when the concentration reaches 1M. For cementitious systems, where the most alkaline pore solution reaches a pH of 13.8, the ionic concentrations rarely exceed 0.6-0.7M.

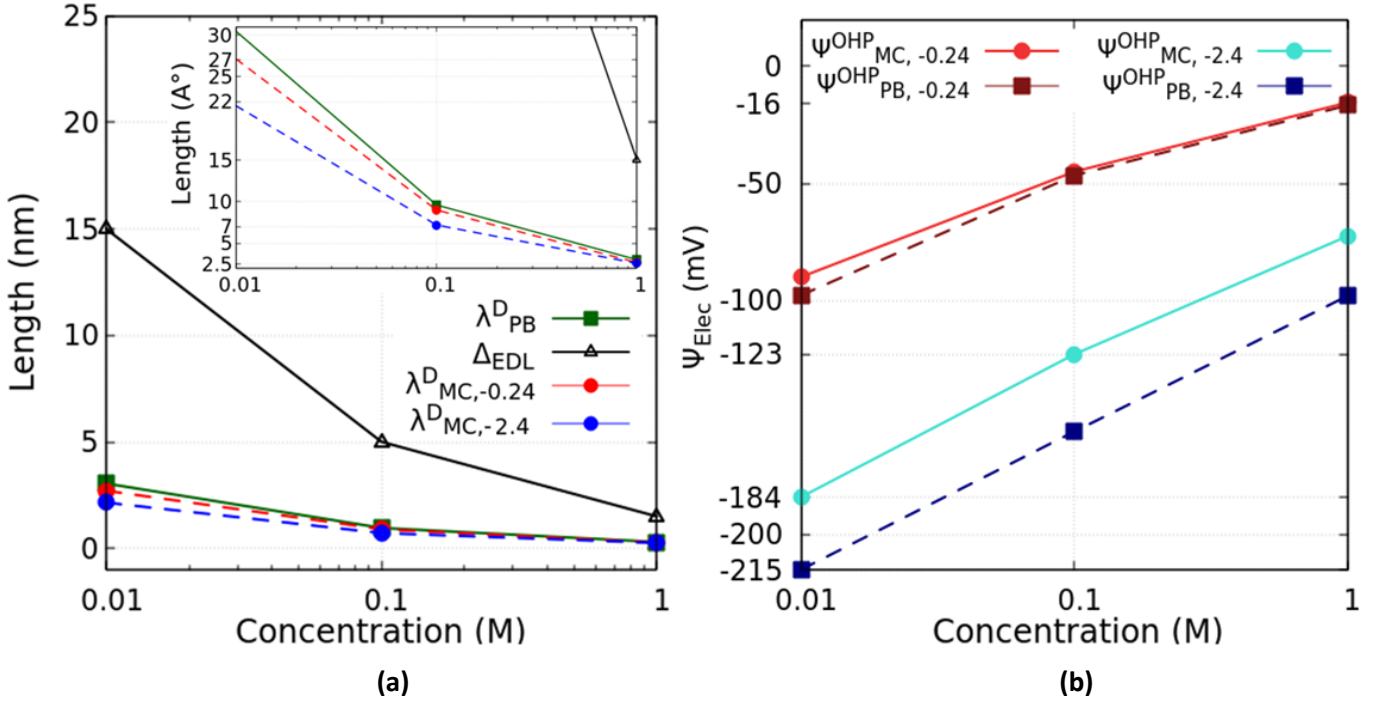


Fig.4.8. Evolution of **(a)** the Debye length  $\lambda_D$  and **(b)** the potential drop in the DL for a 0.1M NaCl solution as a function of the concentration for MC and PB computations

In order to deviate from the mean field assumptions, the same system is simulated through the same range of concentrations but at a surface charge density 10-fold higher i.e.  $\sigma_{C-S-H} = -2.4 \text{ e.nm}^{-2}$ . As a result, the EDL thickness remained unchanged while the Debye length has steadily decreased as we were lowering the concentration by roughly 30% i.e. 21.5 Å (0.01M) and 7 Å (0.1M) (Fig.4.8.(a)). However, it did almost no further regress, for 1M, and slightly decreased to 2.6 Å which is actually close enough to a sodium diameter (2.32 Å [Shan1976]) as set in the simulations. Looking at the potentials for  $\sigma = -2.4 \text{ e.nm}^{-2}$  (Fig.4.8.(b)), we notice a sizable increase in the potential drop. In this case, the PB overestimates the MC results and the shift appears to be near constant and equal to approximately 30mV. In spite of the enhanced screening of sodium at higher concentrations, the potential  $\psi_{OHP}^{MC}$  actually increased, respectively, by factors of 2, 3 and 5 hence reaching respective values of -184 mV (0.01M), -123 mV (0.1M) and -73 mV (1M) compared to the weakly charged surface.

- *Concluding remarks and implications for cementitious systems*

Ultimately, it seems that the classical theory shows clear limitations at high surface charge densities. Still, the PB results at moderate concentrations (<1M) remained reasonably close to MC results, mainly, due to neglecting long-range electrostatic forces between the ions. Also relying on the previous analysis, it appears that it is the concentration of the solution, or more generally the ionic strength, that controls the reach of the EDL. Indeed, increasing the surface charge density by a factor of 10 (from -0.24 to -2.4), only resulted in a moderate drop of 30% of the decay length  $\lambda_D$ . At high

surface charge and high concentration, the magnitude of the potential difference through the diffuse layer is, however, the outcome of two antagonist phenomena:

- The boosting influence of high surface voltages.
- The hindering of increased screening effects due to higher ionic strengths.

In cementitious systems, the alkalinity of the pore solution varies with hydroxide concentrations ranging from 0.1M (pH~13) to 0.7M (pH~13.8) [Loth2010, Sui2019(2)]. Within this interval, the Debye length for monovalent salts varies between 2 Å and 10 Å with diffuse layers extending up to 5nm of width. At this lengthscale, the DL width compares to the size of gel pores or small inter-hydrate pores. But beyond its spatial reach, the actual influence of the electrical double layer is a direct function of the developed surface potential and, equivalently, the magnitude of the charge at the surface of the C-S-H. At high pH, the silanol groups at the C-S-H interface display a relatively high ionization degree [Lab2011]. This deprotonation ratio is a system-dependent parameter which greatly depends on the pore solution (pH, ionic strength...) but, equally so, on the silanol site density (SSD). A high SSD is usually correlated to a low Ca/Si ratio of the C-S-H. And if the increase of the Si/Ca ratio may intuitively indicate stronger surface effects, experimental work on synthetic C-S-H has showed that a decline of the Ca/Si was found to mitigate the binding capacity of chloride [Beaud1990, Elaknes2010, Yosh2022]. This has been imputed to the increased ionization of silanols and, hence, the decrease of available calcium. Due to its double valence,  $\text{Ca}^{2+}$  adsorbs stronger on the negatively charged C-S-H and even builds up to form a net positive charge which is thought to favor chloride binding. So to better model real cement paste, the effect of the calcium on the properties of the EDL is investigated in the next subsection.

### iii) Effect of multivalent ions: The case of $\text{Ca}^{2+}$

An important parameter in the physical adsorption of chloride  $\text{Cl}^-$  on C-S-H surfaces is presumably the presence of multivalent species typically calcium ions  $\text{Ca}^{2+}$ . However, the quantification and prediction of the effects of divalence on ionic transport remains a challenge. This is particularly true in cement science where most empirical models rely on mean field models which fail to capture atomistic features due to neglecting the finite size of ions and the effects of non-ideality within highly alkaline and asymmetric cement pore solutions.

To evaluate the predictions from the classical theory, the results of MC calculations of ionic distributions in a  $\text{CaCl}_2$  0.05 M solution in contact with a C-S-H surface of  $\sigma = -2.4 \text{ e.nm}^{-2}$  are shown in Fig.4.9. The MC simulation box, with periodic boundary conditions in the surface directions ( $y$  and  $z$  as opposed to  $x$  the direction of the surface normal), has a size of 20 x 20 x 20 nm containing 720  $\text{Ca}^{2+}$  and 481  $\text{Cl}^-$  for a total of 1201 ions. In Fig.4.9(a), the ionic distributions in the divalent electrolyte are compared to previously presented MC results of NaCl 0.1M (as we keep a constant  $\text{Cl}^-$  concentration of 0.1 M). The  $\text{Ca}^{2+}$  curve depletes much faster than the  $\text{Na}^+$  distribution. In fact, it reaches an equilibrium concentration close to the bulk value of 0.05 M at around a distance below 3 nm while  $\text{Na}^+$  only equilibrates at 5nm. Distributions of  $\text{Cl}^-$  are also drastically different within the first 1nm around the surface. In the  $\text{CaCl}_2$  salt, it seems that due to the higher valence of calcium, chloride builds up to compensate the accumulation of  $\text{Ca}^{2+}$  in the liquid column around the plane of closest

approach which causes it to reach a peak value of 0.3M (3 times its bulk molarity). Conversely,  $\text{Cl}^-$  in NaCl follows a typical exponential evolution toward its equilibrium concentration.

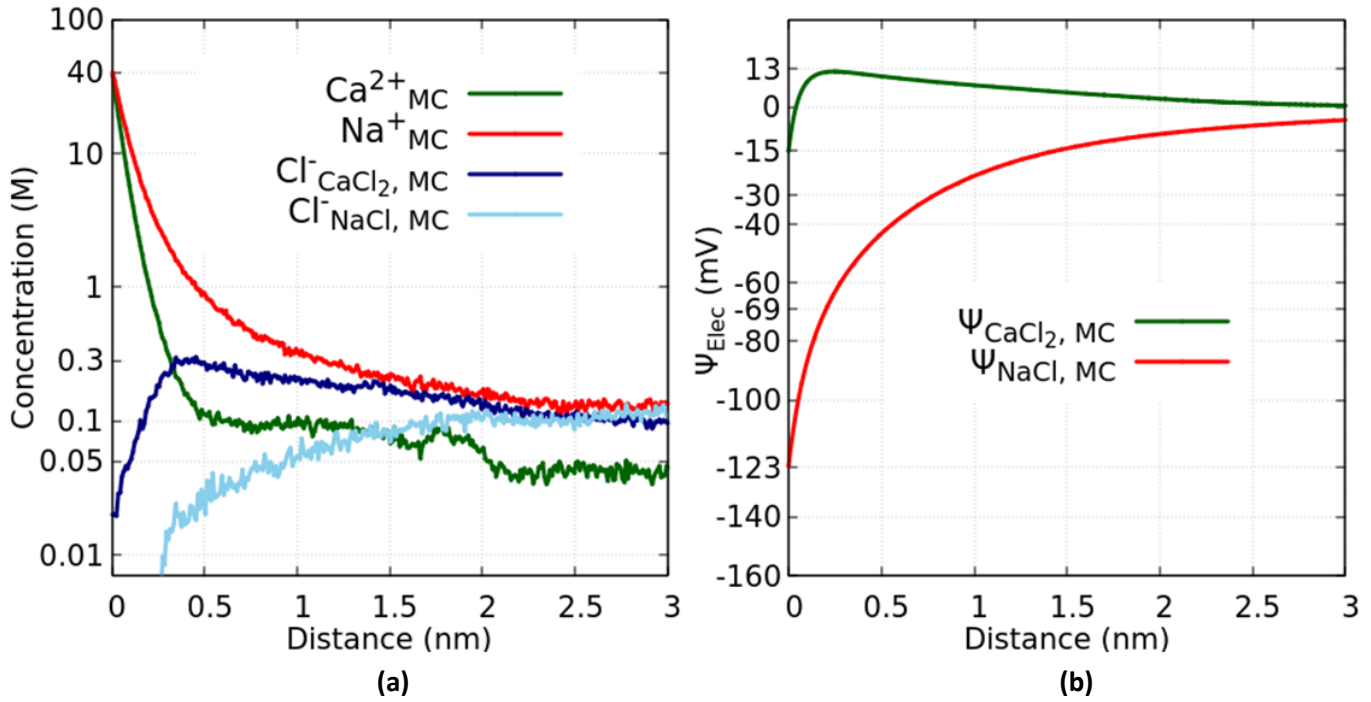


Fig.4.9. Comparison between ionic distributions (a) and electric potential profiles (b) in a  $\text{CaCl}_2$  0.05M and NaCl 0.1M electrolytes at a C-S-H surface of  $\sigma_{\text{C-S-H}} = -2.4 \text{ e.nm}^{-2}$  for MC calculations.

Electric potential profiles in Fig.4.9.(b) confirm observations on the ionic distributions. The thickness of the EDL in the presence of  $\text{Ca}^{2+}$  reduces at approximately 3 nm as opposed to a thickness of 5 nm for the monovalent solution. The potential at the OHP has a value of -15 mV, respectively -122 mV for NaCl which shows a higher screening effect of calcium compared to sodium. The potential then reaches a peak of 13 mV at a distance of 2 Å, respectively -69 mV for NaCl. Using results from MC as a reference, predictions of the classical theory are presented below in Fig.4.10. In this case of an asymmetric  $\text{CaCl}_2$  electrolyte, the PB analytical solution for monovalent electrolyte in Eq.(4.4) is no more valid. Therefore, a full numerical resolution of the Poisson-Nernst-Planck (PNP) equation, via finite element analysis, was achieved.



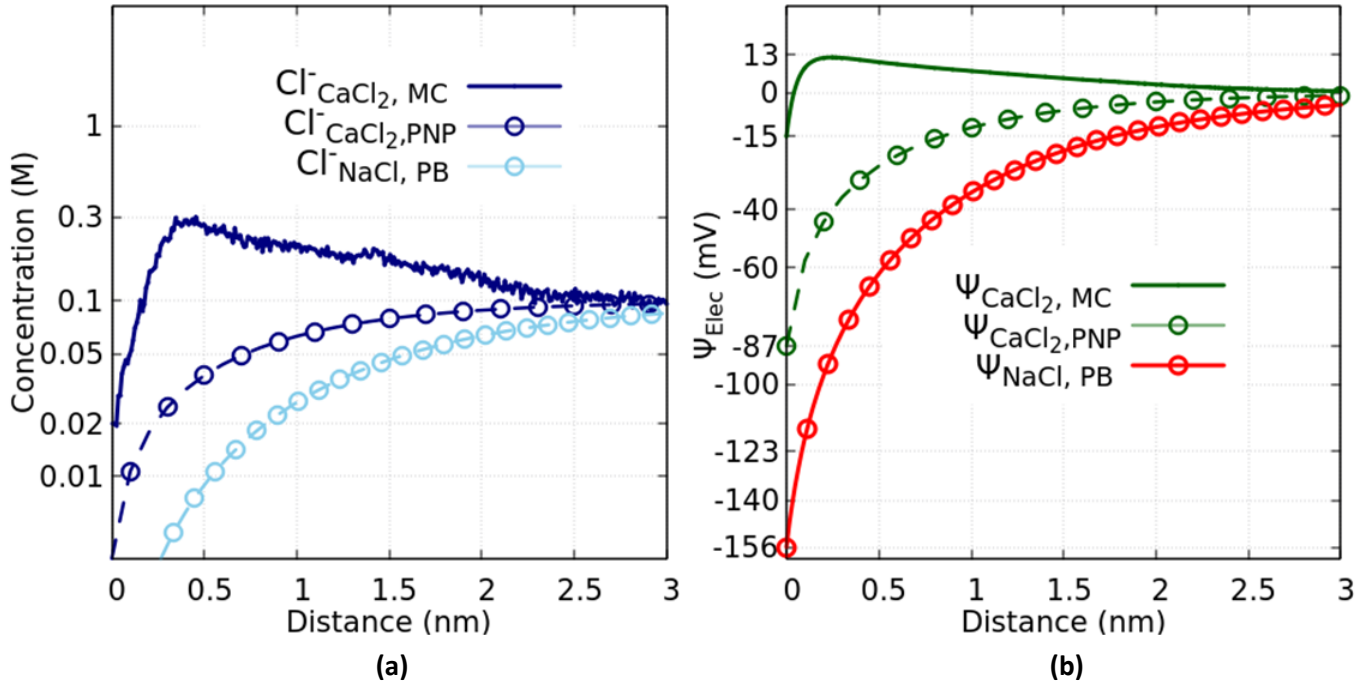


Fig.4.10. Comparison between chloride distributions (a) and electric potential profiles (b) in a  $\text{CaCl}_2$  0.05M and NaCl 0.1M electrolytes at a C-S-H surface of  $\sigma_{\text{C-S-H}} = -2.4 \text{ e.nm}^{-2}$  for MC and PB calculations.

In Fig.4.10.(a), the results from the PNP resolution show that the classical theory partly accounts for the effect of ionic valences. The  $\text{Cl}^-$  profile for the asymmetric salt (dark blue circles) depletes much faster than its homologue in the NaCl solution (light blue circles). In other words, two sodium ions are not equivalent to one single calcium. Due to its higher ionic strength i.e.  $I_{\text{CaCl}_2} = 1.5 I_{\text{NaCl}}$  (at a constant  $\text{Cl}^-$  molarity), the mean field calculations predict a Debye length (Eq.(4.6)) of  $7.9 \text{ \AA}$  for the  $\text{CaCl}_2$  0.05M in contrast with a value of  $9.6 \text{ \AA}$  for NaCl 0.1M. Nonetheless, the ion-ion correlations at the surface remain utterly overlooked. In opposition to MC predictions, there is no observable overcompensation of  $\text{Cl}^-$  (Fig.4.10.(a)) at the surface and, consequently, no charge reversal (Fig.4.10.(b)) of the potential.

### C. Computational validation: Zeta potential ( $\zeta$ ) at a C-S-H surface with $\text{Ca/Si} < 1$

In order to validate our atomistic model of the EDL formation, we use the experimental and simulation results in [Lab2011] as a reference. In this paper, the authors have prepared a C-S-H with a Ca/Si of 0.66 on which they conducted a titration experiment with NaOH, in order to determine the evolution of the surface ionization degree  $\alpha$  as a function of the pH. Afterwards, the Zeta potential of the C-S-H suspension was measured by electrophoresis (ref. chapter 2 section V.C.(ii)). Results of the titration simulations (Fig.4.11.(a)) and the corresponding experimental validation (Fig.4.11.(b)) are presented in the figure below:



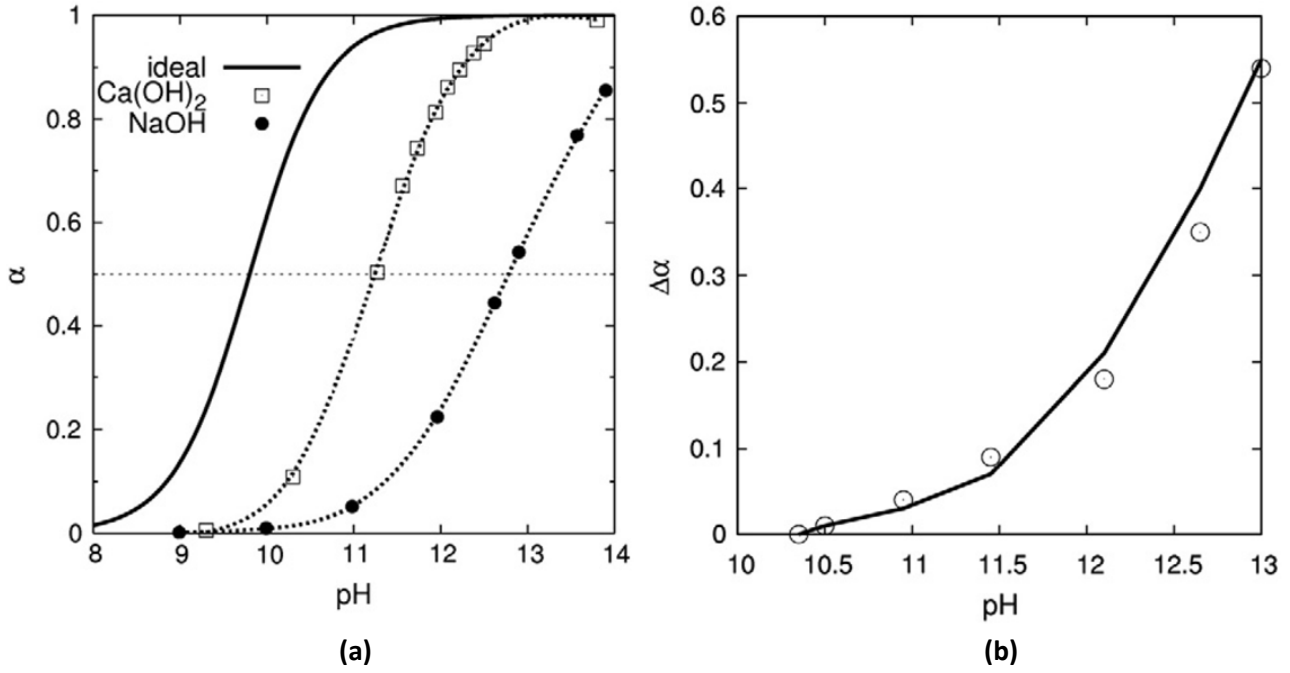


Fig.4.11. (a) Simulated ionization fraction,  $\alpha$ , versus pH for various bulk conditions: dotted line and squares  $\text{Ca(OH)}_2$  salt solution; dotted line and filled circles NaOH salt solution. The ideal curve (solid line) is given for comparison (b) Comparison between experimental (points) and simulated (line) net increase of the ionization fraction ( $\Delta\alpha$ ) as a function of the pH for C-S-H nano-particles dispersed in solution containing a low bulk calcium concentration (below 20 mM). Taken from [Lab2011].

The objective in this part was to compute Zeta potentials of the C-S-H<sub>0.66</sub> sample when titrated with a  $\text{Ca(OH)}_2$  solution. The only input parameter is the surface charge density of the C-S-H which is deduced from values of  $\alpha$  in Fig.4.11.(a) for a tobermorite-like surface of SSD 4.8 sites.nm<sup>-2</sup>. Following the same methodology, the MC algorithm in the Grand Canonical ensemble delivers ionic distributions which are converted to a charge density function  $\rho$  that is injected in the Poisson equation (4.3) then integrated. The computations are done for different values of the  $\text{Ca(OH)}_2$  concentration. The simulation parameters are summarized in the table below:

$\text{Ca(OH)}_2$ (mM)	pH	$\alpha$	$\sigma$ (e.nm <sup>-2</sup> )	$L_{\text{BOX}}$ (Å)	$\text{Ca}^{2+}$	$\text{OH}^-$	$N_{\text{TOT}}$
2	11.6	68%	-3.2	280	1280	52	1332
5	12	83%	-4.0	280	1634	132	1766
10	12.3	90%	-4.3	280	1817	264	2081
20	12.6	96%	-4.6	280	2067	528	2595

Table.4.1. Simulation box for  $\text{Ca(OH)}_2$  in contact with C-S-H surface at different values of the pH

In line with the assumptions made in [Lab2011], the zeta plane is taken at a distance of one and half ionic diameter (3 radii). In our case, we measured the Zeta potential at two locations:  $x=6$  Å and  $x=3.4$  Å. The latter value is calculated by taking 3 times the  $\text{Ca}^{2+}$  ionic radius (1.14 Å [Shan1976]). The former is the value that was chosen in the paper by considering all ions of the same radius 2 Å.

In Fig.4.12 are presented results of the electric potentials for configurations in Tab.4.1 and the corresponding Zeta measurements are plotted and compared to the values in the paper:

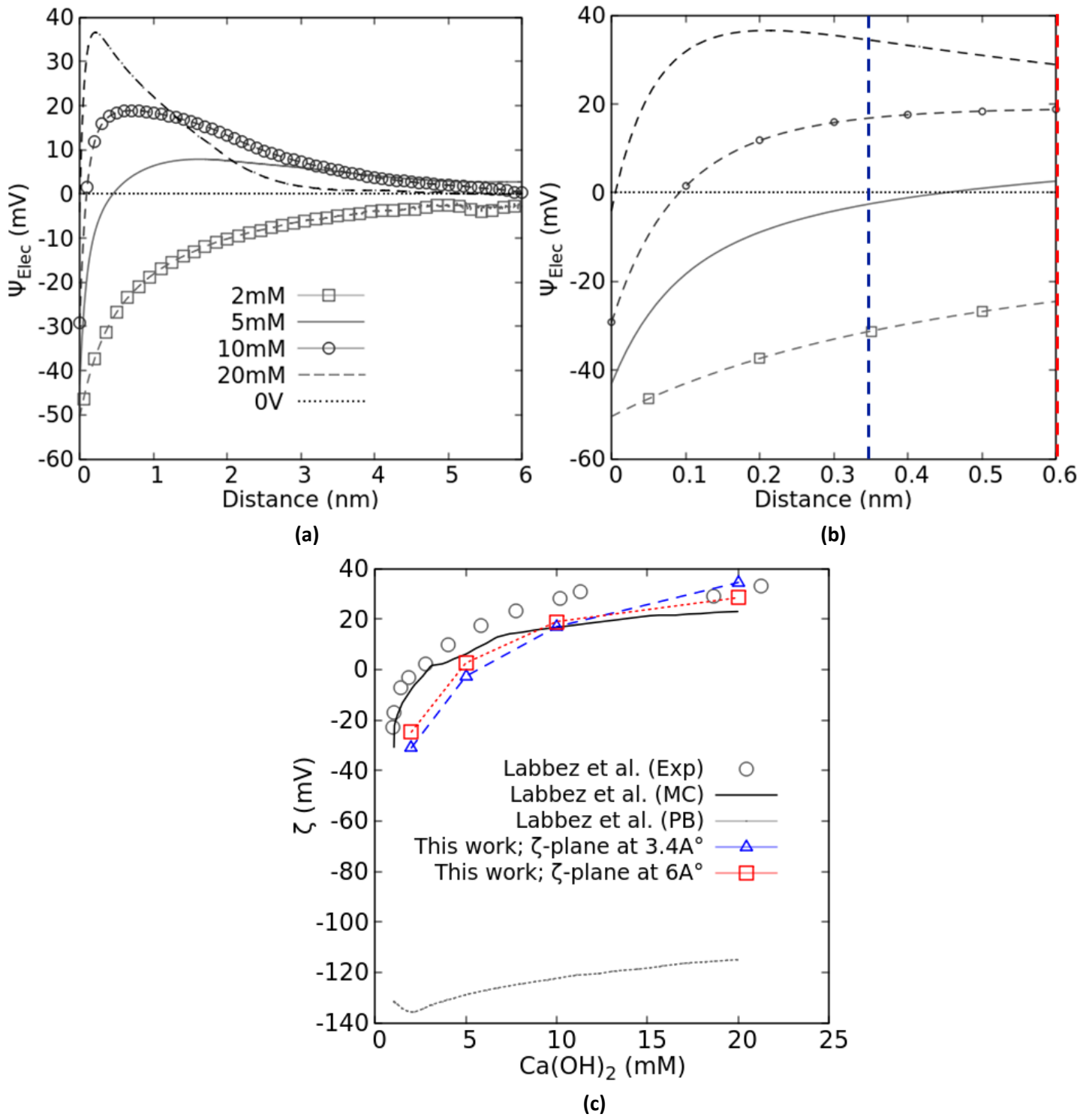


Fig.4.12. **(a)** Electric potential around C-S-H surfaces at different concentrations of  $\text{Ca(OH)}_2$  **(b)** a focus on the first 6 Å with two zeta planes: 3.4 Å (blue) and 6 Å (red) and **(c)** the evolution of the Zeta potential as function of the concentration. Adapted from [Lab2011]

Given that the potential profiles evolve slowly in the region 3.4-6 Å, the choice of the Zeta plane position was not crucial and the simulations in this study remain in close agreement with experimental and simulations results of [Lab2011].

As predicted by zeta measurements, the adsorption of calcium does not only neutralize the negative silanol groups, but shifts the potential to a net positive value. Due to this reversal of charge, chloride ions are thought to form strong ionic pairs with the adsorbed calcium. So with the increasing presence of calcium in the cementitious system, the amount of physically bound chloride would, in principle, be enhanced. In fact, this is in great part responsible for the ordinary Portland cement (OPC) having a higher binding capacity in its C-S-H with Ca/Si around 2 compared to LC3 cement where Ca/Si ratios vary more around 1.5 to 1.75 [Avet2018]. Still, this difference in the measured amount of physically bound chloride does not explain the better chloride resistivity of LC3 compared to OPC [Maraghechi2018]. In their paper, Maraghechi et al. showed the difficulty to correlate the amount of bound chloride with tangible transport properties. The authors managed, however, to find a link between the critical pore size and the apparent diffusion coefficient of each cement paste. More than that, the correlation showed that the chloride diffusion through the more refined pore structure of LC3 was 1 to 2 orders of magnitude lower than through OPC samples. Therefore, it appears that neglecting the pore size and reducing the EDL properties exclusively to the surface and pore solution properties can be misleading. In the porous C-S-H gel, the flow of mobile ions transits through the interconnected pore network. At low water to cement (w/c) ratios, it has been found [Patel2018] that gel porosity is the main pathway for ionic diffusion as it connects the big capillaries. In order to eventually quantify the effect of EDLs on the ionic transport, we will address in the following section the case of electrical double layers forming in slit pores and study the effect of the pore size, along with the other surface and solution variables, on the C-S-H/liquid interactions.

## II. Electrical double layers in slit pores

Experimental measurements to quantify atomistic effects are usually challenging to design and to conduct. The formation of the EDL at the interface of C-S-H surfaces is a good example of a complex multivariable problem driven by nanoscopic phenomena. And to fathom these effects, Zeta potential measurements have proven to be a significant characterization technique to evaluate electrokinetic potentials in colloidal systems i.e. by estimating the surface charges (*ref. chapter 2 section V.C.(ii)*). Such experimental procedures are, however, conducted on colloidal suspensions where the electrolyte (or supernatant) is not confined and only interacts with the colloidal interface at its vicinity. In other words, these experiments are not representative of electrolytes in real cementitious systems. As a matter of fact, in the porous C-S-H gel, the cement pore solution is, by definition, constrained in a pore. And since most saturated pores are only a few nanometers in width, the EDL is predicted to extend through the whole pore space. Moreover, the surface effects are likely to multiply as ions in the confined solution will interact with as many surfaces as they “see”.

In this section, the objective is to extend the atomistic model of the EDL to a more complex configuration of a slit pore where transport related parameters, such as the pore size or the pH value, are explicitly accounted for. Given the limitations of the classical theory and in order to establish quantitative results, only Monte Carlo (MC) results will be presented for the rest of the chapter.

### A. Effect of the pore size

We consider a NaCl 0.1M solution confined in a box of size 32 nm x 32 nm x  $L_x$ .  $L_x$  is the distance separating two identical charged walls each characterized by a constant surface charge density  $\sigma_{C-S-H}$  equal to  $-0.24 \text{ e.nm}^{-2}$ . The surface charge is chosen moderately low in attempt to identify whether pore size effects are of relevance. The system is simulated for three values of the pore width  $L_x$  equal to 4nm, 8nm and 16nm.

#### i) Numerical results

To compare ionic distributions at different pore sizes, the profiles of  $\text{Na}^+$  and  $\text{Cl}^-$  are shown, in Fig.4.13.(a), as function of the normalized position  $X/L_x$  where  $X$  varies between  $-L_x/2$  and  $L_x/2$  with  $L_x$  the pore diameter. Looking at the distributions in the 16nm pore, we retrieve a similar trend that what has been established previously in section I:

- The  $\text{Na}^+$  ions (pink) adsorb on the negatively charged surfaces and deplete as the distance from the walls increases to reach the equilibrium bulk concentration at approximately  $x/L_x \sim -0.3$  and  $0.3$  which corresponds to approximately a 4.8 nm distance from the walls.
- The  $\text{Cl}^-$  (light blue) are repelled from the charged surfaces and follow two symmetrical exponential-like branches that reach bulk molarity at approximately the same position than the  $\text{Na}^+$ .
- Beyond 5nm distance from each wall, the concentrations of the species reach a constant “plateau” value that is characteristic of the bulk area where the EDL effects vanish.

As the pore size reduces, the density of the  $\text{Na}^+$  within the liquid column of closest approach increases gradually reaching  $\sim 0.62\text{M}$  in the 8 nm pore (red squares) and  $\sim 0.67\text{M}$  in the 4 nm (dark red dots). For the  $\text{Cl}^-$  which is repelled from the surfaces, the concentration at the interface is practically zero and does not seem to be notably affected by the decrease of pore radius. Around the center of the pores, we notice a clear separation of the curves. In opposition to the big pore (16 nm),  $\text{Na}^+$  deplete in the 8 nm (red squares) without reaching a clear plateau and equilibrate at a value of approximately 0.14M higher than the bulk concentration (0.1M). The same happens in the smallest pore (4 nm) with an even more marked difference i.e. parabolic profile with no plateau and a minimum of 0.2M at the center. Due to the Coulombic exclusion forces, chloride ions in the pores below 8nm rather increase, in a very similar trend to  $\text{Na}^+$ , to a maximum of roughly 0.13M which also exceeds the bulk molarity.

Ionic distributions in slit pores are indeed notably affected by the size of the pore. Moreover, as the pore size decreases, the bulk area gradually vanishes. Below a certain pore width, the surface effects seem to take over and the diffuse layer basically expands to cover the totality of the pore space.

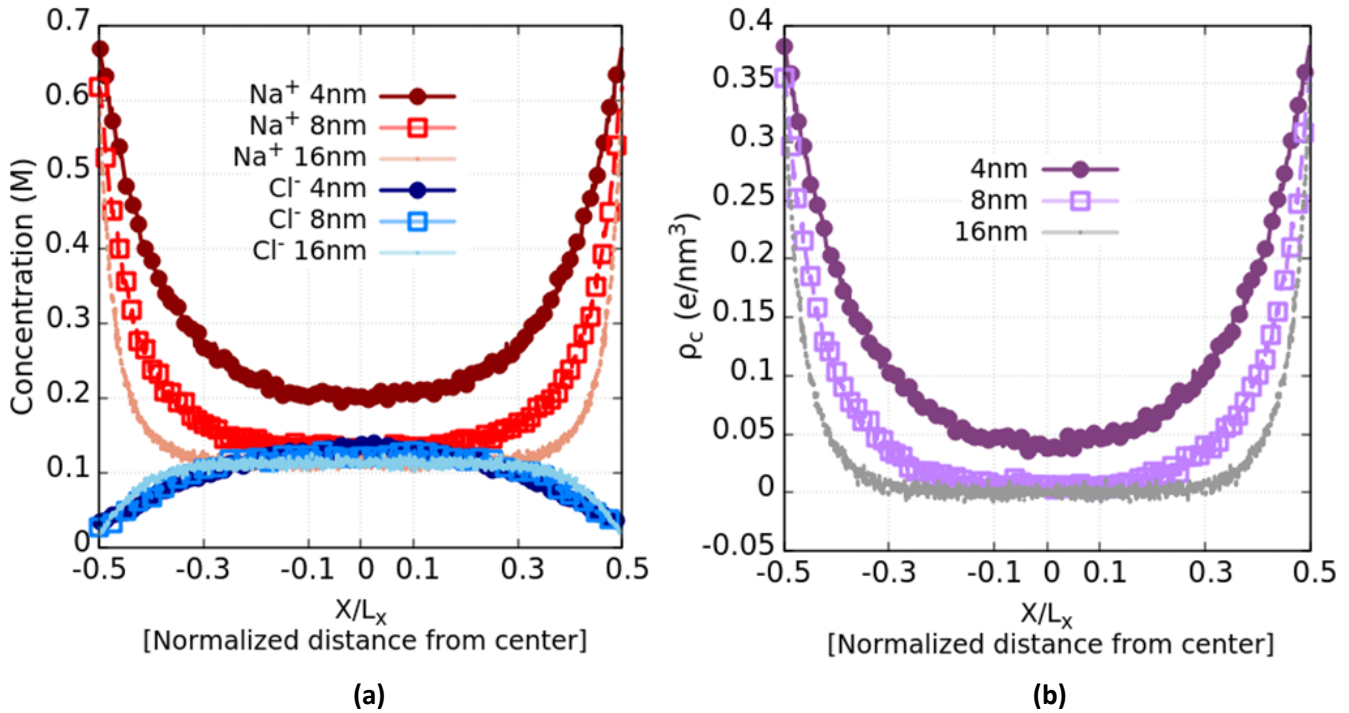


Fig.4.13. Ionic distributions (a) and effective charge densities (b) as function of the normalized distance from the pore center in a NaCl 0.1M electrolyte within pores of various diameters  $L_x$ .

In Fig.4.13.(b), the data are converted in terms of the volumetric charge density in the pore. With respect to the principle of global electroneutrality, the net balance of the charge, which is the sum of the charge of the ions in the solution and the charge of the surface sites, is zero. Nonetheless, the accumulation of  $\text{Na}^+$  at the surfaces, and even in the center of small pores, translates into a locally charged pore solution. In order to quantify these electrostatic effects, the electric potential in the pore is computed by resolving the Poisson equation. The convolution integral (4.7) is, however, no more practical as it is only valid for isolated double layers where the reference potential is taken in

the bulk region. In a slit pore, the pore solution does neither infinitely extend nor necessarily displays a bulk area acting as ground potential (0 V). Hence, a different integration scheme is adopted.

Given the invariance of the system in the directions of the walls (**y** and **z**), the electric potential is only function of **x** the direction normal to the charged walls. Thus, the Poisson equation reduces to its one-dimensional form:

$$\frac{d^2\Psi}{dx^2} = -\frac{1}{\epsilon\epsilon_0}\rho_{Tot} \quad (4.9)$$

Where the effective charge density  $\rho_{TOT}$  contains all charges in the system including both of the surface charges  $\sigma_1 = \sigma_2 = -0.24 \text{ e.nm}^{-2}$  (located at  $x_1 = 0$  and  $x_2 = L_x$ ) and the ionic charge density  $\rho(x)$ :

$$\rho_{Tot}(x) = \rho(x) + \sum_i \sigma_i \delta(x - x_i) \quad (4.10)$$

Firstly, the electric field  $\mathbf{E}(x) = -\frac{d\psi}{dx}$  is determined by a first integral

$$\frac{d\Psi(x)}{dx} = -\frac{1}{\epsilon\epsilon_0} \int_{-\infty}^x \rho_{Tot}(t) dt + K_1 \quad (4.11)$$

Given the symmetry of the pore and since  $\mathbf{E}$  is anti-symmetric i.e.  $\mathbf{E}(-x) = -\mathbf{E}(x)$ , the constant  $K_1$  is determined such as  $\mathbf{E}$  is null at the center i.e.  $\mathbf{E}(L_x/2) = 0$ . Then, the equation (4.11) is once more integrated to obtain the potential  $\psi(x)$  which writes as

$$\Psi(x) = -\frac{1}{\epsilon\epsilon_0} \int_{-\infty}^x \left[ \int_{-\infty}^s \rho_{Tot}(t) dt \right] ds + K_2 \quad (4.12)$$

Unlike  $K_1$ , determining the constant  $K_2$  can be more delicate. As previously mentioned, the potential would have traditionally be set to zero in the bulk as in experimental measurements the reference electrode is somewhere in the bulk and the other at the surface. But in slit pores, the bulk area only exists once the pore is large enough so that ionic profiles rest in a plateau at the center of the pore. Therefore, the value of  $K_2$ , assumed independent of the pore size, is determined, for a given  $\sigma$ , by shifting the potential to zero in a “big enough” pore (typically the pore of 16 nm in Fig.4.13). Equivalently, a value of the potential  $\psi^D$  (D for Diffuse layer) is determined at the plane containing the center of the ions. It is this same value that is used to shift the potential profiles in smaller pores (the pores of 4 and 8 nm). Also, in order to account for the ionic size and since we assume that the charge of an ion is located at its center; the effective charge density is set to zero below a distance of one ionic radius that we consider equal to 1 Å. This will extend the computed potential down to the plane containing the ionized silanols where the potential value is denoted  $\psi_o$ .

Implicitly, this methodology of determining the constant  $K_2$  within the pores assumes that, for a fixed surface density  $\sigma$ , the corresponding surface potential is not affected by the pore size. In practice, this hypothesis is good as long as the pore radius does not fall below the screening length so that surfaces do not interact directly with each other. At a moderate concentration equal to 0.1 M, MC calculations on NaCl (*ref. section I.B.(ii)*) predict a Debye length  $\lambda_{MC}^D$  within the span of 7 to 9 angstroms. As the vast majority of the C-S-H gel pore population ranges between 4 and 10 nm width, the approximation is considered valid. The results of the computations of  $\psi(x)$  at different steps (Eq. (4.10), (4.11) and (4.12)) are presented in Fig.4.14:

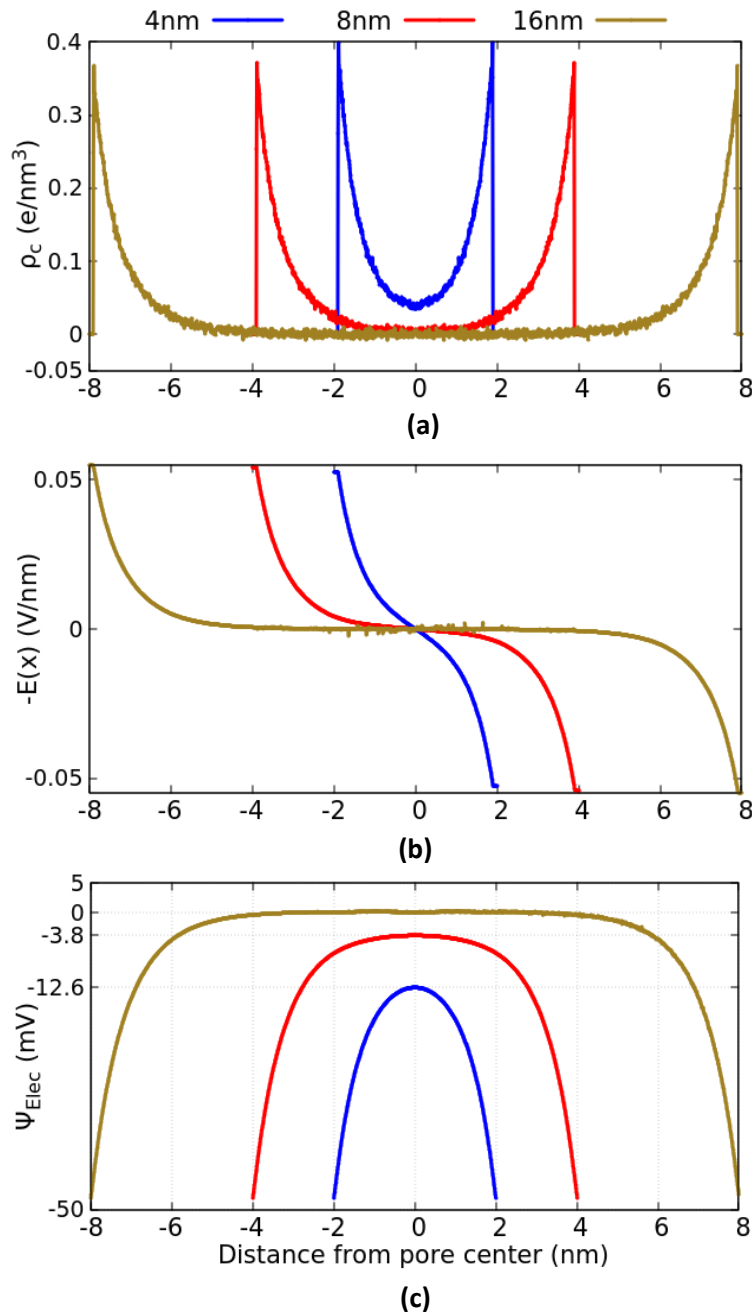


Fig.4.14. (a) Effective charge distribution, (b) the electric field and (c) the electrochemical potential computed from MC data in pores of sizes 4 nm (blue), 8 nm (red) and 16 nm (yellow) for a NaCl 0.1M solution and  $\sigma_{C-S-H} = -0.24 \text{ e.nm}^{-2}$

As expected, the electric potential in the 16nm-pore displays a plateau characteristic of the bulk area. As the solution is electroneutral at the center, the potential is, therefore, constant and set to zero. As a consequence, the surface potential  $\psi_0$  at both facing walls is set at a value of -48 mV. Since we are dealing with pores that are at least 5 times the screening length ( $\sim 7$  to  $9 \text{ \AA}$ ), the potential at the C-S-H surfaces is assumed unchanged as the pore radius reduces i.e. smaller pores have the same value of  $\psi_0$ . However, the potential at the pore center gradually builds up as the diameter decreases to 8 and then 4nm and, respectively, reaches approximately -3.8mV and -12.6mV. In order to directly correlate the pore radius to the electrostatic effects, the average potential  $\tilde{\psi} = \frac{1}{L_x} \int_0^{L_x} \psi(x) dx$  has also been computed for each pore. Ultimately, it is the smallest pore that stands out as the most “negatively charged” pore with an overall average of -21.8 mV as opposed to -11.9 mV and -4.9 mV, respectively, for 8 nm and 16 nm.

## ii) About slit pores in cement paste

In conclusion, it seems that the electric properties of the EDL are greatly enhanced or attenuated due to the effect of the slit width. In cement paste, the pores of 10 nm and beyond are identified as the space between the formed C-S-H foils. In these “inter-hydrate” pores, which can reach up to 50nm size, the diffuse layers at the C-S-H/liquid interface are too localized to overlap. The pore solution is then dominated by the bulk area where the potential gradients normal to the surface are practically null once we get far enough from the hydrate/liquid interfaces. As a result, the diffusing ions predominantly escape the surface effects and their mobility is thereby weakly disturbed. For a given cement paste, the pore size distribution is a result of the mix design and the nature of the binders that are used<sup>♦</sup>. In binary or ternary systems, the addition of supplementary cementitious materials, such as calcined clay; slag or silica fume, was found to effectively refine the pore structure [Gjrv1979, Gjrv1994, Maraghechi2018]. As the pore size reduces, the electrical double layers are predicted to progressively overlap disrupting local electroneutrality and further charging the pores. For negatively charged pores, we can intuitively imagine a stronger repulsion of anions. In fact, this is probably one of the main reasons for the increased resistance to chloride in blended cements. Nonetheless, as explained in the previous section (*ref. section I*), the intensity and the extent of the EDL effects are function of many parameters, namely the C-S-H ionization degree, the solution concentration and surely its alkalinity. The influence of these properties is addressed in the next subsections for the case of a slit pore.

## B. Interactions at the surface: Influence of $\sigma_{\text{C-S-H}}$

In order to cover a wide range of C-S-H surfaces with various Ca/Si ratios, the surface charge density  $\sigma_{\text{C-S-H}}$  is varied from -0.12 to -1.44 e.nm<sup>-2</sup>. We keep the same system; namely NaCl 0.1M solution simulated in slit pores of 4nm, 8nm and 16nm size. Following the same methodology, the GCMC algorithm delivers ionic distributions  $C_i^{MC}(x)$  which are converted, for each configuration, to a charge density function (4.10) that is injected in (4.9) then integrated into a potential function  $\psi(x)$  (4.12) and finally averaged to  $\tilde{\psi}$  over the cross-section of the pore.

---

<sup>♦</sup> The relative humidity (RH) and saturation degree are also critical as only pores containing water can transport ions. This will actually be the main effect limiting the effective pore size for transport.



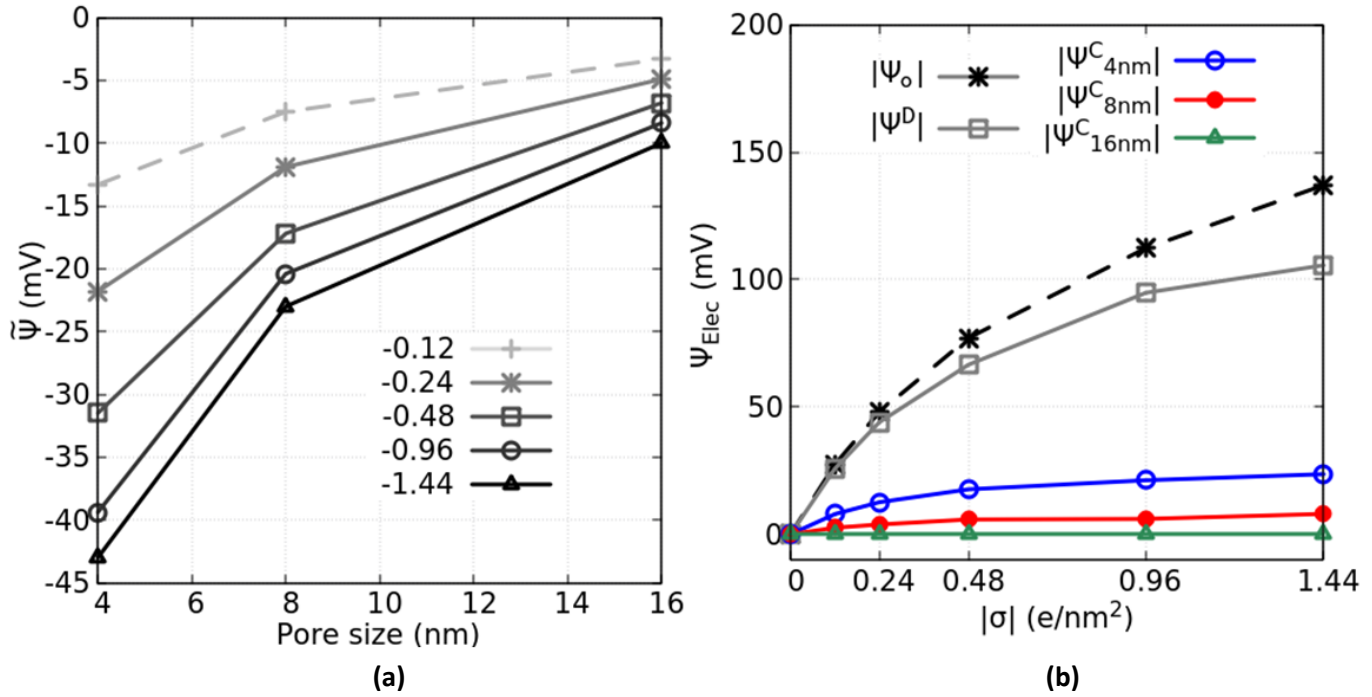


Fig.4.15. (a) Average potential as function of the pore size and (b) evolution of the potential value at the surface ( $\psi_0$ ), the OHP ( $\psi^D$ ) and the center ( $\psi^C$ ) plane in pores of 4, 8 and 16 nm of size.

In Fig.4.15.(a), one can clearly see that the increase of the surface charge categorically translates into an overall more negative potential. However, it is the combined contribution of the surface charge and the reduced pore size that displays the highest effect. In effect, large pores show a mitigated effect of the EDL and increasing the charge at the surface by a factor of 10 has very little impact. In the 8nm slit, the effect is increased but seems to quickly saturate as the Debye length is reducing (with the increasing surface charge) and the ionic cloud is more effectively screening the ionized sites at the surface. By further reducing the size, the potential at the center of the pore gradually increases hence diminishing the potential drop through the diffuse layer. In order to measure the potential drop through the diffuse layer, the potential is computed, as function of  $|\sigma_{C-S-H}|$ , at different locations within the pores; namely at the silanol surface  $\psi_0$  ( $x=0$ ),  $\psi^D$  (at  $x=1$  Å) and at the center of the pores, respectively noted  $\psi^C_{4\text{nm}}$ ,  $\psi^C_{8\text{nm}}$  and  $\psi^C_{16\text{nm}}$  (Fig.4.15.(b)). As the potential at the plane of closest approach  $\psi^D$  is assumed unaltered with the shrinking of the pore, the overlapping of the diffuse layers only results into a higher potential at the center which further deviates from the bulk value as ions are accumulating and locally charging the pore space. In electronics, where it is common to view the EDL as a capacitor, the reduction of the potential drop for a same amount of “stored” charges would translate in an increased capacitance of our EDL i.e. a higher “interception” of the flowing ions. In terms of transport, the magnitude and the sign of the pore potential has been proved to significantly enhance or mitigate the flux of the ions depending on their valence [Fried2008]. For that matter, the repercussions of the EDL properties on chloride’s diffusivity are studied in the next chapter.

### C. Effect of the concentration

In the case of exposure to seawater chloride, where the molarity is around 0.5M, the concentration gradients tend to move chlorides, among other species, toward the steel reinforcement within the structure. To assess the effect of the chloride concentration rise, we simulate the formation of the EDL around a  $-0.24 \text{ e.nm}^{-2}$  C-S-H surface in contact with 0.1M and 0.5M NaCl salt.

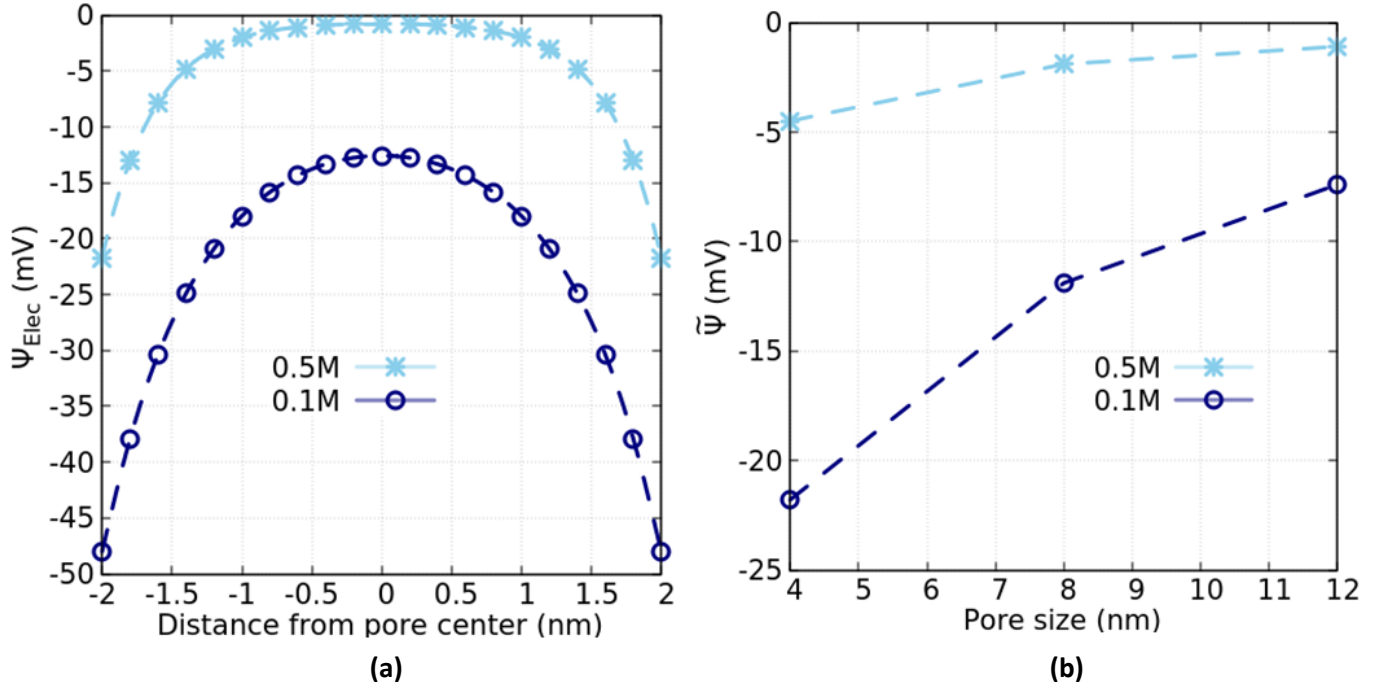


Fig.4.16. **(a)** Electrochemical potentials as function of the position in a 4 nm pore and **(b)** the evolution of the potential average as function of the pore size for NaCl solutions of 0.1M (dark blue) and 0.5M (light blue)

After equilibration, one can see that the electrochemical potentials at high concentration are notably hindered. The potential at the surface in a 4 nm pore (Fig.4.16.(a)) has dropped (in absolute value) from roughly -48 mV (0.1M) to -21.7 mV (0.5M) due to the higher screening of the surfaces. In fact as the concentration of the reservoir rises, the GCMC accordingly adjusts the chemical potential at the surfaces which ultimately determines the amount of adsorbed ions. At 0.5M, the EDL thickness is greatly reduced and seems to localize within the first nanometer so that, even within the 4 nm pore, the overlapping is barely happening. In the critical situation where chloride would have reached 0.5M in the pore solution, the pores will be very weakly charged (Fig.4.16.(b)) and the EDL would have a minor effect on the ionic flux and chloride's ingress. In a real cement paste, the influx of chlorides in the concrete would require the hydroxide to leach out in respect with the electroneutrality of the pore solution. For very long exposure periods (decades), the pH drop below a certain point can be very harmful and irreversibly trigger the corrosion of the reinforcements which would eventually cause the failure of the cement-based structure. The study of the effect of pH (at a constant surface charge) is presented in the following paragraph.

## D. Explicit OH<sup>-</sup> in simulation boxes

Pore solution in cement paste is a highly alkaline electrolyte with values of pH usually beyond 13 [Loth2010, Voll2016]. This alkalinity constitutes a natural protection for rebars in reinforced concrete which find themselves coated with a passivation layer (*ref. chapter 2 section I*). It also plays a critical role in the study of the EDL as it directly links to the deprotonation degree  $\alpha$  of the silanol groups at the C-S-H surface. Given the lack of consistent atomistic models of C-S-H/solution interfaces, it remains difficult to construct predictive models capable of correlating the ionization  $\alpha$  to the pH. It is, however, possible to make simulations of pore solution more realistic by explicitly accounting for OH<sup>-</sup> ions.

For the sake of comparison with previous results on NaCl solutions, a {NaCl 0.1M + NaOH} system was simulated. The concentration of NaCl is kept at 0.1M, so that the chloride content remains unchanged, and it is the value of the fixed pH that determines the molarity of the added NaOH salt. To ensure that pH values are consistent with data from real systems [Ander1989, Loth2010, Voll2016, Plus2017, Sui2019(2)], simulations are run for pHs equal to 13, 13.3 and 13.5 i.e. NaOH at 0.1M, 0.2M and 0.3M, respectively. The computational details are defined as in the homologue NaCl case. Electrostatic and Lennard-Jones potentials for oxygen and hydrogen of the hydroxide ion are added [Vacha2007] (*ref. chapter 3 section I*). In this simplified configuration, we consider a fixed surface charge density, independent of the pH change, set at a value of  $-0.24 \text{ e.nm}^{-2}$ . Ionic distributions and their corresponding potential are obtained using the GCMC algorithm. Firstly, we mitigate the pore size effects by looking at the big 12 nm pore in Fig.4.17.(a).

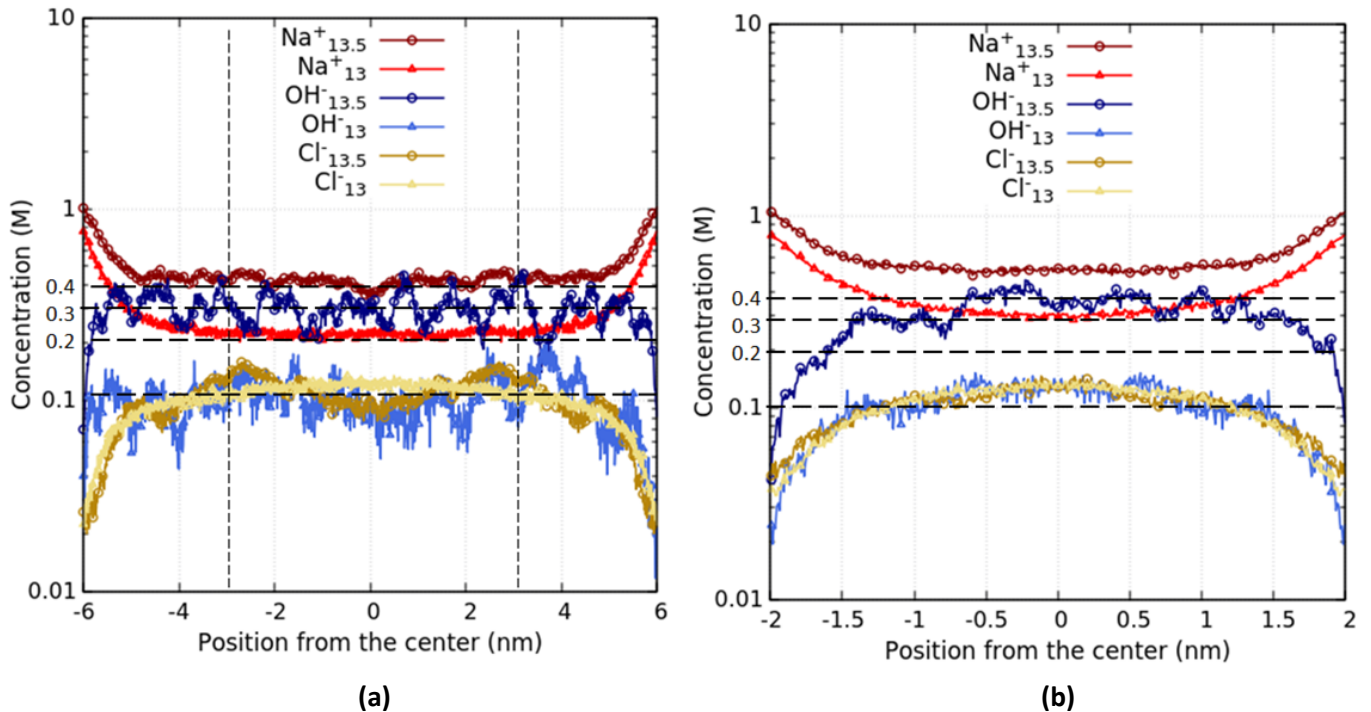


Fig.4.17 Ionic distributions in pores of (a) 12 nm and (b) 4 nm [For simplicity, only distributions at pH values of 13 and 13.5 are shown].

At a pH=13 (light colors),  $\text{Na}^+$  and  $\text{Cl}^-$  reach their respective bulk concentrations of 0.2M and 0.1M at roughly 3nm (vertical dotted lines) i.e. roughly the thickness of the EDL. Despite averaging on a number of simulations ( $10^2$ ), the hydroxide distribution ( $\text{OH}^-$ ) displays noticeable oscillations through the box but remains very close to the  $\text{Cl}^-$  behavior as they both share the same valence. At a higher pH of 13.5 (dark colors), but constant chloride content, only  $\text{Na}^+$  and  $\text{OH}^-$  bulk densities, respectively, increase to 0.4M and 0.3M. In this new configuration, the ionic strength of the solution literally doubles. As a consequence, the EDL thickness is diminished. A good indicator is the  $\text{Na}^+$  which equilibrates at roughly 1nm from the surface. As the pore reduces to a size of 4nm (Fig.4.17.(b)), the bulk area vanishes. Only the  $\text{Na}^+$  at a pH of 13.5 reaches a pseudo-plateau but its concentration remains 25% higher than its bulk molarity. Also, the fluctuations of the  $\text{OH}^-$  distributions are sizably attenuated. So in the absence of chemical reactions at the C-S-H surface (no titration), the increase of pH has a very similar effect to the increase of the ionic strength i.e. a reduction of the EDL thickness accompanied with a stronger depletion of ions at the surface (so a shorter Debye length) (ref. section I).

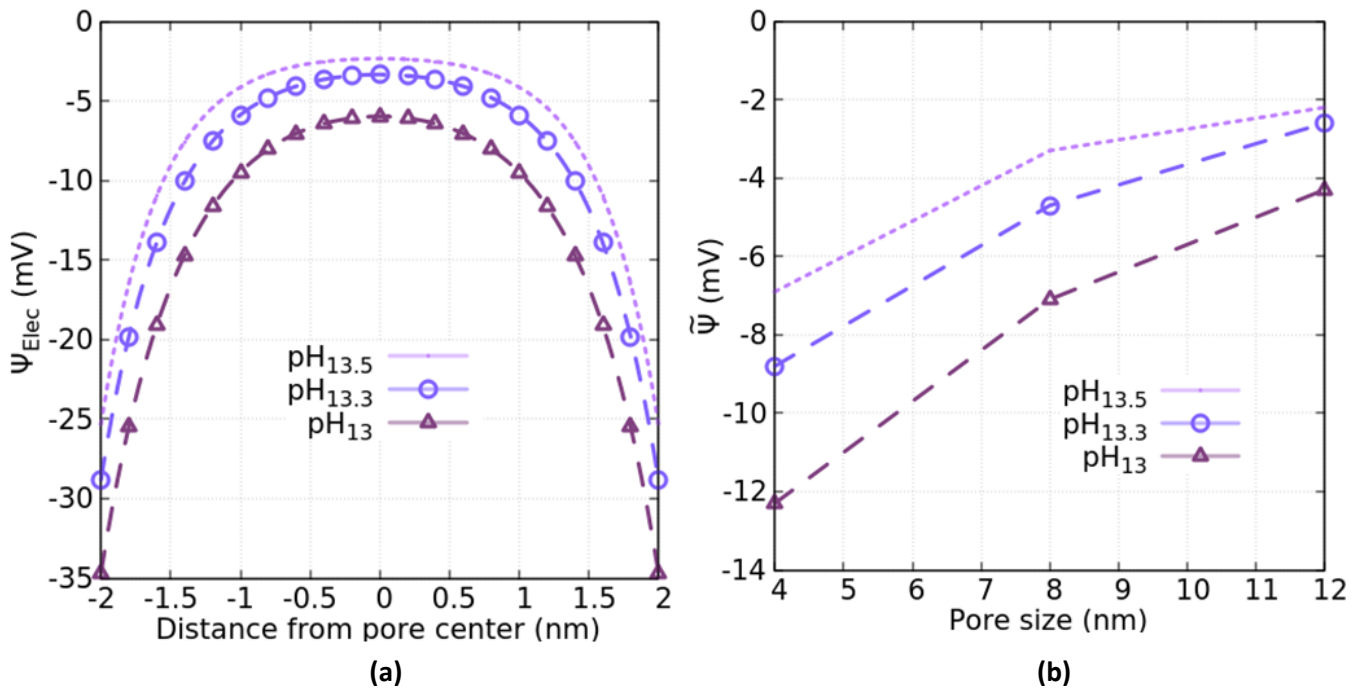


Fig.4.18. (a) Electrochemical potentials as function of the position in a 4nm pore and (b) the evolution of the potential average as function of the pore size for NaCl+NaOH solutions of pH 13 (triangles), 13.3 (Circles) and 13.5 (dotted lines)

As presented in Fig.4.18, the average pore potentials (Fig.4.18.(b)) suggest that a decrease of the alkalinity results in a boosted influence of the surfaces on the ions. At high pH values, the EDL thickness shortens down to a few nanometers; typically below 3 nm for pH>13. Hence, the surface effects are only of noticeable effect in the 4 nm pore where the diffuse layers do overlap. As pH reduces, the ionic strength of the solution drops and, with it, the screening of the negative surface. This results in a higher absolute value of the average potential which denotes a lower potential drop in the DL and a higher “capacitance” of the EDL.

In a more realistic configuration, the previous observations would only apply if the silanol groups at the C-S-H surface are assumed to have reached a saturation of their ionization degree at a certain threshold, denoted  $pH_0$ , that we implicitly set at 13 (also  $pH_0=13$  in  $Ca(OH)_2$  salt as in Fig.4.11.(a) [Lab2011]). For values below  $pH_0$ , a further decrease of pH may result into a change of the deprotonation ratio of silanols and, consequently, a change in the surface charge density which would invalidate our assumption of a constant  $\sigma_{C-S-H}$ . In terms of physical binding, the noted similar behavior of hydroxides and chlorides (Fig.4.17) will make both species compete upon forming ionic pairs with the adsorbed cations [Plus2016]. Experimental investigation on PC pastes has, in fact, showed that the higher the pH of the pore solution, the lower the amount of bound chloride was measured [Tri1989]. This ultimately indicates that the physical binding of chloride in general, and specifically on C-S-H, tends to increase as pH drops. In more recent work, it has also been found that while chloride binding increases with lowering pH from a value of 13 to 12 (mainly attributed to adsorption on AFm phases), a further decrease of the alkalinity resulted into dissolution of the hydrates and, thus, a consequent collapse of the binding capacity [DeWeerd2015]. In reality, the decrease of pH is a great deal more complex than it seems as it literally changes the chemistry of the system. The increase of the solution acidity and its effects are actually intimately linked to the present alkali in the solution.

To better model the behavior of actual cement pastes, the next chapter focuses on the study of the EDL formation in calcium containing systems and the ensuing implications on the physical binding of ions.

### III. Summary

In this chapter, Monte Carlo calculations were compared to results from the Poisson-Boltzmann. It was found that the agreement between the two methods was best at moderate surface charges and moderate ionic concentrations. Beyond a certain value of the surface charge density, the PB clearly overestimated concentrations around the interface due to an excessive packing of the point-like ions. Upon the addition of calcium cations, as an example of a multivalent species, the classical resolution failed to predict the overcompensation of the negative surface and the reversal of charge due to the Calcium adsorption on the C-S-H. The computations of the model were then successfully validated with computational results and Zeta potential measurements published in [Lab2011].

Once considering the case of a slit pore, it was shown that electrostatic properties of the EDLs were sizably affected by the pore radius. The decrease of the pore size resulted into a stronger overlapping of the developed EDLs and a disturbance of the local electroneutrality in the pore solution. The increase of the surface charge density equally showed stronger interactions at the surface with a higher value of the electrochemical potential at the C-S-H/liquid interface. However, the increase in the ionic strength was followed by a reduction of the EDL thickness, due to the higher screening of adsorbing cations, and consequently an attenuation of its influence over the surrounding ions.

## IV. References

- [Avet2018] Avet, François, and Karen Scrivener. "Investigation of the calcined kaolinite content on the hydration of Limestone Calcined Clay Cement (LC3)." *Cement and Concrete Research* 107 (2018): 124-135.
- [Ander1989] Andersson, Karin, et al. "Chemical composition of cement pore solutions." *Cement and Concrete Research* 19.3 (1989): 327-332.
- [Beaud1990] Beaudoin, James Joseph, Vangipuram Seshachar Ramachandran, and Raouf F. Feldman. "Interaction of chloride and C-S-H." *Cement and Concrete Research* 20.6 (1990): 875-883.
- [Bernal1952] Bernal, J. D. "The structures of cement hydration compounds." *Proc. 3rd Int. Symp. Chem. Cem., London: Cement and Concrete Association*. 1952.
- [Chu2014] Churakov, Sergey V., et al. "Intrinsic acidity of surface sites in calcium silicate hydrates and its implication to their electrokinetic properties." *The journal of physical chemistry C* 118.22 (2014): 11752-11762.
- [Chatterji1992] Chatterji, Susanta, and M. Kawamura. "Electrical double layer, ion transport and reactions in hardened cement paste." *Cement and Concrete Research* 22.5 (1992): 774-782.
- [DeWeerdt2021] De Weerdt, Klaartje. "Chloride binding in concrete: recent investigations and recognised knowledge gaps: RILEM Robert L'Hermite Medal Paper 2021." *Materials and Structures* 54.6 (2021): 1-16.
- [DeWeerdt2015] De Weerdt, Klaartje, et al. "Impact of the associated cation on chloride binding of Portland cement paste." *Cement and Concrete Research* 68 (2015): 196-202.
- [Elaknes2010] Elakneswaran, Yogarajah, et al. "Ion-cement hydrate interactions govern multi-ionic transport model for cementitious materials." *Cement and concrete research* 40.12 (2010): 1756-1765.
- [Elaknes2009(2)] Elakneswaran, Y., T. Nawa, and K. Kurumisawa. "Electrokinetic potential of hydrated cement in relation to adsorption of chlorides." *Cement and Concrete Research* 39.4 (2009): 340-344.
- [Fried2008] Friedmann, Hubert, Ouali Amiri, and Abdelkarim Aït-Mokhtar. "Physical modeling of the electrical double layer effects on multispecies ions transport in cement-based materials." *Cement and Concrete Research* 38.12 (2008): 1394-1400.
- [Fix1979] Fixman, Marshall. "The Poisson–Boltzmann equation and its application to polyelectrolytes." *The Journal of Chemical Physics* 70.11 (1979): 4995-5005.
- [Gjorv1994] Gjorv, Odd E., Kefeng Tan, and Min-Hong Zhang. "Diffusivity of Chlorides from Seawater Into High-Strength Lightweight Concrete." *Materials Journal* 91.5 (1994): 447-452.
- [Gjorv1979] Gjorv, O. E., and Ø. Vennesland. "Diffusion of chloride ions from seawater into concrete." *Cement and Concrete Research* 9.2 (1979): 229-238.
- [Gra1947] Grahame, David C. "The electrical double layer and the theory of electrocapillarity." *Chemical reviews* 41.3 (1947): 441-501.



- [Harris2022] Harris, Maya, et al. "A method for the reliable and reproducible precipitation of phase pure high Ca/Si ratio ( $> 1.5$ ) synthetic calcium silicate hydrates (CSH)." *Cement and Concrete Research* 151 (2022): 106623.
- [Haas2015] Haas, Jeremy, and André Nonat. "From C–S–H to C–A–S–H: Experimental study and thermodynamic modelling." *Cement and Concrete Research* 68 (2015): 124-138.
- [Kunhi2022] Kunhi Mohamed, Aslam, et al. "The atomic-level structure of cementitious calcium aluminate silicate hydrate." *Journal of the American Chemical Society* 142.25 (2020): 11060-11071.
- [Lab2011] Labbez, Christophe, et al. "CSH/solution interface: Experimental and Monte Carlo studies." *Cement and Concrete research* 41.2 (2011): 161-168.
- [Lopez2011] Lopez-Garcia, Jose Juan, José Horno, and Constantino Grosse. "Poisson–Boltzmann description of the electrical double layer including ion size effects." *Langmuir* 27.23 (2011): 13970-13974.
- [Loth2010] Lothenbach, Barbara. "Thermodynamic equilibrium calculations in cementitious systems." *Materials and Structures* 43.10 (2010): 1413-1433
- [Lab2006] Labbez, Christophe, et al. "Surface charge density and electrokinetic potential of highly charged minerals: experiments and Monte Carlo simulations on calcium silicate hydrate." *The Journal of Physical Chemistry B* 110.18 (2006): 9219-9230.
- [Maraghechi2018] Maraghechi, Hamed, et al. "Performance of Limestone Calcined Clay Cement (LC3) with various kaolinite contents with respect to chloride transport." *Materials and structures* 51.5 (2018): 1-17.
- [Old2008] Oldham, Keith B. "A Gouy–Chapman–Stern model of the double layer at a (metal)/(ionic liquid) interface." *Journal of Electroanalytical Chemistry* 613.2 (2008): 131-138.
- [Outh1983] Outhwaite, Christopher W., and Lutful B. Bhuiyan. "An improved modified Poisson–Boltzmann equation in electric-double-layer theory." *Journal of the Chemical Society, Faraday Transactions 2: Molecular and Chemical Physics* 79.5 (1983): 707-718.
- [Patel2018] Patel, Ravi A., et al. "Effective diffusivity of cement pastes from virtual microstructures: Role of gel porosity and capillary pore percolation." *Construction and Building Materials* 165 (2018): 833-845.
- [Plus2017] Plusquellec, Gilles, et al. "Determination of the pH and the free alkali metal content in the pore solution of concrete: Review and experimental comparison." *Cement and Concrete Research* 96 (2017): 13-26.
- [Plus2016] Plusquellec, Gilles, and Andre Nonat. "Interactions between calcium silicate hydrate (CSH) and calcium chloride, bromide and nitrate." *Cement and Concrete Research* 90 (2016): 89-96.
- [Puertas2011] Puertas, Francisca, et al. "A model for the CASH gel formed in alkali-activated slag cements." *Journal of the European Ceramic Society* 31.12 (2011): 2043-2056.
- [Sui2019(2)] Sui, Shiyu, et al. "Towards a generic approach to durability: Factors affecting chloride transport in binary and ternary cementitious materials." *Cement and Concrete Research* 124 (2019): 105783.

[Shan1976] Shannon, Robert D. "Revised effective ionic radii and systematic studies of interatomic distances in halides and chalcogenides." *Acta crystallographica section A: crystal physics, diffraction, theoretical and general crystallography* 32.5 (1976): 751-767.

[Tri1989] Tritthart, Josef. "Chloride binding in cement II. The influence of the hydroxide concentration in the pore solution of hardened cement paste on chloride binding." *Cement and Concrete Research* 19.5 (1989): 683-691.

[Torrie1982] Torrie, G. M., and J. P. Valleau. "Electrical double layers. 4. Limitations of the Gouy-Chapman theory." *The Journal of Physical Chemistry* 86.16 (1982): 3251-3257.

[Voll2016] Vollpracht, Anya, et al. "The pore solution of blended cements: a review." *Materials and Structures* 49.8 (2016): 3341-3367.

[Vacha2007] Vácha, Robert, et al. "Autoionization at the surface of neat water: is the top layer pH neutral, basic, or acidic?." *Physical Chemistry Chemical Physics* 9.34 (2007): 4736-4747.

[Vall1982] Valleau, J. P., and G. M. Torrie. "The electrical double layer. III. Modified Gouy–Chapman theory with unequal ion sizes." *The Journal of Chemical Physics* 76.9 (1982): 4623-4630.

[Yosh2022] Yoshida, Satoshi, Yogarajah Elakneswaran, and Toyoharu Nawa. "Electrostatic properties of C–S–H and CASH for predicting calcium and chloride adsorption." *Cement and Concrete Composites* 121 (2021): 104109.

[Zhang2017] Zhang, Yunsheng, et al. "Modelling of diffusion behavior of ions in low-density and high-density calcium silicate hydrate." *Construction and Building Materials* 155 (2017): 965-980.



# Chapter 5 Insight on the EDL formation in Ca-containing systems

In the context of studying chloride binding in cementitious materials, it was shown in the previous chapter that the electrical double layer formation is the result of atomistic phenomena affected by the properties of the C-S-H surface and the pore solution surrounding it. To first validate our approach, the focus was narrowed to the case of monovalent electrolytes where the only counter-ion was sodium. The use of atomistic modelling techniques brought valuable insight on the correlation between the EDL properties and a variety of system-dependent parameters namely the pore size, the ionization degree of C-S-H and the ionic strength of the solution (concentration and pH). In the simulations conducted, we attempted to decouple these variables and, hence, gained insight into the pertinence of each of them.

In this chapter, the objective is to extend the EDL model to a more realistic representation of actual cement paste. In this respect, calcium ions are thought to have a major role in the binding of chloride on C-S-H. However, the characterization of the surface via Zeta potential measurements (*ref. chapter 4 section I.C*) showed that Ca-containing systems behaved differently from symmetric salts. First, the adopted C-S-H surface is characterized and its properties discussed. Secondly, a more representative pore solution model is formulated based on thermodynamic data collected from actual cement paste. Finally, we run the developed atomistic model of the EDL on the new C-S-H interface/pore solution configuration to best approach the physical binding of chloride in real cementitious materials.

Chapter 5 Insight on the EDL formation in Ca-containing systems.....	125
I.    Choice of the C-S-H surface .....	127
A.    A more realistic surface charge density.....	127
B.    Zeta potential calculation: Titration of a C-S-H suspension in a $\text{Ca}(\text{OH})_2$ solution .....	127
II.   Modelling the pore solution in cement paste.....	130
III.  Calcium adsorbed surfaces in C-S-H.....	131
A.    Effect of calcium adsorption in slit pores .....	131
B.    The pore size effect.....	137
C.    Case of the full calcium occupancy of the ionized C-S-H surface (Ca-Si occupancy ratio equal to 100%) .....	140
IV.  Conclusions .....	143
V.   Appendix A: Multi-parameter study of the EDL in Ca-containing environments .....	145
A.    Effect of the ionization degree .....	145
B.    Effect of pH decrease.....	148
VI.  References .....	150



## I. Choice of the C-S-H surface

### A. A more realistic surface charge density

The properties of the C-S-H gel including its composition, atomistic structure and its morphology remain among the most puzzling themes in cement science even after over 70 years of research [Bernal1952]. In this area, the most accepted and commonly used empirical model of C-S-H is Taylor's tobermorite-like structure [Tay1986]. Relying on this representation, a family of models adopting a "defective tobermorite" structure has been developed since the late 2000s [Pellenq2009, Kovac2015, Kunhi2018]. Although these bulk models have proved to be very good at describing low Ca/Si ratios (typically <1), they do not align with experimental results once the Ca/Si ratio exceeds 1. The Ca/Si of C-(A)-S-H gel in real cement paste is usually above 1.5; for e.g. Ca/Si around 2 for OPC and between 1.5 and 1.75 for LC3 cement [Avet2018]. There is still a lot that is left to do. In [Duque2022], the authors have collected a substantial amount of data representing how the mean chain length (MCL) of the silicate chains (*ref. chapter 2 section IV.C.*) decreases as function of the increasing Ca/Si of the C-S-H but never falls below a value of 2 (MCL = Infinity for Tobermorite). Based on the brick model [Kunhi2018] of C-S-H bulk, Casar et al. extend the model to the surface and predict that for C-S-H with Ca/Si  $\sim 1.7$ , the silanol site density (SSD) has a maximum value of  $1.2 \text{ sites.nm}^{-2}$  [Casar2022] with ionization degrees depending on the titrating solution and its concentration.

For our simulations of the EDL forming around a realistic C-S-H surface charge density, we set the value of  $-1.2 \text{ e.nm}^{-2}$  as an absolute maximum for the considered  $\sigma_{\text{C-S-H}}$ .

### B. Zeta potential calculation: Titration of a C-S-H suspension in a $\text{Ca(OH)}_2$ solution

Prior to simulating the formation of the EDL in confined spaces, we first characterize the C-S-H surface electrostatic properties. Experimentally, this is usually done by Zeta potential measurements (*ref. chapter 2 section V.C.(ii)*). From a computational perspective, the evolution of the electrostatic potential around a charged surface can be carried out through the simulation of a single wall/electrolyte configuration. In a very similar way to actual measurements on colloidal systems, the surface charge interacts with an unconstrained infinitely wide electrolytic solution. As the value of  $1.2 \text{ sites.nm}^{-2}$  was previously set as an upper bound for the SSD on C-S-H<sub>1.7</sub>, we assume a 100% ionization degree of the surface (i.e.  $\sigma_{\text{C-S-H}} = -1.2 \text{ e.nm}^{-2}$ ). In order to portray surface effects in a Ca-containing system, the C-S-H is "virtually" titrated with a  $\text{Ca(OH)}_2$  solution at different concentrations. By taking into account the mentioned inputs, the GCMC algorithm was run following the methodology depicted in the previous chapter (*ref. chapter 4 section I*). After equilibration of the system, the electrostatic potential perpendicularly to the surface is computed using the convolution integral of the Poisson equation (Eq.(4.7)).

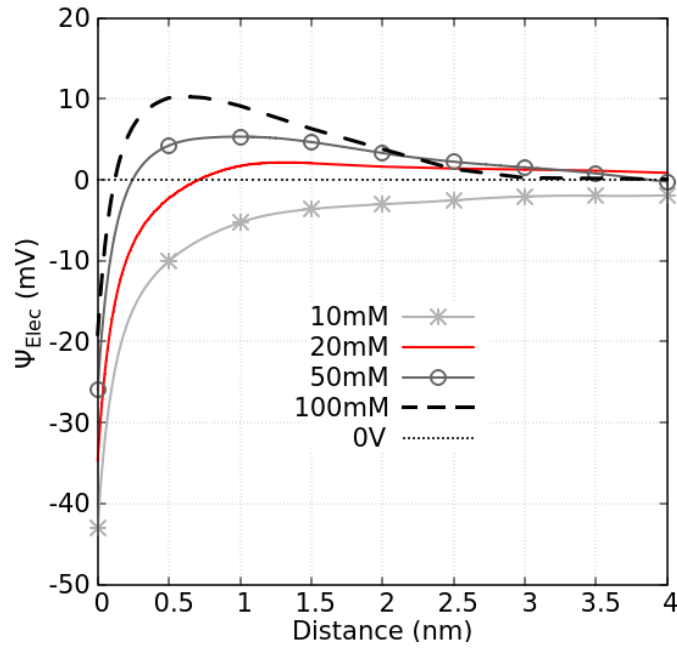


Fig.5.1. Electric potential around C-S-H with  $\sigma_{C-S-H} = -1.2 \text{ e.nm}^{-2}$  at different concentrations of  $\text{Ca(OH)}_2$

In Fig.5.1, one can see that on addition of calcium in the system, the electrostatic potential becomes more and more positive. As the concentration goes up, the surface potential, takes respectively values of -43, -34, -26 and -19mV for 10, 20, 50 and 100mM. Between 10 and 20mM concentration, there is a clear shift of the potential moving from strictly negative values to actual positive potentials. The measurement of the Zeta potential remains approximate given there is no clear consensus on the actual location of the  $\zeta$ -plane. At the usually considered location ( $\sim 6 \text{ \AA}$  from surface), the zeta potential, in our case (Fig.5.1), ranges from approximately -10 to 10mV for concentrations between 10mM and 100mM. This so-called reversal of charge is usually attributed to the higher screening capacity of calcium (compared to  $\text{Na}^+$  for example) due to its divalence [Lab2011]. A similar trend has previously been demonstrated in the case of C-S-H<sub>0.66</sub> (ref. chapter 4 section I.C) where the reversal of charge occurred around 5mM of  $\text{Ca}^{2+}$  concentration at a surface charge density close to  $-4 \text{ e.nm}^{-2}$ . It seems that the threshold  $\text{Ca}^{2+}$  concentration for which the potential shift occurs is closely related to the charge density of the surface of interest. The higher the surface charge, the lower Ca is needed to reverse the  $\zeta$  potential.

An important point to stress, in our simulations, is that the C-S-H surface charge density has been kept unchanged while adding  $\text{Ca}^{2+}$  in the solution. As the number of available ionized silanols was constant, the maximum number of adsorbed  $\text{Ca}^{2+}$  occupying these sites also remained unchanged. In other words, it was rather the accumulation of the calcium in the diffuse layer that was most likely responsible for the observed reversal of charge. However, the definition of  $\text{Ca}^{2+}$  adsorption on the C-S-H and the actual location of calcium at the interface remains a topic of discussion. Due to the sheet structure of C-S-H and its varying calcium to silicon ratio, the surface of C-S-H can be viewed in two ways.

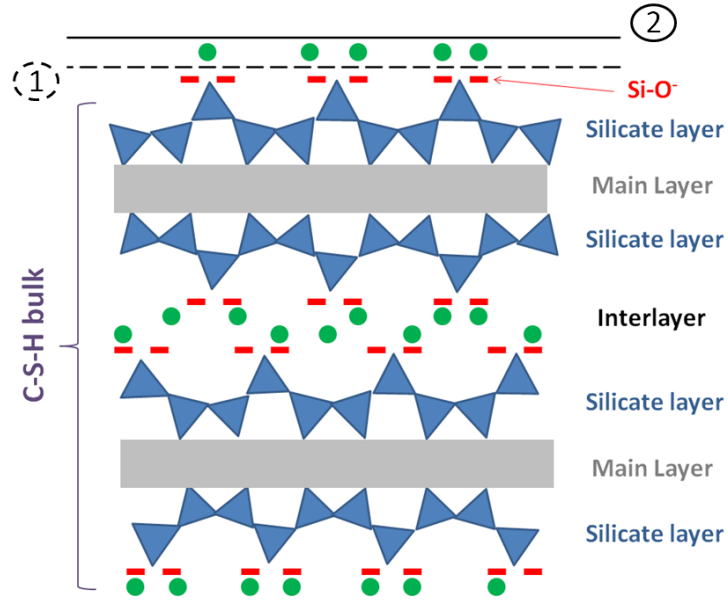


Fig.5.2. Schematic of the C-S-H silicate chains with two ways to define calcium adsorption on the C-S-H surface. In the surface (1),  $\text{Ca}^{2+}$  (green balls) are adsorbed in the Stern layer and the surface is defined by the silicate chains with the silanols ionization dependent on pH. In the definition (2) of the surface, the  $\text{Ca}^{2+}$  ions are incorporated in the structure. Image inspired from [Viallis2000]

The first approach (surface (1) in Fig.5.2.) consists in considering that the calcium ions are located in the Stern layer where they are specifically adsorbed [Gra1947] on the ionized silanol sites of the C-S-H. From this point of view, the surface is then defined by the position of the silicate chains. The calcium layer at the surface would occupy equivalent sites to the calcium atoms in the C-S-H interlayer. The other option (surface (2) in Fig.5.2.) is to consider that calcium is a constituent ion of the structure. The surface of C-S-H then contains both the silanol sites and the calcium ions associated with them. In this situation, a change in the concentration of calcium ions in the solution would result into a different surface charge and a different Ca/Si ratio [Viallis2000]. In our case, as the surface is described as an implicit plane, this is only a matter of definition. Additionally, given that the solvent is seen as an implicit medium, it is considered that all ions are “specifically” adsorbed (no water salvation shell) with their centers of mass located at the plane of closest approach (the IHP in Grahame’s theory which confounds with the OHP in the absence of explicit solvent) (ref. Fig.2.12). In reality, the actual position of calcium at the C-S-H interface is a key issue. Depending on whether the  $\text{Ca}^{2+}$  form ion pairs with the  $\text{Si-O}^-$  or are rather more strongly bound to the structure, the apparent mobility of calcium may be significantly impacted. As the morphology of the solid surface is considered planar and perfectly even,  $\text{Ca}^{2+}$  ions are viewed in our model as part of the Stern layer. This actually confers them a mobility which, although reduced compared to the bulk, is not null.

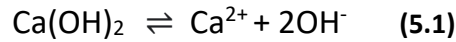
Now, after the C-S-H surface with  $\sigma_{\text{C-S-H}} = -1.2 \text{ e.nm}^{-2}$  has been defined, the next step consists of extending the study of the EDL formation to real cement paste. In that respect, we model the presence of Ca in the pore solution under realistic thermodynamic conditions.

## II. Modelling the pore solution in cement paste

*As the presence of multivalent ions has been proved to significantly deviate from symmetric monovalent electrolytes, the objective of this section is to quantify the concentration of calcium in the highly alkaline pore solution environment.*

The use of supplementary cementitious materials (SCMs) in addition to the ordinary Portland cement (OPC) has been found to affect the kinetics and the mechanisms of the chemical reactions in blended systems. These effects are reflected in the composition of the pore solution which bears is the result of the hydration process. So if the pore solution analysis is of paramount importance in the construction of thermodynamic models to predict the composition of liquid and solid phases, it is also equally critical to understand harmful reactions linked to durability problems [Hooton2010]. Pore solution extraction from a hardened paste using a high pressure device is probably the most common way to obtain these data. Among the main species are hydroxide, sodium, potassium, calcium, sulfate, aluminum and silicon. In real C-(A)-S-H, the aluminates content varies as a function of the used SCMs and this can have a sizable effect on chloride binding. In chloride ingress, all the species have to some extent a certain effect. However, our aim is, first and foremost, to understand the dominant mechanisms behind the physical binding of chloride. With this in mind, we only retain the most important factors and discount the rest so that the model deals with a manageable level of complexity. The considered ions are, therefore, hydroxides, chlorides, sodium (which behaves similarly to potassium<sup>^</sup>) and calcium.

In real cement paste, it was found that varying the alkalinity of the pore solution had implications on the thermodynamic stability of present species. Namely, at a certain pH, the  $\text{Ca}^{2+}$  concentration in the solution is adjusted with respect to the portlandite precipitation/dissolution reactions:



In order to avoid supersaturation and formation of portlandite, the equilibrium constant  $K$  of the reaction (5.1) is determined. The standard Gibbs free energy of reaction  $\Delta_r G^\circ$  is computed using thermodynamic data on the reactants and products from [Loth2018, Thoenen2014]:

$$\begin{aligned} \Delta_r G^\circ &= \sum n_i \Delta G_f^\circ(\text{products}) - \sum n_j \Delta G_f^\circ(\text{reactants}) \\ &= \Delta G_f^\circ(\text{Ca}^{2+}) + 2\Delta G_f^\circ(\text{OH}^-) - \Delta G_f^\circ(\text{Ca(OH)}_2) = 30301 \text{ J/mol} \end{aligned}$$

Knowing that the constant  $K$  is a function of the  $\Delta_r G^\circ$ , we make the calculations using the following relation:

$$\ln K = \frac{-\Delta_r G^\circ}{RT} \quad (5.2)$$

where  $R$  is the universal gas constant and  $T$  the temperature (Kelvin). We obtain  $K=10^{-5.2} \sim 6.31 \times 10^{-6}$  at  $T=298 \text{ K}$  and  $P=1 \text{ bar}$ .

---

<sup>^</sup> However, the sodium and potassium concentrations in pore solution are usually quite different (ref. Tab.2.1) [Loth2018]

Given that our simulator does not account for reactions occurring, it is important that concentrations of  $\text{Ca}^{2+}$ , at a defined pH, remain close to equilibrium, but slightly undersaturated. Also, in order to vary the concentrations of  $\text{Ca}^{2+}$  and  $\text{OH}^-$  independently, the polyelectrolyte chosen to simulate the pore solution is an aqueous solution of  $\{\text{NaCl}+\text{NaOH}+\text{CaCl}_2\}$ . At a fixed chloride concentration of 0.1M, the pH is varied through the whole range of experimental values (12.7-13.8) and, for each case; the corresponding limit  $\text{Ca}^{2+}$  concentration is computed as follows:

$$[\text{Ca}^{2+}]_{\text{lim}} [\text{OH}^-]^2 = K \quad (5.3)$$

Concentrations are calculated under the assumption of a diluted (ideal) solution and assuming that the ions are not involved in any other equilibrium:

pH	NaOH (M)	$[\text{Ca}^{2+}]_{\text{lim}}$ (mM)	$\text{CaCl}_2$ (mM)	NaCl (M)	Na/Ca (in solution)
12.7	0.05	2.5	2.5	0.095	58
13	0.1	1	1	0.098	198
13.3	0.3	<0.2	~ 0	~ 0.1	>2000
13.8	0.63	<0.02			>35000

Table.5.1. Concentration of ionic species in the pore solution model at different values of the pH

In reality, the pore solution should contain slightly higher calcium concentrations due to neglecting the non-ideality of the solution in the computations but also possibly due to oversaturation or overlapping of equilibria. Still, Tritthart [Tri1989] predicts that calcium content will be always below 100 ppm (parts-per-million). In summary, calcium is poorly soluble in the range of pH we are working at and any rise of its concentration results instantaneously in precipitation. So, if not in the solution, the calcium ions must be adsorbed on the surfaces.

### III. Calcium adsorbed surfaces in C-S-H

#### A. Effect of calcium adsorption in slit pores

The main objective of this section is to extend the EDL model developed on Na-systems (*chapter 4*) by including Ca for a better representation of actual cementitious materials. For the computations, the C-S-H gel porosity is modeled as nanoscopic slit pores with ionized surfaces of charge densities equal to  $-1.2 \text{ e.nm}^{-2}$  (Si-terminated surface). The pH of the pore solution is set to a value of 13 (NaOH ~ 0.1M). The chloride content is fixed at a concentration of 0.1M and the  $\text{CaCl}_2$  is added within respect of the thermodynamic conditions specified in *section II*. As shown in Tab.5.1, the presence of  $\text{Ca}^{2+}$  in solution is negligible (roughly 100 times lower than  $\text{Na}^+$ ). So to study the effect of the physical binding of  $\text{Ca}^{2+}$  on C-S-H, we set the amount of  $\text{Ca}^{2+}$  in the solution at the limit of the under saturation (i.e. 1mM for pH=13) and we choose to exchange part of the neutralizing  $\text{Na}^+$  by  $\text{Ca}^{2+}$  and keep the pH and the  $\text{Cl}^-$  content unchanged.

The way of simulating  $\text{Ca}^{2+}$  adsorption consists of initially running the GCMC for a {NaOH 0.1M + NaCl 98mM +  $\text{CaCl}_2$  1mM} electrolyte in a similar way to the previous chapter (*ref. chapter 4*) i.e. compute the chemical potential using the Widom algorithm and run the Metropolis Monte Carlo in the grand canonical ensemble ( $\mu, V, T$ ) until equilibration. Once the system has relaxed, we account for the global number of sodium atoms in the box and we set a new simulation where the neutralizing  $\text{Na}^+$  (equal to the number of ionized sites on the surfaces) are progressively replaced by  $\text{Ca}^{2+}$ . In sum, the substitution of  $\text{Na}^+$  is operated in terms of charge replacement as sketched in the below figure (Fig.5.3).

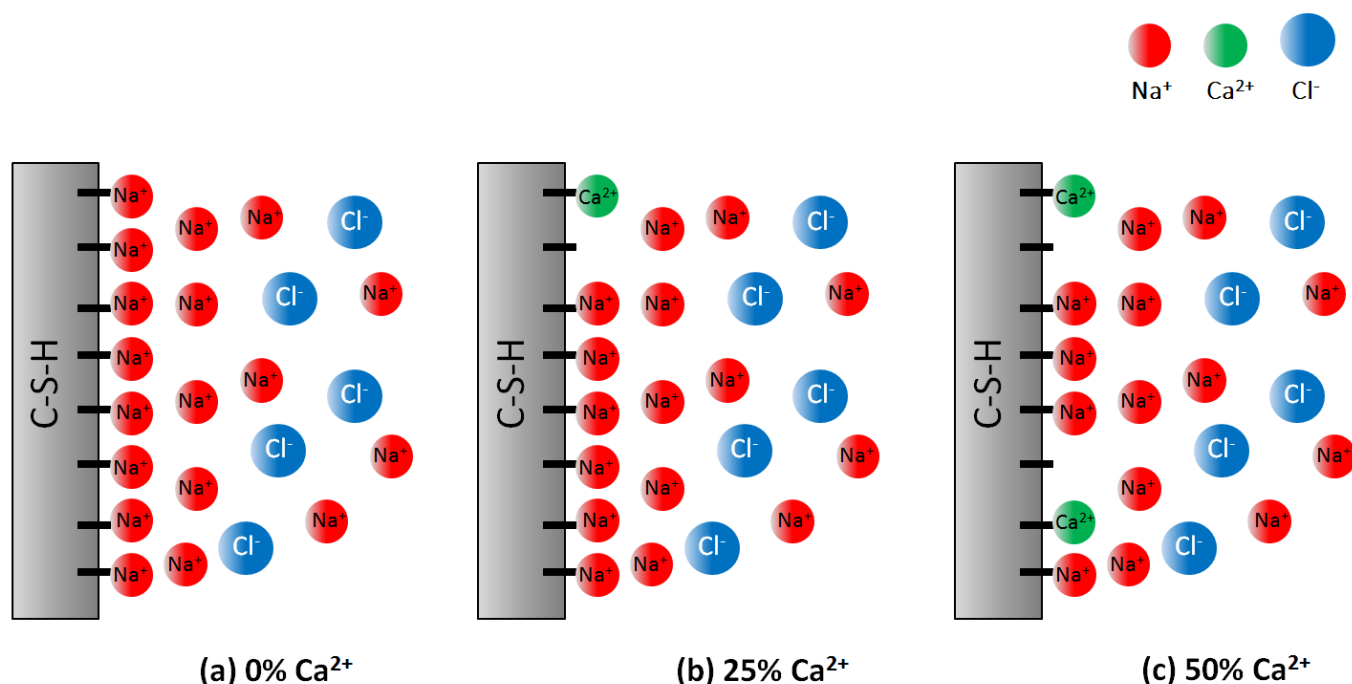


Fig.5.3. Schematic of the  $\text{Ca}^{2+}$  charge replacement ratio at values of 0%, 25% and 50%

In principle, this way of substituting  $2\text{Na}^+$  with one single  $\text{Ca}^{2+}$  is in agreement with the fact that Ca can, indeed, adsorb at a bridging site between two  $\text{Si-O}^-$  [Casar2022]. The case of each  $\text{Ca}^{2+}$  occupying one single site is also energetically plausible; however, the affinity of one type of adsorption or the other has not yet been established. Moreover, the addition of calcium in these proportions aims primarily to maintain the global electroneutrality of the system while disturbing the bulk concentrations of  $\text{Na}^+$  and  $\text{Ca}^{2+}$  as little as possible. Afterwards, the newly set system is relaxed using the Monte Carlo in the canonical ensemble ( $N, V, T$ ) where the total number of ions remains constant and only translation moves are attempted. Below is presented the simulation box, in a 12 nm pore, for charge replacement ratios varying from 0% up to 100%.



pH	Width (Å)	Walls (Å x Å)	Cl <sup>-</sup>	OH <sup>-</sup>	Ca <sup>2+</sup> charge replacement ratios	Ca <sup>2+</sup>	Na <sup>+</sup>	Ca <sup>2+</sup> /Na <sup>+</sup> (x 100)
13	120	160 x 160	185	184	0%	2	979*	0.2
					25%	79	825	9.6
					35%	110	763	14.4
					50%	156	671	23.3
					65%	202	579	34.9
					75%	233	517	45.1
					85%	263	457	57.6
					100%	309	365	84.7

Table.5.2. Simulation box for a pore solution modeled as {NaOH 0.1M + NaCl 98mM + CaCl<sub>2</sub> 1mM} in a 12nm-pore with C-S-H surfaces neutralized with Na<sup>+</sup> and Ca<sup>2+</sup> ions at various replacement ratios. The surface charge density is set at  $\sigma_{C-S-H} = -1.2 \text{ e.nm}^{-2}$

The first step is to ensure convergence of the simulations. As Ca<sup>2+</sup> and Na<sup>+</sup> content are fluctuating with the varying replacement ratios, we choose to use the anionic distributions, whose molarities are the only constant input (along with the surface charge density), as a reference. Once the system has reached equilibrium, the electrochemical potentials are computed through integration of the Poisson equation as detailed in *chapter 4 section II.A.(i)*.

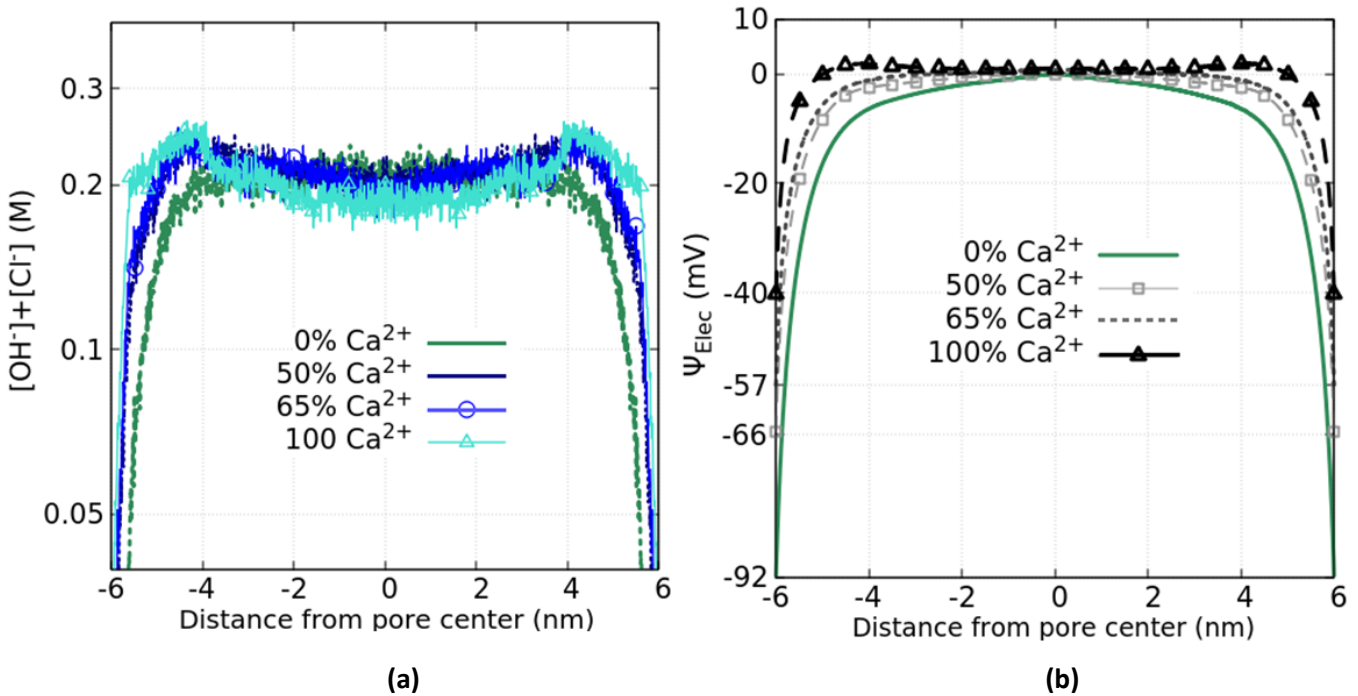


Fig.5.4. Evolution of (a) the anionic distribution and (b) the electrochemical potential in the 12nm pore at different charge replacement ratios of 0%, 50%, 65% and 100%

\* Among which, we count 614 Na<sup>+</sup> to neutralize the 614 silanols on the walls. This is the Na<sup>+</sup> population that is gradually replaced.

At equilibrium, one can see, as expected, that the summed distributions of chloride and hydroxide reach a plateau at the center of the pore. Additionally, one can see that upon addition of Ca, the anionic distribution has slowly evolved from a PB-like exponential profile at 0% (green line) toward the characteristic “shoulder” profile typical of the reversal of charge in Ca electrolytes (*ref. chapter 4 section I.C*). Given that the total number of ions is a constant, the concentration of anions at the center of the box falls below the bulk molarity of both species i.e. 0.2M (Fig.5.4.(a)). This is due to the accumulation of  $\text{Cl}^-$  and  $\text{OH}^-$  close to the surfaces in response to the stronger Coulombic attraction of  $\text{Ca}^{2+}$ . The case of 100% replacement ratio is probably the most obvious to observe (turquoise line). In Fig.5.4.(b), the potential shift is clearly visible at the highest replacement ratio of 100%. At lower ratios, the reversal of charge is less obvious but it is possible to observe the increasing adsorption of  $\text{Ca}^{2+}$  on the surface through the increasing screening of the surface. Along with the increasing number of added Ca, one can clearly notice the surface potential (at the plane containing the ionized silanols) steadily moving from a value of nearly -92mV with nearly 100%  $\text{Na}^+$  on the surface (0%  $\text{Ca}^{2+}$ ), up to -66mV (50%  $\text{Ca}^{2+}$ ) then -57mV (65%  $\text{Ca}^{2+}$ ) and finally -40mV (100%  $\text{Ca}^{2+}$ ). Nonetheless, as we have previously seen (*ref. chapter 4 section I.C*), the potential reversal can only occur upon sufficient accumulation of Calcium in the diffuse layer. In fact, in the case of C-S-H with a surface charge equal to  $-1.2 \text{ e.nm}^{-2}$  (*section I.B*), it was found that Calcium had to build up to a concentration between 10 and 20mM to effectively measure a positive zeta potential. A question then arises: where exactly are the added calcium ions located?

As a matter of fact, unlike the GCMC, MC simulations in the canonical ensemble aim to reach the most energetically stable configuration (at zero temperature). So to ensure that the added calcium is effectively adsorbing on the surfaces rather than equilibrating in the bulk, we compute the Ca occupancy ratio of the available silanols and compare it to the replacement ratio. Given that the C-S-H interface is viewed as a smooth planar wall,  $\text{Ca}^{2+}$  is considered to be adsorbed in the Stern layer and, hence, technically part of the solution. The Stern layer thickness is set to be equal to a ionic radius i.e.  $\sim 1 \text{ \AA}$ . Therefore, the Ca-Si occupancy ratio is computed as the number of  $\text{Ca}^{2+}$  ions within a distance of  $1 \text{ \AA}$  off the surface normalized by the total number of present ions in that area.

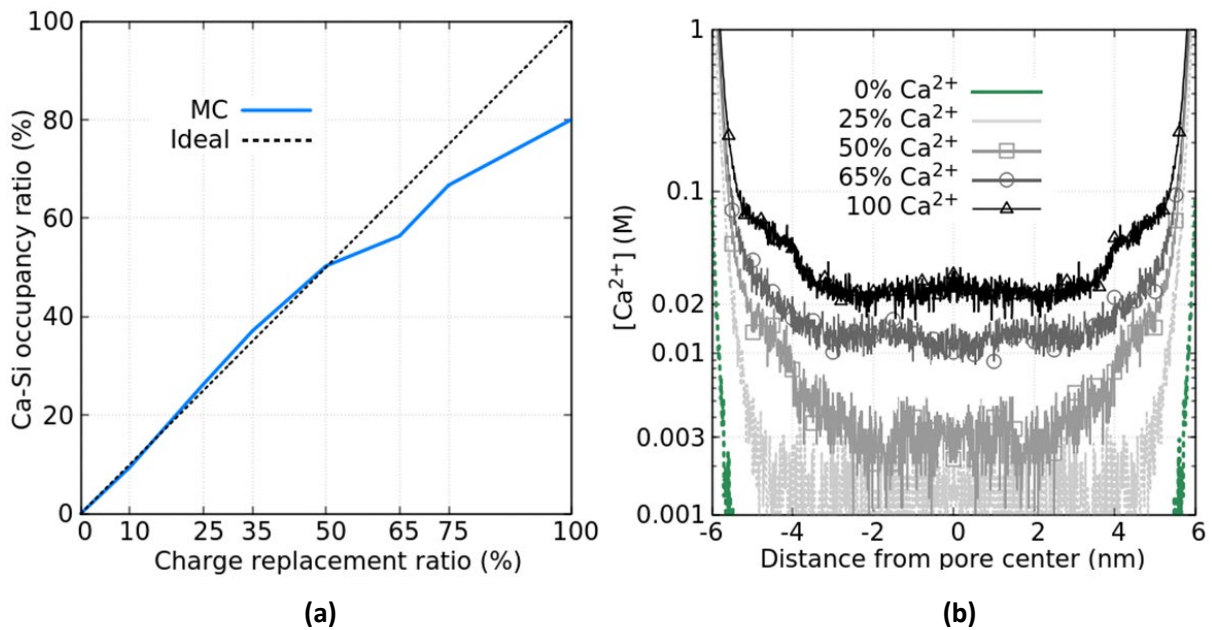


Fig.5.5. Evolution of (a) the Ca occupancy of the available ionized sites and (b) the  $\text{Ca}^{2+}$  distributions in the pore of as function of the charge replacement ratio.

The plot in Fig.5.5.(a) shows that, as part of the initially adsorbed Na is progressively replaced by  $\text{Ca}^{2+}$  ions, the exchange is almost ideal up to 50% of charge replacement ratio. Meaning that once we have exchanged up to 50% of the residing  $\text{Na}^+$  on the Si-O<sup>-</sup> sites, the added  $\text{Ca}^{2+}$  have completely occupied these discharged sites. This can also be observed on Fig.5.5.(b) where the concentration of  $\text{Ca}^{2+}$  for ratios between 0 and 50% varies between 1mM and 3mM, which remains within a reasonable range to assume that we are still under saturation (*ref. last paragraph of section II*). However, once the replacement ratio goes beyond 50%, a clear deviation from the line of ideal adsorption is noted (Fig.5.5.(a)). In other words, although the adsorption of  $\text{Ca}^{2+}$  is still increasing, it seems that part of the added calcium does not adsorb directly on the surface and prefers to reside in the lower energy bulk region. In accordance with this observation, we note an increase of the bulk concentration of calcium once the charge replacement ratio moves to 65% (Fig.5.5.(b)). Also, it is interesting to note that upon this increase, the bulk concentration of  $\text{Ca}^{2+}$  raises within the range of concentrations (between 10 and 20mM) where the reversal of charge is expected to occur for a surface charge density of  $-1.2 \text{ e.nm}^{-2}$  (*section I.B*). In order to measure the consequence of this increase of  $\text{Ca}^{2+}$  content in the bulk, we compute the evolution of both (i) the zeta potential of the surface and (ii) the average potential of the pore as function of the replacement ratios.

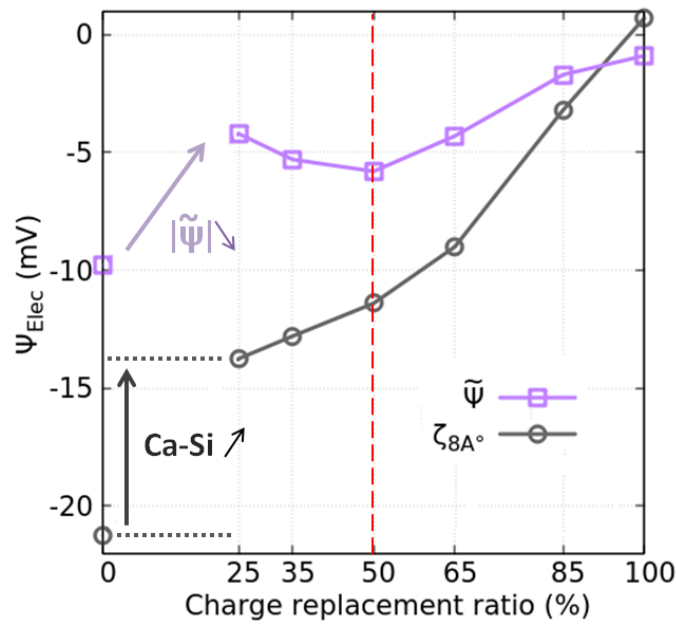


Fig.5.6. Evolution of zeta potential of the surface and the potential average in the 12 nm pore as function of the charge replacement ratio.

As shown in Fig.5.4.(b) where the surface potential was further screened at higher calcium content, one can see that the Zeta potential (Fig.5.6) is equally increasing as the charge replacement ratio is going up. As the potential shift occurred between 7 and 8 Å for the ratio of 100%, the  $\zeta$ -plane has been chosen, for convenience, at 8 Å which remains a physically acceptable value [Zhang2017]. In any case, this choice has very little effect on the veracity of the observations, as potential profiles in Fig.5.4.(b) varied very slowly at distances around 10 Å off the surface. The jump of potential (black arrow in Fig.5.6) is, indeed, most noticeable once we move from a Na-system ( $\zeta_{8\text{\AA}} = -21\text{mV}$ ) to a system where calcium has been added ( $\zeta_{8\text{\AA}} > -14 \text{ mV}$ ). These values remain within the range of the

usually measured Zeta potentials. In a recent study [Barzgar2020], Barzgar et al. measured negative Zeta potentials varying between -30 and 0mV for C-S-H of Ca/Si between 0.6 and 1.4 in a NaOH solution of pH up to 13. For the same range of Ca/Si, Haas and Nonat found that the titration with  $\text{Ca}(\text{OH})_2$  of increasing molarity lead the  $\zeta$ -potential to eventually reverse its sign and go from -10mV ( $\sim 1\text{mM}$ ) up to 20mV ( $\sim 25\text{mM}$ ) [Haas2015]. In a similar fashion, Elakneswaran et al. showed that the increase of chloride concentration in a solution of  $\{\text{Ca}(\text{OH})_2 + \text{NaCl}\}$  increased the negativity of the zeta potential down to -10mV for a chloride concentration of 40mM and a pH up to 12.5 [Elak2009].

Unlike the Zeta potential, the evolution of the average potentials  $\tilde{\psi}$  (Fig.5.6) with the increasing charge replacement ratio is less straightforward: two different regimes seem to take place. As the replacement ratio progressively moves from 25 to 35 then 50%, the average potential of the pore is steadily growing more negative. This is explained by the decrease of the  $\text{Na}^+$  solution due to its substitution with  $\text{Ca}^{2+}$  ions (Fig.5.7.(a)). In fact, the decrease of the  $\text{Na}^+$  concentration seems to be the potential determining mechanism as it affects the ionic strength faster than the increase in  $\text{Ca}^{2+}$  does. In Fig.5.7.(b), one can see the slower depletion of the potential at a charge replacement ratio of 50% compared to the ratio of 25%. It is this increase of the Debye length, and consequently of the EDL thickness, that is at the origin of the more negative potential of the pore.

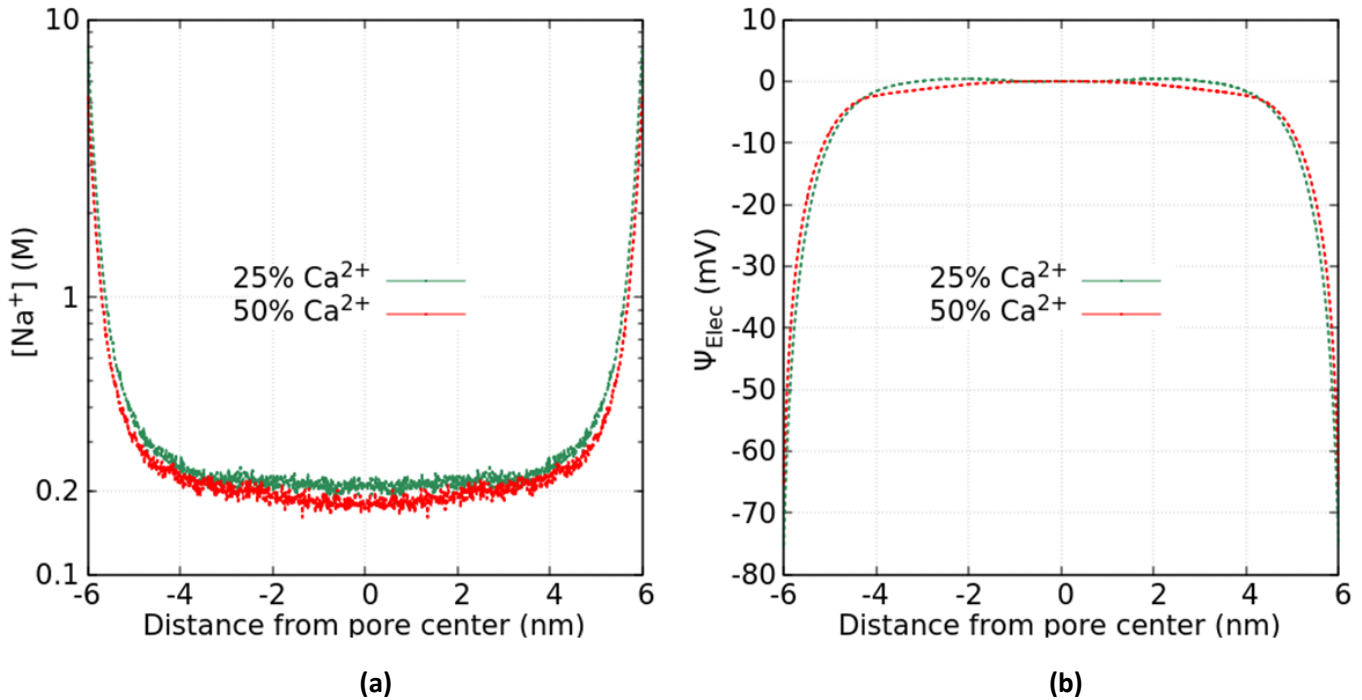


Fig.5.7. Evolution of **(a)** the  $\text{Na}^+$  distributions and **(b)** the electrostatic potential in a 12 nm pore for charge replacement ratios of 25% and 50%.

Once the charge replacement ratio moves to 65% (Fig.5.6), the trend is reversed and the average potential, though still negative, gradually decreases in absolute value. As the adsorption of  $\text{Ca}^{2+}$  is still increasing between ratios of 50% and 65% (Fig.5.5.(a)), the main disrupter appears to be the increase of  $\text{Ca}^{2+}$  concentration (Fig.5.5.(b)) within the area where the reversal of charge was predicted to happen (i.e.  $[\text{Ca}^{2+}]$  between 10mM and 20mM). According to Tab.5.2, this jump actually occurs once the Ca/Na ratio in the whole box exceeds 23% i.e. roughly  $1\text{Ca}^{2+}$  for  $4\text{Na}^+$  in the pore.

## B. The pore size effect

As we introduced Ca into the mix, atomistic simulations showed that Ca-containing electrolytes behaved quite differently from Na-only systems. In this regard, it is imperative to assess the validity of the previously established correlations (namely for NaCl salts) in a more realistic configuration where  $\text{Ca}^{2+}$  ions are considered. For this part, it is the effect of the pore size that is investigated.

Computations in the case of a 12nm pore have already been conducted in the last paragraph. Hence, the same procedure is applied to smaller pores of diameters 8 and 4 nm. The considered electrolyte is the same as in the previous section i.e. {NaOH 0.1M + NaCl 98mM +  $\text{CaCl}_2$  1mM}. The surface charged density is set at  $-1.2 \text{ e.nm}^{-2}$ . At fixed pore size, the charge replacement ratios are varied through the same range of values as in Tab.5.2.

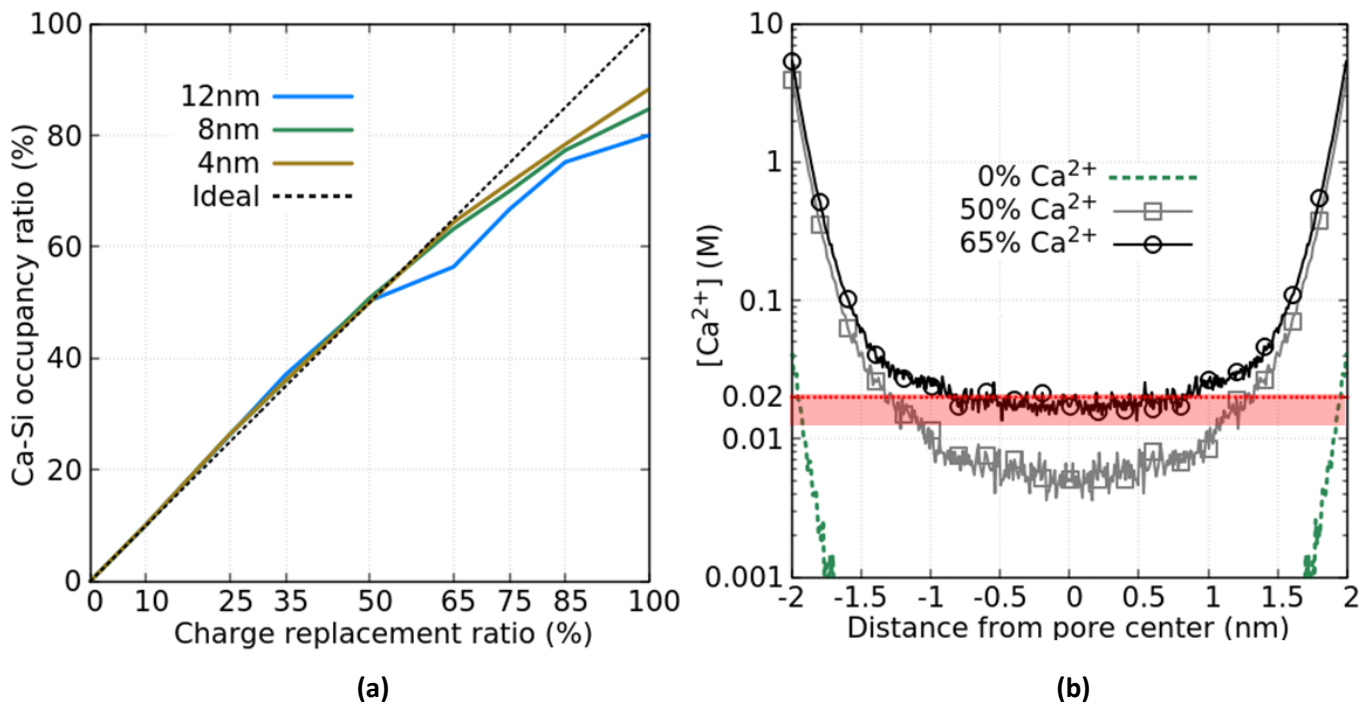


Fig.5.8. Evolution of (a) the Ca occupancy of the available ionized sites and (b) the  $\text{Ca}^{2+}$  distributions in 4nm pore at charge replacement ratios of 0%, 50% and 65%. The red area denotes the interval of  $\text{Ca}^{2+}$  concentration where the reversal of charge happens.

The evaluation of the Ca-Si occupancy in Fig.5.8.(a) shows an increase of the adsorbed  $\text{Ca}^{2+}$  as the pore is reducing in size. Although still beneath the ideal curve, the Ca occupancy in the smaller pores (4 and 8 nm) was the highest with, e.g., 80%, 85% and 90% of Ca-Si occupancy in, respectively, the 12, 8 and 4 nm pores at a charge replacement ratio of 100%. In fact, along with the reduction of the pore radius, the EDL overlapping occurs and the bulk area increasingly vanishes. The  $\text{Ca}^{2+}$  ions experience stronger interactions with the surface and find themselves within the diffuse layer. However, as the adsorption of the added  $\text{Ca}^{2+}$  is not ideal, the concentration of the  $\text{Ca}^{2+}$  in solution continues to build up (Fig.5.8.(b)). In the smallest pore of 4nm, once the replacement ratio goes beyond 50%, the jump in the Ca content is clear and the concentration reaches approximately 20mM i.e. in the area of reversal of charge (red in Fig.5.8.(b)).

In Fig.5.9.(a), one can clearly see, in the pore of 8 nm size, that the increase of  $\text{Ca}^{2+}$  adsorption, due to higher charge replacement ratios, favors the accumulation of  $\text{Cl}^-$  close to the surface. In reality, the chloride profiles for replacement ratios below 50% remain quite similar. At a charge replacement ratio of 100%, the reversal of charge happens and chloride displays the characteristic shoulder-like profile. As the pore size reduces to 4nm (Fig.5.9.(b)), the difference between the distributions at various replacement ratios is more noticeable. As the amount of adsorbing  $\text{Ca}^{2+}$  is going up, the depletion of the chloride distribution is more and more pronounced. Nonetheless, the profiles corresponding to replacements below 50% show the typical Donnan effect observed in monovalent electrolytes where the local electroneutrality is disturbed due to the vanishing of the bulk area. Conversely, in the case of charge replacement of 100%, two interesting features appear. Firstly, we note that the concentration in the center is fairly close to a plateau which denotes the decrease of the EDL thickness due to the  $\text{Ca}^{2+}$  screening. Secondly, the previously observed (Fig.5.9.(a)) accumulation of  $\text{Cl}^-$  due to the overcompensation of  $\text{Ca}^{2+}$  ions seems noticeably hindered. This behavior is attributed to the compact size of the 4nm pore which seems to prevent the chloride from exhibiting the previously called “shoulder” profile.

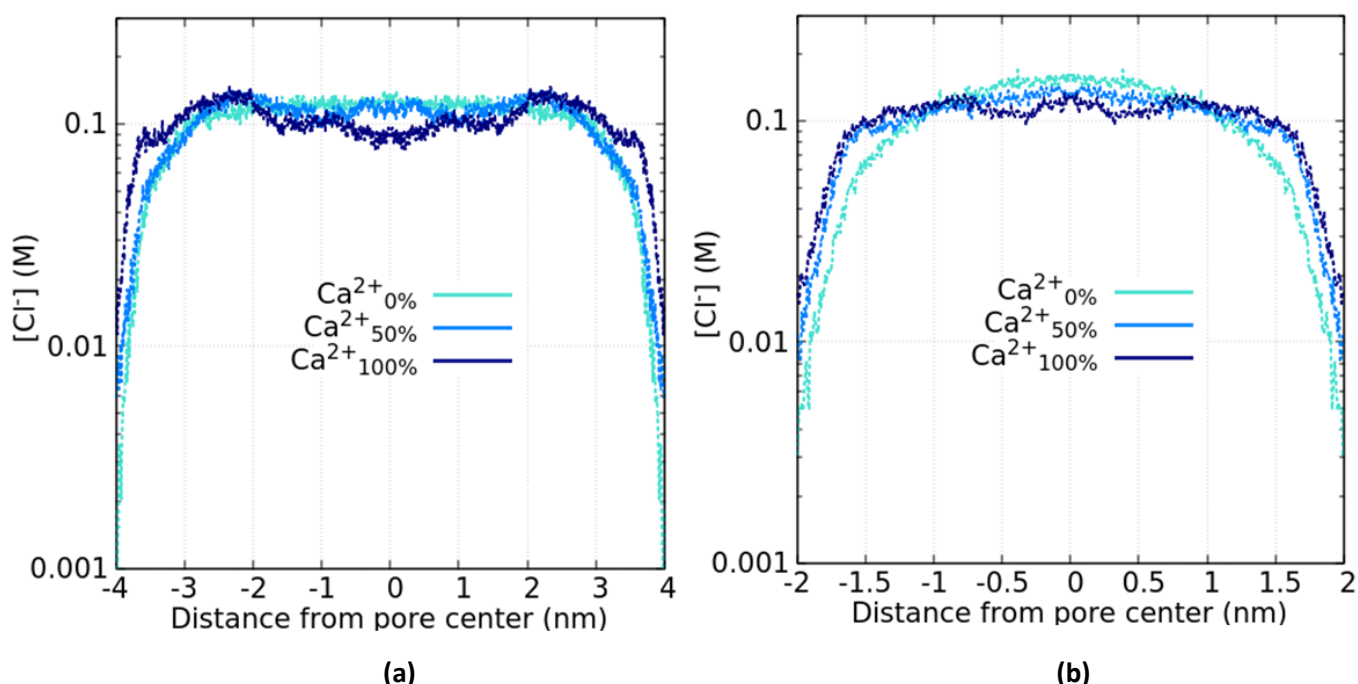


Fig.5.9. Chloride distribution profiles in pores of (a) 8nm and (b) 4nm of diameter. The charge replacement ratios are varied through the whole range with values at 0%, 50% and 100%.



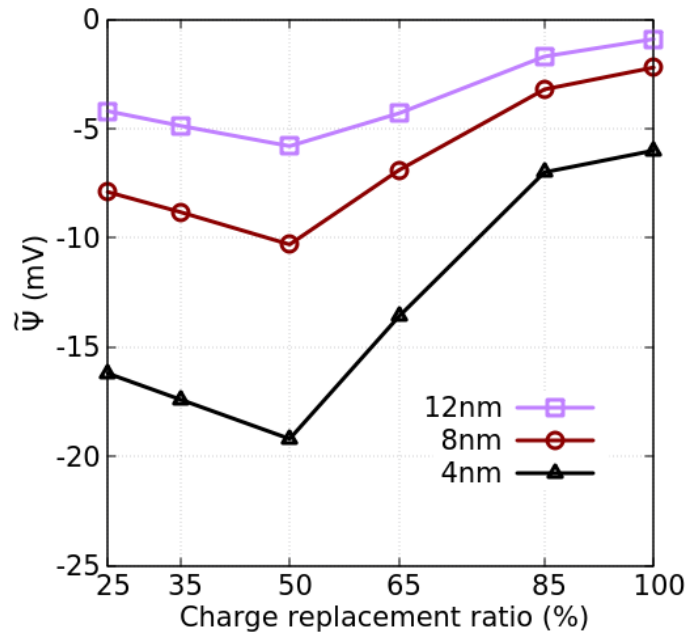


Fig.5.10. Evolution of the potential average as function of the replacement ratio in pores of 4, 8 and 12nm of size

In terms of the electrostatic properties of the EDL, the average potential (Fig.5.10) globally increases in negativity as the pore size goes down and the EDLs become more strongly overlapping. Nonetheless, the reduced pore radius does not seem to prevent the increase of the potential once the  $\text{Ca}^{2+}$  has accumulated in sufficient amount (replacement ratio > 50% for all pore sizes). Moreover, once the threshold of concentration passed, the reversal of charge seems to accelerate the rate at which the average potential is dropping (in negativity). The reason being that with a higher adsorption and a higher accumulation of  $\text{Ca}^{2+}$  in the diffuse layer, the silanols are completely screened within a very short distance. In other words, as the  $\text{Ca}^{2+}$  content goes up in the solution, the Debye length is effectively reducing and the system is further deviating from the initial configuration with  $\text{Ca}^{2+}$  ultimately exceeding by over an order of magnitude ( $\sim 20\text{mM}$ ) its under saturation threshold with respect to Portlandite ( $1\text{mM}$ ).

*In a similar fashion to monovalent salts, and despite the more complex behavior of Ca-containing systems, it appears clear that the pore size has a sizable influence on the EDL properties in realistic pore solutions, in particular on the adsorption of  $\text{Ca}^{2+}$  and  $\text{Cl}^-$ . Nevertheless, the EDL formation in Na-systems was also found to be greatly affected by two additional factors, namely the surface charge density of C-S-H and the variation of the pH. In order to make the text and material easier to read and more relatable, the details of the study of the mentioned parameters is detailed in the **Appendix A** of the present chapter.*

### C. Case of the full calcium occupancy of the ionized C-S-H surface (Ca-Si occupancy ratio equal to 100%)

Through the simulation of  $\text{Ca}^{2+}$  adsorption in the presence of  $\text{Na}^+$  ions, Monte Carlo results suggest that the Ca-Si occupancy is partial and that sodium is able to compete despite its lower valence. However, as the assumed C-S-H surface was implicit and solely characterized by a surface charge density, we may consider that Ca interactions with the surface were simplified. In practice, the competition between  $\text{Na}^+$  and  $\text{Ca}^{2+}$  for the adsorption on the ionized sites remains an open question. Still, the case of full calcium occupancy of the surface is possible [Casar2022]. Here, the implications of this assumption are investigated.

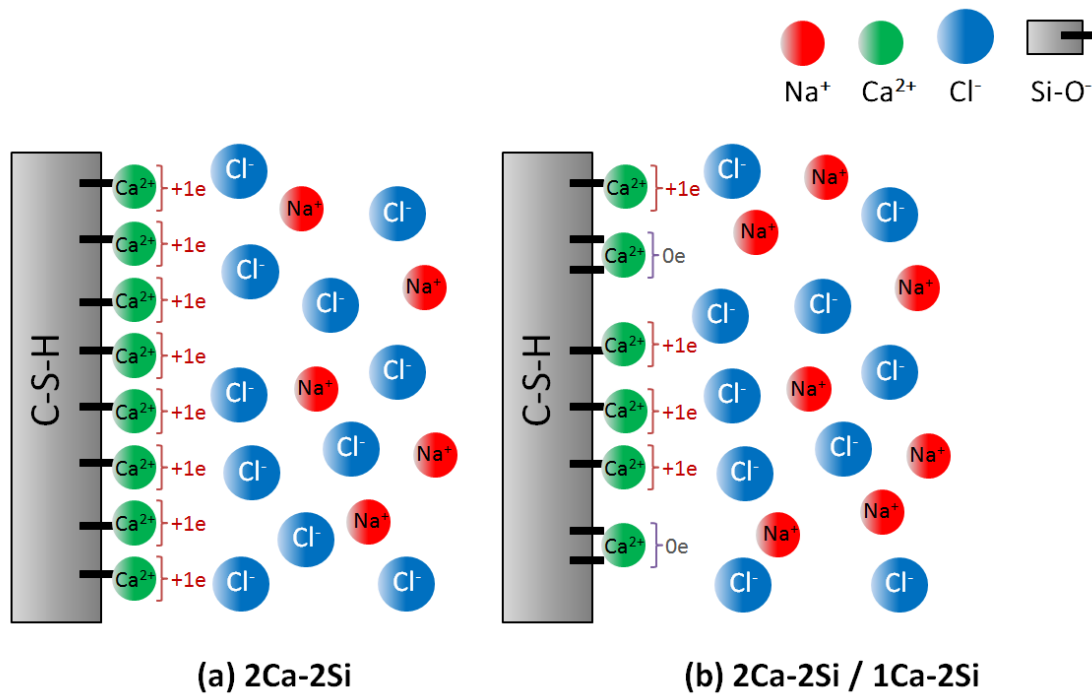


Fig.5.11. Schematic of a fully calcium-covered C-S-H surface. Two adsorption mechanism are suggested: **(a)** Each ionized site  $\text{Si-O}^-$  is occupied by a  $\text{Ca}^{2+}$  ion (Type I) **(b)** Each pair of ionized sites ( $2\text{Si-O}^-$ ) can attract either  $2\text{Ca}^{2+}$  (Type I) or  $1\text{Ca}^{2+}$  (Type II)

Considering a C-S-H surface with a silanol site density of  $1.2 \text{ sites.nm}^{-2}$ , the full deprotonation of the surface implies a surface charge of  $-1.2 \text{ e.nm}^{-2}$ . In Fig.5.11, we present two representations of the C-S-H surface being completely and exclusively occupied by  $\text{Ca}^{2+}$  ions. First, each  $\text{Ca}^{2+}$  ion is assumed to occupy individually a  $\text{Si-O}^-$  site (Fig.5.11.(a)) in which case the charge of each pair of ionized sites (i.e.  $2 \times (\text{Si-O}^-)$ ) is reversed from a value of  $-2\text{e}$  to an apparent charge of  $+2\text{e}$ . In sum, the apparent surface charge density of the surface, post-adsorption, shifts to a positive value of  $+1.2 \text{ e.nm}^{-2}$ . In Fig.5.11.(b), we consider a second type of adsorption in which one  $\text{Ca}^{2+}$  may possibly occupy two sites on its own. In order to measure the effect of such eventuality, we assume, in a second stage, that the two adsorption types are equiprobable (50% Type I + 50% Type II). In other words, half of the pair sites are neutralized by a single calcium ion. As a result, the apparent surface charge is reversed but reduced, in comparison with the first case, with a density of  $+0.6 \text{ e.nm}^{-2}$ . In principle, both adsorption types are possible. However, the frequency of one or the other remains a subject of active research.



For a pore solution modeled as a {NaOH 0.1M + NaCl 98mM + CaCl<sub>2</sub> 1mM}, the GCMC algorithm is run for both adsorption cases in pores of sizes 4, 8 and 12 nm. In the below figure (Fig.5.12) are plotted the chloride distributions around C-S-H for the pores of 4 and 12 nm.

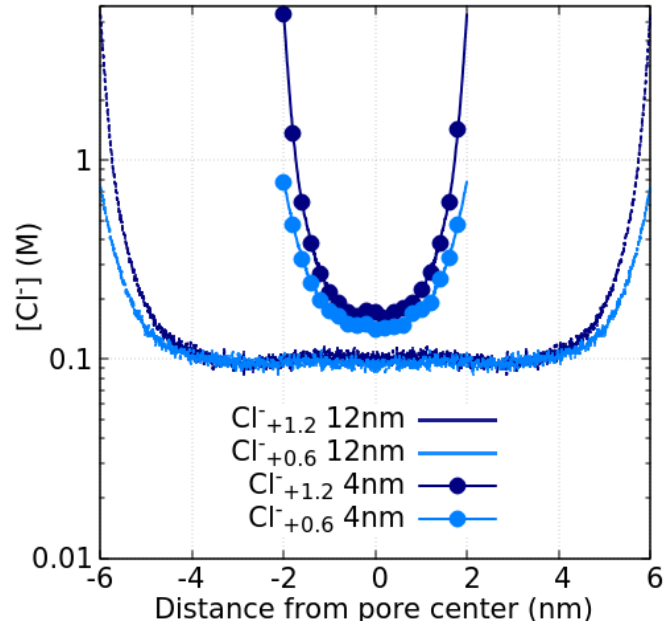


Fig.5.12. Chloride distribution profiles around C-S-H surfaces of charge densities +0.6 and +1.2 e.nm<sup>-2</sup> in pores of 4 and 12 nm size

At a higher Ca-Si occupancy (case of Fig.5.11.(a)), one can see that the accumulation of chloride (Fig.5.12) at the surfaces is higher due to the apparently more positive C-S-H charge density. In the 12nm pore, chloride ions relax to the bulk value of 0.1M at a fairly similar distance from the walls indicating the EDL thickness is independent of the assumed adsorption mechanism. In the pore of 4nm, the overlapping of the diffuse layers is at the origin of the vanishing of the concentration plateau at the center. In definitive, the chloride distribution displays an utterly reversed profile to the case of negative surfaces.

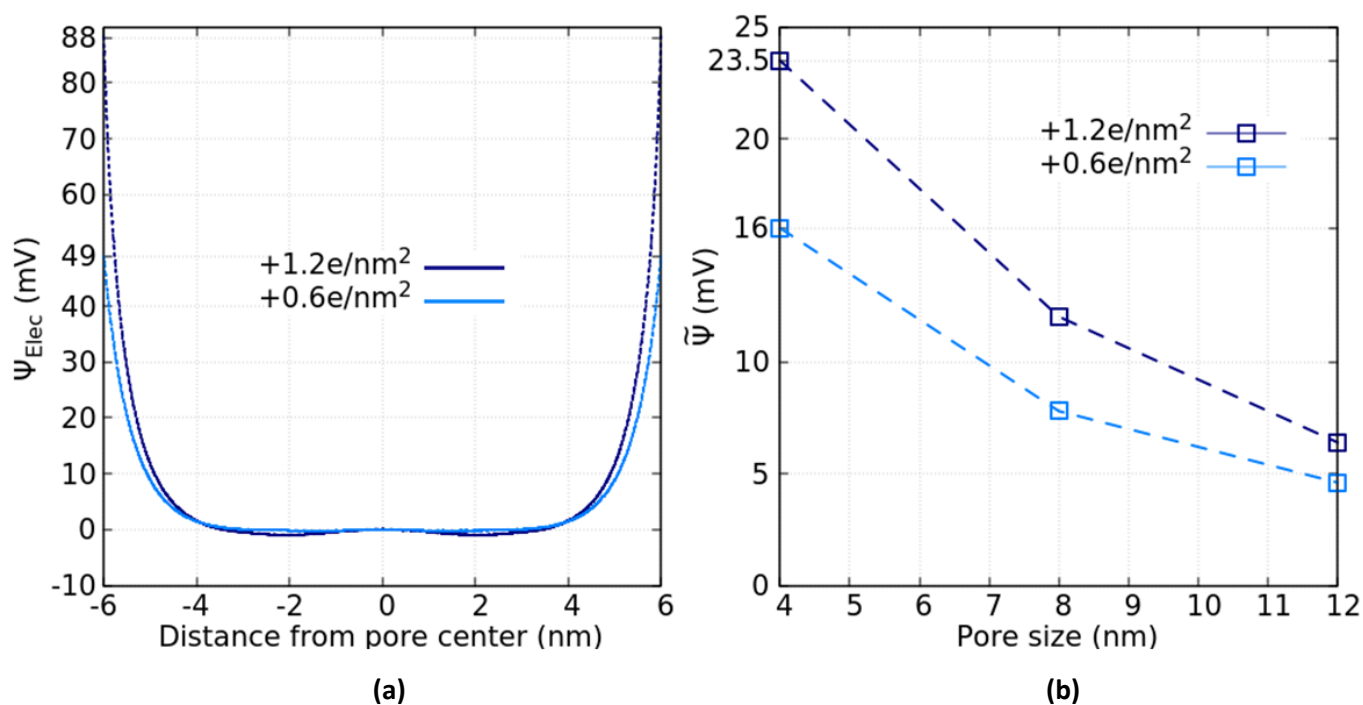


Fig.5.13. (a) Electrochemical potentials as function of the position in a 12nm pore and (b) evolution of the potential average as function of the pore size. The surface charge densities are  $+0.6$  and  $+1.2 \text{ e.nm}^{-2}$  representing, respectively, the high (Fig.5.11.(a)) and low (Fig.5.11.(b)) Ca-Si occupancy cases.

In a slit pore of 12nm width, the computed electrochemical potential (Fig.5.13.(a)) shows the usual layering of the pore solution between a locally negatively charged diffuse layer and an electroneutral bulk area. Depending on the Ca-Si occupancy, the surface\* potential varies from 49mV, at lower occupancy, to approximately 88mV in the case of a full reversal of charge of each pair of sites. The reduction of the pore size does also enhance the average potential of the pore which grows more and more positive

From a practical point of view, the veracity of these “theoretical” cases can be, in part, evaluated through comparison with Zeta potential values. The calculated values of the surface potential seem to be quite high for C-S-H with Ca/Si ratios beyond 1. Labbez et al. did, indeed, find a value close to 40mV but only for a C-S-H with Ca/Si ratio of 0.66 [Lab2011]. For a Ca/Si ratio up to 1.5, Haas and Nonat measured a maximum value of 20mV [Haas2015]. And despite that the zeta potential is a valuable measure of electrokinetic phenomena; combining electrostatics and dynamics of the interfacial liquid, it remains difficult to have accurate values of surface potential when the surface itself remains poorly defined. Moreover,  $\zeta$  potential measurements on C-S-H suspension can only be partially illustrative of electric properties of confined solutions. Another possible route is to measure the Ca/Si ratio of washed and unwashed C-S-H samples. Using the mixed Ca and Si terminated C-S-H surface developed by Casar et al. [Casar2022], the model for a C-S-H with Ca/Si of 1.7 (in the bulk) predicted a global Ca/Si ratio of a C-S-H particle (bulk+surface) equal to 1.58 when  $\text{Ca}^{2+}$  adsorption is null. Once we adsorb  $1\text{Ca}^{2+}$  on each pair of silanols  $2[\text{Si-O}^-]$  (i.e. Type II adsorption Fig.5.11.(b)), the

\* Assuming that the potential of the surface is measured at the plane of adsorption of the  $\text{Ca}^{2+}$  would be more coherent once considering calcium as part of the structure and not only residing in the Stern layer.

ionized sites are neutralized (i.e.  $(2[\text{Si-O}]^-)=\text{Ca}^{2+}$  resulting in an apparent charge of 0e) and the global Ca/Si ratio goes up to 1.62. Considering the adsorption of Type I (Fig.5.11.(a)) where each deprotonated silanol is reversed (i.e.  $\text{Si-O-Ca}^+$ ), the Ca/Si ratio further increase to 1.66. Finally, by occupying the bridging sites, we approach the bulk value of  $\text{Ca/Si} = 1.7$

## IV. Conclusions

The application of the EDL model in presence of  $\text{Ca}^{2+}$  ions in the C-S-H gel pores was discussed. The chemistry of the cementitious system showed a non-negligible influence on the stability of the present ions in the pore solution. At pH values typically beyond 13, calcium ions displayed a very low solubility. It was, hence, concluded that their presence was predominantly within the Stern layer of the ionized C-S-H surface.

In order to increase the amount of Ca on the surfaces without disrupting the system (too much), Monte Carlo simulations were conducted at constant pH constant chloride content where part of the neutralizing  $\text{Na}^+$  were progressively substituted by  $\text{Ca}^{2+}$  (within the respect of electroneutrality). The numerical results revealed two-regimes of behavior of  $\text{Ca}^{2+}$  in solution:

- At charge replacement ratios below 50%, the  $\text{Ca}^{2+}$  showed an affinity to predominantly adsorb on the negatively charged C-S-H surface or at least remain within the diffuse layer without further migration to the bulk area. This behavior was noticeably emphasized as the EDL effect was growing i.e. in smaller pores (overlapping), at high surface charge densities and low pH values. Although mitigated by the higher screening capacity of Ca, very similar trends to the Na-system were globally observed. As  $\text{Ca}^{2+}$  content also stayed below the threshold of portlandite precipitation, this regime was found to best depict surface effects in gel pores despite its limited scope.
- Beyond the limit of 50% charge replacement ratio, the reversal of charge of the surface potential was noted. Given that the model did not account of speciation,  $\text{Ca}^{2+}$  was allowed to build up in the solution beyond the undersaturation threshold. Within this regime, the multi-parametric study of the EDL showed that Ca was the potential determining factor. In the extreme case where the Ca-Si occupancy reaches 100%, it was found the surface potential shifted to positive values and that the adsorption of chloride was enhanced.

To date, Ca adsorbed surfaces are poorly understood. In fact, the exact location of Ca on C-S-H remains an unknown. As a consequence, it is very delicate to affirm if a present Ca on the surface is whether incorporated to the C-S-H structure or belongs to the pore solution (just adsorbed). This constitutes probably among the most challenging and yet urging matters to decipher for a better understanding of C-S-H. Among the interesting directions,  $^{43}\text{Ca}$  NMR spectroscopy is one of the possible methods that may help in the endeavor. It remains, however, a complex procedure due to the low natural abundance of the nuclide  $^{43}\text{Ca}$  and its low resonance frequency. Although most successes were achieved through solid-state spectroscopy, developments are running their course for solution  $^{43}\text{Ca}$  NMR especially in the study of calcium-binding bio-molecules where promising work is in progress [Bryce2010].



## V. Appendix A: Multi-parameter study of the EDL in Ca-containing environments

### A. Effect of the ionization degree

Among the characteristics that change with the Ca/Si ratio in C-S-H is the silanol site density (SSD). At different pH values, the C-S-H interface experiences variations in its ionization degrees and displays a different surface charge density according to the properties of the surrounding solution. In pore solutions where Na<sup>+</sup> is the only counter-ion, it was found that the increase of the surface charge density translated into an increase of the average potential of a pore regardless of its size. The reduction of the pore contributed, however, to the enhancement of the effect due to the overlapping of the forming diffuse layers. Unlike sodium, Ca<sup>2+</sup> is a potential determining ion i.e. its amount controls the potential around the surface (Zeta potential) as much as the ionization degree. To investigate the effect of the ionization degree in Ca-containing environment, the surface charge density is decreased from -1.2 down to -0.48 e.nm<sup>-2</sup>.

pH	Width (Å)	Walls (Å x Å)	Cl <sup>-</sup>	OH <sup>-</sup>	Ca <sup>2+</sup> charge replacement ratios	Ca <sup>2+</sup>	Na <sup>+</sup>	Ca <sup>2+</sup> /Na <sup>+</sup> (x 100)
13	120	180 x 180	234	234	0%	2	774*	0.26
					25%	41	696	5.9
					50%	80	618	13
					65%	103	572	18
					85%	134	510	26.3
					100%	157	464	33.8

Table.A.1. Simulation box for a pore solution modeled as {NaOH 0.1M + NaCl 98mM + CaCl<sub>2</sub> 1mM} in a 12nm-pore with C-S-H surfaces neutralized with Na<sup>+</sup> and Ca<sup>2+</sup> ions at various replacement ratios. The surface charge density is set at  $\sigma_{C-S-H} = -0.48 \text{ e.nm}^{-2}$

The equilibration of the system is ensured by looking at the anionic distribution (Fig.A.1.(a)) which rests at a concentration of 0.2M in the bulk area (in a large enough pore; here 12 nm). After relaxation, the Ca<sup>2+</sup> distribution is studied. Very similarly to the higher ionization case (*ref. section III.A*), the calcium profile displays the characteristic “shoulder” like profile (or W shape) once the addition of the Ca<sup>2+</sup> exceeds a charge substitution ratio of 50% (red profiles in Fig.A.1.(b)).

---

\* Among which, we count 310 Na<sup>+</sup> to neutralize the 310 silanol sites on the walls. This is the Na<sup>+</sup> population that is gradually replaced.

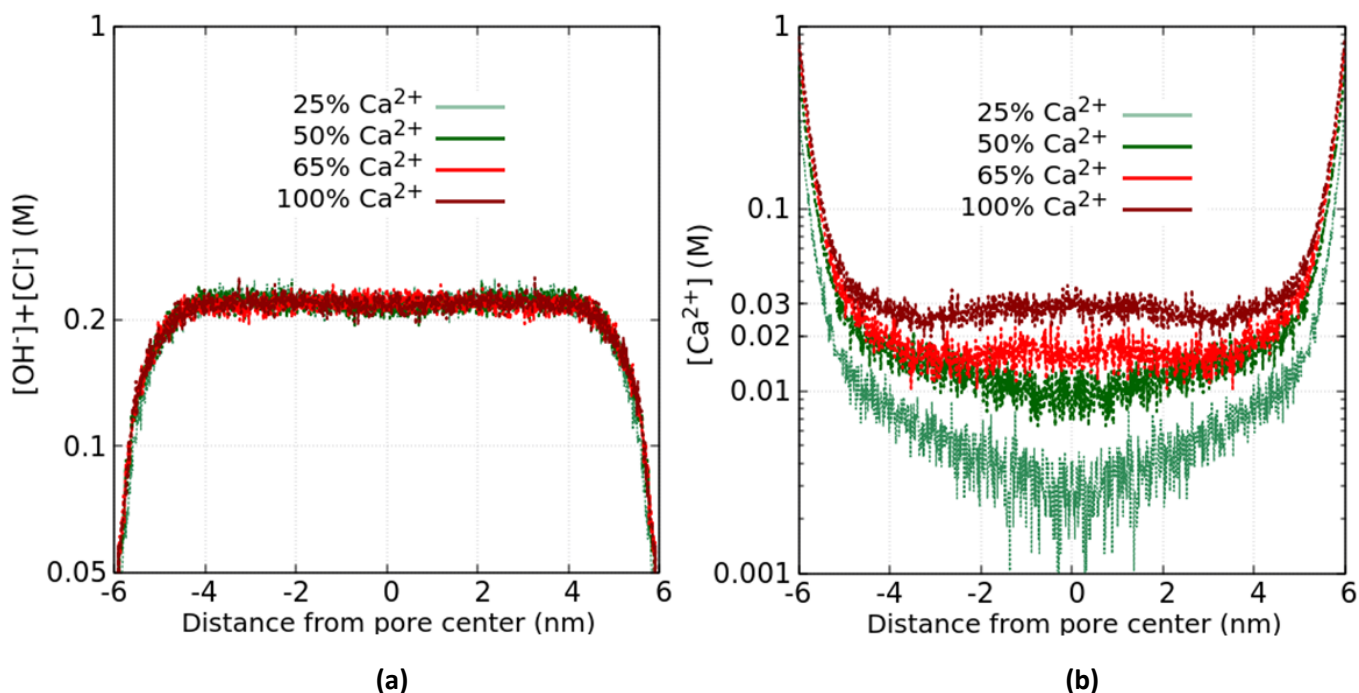


Fig.A.1. Evolution of **(a)** the anionic distribution and **(b)** the  $\text{Ca}^{2+}$  distribution in a 12 nm pore with surface charge density of  $-0.48 \text{ e.nm}^{-2}$  at charge replacement ratios of 25%, 50%, 65% and 100%.

In comparison with the high surface charge density case (Tab.5.2), it is important to note that for a same replacement ratio, the  $\text{Ca}^{2+}/\text{Na}^+$  ratio for  $\sigma_{\text{C-S-H}} = -0.48 \text{ e.nm}^{-2}$  (Tab.A.1) is lower. As a result, one can note that the adsorption of  $\text{Ca}^{2+}$  falls below the line of ideal occupancy (Fig.A.2.(a)) even at low replacement ratios. As the pore radius goes down and the diffuse layer covers more of the pore space, the  $\text{Ca}^{2+}$  occupies more available sites on the surface i.e. roughly 70% of the silanols in the 4nm-pore at a replacement ratio of 100% (or a  $\text{Ca}^{2+}/\text{Na}^+$  ratio of nearly 1/3). It is unlikely that this decay of the Ca-Si occupancy, compared to the case of  $-1.2 \text{ e.nm}^{-2}$ , is due to the  $\text{Na}^+$  competition as  $\text{Ca}^{2+}$  have proved to have a much higher affinity to adsorb. It is probably the result of the weaker potential at the surface and the lowering of the steric effects around it making the solution behave more like an ideal electrolyte (*ref. chapter 4 section I.A*).

In Fig.A.2.(b), the computation of the average potential shows the persistence of a two-regime behavior (regardless of the surface charge). At substitution ratios below 50%, the average potential of the pores is higher (in absolute value) as the surface charge density is bigger. As expected, the potential is most negative in the smallest pore. Beyond 50% replacement, the sudden drop of the pore potential appears to be less significant at a lower ionization degree. The effect of  $\text{Ca}^{2+}$  addition appears to be noticeably mitigated upon decrease of the surface charge magnitude which, in fact, agrees with its lower interaction with the surface (Fig.A.2.(a)).

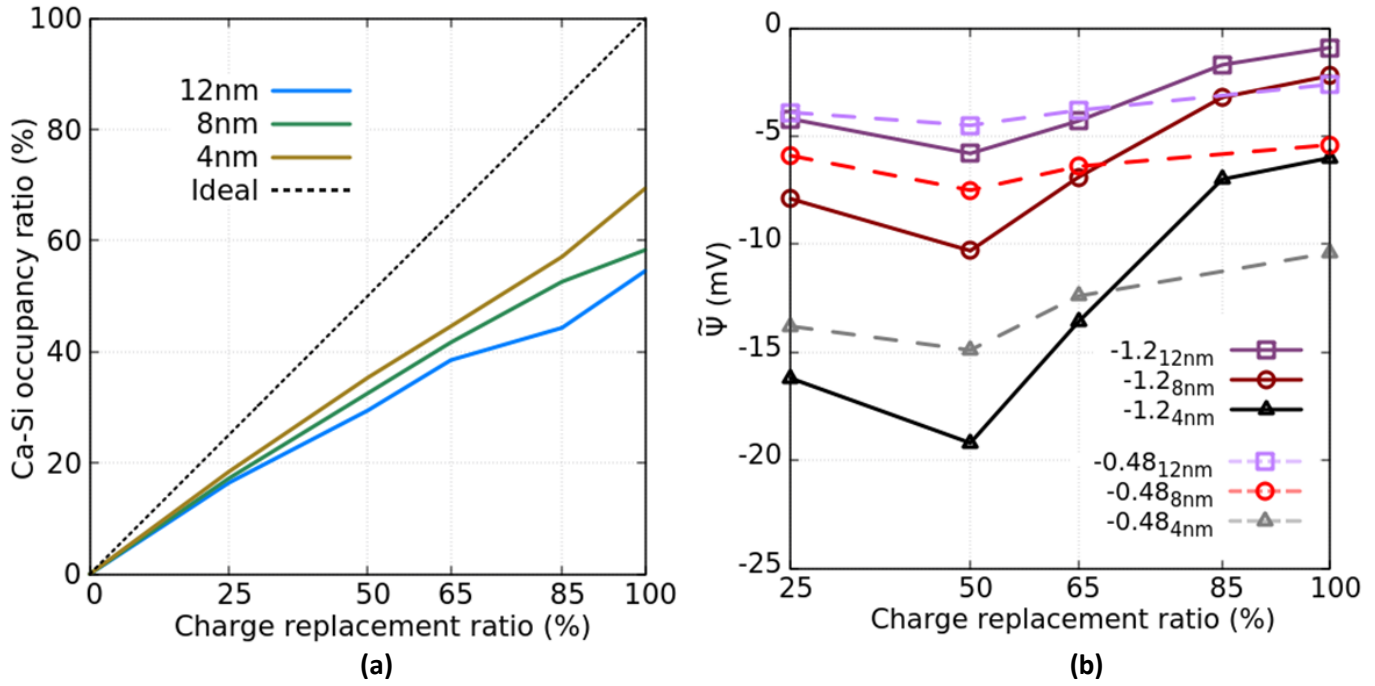


Fig.A.2. **(a)** Evolution of the Ca-Si occupancy as function of the replacement ratio at  $\sigma_{C-S-H}$  equal to  $-0.48 \text{ e.nm}^{-2}$  and **(b)** Comparison of the evolution of the potential average as function of the charge replacement ratio with  $\sigma_{C-S-H}$  varying between  $-0.48$  and  $-1.2 \text{ e.nm}^{-2}$ . Results are presented for pores of 4, 8 and 12 nm.

In comparison with pure Na-systems, it seems that the variation of the surface ionization degree has a very similar behavior in Ca-systems as long as the  $\text{Ca}^{2+}$  content remains low enough to prevent any reversal of the potential. Despite the appreciable decrease in the surface charge, the limiting substitution ratio remained between 50 and 65% for both  $-0.48$  and  $-1.2 \text{ e.nm}^{-2}$ . The reason being that the  $\text{Ca}^{2+}$  concentration necessary to cause the reversal of charge of the  $-0.48 \text{ e.nm}^{-2}$  must be in the order of 20mM (Fig.A.1.(b)) so relatively close to the 10-20mM interval for the  $-1.2 \text{ e.nm}^{-2}$ . As a matter of fact, the necessary  $\text{Ca}^{2+}$  content that generates the non-linear regime of the charge reversal appears to vary within a very small window of concentrations of generally few millimoles for a wide range of surface charge densities ( $\sim 5\text{mM}$  for  $\sigma = -4 \text{ e.nm}^{-2}$  (ref. chapter 4 section I.C) up to  $\sim 20\text{mM}$  for  $-0.48 \text{ e.nm}^{-2}$ ). Nonetheless, given the low solubility of  $\text{Ca}^{2+}$  in real thermodynamic conditions, this potential shift is unlikely to occur in actual cement pore solution (ref. section II).

## B. Effect of pH decrease

In the same spirit, the effect of pH variation is implemented in the presence of Ca in the system. The same methodology is applied. The surface charge density is once more set at  $-1.2 \text{ e.nm}^{-2}$ . As the decrease of pH allows a higher solubility of  $\text{Ca}^{2+}$  and given the partial adsorption of the added  $\text{Ca}^{2+}$  in the previous computations, it was chosen to rather decrease the pH to 12.7 so that simulation results best represented the behavior of cement paste pore solution under realistic thermodynamic conditions.

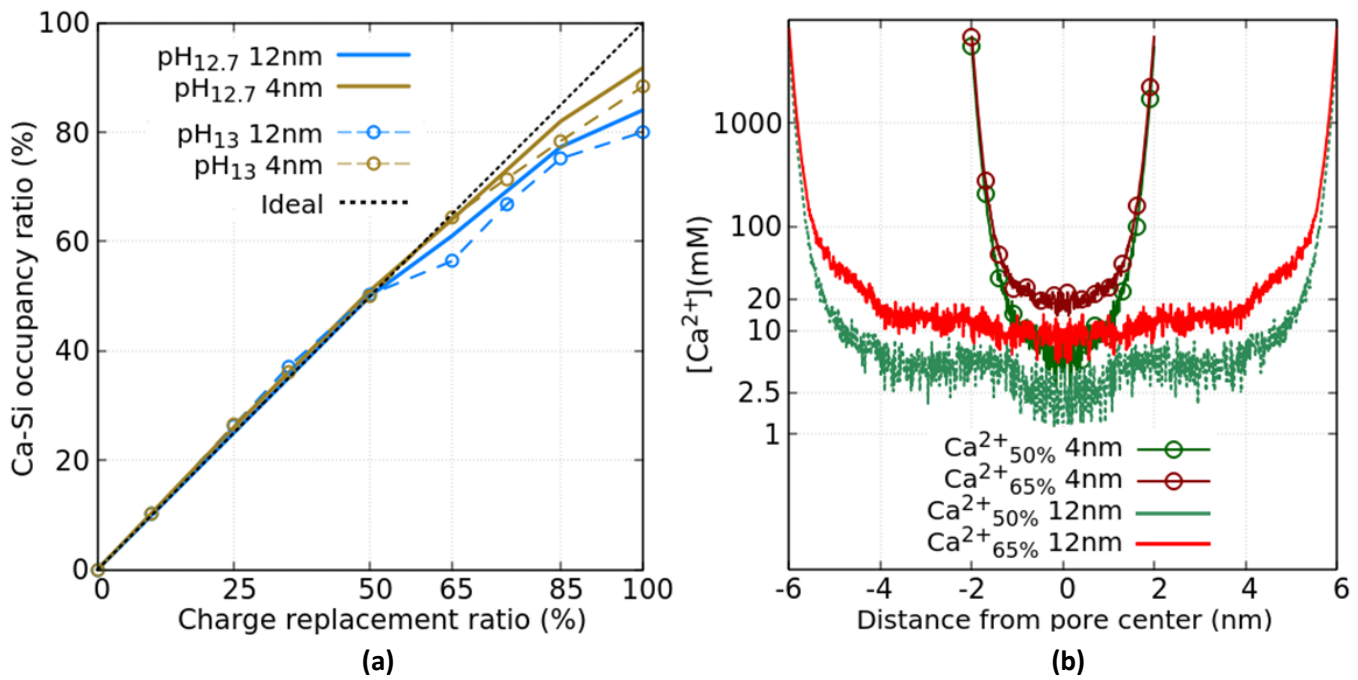


Fig.A.3. **(a)** Evolution of the Ca occupancy of the available ionized sites as function of the replacement ratio in pores of 12 and 4 nm pore at pH equal to 12.7 and 13. **(b)**  $\text{Ca}^{2+}$  distribution in pores of 12 and 4 nm at charge replacement ratios of 50 and 65% for pH=12.7.

In Fig.A.3.(a), one can see the increase of adsorbed  $\text{Ca}^{2+}$  on the surface with the increasing substitution ratio. At lower pH, the width of the EDL expands in the pores due to the decrease of the ionic strength and  $\text{Ca}^{2+}$  ions are involved in stronger interactions with the surface. Due to the overlapping of the diffuse layers, the Ca-Si occupancy reaches its maximum rate in the smaller pores at lower pH i.e. in the 4nm-pore, Ca-Si occupancy is quasi-ideal up to a ratio of 65% and further increased to, respectively, 80% and 90% at pH = 13 and 12.7 for a replacement ratio of 100%. Still, a portion of the added  $\text{Ca}^{2+}$  relaxed in the diffuse layer and further down in the bulk area as the ratio exceeds 50% (Fig.A.3.(b)). For 50% replacement and below (green curves), the concentration remained very close to the undersaturation concentration of 2.5mM (Tab.5.1). Despite the overlapping of the EDLs in the pore of 4nm, the increase of the concentration at the center of the pore remained small (and relatively close to undersaturation). In fact, the limiting ratio prior to charge reversal (red curves) stayed constantly between 50 and 65% and seemed unaffected by the pH value as it was not by neither the pore size nor the ionization degree.



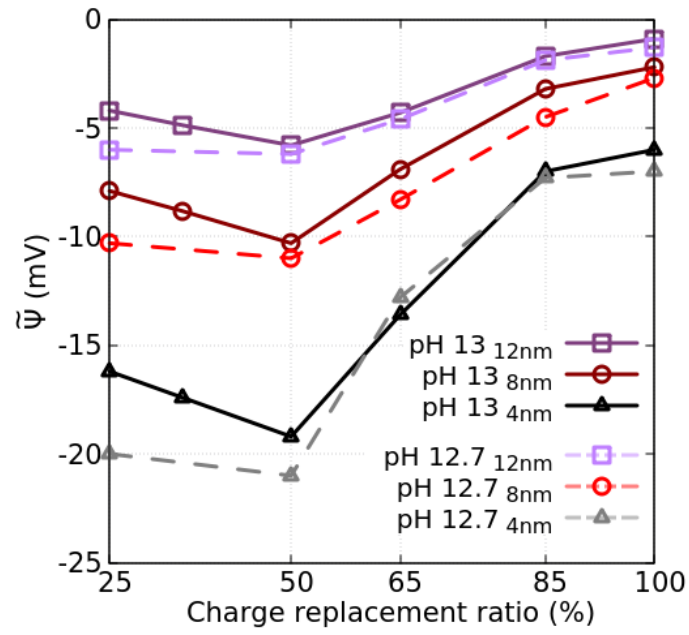


Fig.A.4. Evolution of the potential average as function of the charge replacement ratio in pores of 4, 8 and 12 nm at pH equal to 12.7 and 13

At low  $\text{Ca}^{2+}$  content (ratio < 50%), the average potential of the pores (Fig.A.4) increases in negativity with the decreasing pH. This behavior is very similar to monovalent systems. The influence of pH is, however, hindered as the  $\text{Ca}^{2+}$  concentration the potential to drop. In fact, due to its high screening capacity, the divalent ion induces the decrease of the Debye length and with it the thickness of the EDL which seems to cancel out the effect of the alkaline decrease.

## VI. References

- [Avet2018] Avet, François, and Karen Scrivener. "Investigation of the calcined kaolinite content on the hydration of Limestone Calcined Clay Cement (LC3)." *Cement and Concrete Research* 107 (2018): 124-135.
- [Barzgar2020] Barzgar, Sonya, et al. "The effect of sodium hydroxide on Al uptake by calcium silicate hydrates (CSH)." *Journal of colloid and interface science* 572 (2020): 246-256.
- [Bryce2010] Bryce, David L. "Calcium binding environments probed by  $^{43}\text{Ca}$  NMR spectroscopy." *Dalton Transactions* 39.37 (2010): 8593-8602.
- [Bernal1952] Bernal, J. D. "The structures of cement hydration compounds." *Proc. 3rd Int. Symp. Chem. Cem., London: Cement and Concrete Association*. 1952.
- [Casar2022] Z. Casar, K. Scrivener, P. Bowen, A. Kunhi Mohamed, Towards a representative model of the calcium silicate hydrate surface (2022, in preparation)
- [Duque2022] Duque-Redondo, Eduardo, Patrick A. Bonnaud, and Hegoi Manzano. "A comprehensive review of CSH empirical and computational models, their applications, and practical aspects." *Cement and Concrete Research* 156 (2022): 106784.
- [Elak2009] Elakneswaran, Y., T. Nawa, and K. Kurumisawa. "Electrokinetic potential of hydrated cement in relation to adsorption of chlorides." *Cement and Concrete Research* 39.4 (2009): 340-344.
- [Gra1947] Grahame, David C. "The electrical double layer and the theory of electrocapillarity." *Chemical reviews* 41.3 (1947): 441-501.
- [Haas2015] Haas, Jeremy, and André Nonat. "From C-S-H to C-A-S-H: Experimental study and thermodynamic modelling." *Cement and Concrete Research* 68 (2015): 124-138.
- [Hooton2010] Hooton, R. D., M. D. A. Thomas, and T. Ramlochan. "Use of pore solution analysis in design for concrete durability." *Advances in cement research* 22.4 (2010): 203-210.
- [Kunhi2018] Mohamed, Aslam Kunhi, et al. "An atomistic building block description of CSH-Towards a realistic CSH model." *Cement and Concrete Research* 107 (2018): 221-235.
- [Kovac2015] Kovačević, Goran, et al. "Atomistic modeling of crystal structure of  $\text{Ca}_{1.67}\text{SiHx}$ ." *Cement and concrete research* 67 (2015): 197-203.
- [Loth2018] Lothenbach, Barbara, et al. "Cemdata18: A chemical thermodynamic database for hydrated Portland cements and alkali-activated materials." *Cement and Concrete Research* 115 (2019): 472-506.
- [Lab2011] Labbez, Christophe, et al. "CSH/solution interface: Experimental and Monte Carlo studies." *Cement and Concrete research* 41.2 (2011): 161-168.
- [Pellenq2009] Pellenq, Roland J-M., et al. "A realistic molecular model of cement hydrates." *Proceedings of the National Academy of Sciences* 106.38 (2009): 16102-16107.
- [Thoenen2014] Thoenen, Tres, et al. "The PSI/Nagra Chemical Thermodynamic Database 12/07." (2014). Page 430

[Tri1989] Tritthart, Josef. "Chloride binding in cement II. The influence of the hydroxide concentration in the pore solution of hardened cement paste on chloride binding." *Cement and Concrete Research* 19.5 (1989): 683-691.

[Tay1986] Taylor, Harry FW. "Proposed structure for calcium silicate hydrate gel." *Journal of the American Ceramic Society* 69.6 (1986): 464-467.

[Viallis2000] Viallis-Terrisse, Hélène. *Interaction des silicates de calcium hydratés (CSH), principaux constituants du ciment, avec les chlorures d'alcalins. Analogie avec les argiles*. Diss. Dijon, 2000.

[Zhang2017] Zhang, Yunsheng, et al. "Modelling of diffusion behavior of ions in low-density and high-density calcium silicate hydrate." *Construction and Building Materials* 155 (2017): 965-980.



# Chapter 6 Diffusion of chloride ions in the nanoscopic C-S-H gel pores

This chapter starts with a presentation of the governing equations of ionic transport at the pore scale. The numerical resolution is conducted in two ways. Firstly, a finite element analysis (FEA) was carried out on the usual Poisson-Nernst-Planck (PNP) equations within the scope of the theory of dilute solutions. Thereafter, a second approach, combining the Poisson-Boltzmann formalism with Monte Carlo calculations of the non-ideal electrochemical potential, is developed. The results of the two approaches are presented and compared in the cases of monovalent electrolytes. Finally, the resolution is extended to the case of Ca-containing pore solutions and the simulation results discussed in the light of experimental work done to characterize the chloride resistance of different blended cements.

Chapter 6 Diffusion of chloride ions in the nanoscopic C-S-H gel pores .....	153
I.    Introduction .....	155
A.    Definition of the nanoscopic transport problem and objectives.....	155
B.    Choice of the resolution method .....	156
II.   The governing equations of ionic transport in saturated cement paste .....	157
A.    Case of an ideal solution: The classical Poisson-Nernst-Planck (PNP) equations.....	158
i) The governing equations .....	158
ii) Initial and boundary conditions .....	159
B.    Extension to non-ideal electrolytes: the modified Poisson-Boltzmann (MPB) .....	160
III.  Results and discussion .....	163
A.    Transport in symmetric monovalent electrolytes .....	163
i) Effect of the surface charge density .....	163
ii) Effect of the ionic strength .....	166
•    Effect of the concentration .....	166
•    Effect of pH at constant surface charge density.....	168
iii) First conclusions: The nanoscopic diffusion of chloride in monovalent systems .....	169
B.    Transport in a more realistic model of the cement paste .....	170
i) Ca-adsorbed surfaces.....	170
•    Validity of the transport model .....	170
•    Effect of the surface charge density .....	172
•    Effect of the pH at constant surface charge density .....	173
ii) Fully Ca-occupied C-S-H surface: case of a positive surface charge density.....	175
iii) Implications for real cementitious systems .....	176
IV.   Summary .....	178
V.    References .....	179



## I. Introduction

### A. Definition of the nanoscopic transport problem and objectives

Given today's imperative to reduce the carbon footprint of manufactured cements, the question of the long-term durability of blended systems, and in particular their resistance to harmful ions such as chloride, is more crucial than ever. Despite decades of research, the mechanisms that control the diffusion of ions at the nanoscale remain vaguely understood. To quantify the transport properties of a given material, we measure "a" diffusion coefficient. However, it is possible to define a multitude of diffusion coefficients, at different scales, when it comes to cement-based materials. The reason being that cement paste is a composite that contains liquid, solid and gaseous phases with pores and heterogeneities covering a wide range of length scales. From an experimental perspective, it is usual to refer to an "apparent" diffusion coefficient,  $D_a$ , (*ref. chapter 2 section III*). For a saturated cement paste, Atkinson et al. [Atk1984] defined  $D_a$ , assuming Fick's law of diffusion, as the diffusivity that correlates the average flux to the average concentration gradient.

$$\langle J_{i,x} \rangle = -D_a \frac{\partial \langle C_i \rangle}{\partial x} \quad (6.1)$$

Where  $x$  is the longitudinal (axial) direction in the pore and  $\langle . \rangle$  is the average over the whole medium (in both liquid and solid phases). Once considering the microstructure of cement paste, it is also possible to define a macroscopic effective diffusivity  $D_{eff}^{Macro}$  that encapsulates a number of system-dependent variables. A simple way to explicit these parameters is to write  $D_{eff}^{Macro}$  as function of  $D_0$ ; the diffusivity in free water:

$$D_{eff}^{Macro} = D_0 \frac{\delta}{\tau^2} \frac{\epsilon}{\alpha} \quad (6.2)$$

where  $\delta$  and  $\tau$  are, respectively, the constrictivity and the tortuosity of the pore network. The parameter  $\epsilon$  represents the volume fraction of porosity and  $\alpha$  is a term that accounts for the adsorption on the solid phases. In reality the averaging process of transport in multi-phase systems is not so obvious. In 1979, Hassanizadeh and Gray [Hassan1979(1), Hassan1979(2)] were the first to fully develop the homogenization equations of ionic transport in cement paste. It was shown that the up-scaled ionic flux could be obtained by averaging the microscopic equation as it follows:

$$\langle J_i \rangle = -D_{i,e} \nabla \langle a_i^{micro} \rangle - \frac{Fz_i D_{i,e} \langle C_i^{micro} \rangle}{RT} \nabla \langle \Psi^{micro} \rangle \quad (6.3)$$

Where  $D_{i,e}$  is a microscopic effective diffusion coefficient for each species  $i$ . The variables  $a_i^{micro}$ ,  $C_i^{micro}$  and  $\Psi^{micro}$  are, respectively, the activities, concentrations and the potential at the pore scale. A

subtle detail to note is the difference of the averaging operator  $\langle \cdot \rangle$  in Eq.(6.1) and Eq.(6.3). In the latter, the homogenization is conducted over a well-defined representative volume element (RVE). Given the wide range of heterogeneities in cement paste going from gel pores (3nm) up to aggregates (1cm), one can see the difficulty of constructing a satisfactory RVE. But, an even more troublesome issue is the mischaracterization of the microscopic terms  $a_i^{micro}$  (includes  $c_i^{micro}$ ) and  $\psi^{micro}$ .

In this chapter, we will use the previously developed EDL model to rigorously compute the microscopic driving forces and resolve the transport equation at the pore scale. In order to solely consider the surface effects in the C-S-H gel pores, we dismiss all the micro-structural parameters depicted in Eq.(6.2). In our case, the nanoscale ionic transport will be fully determined through the computation of the microscopic effective diffusion coefficients of flowing ions denoted as  $D_{i,e}$ .

## B. Choice of the resolution method

To compute microscopic transport properties, two main options are open to us:

1. Explicit or atomistic methods such as Molecular dynamics or Brownian dynamics. Although very accurate, these methods usually require computationally time-consuming simulations to determine the dynamic properties of the particles in a system or obtain representative averages of the observables of interest. They can also prove quite inflexible, often spending a huge computational effort to characterize quasi-uniform regions of the system such as bulk solutions in the EDL adsorption problems.
2. Implicit or continuum methods rely by definition on a continuous description of the system components i.e. the solvent, the ions, the surfaces... They usually consist in the numerical resolution of a closed-form partial differential equation (PDE). They offer a great flexibility in the choice of the resolution. Also, the boundary value problem of these PDEs offers a very faithful representation of the experiment such as electro-migration measurements.

Given the computational cost, the atomistic models are, in fact, quite unpopular especially in the resolution of diffusion related problems. In cement science, the inexistence of realistic C-S-H atomistic surface models makes it even less worthwhile. While it seems clear that the continuum methods are a better alternative, the actual choice of a good enough model is less straightforward. The most obvious approach is with no doubt the Fickian law of transport. Although very intuitive, the limitations of the equation are common knowledge. For the usually concentrated and asymmetric pore solution in cement paste, Zhang and Gjørsvik [Zhang1996] showed the importance to account for steric effects. It was essentially demonstrated that, due to the non-ideality of the electrolyte, ionic interactions reduced the chemical potential and, with it, the driving forces of ionic fluxes. The EDL formation and the effects of its overlapping were also shown (*ref. chapters 4 and 5*) to significantly alter the electrochemical properties of the solution which is expected to interfere with the mobility of ions depending on their size and valence. Fick's law stems, however, from a simplified version of the more general Poisson-Nernst-Planck (PNP) equations. The PNP system is, indeed, the natural set of equations to describe the motion of ionic species in a fluid under the effect of electrostatic gradients. There also exists a variety of formulations of these equations that account for the finite size of ions with the main challenge being the numerical implementation and resolution of these



more complicated versions. The appropriate choice of the model within a manageable level of sophistication is paramount.

In the next section, we firstly set the initial and boundary value problems for the finite element method resolution of the conventional PNP equations. Second, we propose a novel methodology to resolve the PNP equations using the Poisson-Boltzmann theory in combination with computations of the ionic concentrations by the Metropolis Monte Carlo in the Grand Canonical ensemble.

## II. The governing equations of ionic transport in saturated cement paste

The Poisson-Nernst-Planck equations are a system of partial differential equations that describe the motion of ionic species in a fluid. At the pore scale, the driving forces of ionic diffusion include both atomistic and continuum effects and the ionic flux  $J_i$  [mol/(m<sup>2</sup>.s)] writes as a sum of a number of contributing terms [Fen2021]:

$$\mathbf{J}_i = \mathbf{J}_i^D + \mathbf{J}_i^A + \mathbf{J}_i^E + \mathbf{J}_i^{C,T} \quad (6.4)$$

with  $\mathbf{J}_i^D$  the ideal matter diffusion term,  $\mathbf{J}_i^A$  the advection flux due to the velocity of water in the pore,  $\mathbf{J}_i^E$  the migration flux due electrostatic gradients and  $\mathbf{J}_i^{C,T}$  the flux due to gradients of temperature and non ideal diffusion. These terms can be expressed as it follows

$$\left\{ \begin{array}{l} \mathbf{J}_i^D = -D_{i,0} \nabla C_i \\ \mathbf{J}_i^A = C_i \mathbf{v} \\ \mathbf{J}_i^E = -D_{i,0} \frac{z_i e C_i}{k_B T} \nabla \Psi \\ \mathbf{J}_i^{C,T} = -D_{i,0} C_i \left[ \frac{\nabla \gamma_i}{\gamma_i} + \ln(a_i) \frac{\nabla T}{T} \right] \end{array} \right. \quad (6.5)$$

Where  $D_{i,0}$  [m<sup>2</sup> s<sup>-1</sup>] is the diffusion coefficient in free water,  $C_i$  [mol m<sup>-3</sup>] the concentration,  $\mathbf{v}$  [m s<sup>-1</sup>] the advection velocity,  $e$  [C] the absolute charge of electron,  $k_B$  [J K<sup>-1</sup>] the Boltzmann constant,  $\psi$  [V] the electrostatic potential,  $\gamma_i$  [m<sup>3</sup> kg<sup>-1</sup>] the chemical coefficient,  $a_i$  [-] the chemical activity and  $T$  [K] the temperature.

In the context of studying the long-term durability of cement, we assume chemical equilibrium achieved and chemical reactions negligible. In that case, sink terms are dismissed and the equation of transport finally writes as

$$\frac{\partial C_i}{\partial t} + \nabla \cdot \mathbf{J}_i = 0 \quad (6.6)$$

To quantify the EDL effects on ionic diffusion, the equation (6.6) is resolved in the two cases of ideal and non-ideal pore solutions.

#### A. Case of an ideal solution: The classical Poisson-Nernst-Planck (PNP) equations

In this section, we aim to present the boundary value problem for the finite element resolution of the classical Poisson-Nernst-Planck (PNP) equations for ideal solutions. In the case of ideal electrolytes, the chemical potential simplifies into its ideal term (*ref. chapter 3 section III.A*) where the activity coefficient  $\gamma_i$  is equal to 1 and the ionic concentrations are confounded with the activities. By assuming a constant temperature of the pore, the chemical and thermal flux is set to zero i.e.  $\mathbf{J}_i^{CT} = \mathbf{0}$  in (6.5). In sum, the chemical potential gradient simplifies to the usual matter diffusion gradient  $\nabla C_i$ .

##### i) The governing equations

The first equation of the ideal PNP system is Gauss's law of charge conservation, also known as the Poisson equation, which correlates the volumetric charge distribution  $\rho$  with the resulting electric field  $\mathbf{E}$ . The differential form of the law can be written as

$$\nabla \cdot \mathbf{E} = \frac{\rho}{\varepsilon_0 \varepsilon_r} \quad (6.7)$$

where  $\nabla \cdot \mathbf{E}$  is the divergence of  $\mathbf{E}$ . As we assume the medium to be isotropic with a constant relative permittivity  $\varepsilon_r$  and since the electric field is a conservative vector field, it writes as the gradient of a scalar potential  $\psi$  representing the electrostatic potential in volts:

$$\mathbf{E} = -\nabla \Psi \quad (6.8)$$

Secondly, the ionic fluxes  $\mathbf{J}_i$  are expressed as function of the considered driving forces  $\mathbf{E}$  ( $-\nabla \psi$ ) and  $\nabla a_i$ . As convection in the pore solution is neglected ( $\mathbf{J}^A = \mathbf{0}$  in (6.5)), the Nernst-Planck equations simplifies to

$$\mathbf{J}_i = -D_{i,0} \nabla C_i - D_{i,0} \frac{z_i e C_i}{k_B T} \nabla \Psi \quad (6.9)$$

Finally, the law of conservation of mass can be written as

$$\frac{\partial C_i}{\partial t} = \nabla \cdot (D_{i,0} \nabla C_i + D_{i,0} \frac{z_i e C_i}{k_B T} \nabla \Psi) \quad (6.10)$$

## ii) Initial and boundary conditions

The pore is represented by a rectangular domain a length  $L$  representing the length of the walls in the longitudinal direction  $x$  and a width  $W$  that represents the width of the slit in the transversal direction  $y$  (Fig.6.1). The ratio  $L/W$  is set to 5 for different values of the pore size. The initial conditions are

$$\begin{cases} \forall (x, y) \in ]0, L[ \times ]0, W[ \\ \Psi(x, y, t = 0) = 0 \\ C_i(x, y, t = 0) = C_{b,i} \end{cases} \quad (6.11)$$

Boundaries conditions are also imposed at the edges of the box. Firstly, the conditions on the C-S-H charged walls at  $y=0$  (bottom wall) and  $y=W$  (the upper wall) are

$$\begin{cases} \mathbf{n} \cdot (\mathbf{E}_{in} - \mathbf{E}_{out}) = \frac{\sigma_s}{\epsilon_0} \\ \frac{\partial C_i}{\partial y} |_{y=0, W} = 0 \end{cases} \quad (6.12)$$

where  $\sigma_s$  represents the surface charge density and  $\mathbf{n}$  the normal vector to the walls with  $\mathbf{E}_{in} - \mathbf{E}_{out}$  the discontinuity of the electric field through the surface separating the interior media (electrolyte) from the outside (reference value). On the same walls, the condition of no flux is imposed on the concentration of all species. Secondly, the boundary conditions at the pore's entry ( $x=0$ ) and exit ( $x=L$ ) are summarized as below

$$\begin{cases} \Psi(x = 0, L) = 0 \\ C_i(x = 0) = 1.05 C_{b,i} \\ C_i(x = L) = 0.95 C_{b,i} \end{cases} \quad (6.13)$$

such as only a concentration gradient is imposed at the pore sides with a mean concentration difference of  $\Delta C_i$  equal to 10% of  $C_{b,i}$  [Yang2019]. Hence, an increased inlet concentration of  $C_{inlet} = 1.05 C_{b,i}$  (+5%  $C_{b,i}$ ) and a reduced concentration at the outlet  $C_{outlet} = 0.95 C_{b,i}$  (-5%  $C_{b,i}$ ). The meshing of the domain (Fig.6.1) is refined at the surfaces with a maximum cell size of  $\lambda_D/100$  where  $\lambda_D$  is the Debye length i.e. a maximum size of 0.1 Å for a 0.1M NaCl electrolyte. For computational efficiency, the refinement is gradually diminished as one approaches the center of the pore with a growth rate of 1.13.

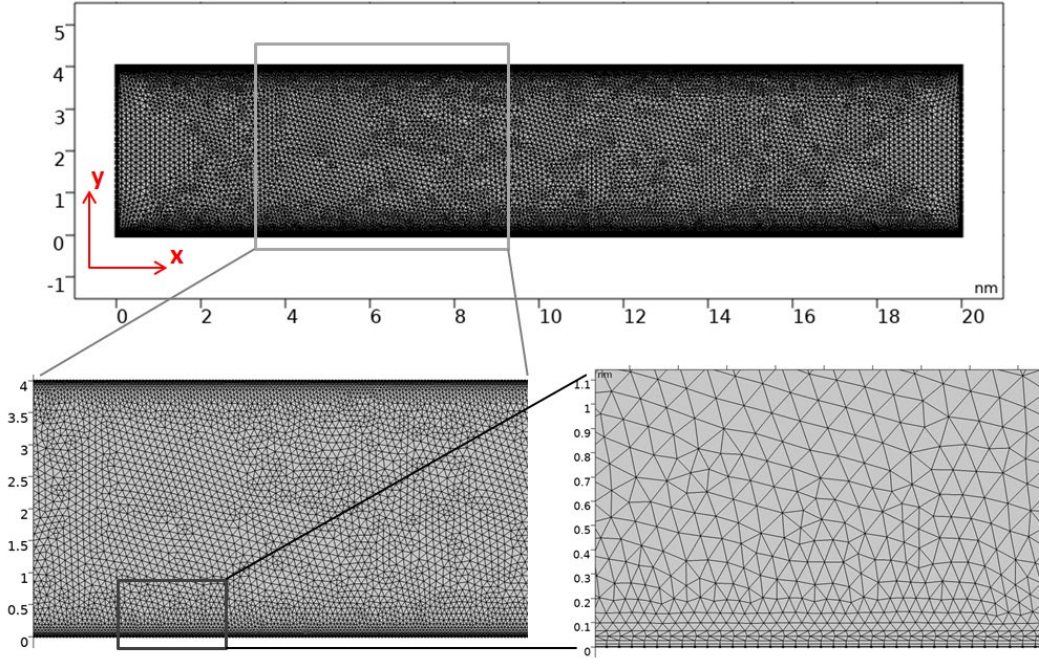


Fig.6.1. Capture of the finite element mesh of the pore space used for the simulation of the electrical double layer formation in a slit pore with a focus on different regions of the domain.

For the rest of the chapter, all the results obtained by this approach will be referred to by the notation PNP.

## B. Extension to non-ideal electrolytes: the modified Poisson-Boltzmann (MPB)

In this approach, the idea is to resolve the non-ideal PNP ( $\nabla \gamma_i \neq \mathbf{0}$  in (6.5)) by keeping the advantageous PB formalism and modify it in order to account for surface effects predicted by the GCMC in the resolution of the transport problem. As mentioned in the previous chapter (*ref. chapter 4 section I*), the PB equation is a steady state reformulation of the conventional PNP (6.10). It assumes a Boltzmann distribution where ions distribute, around a given charged surface, in function of their thermal and electrostatic energies. Mathematically, this translates into concentration profiles that write as decaying exponential functions. In the case of monovalent salts, GCMC computations have provided better insight on the non-ideality effects of the interfacial solution but, ultimately, also resulted in similar exponential-like distributions. So to find a convenient formulation of the ionic fluxes in the diffuse layer (DL) of the EDL, we assume that ionic concentrations at equilibrium write as follows

$$C_i(y) = C_{b,i} \exp\left(\frac{-z_i e \Psi(y)}{k_B T}\right) \quad (6.14)$$

where  $y$  is the normal direction to the charged surfaces. Once we insert the distributions (6.14) in the Nernst-Planck equations (6.9), the equation becomes

$$\mathbf{J}_i = -D_{i,0} \nabla [C_{b,i} \exp(\frac{-z_i e \Psi(y)}{k_B T})] - D_{i,0} \frac{z_i e C_{b,i}}{k_B T} \exp(\frac{-z_i e \Psi(y)}{k_B T}) \nabla \Psi \quad (6.15)$$

Assuming the invariance of distributions in the direction  $\mathbf{x}$  (normal to the cross section and parallel to the walls), the longitudinal ionic fluxes  $\mathbf{J}_i$  rewrite as function of the flux in the bulk area  $\mathbf{J}_{b,i}$  as it follows

$$\mathbf{J}_i = \exp\left(\frac{-z_i e \Psi(y)}{k_B T}\right) \mathbf{J}_{b,i} \quad (6.16)$$

With

$$\mathbf{J}_{b,i} = -D_{i,0} \nabla C_{b,i} - D_{i,0} \frac{z_i e C_{b,i}}{k_B T} \nabla \Psi_b \quad (6.17)$$

Where  $\nabla C_{b,i}$  and  $\nabla \psi_b$ , respectively, represent the concentration gradient and the imposed difference of potential between the pore's entry and its exit (in the direction  $\mathbf{x}$ ). As the bulk solution is out of the EDL area, we consider there are no transversal fluxes i.e.  $\mathbf{J}_{b,i} \cdot \mathbf{y} = 0$

By averaging the fluxes in (6.16) over the cross-section of the pore of width  $W$ , we obtain non-dimensional values  $K_i$  that represent the ratios between the ionic fluxes in the EDL and the flux in the bulk area [Fried2008] i.e.

$$\begin{cases} \bar{\mathbf{J}}_i = K_i \mathbf{J}_{b,i} \\ K_i = \frac{1}{W} \int_0^W e^{\frac{-z_i e \Psi(y)}{k_B T}} dy \end{cases} \quad (6.18)$$

In terms of transport, it is usually the diffusion coefficient that we measure to characterize the mobility of an ion. As developed in [Yang2019], the effective ionic diffusivities  $D_{i,e}$  can ultimately be expressed as

$$D_{i,e} = \frac{\int \mathbf{J}_i dS}{S} \cdot \frac{L}{\Delta C_i} \quad (6.19)$$

Where  $\frac{\int \mathbf{J}_i dS}{S}$  is the species flux per unit cross-section in the steady state,  $L$  the medium length and  $\Delta C_i$  the mean concentration difference between the two boundaries of the medium. As a consequence, the ratios  $K_i$  actually represent the net contribution of the surface effects on the ions diffusion such as

$$D_{i,e} = K_i D_{i,b} \quad (6.20)$$

Where  $D_{i,b}$  is the diffusivity in the bulk assumed close to the diffusivity  $D_{i,0}$  in free water (Tab.6.1.) as EDL overlapping is minor in the bulk area.

Species	$D_{i,0}$ ( $10^{-9} \text{ m}^2 \text{ s}^{-1}$ )
$\text{Na}^+$	1.334
$\text{Ca}^{2+}$	0.792
$\text{OH}^-$	5.273
$\text{Cl}^-$	2.032

Table.6.1. Ionic diffusion coefficients in water at infinite dilution at 25°C [Lide1994]

This approach represents a significant simplification from the usually necessary finite element analysis of the Eq.(6.6). Determining the diffusion coefficients as presented in (6.20) also allows to implicitly account for non-ideality effects by using, in (6.16), the electrochemical potential  $\psi^{GCMC}$  obtained from the GCMC simulations rather than of the usual PB solution  $\psi^{PB}$  (ref. Eq.(4.4)). In Monte Carlo simulations, the resulting potential  $\psi^{GCMC}$  is a compound of two effects:

- (i) The electrostatic interactions between the surface and the ions calculated through Coulombic short range potentials.
- (ii) The steric effects of non-ideal solutions which are accounted for by the very nature of the insertion moves in the MC algorithm. The excess chemical potential  $\mu_{ex}$  is the physical quantity that measures, in simple terms, “the packing” of the system at a certain location (ref. chapter 3 section III.B).

To compute  $\psi^{GCMC}$ , the same methodology of the previous chapter (ref. chapter 4 section II.A.) is followed through integration of the modified Poisson equation as presented below:

$$\begin{cases} \Delta \Psi^{GCMC} = -\frac{\rho^{GCMC}}{\epsilon_0 \epsilon_r} \\ \rho^{GCMC} = e N_A \sum_i z_i C_i^{GCMC} \end{cases} \quad (6.21)$$

Despite its mathematical appeal, the previous developments are only rigorously valid under the assumption that ions are in quasi-thermal equilibrium with a Boltzmann-like distribution. As the surface electric potential arises above the thermal voltage  $\psi_T = \frac{k_B T}{z_0 e}$  ( $\sim 25\text{mV}$  for a 1:1 electrolyte at 25°C), the non-linearity in the Poisson-Boltzmann proportionally increases to invalidate the assumptions of an ideal solution. Nonetheless, in the context of studying steric effects in the dynamics of electrolytes submitted to large applied voltages, Bazant et al. [Bazant2004, Kilic2007] discovered what they called a “weakly non-linear regime” of potentials within the interval of 25–200mV, where Boltzmann-like statistics (6.14) remains applicable. In order to remain within the validity scope of the PB equations, the C-S-H surface potential is limited to a value of -92mV

(corresponds to  $-1.2 \text{ e.nm}^{-2}$  which is also a good physical assumption), the concentration to an upper bound of 0.2M and the pH to a value of 13 i.e. NaCl 0.1M + NaOH 0.1M (*ref. chapters 4 and 5*).

Results obtained by this approach will be referred to by the notation MPB (Modified Poisson-Boltzmann) as the method combines MC results of the electrochemical potentials along with the PB formalism.

### III. Results and discussion

In this section, the equations of ionic transport are solved using the two methodologies previously presented. The objective is to quantify the diffusivity of ions through nanoscopic pores as a representation of gel pores in the C-S-H gel. In the first instance, the pore solution is modeled as a simple monovalent salt where  $\text{Na}^+$  is the only counter-ion. Afterward, calcium ions  $\text{Ca}^{2+}$  are added for a better representation of the system and their effects investigated. As the electrical double layer was demonstrated to be very intimately correlated to the characteristics of the pore network, the ionic diffusivities of the present species are computed for different pore radii within the range of gel pores entry sizes i.e. from 16 nm down to 4 nm. In order to assess the sensitivity of the diffusion process to the properties of the C-S-H surface and the surrounding electrolyte, two main parameters are varied through the study:

- (i) The ionization degree of the C-S-H surface
- (ii) The pH of the pore solution at constant surface charge density

In the first set of simulations, the pore solution is approached as a simple NaCl salt. Firstly, the surface charge density, indicative of the ionization degree, is varied and its effects quantified. Then, hydroxides ( $\text{OH}^-$ ) are explicitly accounted for to better fathom the effect of alkalinity on the diffusivity of chloride ions.

In the second part of the section, the resolution is extended to the case of the pore solution model that was developed in Chapter 4 section II and the effect of the adsorbed calcium is discussed.

#### A. Transport in symmetric monovalent electrolytes

##### i) Effect of the surface charge density

As developed in the cases of single-wall and slit pore solutions, the ionization degree of the C-S-H surface has been shown to have a sizable effect on the electrostatic properties of the electrolytic solution in saturated pores. The choice of the range of values can cover a wide interval depending on the stoichiometric Calcium to silicon ratio. If the 14 Å tobermorite provides a good model for C-S-H having Ca/Si ratios below 1 with silanol sites densities (SSD) going up to  $4.8 \text{ sites.nm}^{-2}$  [Tay1986, Lab2006, Lab2011], it is not the case when the Ca/Si ratio goes beyond 1. Unfortunately, the C-S-H in real cement paste is usually characterized with Ca/Si ratios above 1.5 for example approaching 2 for OPC and varying between 1.5 and 1.6 for the LC3 blend depending on the calcined kaolinite content [Avet2018]. Very recent studies on the atomistic structure of pure C-SH suggest that the SSD decreases as the Ca/Si ratio increases to reach values around 0.9 to  $1.2 \text{ sites.nm}^{-2}$  for calcium to silicon ratios, respectively, between 2 and 1.75. Hence, we will fix the value of  $-1.2 \text{ e.nm}^{-2}$  as an absolute maximum for the range of values that will be chosen for the simulations. From a modelling point of view, it will also be showed that, within the defined range of values, we will remain within

the “weakly non-linear regime” of low voltages where the assumptions of the Poisson-Boltzmann theory remain acceptable.

The simulated system is a NaCl solution of 0.1M confined in a C-S-H slit pore with surfaces of charge densities varying between  $-0.12$  and  $-1.2$   $\text{e.nm}^{-2}$ . For the sake of comparison, the resolution of the transport equation is conducted in the ideal and non-ideals cases, respectively, using the approaches explained in sections II.A and II.B.

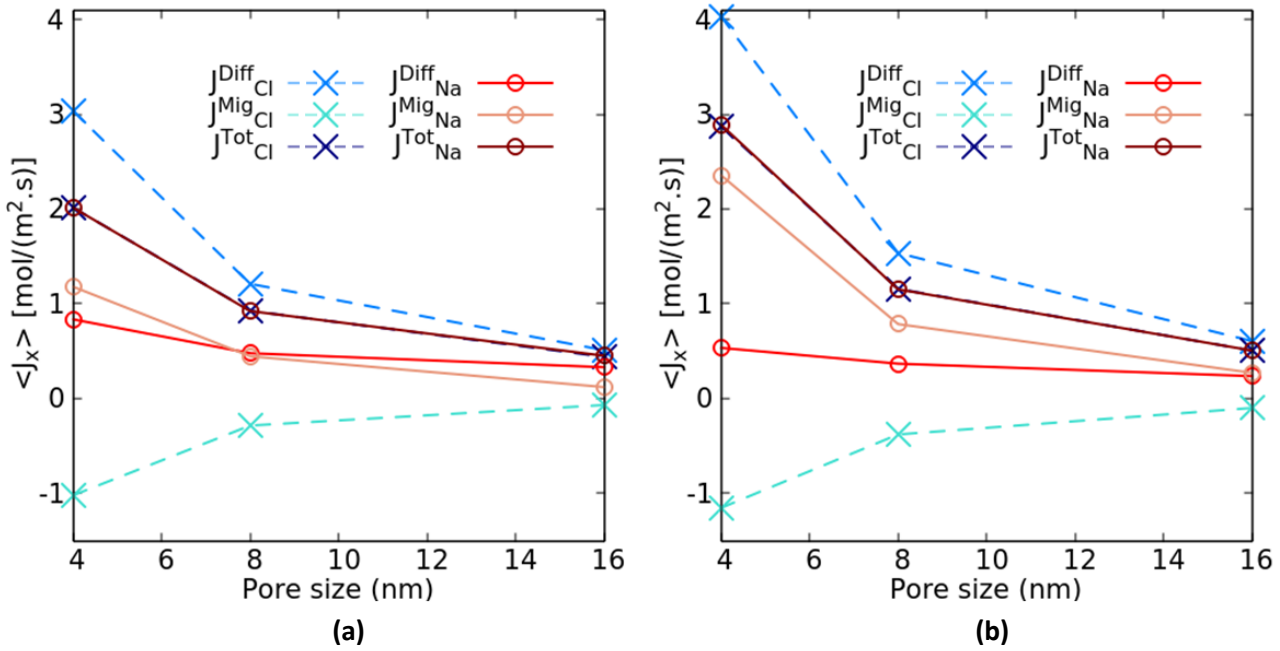


Fig.6.2. Evolution of the average  $x$ -component of ionic fluxes (diffusive, electrophoretic (migration) and total) of sodium  $\text{Na}^+$  and chloride  $\text{Cl}^-$  in a 0.1M NaCl pore solution as function of the pore size around C-S-H surfaces of charge densities  $\sigma_{\text{C-S-H}}$  equal to (a)  $-0.24$  and (b)  $-0.48$   $\text{e.nm}^{-2}$ .

In Fig.6.2.(a), one can see that for a fixed surface charge density equal to  $-0.24$   $\text{e.nm}^{-2}$ , the longitudinal  $x$ -component of the total flux, for both sodium and chloride ions, is increasing in average as the pore size is reducing. This is mainly due to the increase of the diffusive flux  $\langle J_x^{\text{Diff}} \rangle$  resulting from the matter diffusion term  $\nabla a_i$  at the edges of the channel (which usually simplifies to  $\nabla C_i$  (Eq.(6.9)) for the case of moderately concentrated solutions). Concerning the electrophoretic (or migration) term, it seems that although the value of the flux  $\langle J_x^{\text{Mig}} \rangle$  increases in absolute value for both species, its contribution to the total flux depends on the charge of the considered ion. In fact, while the sodium migration flux  $\langle J_{x,\text{Na}}^{\text{Mig}} \rangle$  is oriented in the  $x$  direction (positive) pushing the  $\text{Na}^+$  ions toward the outlet, the chloride flux  $\langle J_{x,\text{Cl}}^{\text{Mig}} \rangle$  grows more and more negative for smaller pores hence impeding its progression in the same direction. Nonetheless, we see that, in accordance with the law of charge conservation (Eq.(6.7)), the total fluxes of chloride and sodium are equal i.e.  $\langle J_{x,\text{Na}}^{\text{Tot}} \rangle = \langle J_{x,\text{Cl}}^{\text{Tot}} \rangle$  which translates into a flux of charge  $\langle J_{x,\text{Na}}^{\text{Tot}} - J_{x,\text{Cl}}^{\text{Tot}} \rangle$  equal to zero, thus ensuring the electroneutrality of the system. In the case of  $\sigma_{\text{C-S-H}} = -0.48$   $\text{e.nm}^{-2}$  (Fig.6.2.(b)), all the trends are conserved although enhanced due to the higher surface charge density of the C-S-H.



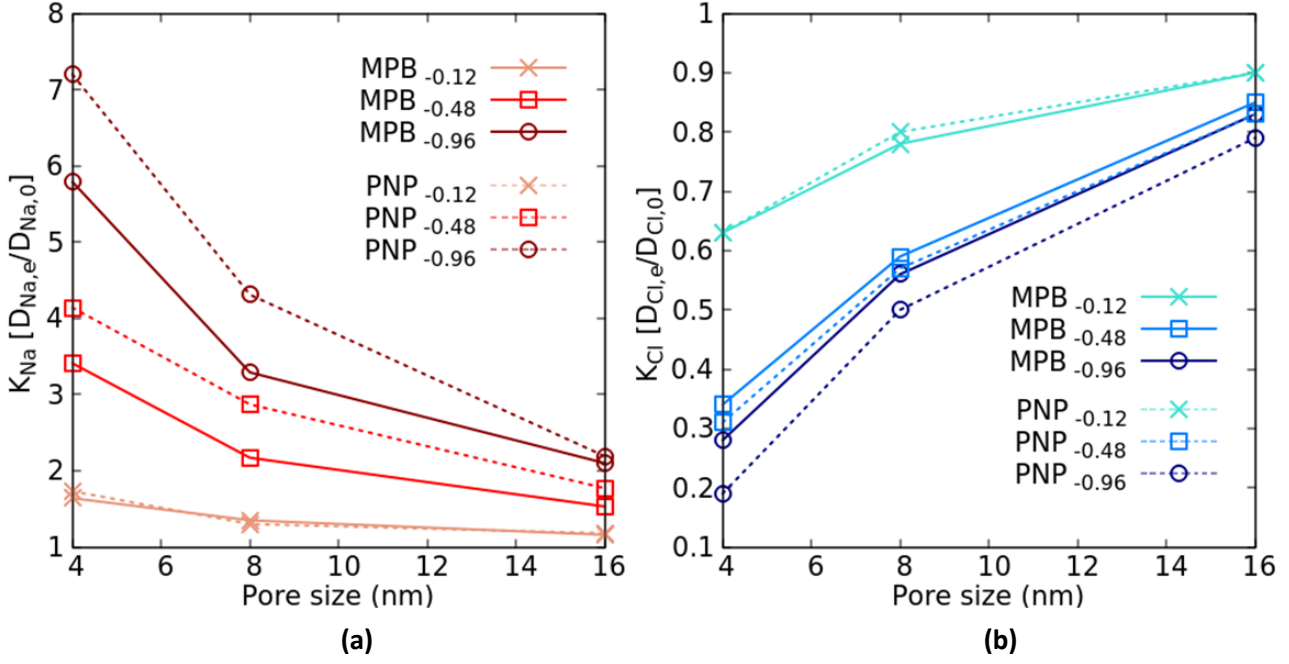


Fig.6.3. Normalized diffusivity of **(a)** sodium  $\text{Na}^+$  and **(b)** chloride  $\text{Cl}^-$  in a 0.1M NaCl pore solution as function of the pore size around C-S-H surfaces of charge densities  $\sigma_{\text{C-S-H}}$  equal to -0.12, -0.48 and -0.96  $\text{e.nm}^{-2}$ . PNP calculations represent results for the ideal case and MPB computations account for non-ideality of the solution.

In a global view, we see in Fig.6.3 that, for a negatively charged C-S-H surface, the diffusivity of  $\text{Na}^+$  is boosted (Fig.6.3.(a)) while the flux of  $\text{Cl}^-$  is diminished (Fig.6.3.(b)). This stems from the fluxes expression in (6.16) where, with respect to bulk fluxes, the counter-ions current is enhanced ( $\frac{-zie\psi}{k_B T} > 0$ ) while co-ions are slowed down ( $\frac{-zie\psi}{k_B T} < 0$ ). This trend is retrieved for both PNP and MPB resolutions. Also both methods are in very good agreement at low surface charge density i.e.  $\sigma = -0.12 \text{ e.nm}^{-2}$ . As the surface charge density is rising, the assumption of non-ideality breaks down as one gets closer to the surfaces. In that regard, and due to neglecting ionic sizes or ion-ion correlations, the classical PNP underestimates the screening of the surfaces and results in pores which are seemingly more negatively charged. As a consequence, the diffusivity of chloride is further lowered (Fig.6.3.(b)) while the flux of sodium is increasingly overestimated (Fig.6.3.(a)). As the pore size reduces, the EDLs gradually overlap, the diffuse layers cover the integrality of the pore space and the effect of the surface on the solution is increased i.e.  $\text{Na}^+$  diffuse even faster (Fig.6.3.(a)) and chloride slower (Fig.6.3.(b)). It is when the deprotonation degree of C-S-H is at its highest that the chloride diffusion is most mitigated. In fact, at  $\sigma$  equal to  $-0.96 \text{ e.nm}^{-2}$ , the MPB solution (Fig.6.3.(b)) predicts that while the chloride anions diffuse at 83% of their bulk flux in the 16nm pore, the ratio  $K_{\text{Cl}}$  progressively decreases and falls to a value of 0.28 for a pore width of 4nm (MPB). The only porosity parameter that was accounted for was, indeed, the pore size. And without consideration of any further properties of the pore network (such as the tortuosity of the path or the connectivity of the pores), it is found that solely the ion-surface electric interactions reduced the effective diffusion coefficient of chloride by up to a factor of 3.

In this case where the concentration was kept at a value of 0.1M, it is important to stress that the thickness of the EDL was unchanged for the whole range of ionization degrees. In fact, both PB and

MC computations (*ref. chapter 4*) estimate the thickness of the EDL to be around 5 nm. Hence, the drop of chloride diffusivity, in the above configuration, is uniquely due to the increasingly more negative average potential of the pore; the latter being, here, only function of the pore radius and the magnitude of the surface potential.

Another point of interest is actually the rate at which the diffusivity of chloride is decreasing as the pore reduces. At fixed surface charge of  $-0.96 \text{ e.nm}^{-2}$ , one can notice (Fig.6.3.(b)) that by reducing the pore width by moving from 16 to 8 nm, the normalized diffusivity falls from 0.83 down to 0.56 i.e. a decrease of 33%. In the interval of pore sizes  $>10\text{nm}$ , we have previously showed (*ref. chapter 4*) that, given the weak overlapping of the EDLs, the surface effects are of relatively small importance (depending on the surface charge density). As the pore radius falls below the EDL thickness, the decrease rate almost doubles once passing from a pore of 8 to 4nm, with  $K_{Cl}$  going from 0.56 to 0.28 i.e. a factor of 2.

From an experimental perspective, it is very hard to isolate surface effects when measuring the diffusion coefficient of ionic species. In cement science, the standardized approach to evaluate the mobility of ions is to compute apparent diffusion coefficients. These empirical diffusivities (*ref. chapter 2 section III*) can be seen as the averaged contribution of a number of microstructure parameters including adsorption phenomena. In the case of blended systems, recent studies on LC3 cements have showed that there was no obvious correlation between the apparent diffusivity of chloride and the binding capacity of C-S-H [Maraghechi2018]. However, Sui et al. [Sui2019(2)] found that the apparent diffusion coefficient increased with the alkali ions content (namely sodium  $\text{Na}^+$  and potassium  $\text{K}^+$ ) in the pore solution (*ref. Fig.2.7*) of binary and ternary blends. In the next section, we investigate the effects of ionic strength on the effective diffusivity of present species.

## ii) Effect of the ionic strength

### • Effect of the concentration

In the study of the electrostatic properties of confined pore solutions in slit pores, it was shown how the increase of the ionic concentration resulted in the decrease of the average electrochemical potential of the pore (*ref. chapter 4 section II.C*). This has been attributed to the increase of the screening capacity of the counter-ions to shield the negative surface along with the decrease of the thickness of the electrical double layer as the ionic strength increased. In order to measure the implication of these effects as function of the ionic molarity, we assume that the ionization degree of the C-S-H does not change with respect to the concentration of chloride in the pore solution. The surface charge density is set at a moderate value of  $-0.24 \text{ e.nm}^{-2}$ . The concentration of the pore solution modelled as a symmetric NaCl salt is varied from 0.1M to 0.5M (roughly the average concentration of chloride in seawater). The evolution of the normalized effective diffusivity as function of the pore size is represented in Fig.6.4 for the present sodium (Fig.6.4.(a)) and chloride (Fig.6.4.(b)) species.

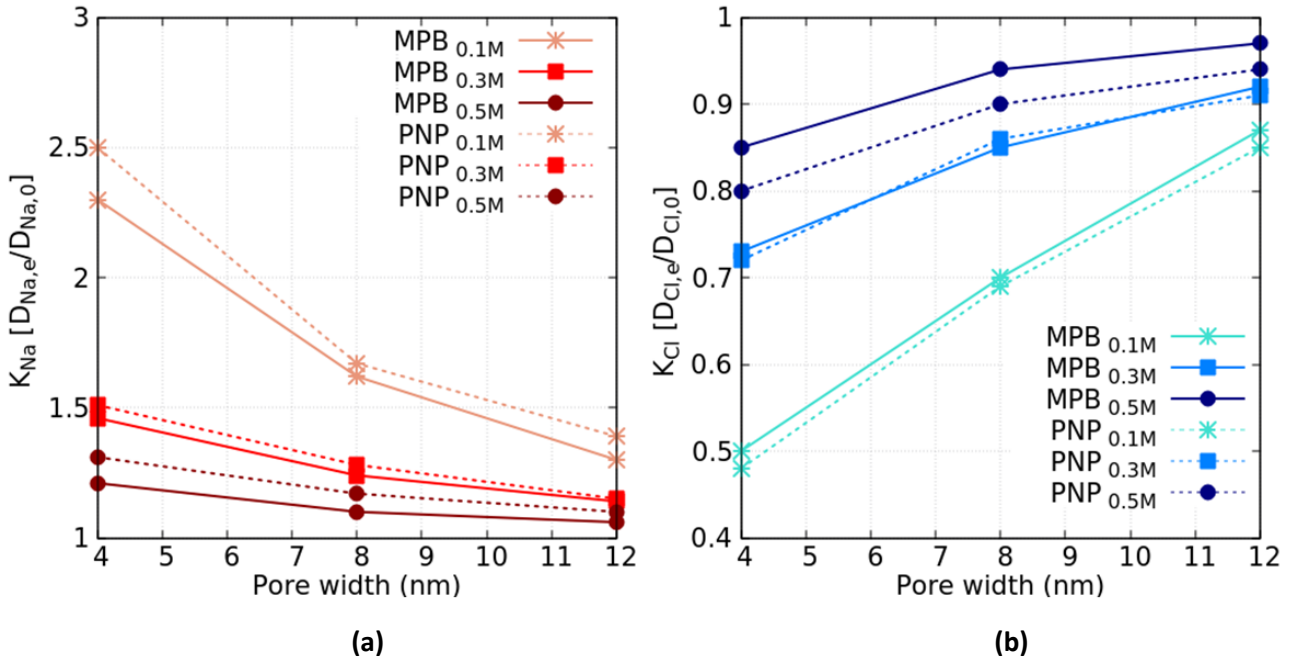


Fig.6.4. Normalized diffusivity of **(a)** sodium  $\text{Na}^+$  and **(b)** chloride  $\text{Cl}^-$  as function of the pore size in NaCl solutions of concentrations 0.1M, 0.3M and 0.5M around C-S-H surfaces of charge density equal to  $-0.24 \text{ e.nm}^{-2}$ . PNP calculations represent results for the ideal case and MPB computations account for non-ideality of the solution.

As steric effects and ionic sizes are neglected, the PNP overestimates the diffusivity of sodium (Fig.6.4.(a)) and, equivalently, underestimates the chloride effective diffusivity (Fig.6.4.(b)). This is most noticeable in the case of highest concentration i.e. 0.5 M. As the concentration is increasing, the negative potential of the pore decreases in absolute value (*ref. chapter 4 section II.C*). Hence, the general trend in which sodium is transiting faster than chloride is maintained. It is, however, noticeably mitigated as the concentration is building up. In the high concentration case (0.5 M), MC computations of the electrostatic profile (*ref. chapter 4 section II.C*) reveal that the bulk area is retrieved within 1 nm distance off the surfaces i.e. high screening and very short Debye length. At such ionic strength, the overlapping of the EDLs does not occur and the surfaces predominantly interact with the nearby ions which are mainly sodium cations. As a result, the diffusion coefficient of chloride does not fall below 85% of its bulk value even within the smallest pores i.e. at 0.5M in a 4nm pore (MPB in Fig.6.4.(b)). In real cementitious structures, once the concentration of chloride reaches such a deleterious amount, it usually accompanied by a depassivation of the steel and a start of the corrosion reaction. Nonetheless, the correlation between pH and transport or binding is not an obvious one. Indeed, De Weerd et al. have shown in [DeWeerd2015] that within a certain interval of values, normally beyond 12, the decrease of the alkalinity could result in an enhanced binding capacity of the hydrates and, hence, a better resistance to chloride diffusion. The relationship between pH (at constant surface potential) and diffusion is studied in the following section.

- Effect of pH at constant surface charge density

The values of pH along with the chloride content at the vicinity of reinforcement steel rebars are key parameters in the initiation of corrosion reactions. And if alkalinity is one of the important characteristics of the pore solution of cement paste, it also has great influence on the surface properties of the formed hydrates and particularly C-S-H.

In the optic of comparing the chloride resistivity of different cement blends, the experimental studies are typically conducted at high pH (for example at pH=13.3 with NaOH = 0.3M in [Wilson2021]). Within this range of pH values ( $>13$ ), we assume silanols ionization to have reached a saturation degree and that, consequently, the surface charge density remains constant. In order to isolate the effect of pH, we set a low value of the C-S-H surface charge density fixed at  $-0.24 \text{ e.nm}^{-2}$ . The numerical resolution of the transport equations is twofold. Firstly, we resolve the classical PNP equation under the assumptions of an ideal pore solution. Then, the steric effects are included and the transport problem is resolved using the MPB formalism. For the latter resolution method, the pH is explicitly accounted for by modelling the pore solution as a {NaCl 0.1M + NaOH} electrolyte. To cover a reasonable range of experimental values, the pH is set at values of 13, 13.3 and 13.5 which approximately correspond to NaOH of concentrations, respectively, 0.1, 0.2 and 0.3M. In the case of the PNP resolution, the pH is implicit and as the model depicts ions as point charges only characterized by their valences, there is no difference between chloride and hydroxide ions in terms of ion-ion interactions. However, the mean concentration difference of  $\text{OH}^-$  between the pore boundaries is set to zero (i.e.  $C_{\text{OH}}^{\text{inlet}} = C_{\text{OH}}^{\text{outlet}} = C_{\text{OH}}^{\text{bulk}}$ ), while the concentration gradient for chloride and sodium at the boundaries of the pore is implemented as explained in section II.A.(ii).

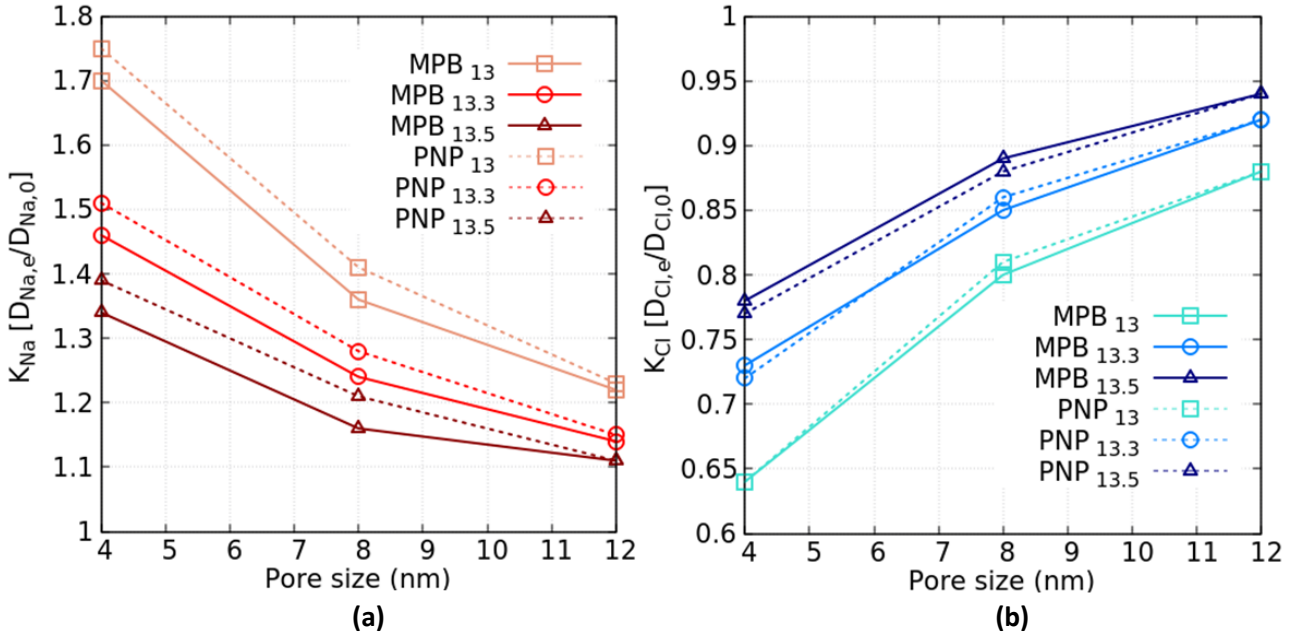


Fig.6.5. Normalized diffusivity of (a) sodium  $\text{Na}^+$  and (b) chloride  $\text{Cl}^-$  as function of the pore size in NaCl solutions of pH values at 13, 13.3 and 13.5 around C-S-H surfaces of charge density equal to  $-0.24 \text{ e.nm}^{-2}$ . PNP calculations represent results for the ideal case and MPB computations account for non-ideality of the solution.

As expected, one can see that due to the negative surface potential of C-S-H, the chloride (Fig.6.5.(b)) diffuses more slowly in the EDL than in the bulk area while it is the opposite for sodium (Fig.6.5.(a)).

The PNP solution overestimates the diffusivity of sodium due to the underestimation of the surface screening and neglecting the intermolecular ion pairs correlations. For chloride (Fig.6.5.(b)), it appears that the decrease of pH attenuates the flux of chlorides. These results are in good agreement with MC predictions of the EDL formation (*ref. chapter 4 section II.D*) where the increase of pH, at constant surface charge density  $\sigma$ , had a very similar effect to the increase of ionic strength i.e. enhanced screening of the surface along with a reduction of the Debye length and a shortening of the diffuse layer thickness. Additionally, it is interesting to note that the mismatch between the PNP and the MPB in Fig.6.5.(b), although relatively small, does not follow an obvious pattern. In fact, at a pH of 13, the diffusivity of chloride from MPB is initially lower than its PNP homologue. As the hydroxyl content increases to 0.3M (pH =13.5), it seems that this is reversed and it is the PNP values that rather fall below the Monte Carlo predictions. This is partly due to the difference in the force fields between chloride and hydroxide ions in the MC computations. Another reason for that is probably the increasing competition of the enhanced presence of hydroxide ions with chlorides for the adsorption on the limited number of available ionized sites. As a matter of fact, that would not only explain, in part, the mismatch of the two solutions but also the general tendency of the binding capacity of C-S-H to fall at higher pH values [Plus2016, Tri1989].

### iii) First conclusions: The nanoscopic diffusion of chloride in monovalent systems

The surface effects that generate the EDL structure around C-S-H have a sizable effect on ionic transport. The magnitude of these effects is measured through the normalized diffusion coefficient i.e.  $K_{counter}$  for the counter-ions ( $\text{Na}^+$ ) and  $K_{co}$  for the co-ions (essentially  $\text{Cl}^-$ ). The negative electrical potential of the pore translated in an attenuation of the chloride flux ( $K_{Cl} < 1$ ) and an amplification of that of  $\text{Na}^+$  ( $K_{Na} > 1$ ). As the EDL overlapped stronger within smaller pores, the disruption of the local electroneutrality of the pores resulted in a disappearance of the bulk area and an overall increase of the negativity of the pore, hence, an increase of  $K_{Na}$  and a reduction of  $K_{Cl}$ .

Through the investigation of a wide range of system-related parameters, it was equally shown that, along with the pore size, the ionization degree of the C-S-H and the ionic strength of the solution greatly influenced the diffusivity of ions. The increase of the surface charge density was found to significantly alter the ideality of the electrolyte especially at the interface. It resulted in stronger correlations between the ionized silanols and the adsorbed sodium which indirectly reduced the chloride mobility. On the other hand, the increase of the ionic concentration favored a higher screening of the negatively charged surface which, in turn, decreased the Debye length and with it the extent of the diffuse layer. At a constant surface charge density, it also appeared that the lowering of the system alkalinity hindered chloride diffusion. Experimental work on the effects of the pH drop showed that with a lower presence of hydroxides, chloride binding was less inhibited by the competition of  $\text{OH}^-$ . That not only resulted in an enhanced binding capacity of the hydrates but, eventually, to an improved chloride resistance of the cement sample.

In cement science, one can actually speak of the semi-permeable character of cementitious materials with respect to the ionic flows [Goto1981]. As the connectivity of the capillary pores is assured by nanopores, the C-S-H gel pores (<10nm) appear to form a major obstacle to chloride ingress. Still, the pore network remains one factor that does not explain all the aspects of the EDL phenomenon. In fact, the sensitivity study conducted has proved that, the pore solution, as much as the surface deprotonation plays a part. Given the remaining knowledge gap on C-S-H interfaces, it was chosen to model the surface as simply as possible i.e. a 2D wall with an implicit homogeneous surface charge

density. It is, however, possible to reach a better understanding of the role the pore solution plays in chloride diffusion by including  $\text{Ca}^{2+}$  ions in the simulation box.

## B. Transport in a more realistic model of the cement paste

In this section, the equations of ionic transport are resolved by accounting for Ca in the system. Given the low solubility of  $\text{Ca}^{2+}$  at high pHs ( $> 12.5$ ), the presence of calcium in the pore solution is negligible. Hence,  $\text{Ca}^{2+}$  ions are only considered as adsorbed species on C-S-H. See *section III in previous chapter for further detail*. To measure the effect of the Ca content on the ionic transport, C-S-H surfaces with various ratios of adsorbed  $\text{Ca}^{2+}$  are considered.

### i) Ca-adsorbed surfaces

- Validity of the transport model

Following the developments on the Ca adsorption on ionized C-S-H surfaces (*ref. chapter 5*), Monte Carlo simulations showed that, in presence of  $\text{Na}^+$  ions, it was possible to reach a Calcium-Silanols occupancy ratio of 50% while keeping  $\text{Ca}^{2+}$  concentration in the bulk at under saturation i.e. without precipitation of portlandite ( $\text{Ca}(\text{OH})_2$ ). Beyond a ratio of 50%, it was found that, without a speciation model where chemical reactions were accounted for, the  $\text{Ca}^{2+}$  concentration in the pore solution continued to build up and simulations failed to generate realistic configurations that respected the thermodynamics of the real system. So to best model the problem of chloride ingress in real cement paste, we will restrain Ca content to the case where Ca-Si occupancy varied between 0% and 50%. As a reminder, a ratio of 0% means that no adsorbed sodium is replaced i.e. almost 100% of adsorbed counter-ions on C-S-H are  $\text{Na}^+$  ions. The other cases represent the situation where 25% and 50% of the adsorbed  $\text{Na}^+$  are replaced by  $\text{Ca}^{2+}$  while keeping the charge constant (*ref. chapter 5 section III*).

In practice, the absence of  $\text{Ca}^{2+}$  in the bulk area and forbidding its accumulation in the diffuse layer means an exclusive presence of monovalent ions in the solution. Within the considered range of concentrations ( $< 0.2\text{M}$ ) and moderate ionization degrees ( $|\sigma_{\text{C-S-H}}| < 1.2 \text{ e.nm}^{-2}$  equivalent to a surface potentials below 92 mV at pH of 13 (*ref. chapter 5 section III*)), one can assume, also according to developments by Bazant et al. [Bazant2004, Kilic2007], that assumptions of ideality remain reasonably valid. Hence, the use of Boltzmann-like distributions in the resolution of the transport problem (*ref. section II.B*).

As a first step, we compare results of ionic diffusivities calculated through the two implemented methods i.e. (i) the PNP equation and (ii) the MPB with an increasing  $\text{Ca}^{2+}$  content. With respect to the thermodynamic data on real pore solutions (*ref. chapter 5 section II*), the solution is modeled as a  $\{\text{NaCl } 98\text{mM} + \text{CaCl}_2 \text{ 1mM} + \text{NaOH } 0.1\text{M}\}$ . The pH is equal to 13. The surface charge density is set at a value of  $-1.2 \text{ e.nm}^{-2}$  (100% ionization degree). As  $\text{Ca}^{2+}$  is essentially adsorbed, chloride and sodium are assumed to be the main diffusing species. The boundary value problem is accordingly defined following the steps in *section II.A*.



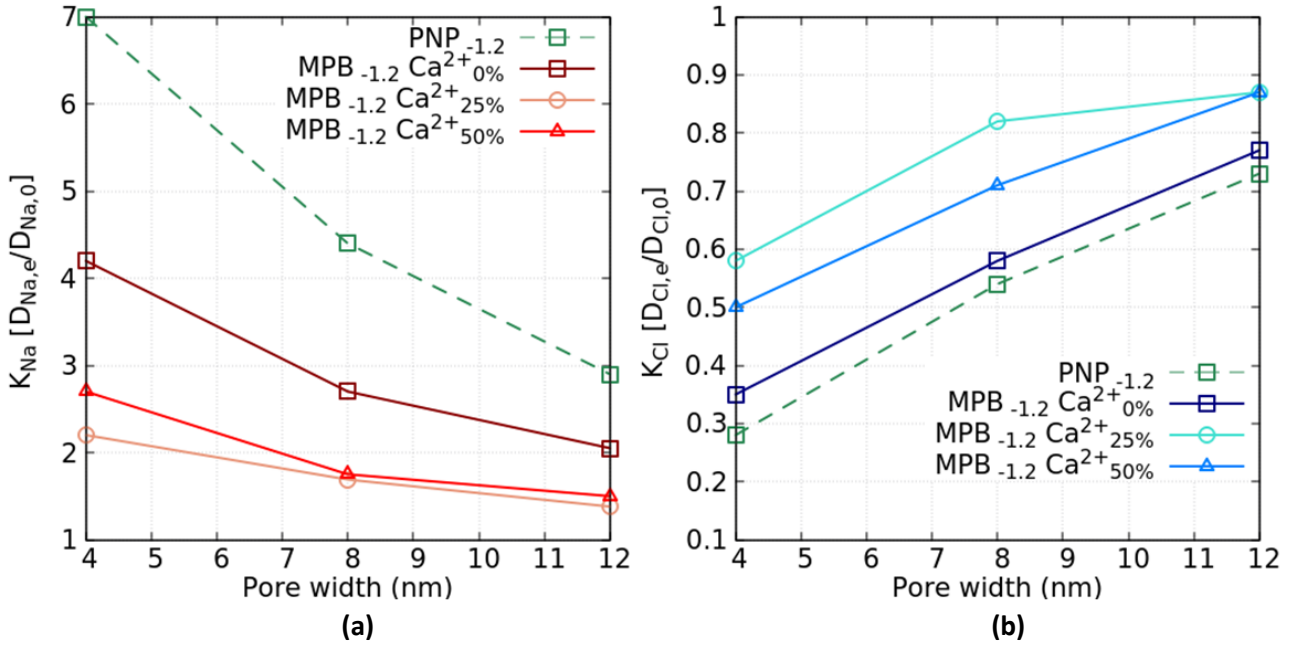


Fig.6.6. Normalized diffusivity of **(a)** sodium  $\text{Na}^+$  and **(b)** chloride  $\text{Cl}^-$  as function of the pore size. The pore solution is modeled as a  $\{\text{NaCl } 98\text{mM} + \text{CaCl}_2 \text{ 1mM} + \text{NaOH } 0.1\text{M}\}$  with a pH of 13. The surface charge density of C-S-H ( $\sigma_{\text{C-S-H}}$ ) is set at  $-1.2 \text{ e.nm}^{-2}$ . PNP calculations represent results for the ideal case and MPB computations account for non-ideality of the solution at charge replacement ratios of 0, 25 and 50%.

For the case where no replacement of  $\text{Na}^+$  (Ca 0%) is considered, the PNP (green squares) seems to overestimate sodium mobility (Fig.6.6.(a)) and underestimate chloride's diffusion (Fig.6.6.(b)) in comparison with the MPB (respectively dark red squares (Fig.6.6.(a)) and dark blue squares (Fig.6.6.(b)) ). This behavior was previously witnessed in the Na-systems. Yang et al. [Yang2019] have also noted the same error once completely neglecting steric effects at the surface. The authors have implemented a non-ideal version of the PNP accounting for the chemical potential as a main driving force for diffusion. The numerical resolution through the Lattice-Boltzmann method showed the general tendency of the classical PNP to deviate from atomistic computations. However, the results in the paper rather predicted an increase of the diffusivity of chloride and a decrease in sodium mobility for pore ranges between 10 and 4 nm i.e. the opposite of Fig.6.6. This divergence in the results may be due to the fact that Yang et al. did not only include a porosity factor in their computation but also did not (at least not explicitly) account for the undersaturation limit of  $\text{Ca}^{2+}$ . As it was shown in *chapter 5 section III*, the accumulation of  $\text{Ca}^{2+}$  in the diffusion layer is a contributing factor for the reversal of charge at the C-S-H surface and the decrease of the pore negativity.

Considering now the case of Ca adsorption on the C-S-H, one can note, in Fig.6.6.(b), that passing from 25% (turquoise circles) to 50% (blue triangles) calcium occupancy of the ionized silanols results in a reduction of chloride diffusivity. As a matter of fact, the EDL study (*ref. chapter 5*) showed that a high Ca adsorption along with a low bulk molarity (typically below the necessary concentration for the potential shift to occur) leads to an increase of the negativity of the potential average of the pore. In perspective with experimental work on different cement samples, it has been shown that the ordinary Portland cement (OPC) has a higher chloride binding in its C-S-H compared to LC3 cements. A major difference between the two pastes is the Ca/Si ratio (indicative of both Ca content and the Silanols site density (SSD)) which approaches 2 for OPC and varies between 1.5 and 1.75 for

LC3 [Avet2018]. This difference in the measured amount of physically bound chloride does not, however, explain the lower chloride diffusive fluxes in LC3 compared to OPC. MIP (Mercury intrusion porosimetry) measurements indicate that the pore size distribution in the LC3 is significantly more refined than the OPC reference [Maraghechi2018]. The connected porosity in LC3 is predominantly constituted of pores of around 3 to 5 nm while in OPC (and LC3 with low kaolinite content) the size is more around 10nm. In a parallel representation, chloride diffusion in Fig.6.6.(b) appears to be further affected by the pore size as the diffusivity at a substitution ratio of 25% in a 4nm-pore remains lower than at a higher adsorption (50%) in a larger pore (8nm for example). However, as mentioned, the difference in Ca/Si of the C-S-H does also impact the SSD and, eventually, the ionization degree of the silanol groups. In the next section, the effect of the surface charge density is investigated in presence of Ca. For the rest of the chapter, we will essentially consider results from the MPB given its versatility with respect to the Ca content.

- Effect of the surface charge density

In this part, we choose to keep the pore solution unchanged i.e. a {NaCl 98mM + CaCl<sub>2</sub> 1mM + NaOH 0.1M} solution with a pH equal to 13. Only the C-S-H surface is modified and the surface charge density is varied between -0.48 and -1.2 e.nm<sup>-2</sup>. In the context of comparing transport in different blended systems, the simulations approach a situation where two distinct surfaces (with different SSD), at the same ionization degree, develop surface charges of different magnitudes.

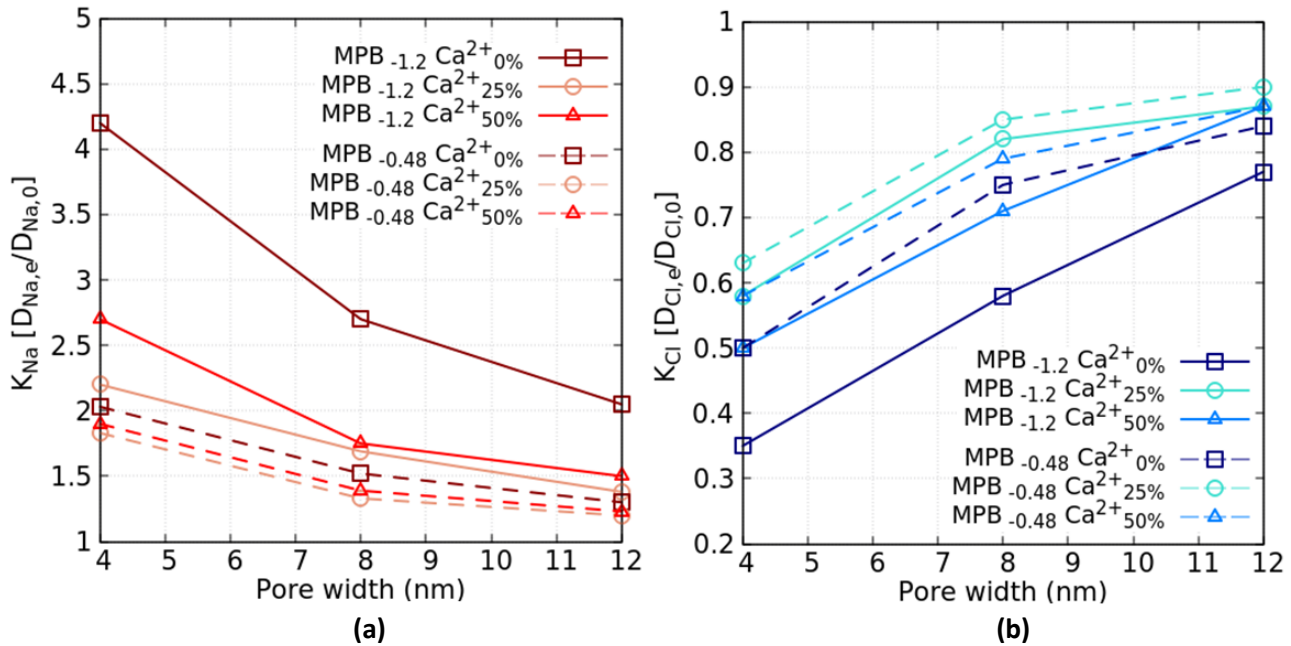


Fig.6.7. Normalized diffusivity of (a) sodium Na<sup>+</sup> and (b) chloride Cl<sup>-</sup> as function of the pore size. The pore solution is modeled as a {NaCl 98mM + CaCl<sub>2</sub> 1mM + NaOH 0.1M} with a pH of 13. The effect of the surface charge density of C-S-H ( $\sigma_{C-S-H}$ ) is investigated and varied between -0.48 and -1.2 e.nm<sup>-2</sup>. MPB computations account for non-ideality of the solution at charge replacement ratios of 0%, 25% and 50%.



Focusing on chloride ions (Fig. 6.7.(b)), one can see that, for a given  $\text{Ca}^{2+}$  charge replacement ratio, the increase of the surface charge density, from  $-0.48$  to  $-1.2 \text{ e.nm}^{-2}$ , systematically resulted in a decrease of the diffusivity of chloride i.e.  $D_{\text{Cl},-1.2} < D_{\text{Cl},-0.48}$ . At a constant surface charge density (for e.g.  $-1.2 \text{ e.nm}^{-2}$ ), a clear hierarchy emerges between the different systems with the Na-system ( $0\% \text{ Ca}^{2+}$ ) showing lower chloride diffusive fluxes than the “Ca-doped” cases. This is mainly due to the lower screening of the negative surface in the absence of Ca in the system (squares). Less obviously, the increase in  $\text{Ca}^{2+}$  adsorption, from  $25\%$  to  $50\%$ , led to the decrease of chloride diffusion. In fact, the increased Ca occupancy of the  $\text{Si-O}^-$  sites does result in a higher screening of the surface charge. However, the substitution of a portion of the neutralizing  $\text{Na}^+$  at the surface by  $\text{Ca}^{2+}$  was found (*ref. chapter 5 section III.A*) to move part of the sodium from the bulk to “preferentially” accumulate in the diffuse layer. The consequence was a decrease of the  $\text{Na}^+$  bulk molarity and, hence, of the ionic strength of the solution. The computation of the electrochemical potential (*ref. chapter 5 section III.A Fig. 5.6*) revealed that the average potential of the pore increased in negativity. In other words, the ionic strength of the solution decreased faster (with the migration of  $\text{Na}^+$  toward the surface) than the surface screening was increasing due to the higher amount of adsorbed Ca. This behavior was, however, only observed within the range of replacement ratios between  $25\%$  and  $50\%$  where no reversal of charge was noted. At a lower surface charge ( $-0.48 \text{ e.nm}^{-2}$ ), the trend is conserved with the same ranking of the systems in terms of chloride resistance. Still, the interactions between the surface and the ions have weakened which sizably diminished steric effects at the interface. Also, given the lower number of ionized silanol sites at the surface, the number of added  $\text{Ca}^{2+}$ , for a same substitution ratio, was significantly lower than for the  $-1.2 \text{ e.nm}^{-2}$  case. In sum, the lower addition of  $\text{Ca}^{2+}$  reflected less on the ideality of the solution which explains a smaller deviation between the cases of  $0\%$ ,  $25\%$  and  $50\% \text{ Ca}^{2+}$  ratios for the weaker surface charge ( $-0.48$ ).

- Effect of the pH at constant surface charge density

In the context of studying the EDL formation and its effects on ionic transport, it has been shown that the increase of pH at a constant surface charge density had a very similar effect than concentration (*ref. section III.A.(ii)*). Hence, we will limit our investigation to the effect of pH as a major indicator of the ionic strength of the solution. The  $\text{Ca}^{2+}$  solubility was also found to be a direct function of the concentration of hydroxides. Hydroxide ions are, in fact, the explicit manifestation of the solution alkalinity and they showed an affinity, at high pH, to form covalent bonds with  $\text{Ca}^{2+}$  and precipitate into calcium hydroxide (portlandite). MC simulations have provided valuable insight on the EDL structure in Ca environments but their applicability to describe realistic systems showed to be of a limited scope in the absence of a speciation model. In order to extent the validity of atomistic results, it was chosen to study the decrease of pH on ionic transport. As the solubility of  $\text{Ca}^{2+}$  increases with the pH drop, the precipitation threshold of  $\text{Ca(OH)}_2$  is increased and a higher  $\text{Ca}^{2+}$  concentration in the solution is realistically possible.

For a pH value of  $12.7$ , it was determined that the limiting  $\text{Ca}^{2+}$  molarity in solution increased to  $2.5\text{mM}$  compared to  $1\text{mM}$  for pH equal to  $13$  (*ref. Tab. 5.1*). The pore solution is, hence, modeled as  $\{\text{NaCl } 95\text{mM} + \text{CaCl}_2 \text{ } 2.5\text{mM} + \text{NaOH } 50\text{mM}\}$ . The surface charge density is fixed at  $-1.2 \text{ e.nm}^{-2}$ .

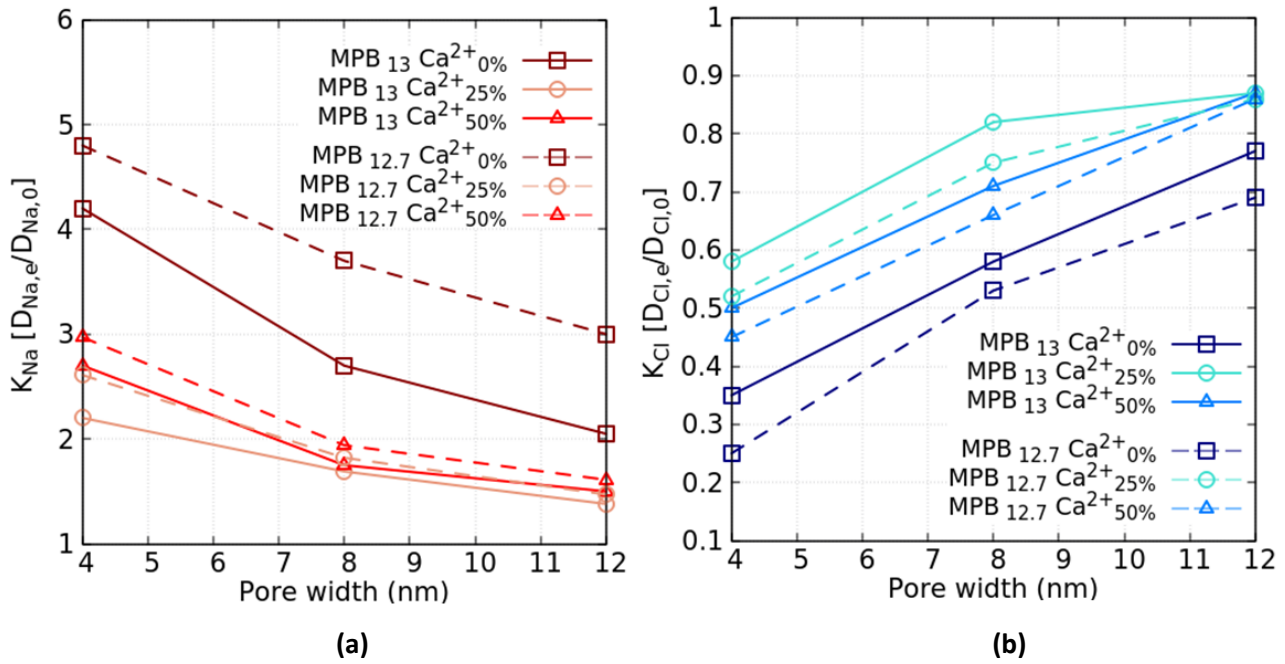


Fig.6.8. Normalized diffusivity of (a) sodium  $\text{Na}^+$  and (b) chloride  $\text{Cl}^-$  as function of the pore size. The pore solution is modeled as a  $\{\text{NaCl} + \text{CaCl}_2 + \text{NaOH}\}$ . The effect of pH is investigated and, hence, varied between 12.7 and 13. The surface charge density of C-S-H ( $\sigma_{\text{C-S-H}}$ ) is set at  $-1.2 \text{ e.nm}^{-2}$ . MPB computations account for non-ideality of the solution at charge replacement ratios of 0, 25 and 50%.

Obviously, a decrease in pH means, in our case, a lower ionic strength of the electrolyte. It also means an increase of the EDL thickness and a stronger overlapping of the diffuse layers in smaller pores which showed, for both Na-systems and Ca-adsorbed surfaces, a rise in the negativity of the electrochemical potential of the pore. The most noticeable case is, as expected, the pore of 4 nm. At a substitution ratio of 0% (squares in Fig.6.8.(b)), the decrease of pH from 13 to 12.7 resulted in a drop of the normalized diffusivity  $K_{\text{Cl}}$  from 0.36 to 0.25 i.e. by factors of, respectively, 1/3 and 1/4. Upon the adsorption of Ca, the interface/solution correlation is hindered due to the screening. However, the increasing amount of adsorption between 25 % (circles) and 50 % (triangles) mitigates the effect of the screening with a higher binding capacity through stronger interactions between the adsorbed  $\text{Ca}^{2+}$  and the migrating  $\text{Cl}^-$  in the diffuse layer. These  $\text{Ca}^{2+}\text{-Cl}^-$  pair interactions appear to be equally boosted by the decrease of pH.

In this regard, Machner et al. [Mach2018] have found that, for PC pastes, a moderate leaching of hydroxyle with a pH lowering within a range of 12.2 to 13.2 lead to an increase of the binding capacity. This was explained by (i) a reduced presence of the competing hydroxyls in the diffuse layer of C-S-H and (ii) a slight increase of the Ca/Si. In the case of blended systems, the LC3-50 mix which contains only 50% of clinker (with alkalis) was found to have an excellent chloride resistance (i.e. slower diffusive fluxes), in part, due to its low alkali content [Wilson2021]. In the same paper, Wilson et al. have attempted to correlate the pore solution properties of different blends to diffusivity measurements via mini-migration experiments. It was revealed that not only is there no obvious correlations could be observed but that some measurements actually led to contradictory trends (most likely because geometrical effects are still important). For instance, the increase of the conductivity of pore solution, which is indicative of high ionic concentration, showed a decrease of the measured effective diffusivities while it was expected to promote the ingress of external chlorides due to higher exchange with hydroxide ions (electroneutrality). This not only shows the

challenge that it is to experimentally bridge the atomistic phenomena with their macroscopic manifestation but it equally means the difficulty to validate molecular models.

## ii) Fully Ca-occupied C-S-H surface: case of a positive surface charge density

In the previous chapter (*ref. chapter 5 section III.C*), we also considered the case where the totality of the ionized sites at the interface was occupied solely by  $\text{Ca}^{2+}$  ions. Two types of Ca adsorption were assumed, both leading to the complete reversal of the surface charge density to a positive value. And while in both cases the Ca-Si occupancy was 100%, the tendency of Ca to occupy one or two ionized sites clearly reflected on the magnitude of the surface charge. For an ionized C-S-H surface of surface charge  $-1.2 \text{ e.nm}^{-2}$  (pre-adsorption), we assumed that upon adsorption of calcium, the surface charge density could vary, in theory, from 0 to  $+1.2 \text{ e.nm}^{-2}$ . To measure the effect on chloride diffusivity, we consider two values:  $+0.6 \text{ e.nm}^{-2}$  and  $+1.2 \text{ e.nm}^{-2}$ . The pore solution is once more modeled as a  $\{\text{NaCl } 98\text{mM} + \text{CaCl}_2 \text{ 1mM} + \text{NaOH } 0.1\text{M}\}$  with a pH roughly equal to 13.

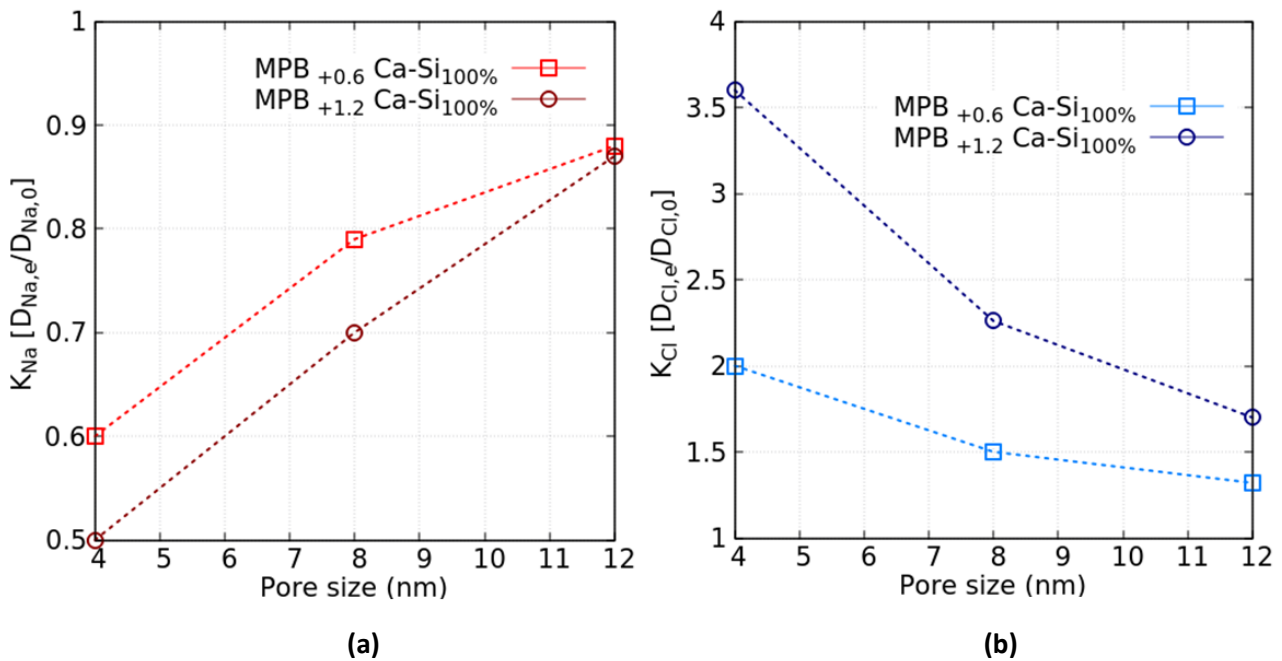


Fig.6.9. Normalized diffusivity of (a) sodium  $\text{Na}^+$  and (b) chloride  $\text{Cl}^-$  as function of the pore size. The pore solution is modeled as a  $\{\text{NaCl } 98\text{mM} + \text{CaCl}_2 \text{ 1mM} + \text{NaOH } 0.1\text{M}\}$ . Due to the high  $\text{Ca}^{2+}$  adsorption, we consider two positive surface charge densities:  $+0.6$  and  $1.2 \text{ e.nm}^{-2}$ . MPB computations account for the non-ideality of the solution.

In Fig.6.9, one can note that the trends previously established for negative surfaces are completely reversed i.e.  $\text{Na}^+$  are slowed down while  $\text{Cl}^-$  are now accelerated. In reality, the positive potential at the surfaces induces a globally positively charged pore which repels co-ions ( $\text{Na}^+$  in this case) from diffusing through the pore while facilitating the passage of counter-ions; this is the consequence of the Donnan effect [Donnan1924]. As expected, the effect is more accentuated when the pore size is smaller and the EDL overlapping. In reality, the acceleration of chloride due to such electrostatic surface effects may presuppose a high binding of calcium the nature of which remains uncertain. Also the zeta potential values that would ensue for considering such positive surface are of the order

of 50 and 90mV, respectively, for +0.6 and +1.2 e.nm<sup>-2</sup> (*ref. chapter 5 section III.C*). These numbers have not been recorded for C-S-H suspensions of Ca/Si>1 where the usual order of magnitude is more around 20mV for pure Ca(OH)<sub>2</sub> titration solutions [Haas2015]. At constant Ca<sup>2+</sup> concentration, Elakneswaran et al. also found that the increase of chloride concentration in the solution decreases the  $\zeta$  value to increasingly more negative values [Elak2009].

### iii) Implications for real cementitious systems

All the previously discussed results have implications for the ionic transport through cementitious materials.

A first outcome from investigating the effects of the pore solution at the interface of ionized C-S-H surfaces is that Ca-containing systems behave very similarly to Na-systems as long as Ca remains adsorbed on the surface and does not accumulate in the solution. The high alkalinity of cement paste acts, in reality, as a sink that prevents Ca content from building up outside of the Stern layer. So in practice, it seems very unlikely that the reversal of charge that usually characterizes divalent electrolytes in Zeta potential measurements occurs. Unlike unconfined C-S-H suspensions, the chemistry of real cementitious systems along with the confinement of the solution within nanometric pores proves to significantly hinder the dominance of the electrolytic effects. No matter how close Na and Ca systems may appear, a clear ranking in terms of chloride resistivity was still noted. Due to the lower screening of the surfaces in monovalent solutions, the more negatively charged pore creates a repulsion barrier that impedes chloride diffusion. This effect was lowered in the presence of adsorbed Ca<sup>2+</sup>. A very similar ranking was actually established by Zhang and Gjrv [Zhang1996] within the study of chloride diffusion in cement pastes exposed to different external salts:  $D_{NaCl} < D_{KCl} < D_{CaCl_2}$ . This trend was demonstrated for low concentration of salts (up to 0.1M) in good agreement with experimental data [Ushiyama1974, Gjrv1987]. The authors argued that due to higher ionic interactions with the charged surfaces, the chemical potential and, hence, the diffusing driving forces were noticeably hindered for Ca-systems. It was also shown that sodium had a higher dragging force than that of calcium which resulted in a reduction of the chloride diffusion with up to a factor of 2 (very close to the deviations in Fig.6.8.(b) between the cases of Ca<sup>2+</sup> at 0% and 50% ).

A second important result was to establish the determining role of the pore size on the double layer effects over ionic diffusion. Within small pores of 4nm of diameter, it was found that the diffusivity of chloride experienced the highest drop from its bulk mobility. The difficulty remained, however, to confront the results with atomic-scale experiments. So the validation was carried out indirectly by comparison to “macroscopically” measured diffusion coefficients. In the context of comparing chloride resistivity of cement pastes, Maraghechi et al. [Maraghechi2018] found that the apparent diffusion coefficient of chloride was much lower for LC3 samples compared to OPC. This difference in the chloride resistivity was attributed to the refined pore structure of the LC3 blend as Mercury Intrusion porosimetry (MIP) indicates in Fig.6.10.(a).

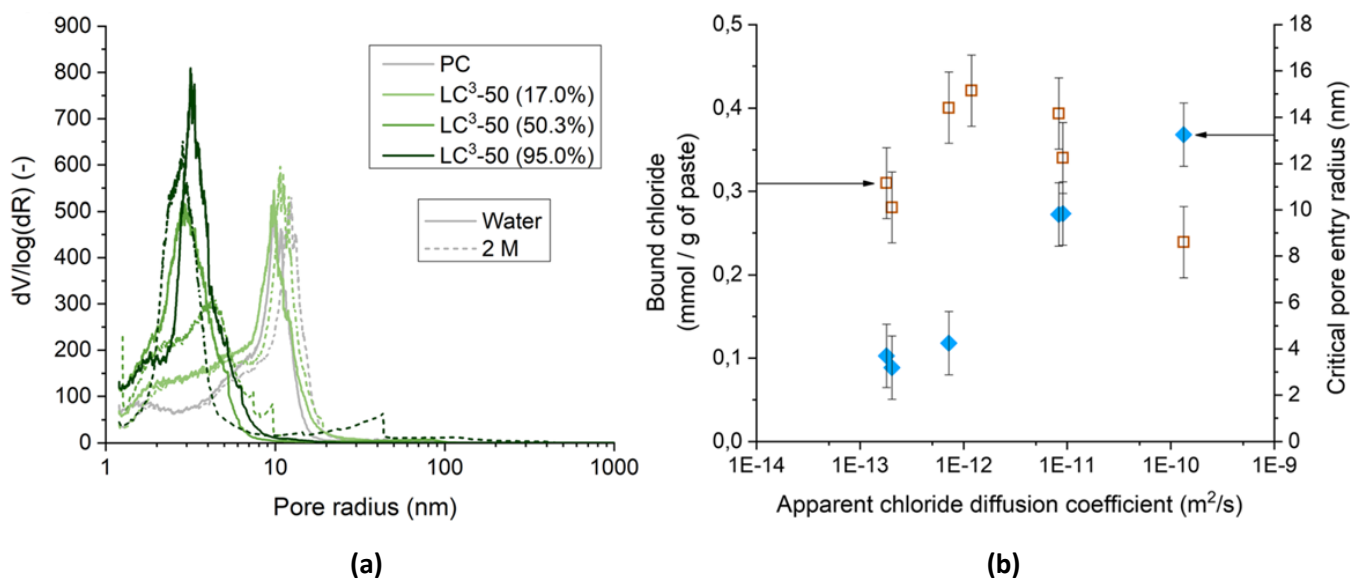


Fig.6.10. (a) Porosity distribution of PC and LC3-50 (with increasing kaolinite content) paste samples after 6-month exposure to water or 2M NaCl solution and (b) Correlation between the bound chloride, the critical pore entry radius with the apparent chloride diffusion coefficient. Taken from [Maraghechi2018]

The apparent diffusion coefficients in Fig.6.10.(b) were obtained through bulk diffusion experiments (chloride ponding tests). They show, in fact, a sizable drop of the diffusivity of at least one order of magnitude once the pore entry size decreased from 10 to 4 nm. In small pores of 4 nm, it was found that the EDL overlapping in small pores has a non negligible contribution reducing the diffusivity of chloride by up to a factor of 3 to 4 (Fig.6.8.(b)). It remains; nonetheless, clear that geometrical effects such as the tortuosity of the pore network also contributed to lengthen the average diffusion path of chlorides. As a matter of fact, it is important to remember that, unlike the microscopic effective diffusivities  $K_i$  that were computed through the chapter, apparent diffusivities are empirically fitted coefficients where microstructure parameters are lumped together on top of the surface effects. Results in Fig.6.10.(b) also show a decrease by a factor of 10 as the pore size goes from around 14 nm to 10 nm. At this length scale, the EDL overlapping was proved to be minor (especially at high pHs) and only the geometry of the pore network could explain such a drop. However, the error on the measured pore size entries by MIP was, unfortunately, not discussed in the paper which forces caution when interpreting the results.

Finally, it was found that reversing the surface charge density to positive values, presumably due to high Ca-Si occupancy, lead to an increase of the chloride diffusivity. For a solution of pH=13, the normalized diffusion coefficient increased by a factor of approximately 2 and 1.5 for surface charges, respectively,  $+0.6 \text{ e.nm}^{-2}$  and  $+1.2 \text{ e.nm}^{-2}$  once the pore size reduced from 12 to 4nm of width. A very similar behavior was noted by Yang et al. which for a similar chloride content (NaCl at 0.1M) at a pH of 12.5 registered an increase of chloride diffusivity by a factor of roughly 1.4 once the channel width went from 11 nm to 4 nm [Yang2019]. Although there is no conclusive experimental validation of these results, the question on the location of Ca and the mechanisms of its adsorption on C-S-H appear to be a decisive factor which regulates the binding and transport of chloride.

## IV. Summary

In this chapter, the numerical resolution of the equations of ionic transport was carried out through the implementation of two methods:

- The first approach consists in conducting a finite element analysis of the conventional ideal Poisson-Nernst-Planck equations (PNP)
- The second method relied on the combination of the Poisson-Boltzmann formalism with Monte Carlo calculations of the ionic concentrations and electric potential at equilibrium (MPB)

The two implementations were, first, applied to the case of monovalent electrolytes (NaCl and NaCl+NaOH) and, then, extended to Ca-containing pore solutions. Under the assumptions of ideality, the PNP results showed an underestimation of chloride diffusivity due to neglecting the finite ionic size and the contribution of the Stern layer. On the other hand, the MPB solution offered a better quantification of the steric effects on the mobility of ions. It also showed that, up to a 50% Ca occupancy of ionized silanol sites, the Ca-containing pore solution behaved in a very similar manner to monovalent salts where  $\text{Na}^+$  is the only counter-ion. In sum, it was found that chloride diffusivity was further lowered as:

1. The pore size was reduced
2. The ionization of the C-S-H was higher and the surface was more negatively charged
3. The ionic strength was lower i.e. lower  $\text{Cl}^-$  concentration and/or lower pH (down to 12.7)

In the case where  $\text{Ca}^{2+}$  ions occupied the integrity of available ionized silanol sites, a clear deviation between Na-systems and Ca-systems was marked. And while the pore size reduction still enhanced the effect of the double layer, the electrochemical potential of the pore was rather determined by the Ca content. At the highest calcium-silanol (Ca-Si) occupancy, the pore displayed an overall positive potential than seemed to boost the chloride mobility.

Finally, we compared the predictions of our model with experimental and computational results in the literature which seemed to indicate that calcium occupancy of the C-S-H surface is partial and possibly shared with sodium. If the surface potential of C-S-H remained negative that, along with the pore size and other discussed factors, might explain the high chloride resistance of some blended cementitious systems.

## V. References

- [Avet2018] Avet, François, and Karen Scrivener. "Investigation of the calcined kaolinite content on the hydration of Limestone Calcined Clay Cement (LC3)." *Cement and Concrete Research* 107 (2018): 124-135.
- [Atk1984] Atkinson, A., and A. K. Nickerson. "The diffusion of ions through water-saturated cement." *Journal of materials science* 19.9 (1984): 3068-3078.
- [Bazant2004] Bazant, Martin Z., Katsuyo Thornton, and Armand Ajdari. "Diffuse-charge dynamics in electrochemical systems." *Physical review E* 70.2 (2004): 021506.
- [DeWeerdt2015] De Weerdt, Klaartje, et al. "Impact of the associated cation on chloride binding of Portland cement paste." *Cement and Concrete Research* 68 (2015): 196-202.
- [Donnan1924] Donnan, Frederick George. "The theory of membrane equilibria." *Chemical reviews* 1.1 (1924): 73-90.
- [Elak2009] Elakneswaran, Y., T. Nawa, and K. Kurumisawa. "Electrokinetic potential of hydrated cement in relation to adsorption of chlorides." *Cement and Concrete Research* 39.4 (2009): 340-344.
- [Fen2021] Fenaux, Michiel, et al. "On the Tortuosity-Connectivity of Cement-Based Porous Materials." *Applied Sciences* 11.13 (2021): 5812.
- [Fried2008] Friedmann, Hubert, Ouali Amiri, and Abdelkarim Aït-Mokhtar. "Physical modeling of the electrical double layer effects on multispecies ions transport in cement-based materials." *Cement and Concrete Research* 38.12 (2008): 1394-1400.
- [Gjorv1987] Gjorv, Todd E., and Oystein Vennesland. "Evaluation and control of steel corrosion in offshore concrete structures." *Special Publication* 100 (1987): 1575-1602.
- [Goto1981] Goto, Seishi, and Della M. Roy. "Diffusion of ions through hardened cement pastes." *Cement and Concrete Research* 11.5-6 (1981): 751-757.
- [Haas2015] Haas, Jeremy, and André Nonat. "From C–S–H to C–A–S–H: Experimental study and thermodynamic modelling." *Cement and Concrete Research* 68 (2015): 124-138.
- [Hassan1979(1)] Hassanizadeh, Majid, and William G. Gray. "General conservation equations for multi-phase systems: 1. Averaging procedure." *Advances in water resources* 2 (1979): 131-144.
- [Hassan1979(2)] Hassanizadeh, Majid, and William G. Gray. "General conservation equations for multi-phase systems: 2. Mass, momenta, energy, and entropy equations." *Advances in water resources* 2 (1979): 191-203.
- [Kilic2007] Kilic, Mustafa Sabri, Martin Z. Bazant, and Armand Ajdari. "Steric effects in the dynamics of electrolytes at large applied voltages. I. Double-layer charging." *Physical review E* 75.2 (2007): 021502.
- [Lab2011] Labbez, Christophe, et al. "CSH/solution interface: Experimental and Monte Carlo studies." *Cement and Concrete research* 41.2 (2011): 161-168.



[Lab2006] Labbez, Christophe, et al. "Surface charge density and electrokinetic potential of highly charged minerals: experiments and Monte Carlo simulations on calcium silicate hydrate." *The Journal of Physical Chemistry B* 110.18 (2006): 9219-9230.

[Lide1994] Lide, David R. Handbook of organic solvents. CRC press, 1994.

[Mach2018] Machner, Alisa, Petter Hemstad, and Klaartje De Weerd. "Towards the understanding of the pH dependency of the chloride binding of Portland cement pastes." (2018).

[Maraghechi2018] Maraghechi, Hamed, et al. "Performance of Limestone Calcined Clay Cement (LC3) with various kaolinite contents with respect to chloride transport." *Materials and structures* 51.5 (2018): 1-17.

[Plus2016] Plusquellec, Gilles, and Andre Nonat. "Interactions between calcium silicate hydrate (CSH) and calcium chloride, bromide and nitrate." *Cement and Concrete Research* 90 (2016): 89-96.

[Sui2019(2)] Sui, Shiyu, et al. "Towards a generic approach to durability: Factors affecting chloride transport in binary and ternary cementitious materials." *Cement and Concrete Research* 124 (2019): 105783.

[Tri1989] Tritthart, Josef. "Chloride binding in cement II. The influence of the hydroxide concentration in the pore solution of hardened cement paste on chloride binding." *Cement and Concrete Research* 19.5 (1989): 683-691.

[Tay1986] Taylor, Harry FW. "Proposed structure for calcium silicate hydrate gel." *Journal of the American Ceramic Society* 69.6 (1986): 464-467.

[Ushiyama1974] Ushiyama, H. "Diffusion of various ions in hardened portland cement paste." *Proc. 6th Int'l Cong. Chem. Cement, Moscow* (1974): 331-337.

[Wilson2021] Wilson, William, Fabien Georget, and Karen Scrivener. "Unravelling chloride transport/microstructure relationships for blended-cement pastes with the mini-migration method." *Cement and Concrete Research* 140 (2021): 106264.

[Yang2019] Yang, Yuankai, et al. "Multiscale modeling of ion diffusion in cement paste: electrical double layer effects." *Cement and Concrete Composites* 96 (2019): 55-65.

[Zhang1996] Zhang, Tiewei, and Odd E. Gjrv. "Diffusion behavior of chloride ions in concrete." *Cement and Concrete Research* 26.6 (1996): 907-917.



# Chapter 7 Summary and Outlook

In the context of studying the resistance of cement-based materials to chloride ingress, two main themes were investigated in this thesis:

- (i) The mechanisms of adsorption of chloride ions on the surface of the C-S-H gel i.e. the so-called physical binding of chloride in the electrical double layer.
- (ii) The effects of the binding on ionic transport in general and specifically on the mobility of the harmful chloride ions at the pore scale.

In this chapter, we summarize the contributions of the thesis on these matters and discuss the future prospects on both theoretical and experimental grounds to answer the most urgent questions raised by this work.

Chapter 7 Summary and Outlook .....	181
I. Physical binding of chloride: The electrical double layer.....	183
A. Methodology .....	183
B. Contribution.....	183
C. Outlook .....	185
i) Experimental.....	185
ii) Theoretical .....	185
II. Diffusion of chloride in the nanoporous C-S-H gel .....	187
A. Contribution.....	187
B. Outlook .....	187
i) Experimental.....	187
ii) Theoretical .....	188
III. Closing words.....	188
IV. References .....	189



# I. Physical binding of chloride: The electrical double layer

## A. Methodology

The first objective of this thesis was to construct a model that would improve the understanding of the mechanisms of ionic adsorption on cement hydrates. Relying on experimental data, the study was conducted on the C-S-H “gel” as it was the main hydration phase and the major contributor to ionic diffusion in concrete. Interhydrate and gel porosity (<10nm of diameter) was also considered as the determining structure at which atomistic effects were the most noticeable. At such a scale, two main phenomena arise:

- Surface effects due to the negative charge density that develops on the C-S-H surface upon ionization of the silanol groups at high pH values (>12.5)
- Steric effects that dominate the strongly non-ideal pore solution of cement paste. They encapsulate all the ion-ion correlations due to short-range pairwise potentials and the finite size of ionic species.

These atomic effects were considered to be at the origin of the electrical double layer. The atomistic modelling of the electrical double layer is a well-known problem in the field of colloidal and interfacial physics. In cement science, however, one main impediment to the full characterization of interfacial phenomena is the poorly understood C-S-H structure. Given that the study of C-S-H/liquid interfaces falls outside the scope of our investigation, we describe the C-S-H surface as an implicit plane entirely characterized by its homogeneous surface charge density.

## B. Contribution

The novelty of the present work lies in the quantification of the many mechanisms in actions behind the EDL formation in cement paste which is limited in the current literature. Through Monte Carlo simulations, we conducted a multi-parameter study to depict all of (i) the pore size effect, (ii) the influence of the C-S-H surface and of (iii) the pore solution on the development of the EDL. The considered variables were:

1. The pore size
2. The ionization degree of the silanol groups i.e. the C-S-H surface charge density
3. The ionic strength of the pore solution (concentration, ionic valences)
4. The pH

First, the developed model was compared to the classical Gouy-Chapman-Stern theory. The limitations of the latter were shown, in accordance with verified results (both experimental and theoretical) in the literature, and the necessity of using atomistic techniques was established. The study of the EDL was carried out on two pore solution models:

- a) The simpler case was to consider a monovalent pore solution which was firstly modeled as a NaCl salt and, then, extended to a multispecies salt modelled by a mix of NaCl and NaOH solutions (*ref. chapter 4*). In this case study, it was established that when the pore diameter is within the order of a few Debye lengths, the overlapping of the diffuse layers occurs and leads to the disruption of the local electroneutrality of the pore solution. As the pore size

reduces, the average electrochemical potential within the pore grows more negative. The increase of the surface charge density of C-S-H was also shown to increase the electrostatic interactions with the ions in the solution and resulted in a higher adsorption of the counter-ions. Conversely, the increase of either the ionic concentration or the pH (at constant surface charge density) of the solution translated into a stronger shielding of the surface due to a higher accumulation of the counter-ions. As a result, the Debye length decreased and with it the EDL thickness within the pore i.e. no sizable overlapping even in small pores below 5 nm of size.

- b) For a more realistic representation of cement paste,  $\text{Ca}^{2+}$  ions were added in the solution (*ref. chapter 5*). Unlike  $\text{Na}^+$ ,  $\text{Ca}^{2+}$  has a very low concentration in high pH environments ( $\text{pH} > 13$ ). It was, hence, concluded that the present calcium ions were essentially adsorbed on the C-S-H surface. The subsequent study showed that the amount of adsorbed  $\text{Ca}^{2+}$  on the available Si-O<sup>-</sup> sites had a determining effect on the nature of the interactions between chloride and the C-S-H surface. Two main regimes were identified:
  - i. **Ca-Si occupancy < 50%** where  $\text{Ca}^{2+}$  ions only occupy up to half the ionized silanol groups; the rest of the sites being occupied by  $\text{Na}^+$  ions. Within this interval, Ca-containing systems displayed a very similar behavior to pure Na-systems and the parametric study lead to the same effects of the solution and the surface properties as previously depicted in (a).
  - ii. **Ca-Si occupancy > 50%:** At such Ca content, the surface is not only shielded but the Zeta potential at its vicinity is reversed to positive values due to the divalence of  $\text{Ca}^{2+}$ . Along with the accumulation of  $\text{Ca}^{2+}$  at the surface, the electrochemical potential of the pore grows less and less negative. At 100% Ca-Si occupancy, the apparent surface potential of C-S-H is positive. Depending whether  $\text{Ca}^{2+}$  ions occupy one or two sites, the pore turns more or less positive in charge. In brief, in this regime,  $\text{Ca}^{2+}$  is the potential determining species independently of the ionization degree of the silanols, the bulk concentration or the pH value.

To sum up, the developed model of the EDL predicts that depending on the Ca-Si occupancy, the global electric potential of the pore could turn from negative to positive values. In practice, simulations in the NVT ensemble show that it is more likely that  $\text{Ca}^{2+}$ , despite their affinity to adsorb, will tend to share the occupancy of the ionized sites with  $\text{Na}^+$  (or even  $\text{K}^+$  in real systems) ions. However, the interpretation of the results can only be limited given the obvious shortage in experimental data at the atomic scale.

## C. Outlook

### i) Experimental

Experimental investigation is without doubt the natural step forward. A primary validation step of the previously discussed results can be the measurement and the comparison of Ca/Si ratios of C-S-H when exposed to different solutions (for e.g. containing Na<sup>+</sup> and/or K<sup>+</sup> ions) as a first quantification of the different amounts of adsorbed cations. Another urgent and yet challenging question remains the location of Ca at the C-S-H/liquid interface. To this day, it is still unclear whether the interfacial calcium atoms are an integrated part of the C-S-H structure or, rather, specifically adsorbed ions located at the Stern layer. The affinity of Ca<sup>2+</sup> ions to occupy one or multiple ionized sites is an equally important facet of the question. In this regard, Extended X-ray absorption fine structure (EXAFS) spectroscopy is a powerful technique that provides valuable insight on the chemical environment of a particular element. If applied to Ca in C-S-H, it may allow the determination of atomic-scale information such as the type of the neighboring atoms and their number. Additionally, EXAFS analysis is well adapted to amorphous materials as it only requires a short-range order i.e. up to 1nm around the element of interest [Teo2012]. Likewise, <sup>43</sup>Ca NMR spectroscopy remains a promising alternative, although quite challenging to apply to binding problems in solutions [Bryce2010].

The experimental investigation of the amount of bound chloride on C-S-H (or more generally C-A-S-H) remains equally challenging. In many studies [DeWeerdt2015, Machner2018, Maraghechi2018], the physically bound chloride on C-A-S-H is indirectly measured by subtracting the chemically trapped chloride (in Friedel's salt) from the total amount of bound chloride. Direct measurement methods do however exist, in particular, through the image analysis of hypermaps obtained by scanning electron microscopy with energy dispersive spectroscopy (SEM-EDS) [DeWeerdt2014, Sui2019, Georget2021, Wilson2022]. The difficulty of the SEM-EDS lies, in fact, in the preparation step of the polished samples, at which precipitation of chloride may occur and induce errors on the determined Cl/Ca, Cl/Si or Cl/(Si+Al) ratios.

### ii) Theoretical

As the main focus of this work is interfacial phenomena, the most urgent matter remains the construction of a consistent C-S-H surface model. Atomistic models based on the 14 Å tobermorite structure have significantly helped in the understanding of C-S-H structure with low Ca/Si ratios (<1). These same models, however, showed clear limitations when confronted to experimental observations over C-S-H samples with Ca/Si>1 mostly due to the undervaluation of the Ca/Si ratio and the overestimation of the main chain length (MCL) [Duque2022, Moh2022]. A very recent study shows, in fact, that C-S-H surfaces are essentially calcium terminated and not silicate terminated as usually assumed [Casar2022]. The authors show that the mix model of silicon-calcium terminated surfaces agrees best with <sup>1</sup>H and <sup>29</sup>Si NMR data. In fact, more representative models of both C-S-H bulk and surfaces would constitute a big leap in the development of thermodynamic models to predict the variation of C-S-H composition in different blended systems.

Given these latest advances [Casar2022], it becomes interesting to use Molecular Dynamics simulation for a better representation of the surface morphology. A more realistic distribution of the surface silanol sites also allows a more accurate study of the ionization process and the development

of the surface charge density. Another key prerequisite is the choice of a well constructed and validated Force Field. Ongoing work is in progress with the ERICA FF, a force field primarily developed for the simulation of cementitious materials [Valavi2022]. Promising results were demonstrated for the simulation of portlandite and tobermorite systems. The extension to C-S-H is the next logical step.

Furthermore, moving toward all-atom explicit models can offer a better description of the water molecules at the interface of the solid but also in very small pores (around 3nm and below) where the solvent density may play a role in ionic diffusion. At high surface charge density, it is expected that the dielectric constant of the solvent would be different in the Stern layer compared to its value in the bulk solution. The restructuring of water molecules due to the high electric field at the interface [Ker2005] will not only influence the ion-ion pair interactions but equally so the needed work to bring a given ion from the interior of the solution to a point within the EDL (and equivalently the necessary energy to push a solvent from a given point toward the bulk solution). In other terms, the electric potential profile in the pore may be significantly altered. MD simulations corroborated with atomic force microscopy on calcite surfaces showed that the thickness of the Stern layer is function of the involved ions and that non-continuum effects dominated at least within the first 10 Å around the surface [Ricci2013]. The same trend was established once comparing sodium ( $\text{Na}^+$ ) and strontium ( $\text{Sr}^{2+}$ ) distributions at a quartz-water interface obtained by MD with an explicit water description [Kroutil2015] with Monte Carlo computations in an implicit solvent (Fig.7.1.)

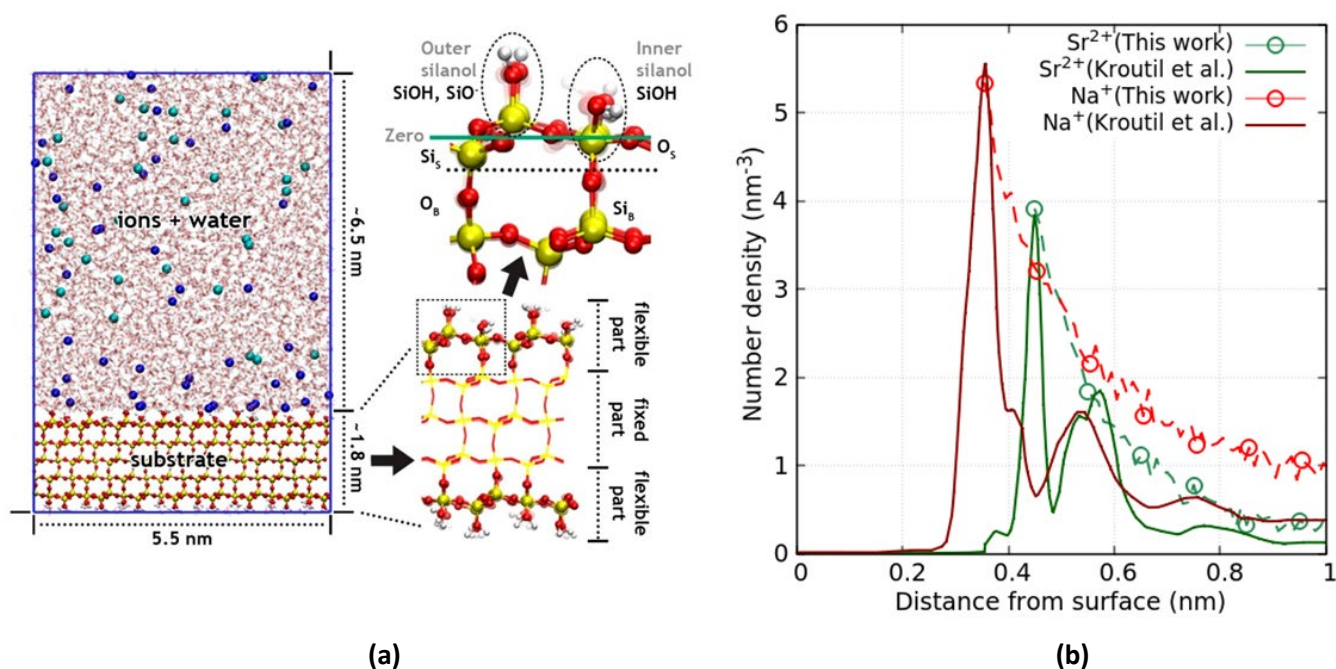


Fig.7.1. **(a)** Representation of the simulation setup and the considered Quartz surface of charge density  $-0.12 \text{ C/m}^2$  where the green line defines the zero plane. **(b)** Ionic distributions of sodium ( $\text{Na}^+$ ) and strontium ( $\text{Sr}^{2+}$ ) ions, respectively, in  $\text{NaCl}$  0.38M and  $\text{SrCl}_2$  0.38L solutions. MD results from the paper are compared to GCMC predictions from the present work. Adapted from [Kroutil2015].

## II. Diffusion of chloride in the nanoporous C-S-H gel

### A. Contribution

In order to resolve the transport problem at the pore scale, we relied on a novel approach which allied Monte Carlo computations of the electrochemical potential and the appealing formalism of the Poisson-Boltzmann equation. The comparison and validation of the method with the conventional finite element analysis of the Poisson-Nernst-Planck equations system was conducted. The agreement between the two methods was best when the pore solution was modelled as an ideal electrolyte. In the case of pure Na-systems, the surface effects due to the overlapping of EDLs in pores of 3 to 5 nm size mitigated the diffusion of chloride by a factor of 2 up to 4 compared to pores of 10nm diameter and more. The same trends, although hindered due to calcium adsorption, were equally predicted for Ca-containing systems but only when Ca-Si occupancy remained below 50%. These results explained, in part, why cement pastes with refined pore structure (such as LC3 blends) had a better resistance to chloride ingress than OPC. However, the model also predicted that, in the case where  $\text{Ca}^{2+}$  occupied the totality of the ionized sites, the mobility of chloride may rather be increased. And while atomistic simulations (MC in the canonical ensemble) incline towards a more Na-like pattern, such a behavior where chlorides are accelerated was also anticipated in the literature [Yang2019].

### B. Outlook

Once more, the structure of the C-S-H surface and the nature of its interactions with the surrounding species appears to be the inescapable riddle that needs to be cracked. In a nutshell, by elucidating the residency of the different cations on C-S-H, it will follow whether it is the surface interactions or the geometrical effects of the pore network that constitute the major obstacle to chloride ingress (and possibly other harmful agents such as sulfates...)

#### i) Experimental

More specifically on the question of transport, there is a lot that remains to be done on the experimental front. The usual set of experiments such as the electromigration test or the bulk diffusion experiments have provided valuable insight but only on the macroscopic properties of cement paste. But when it comes to extracting data at the atomistic scale, it is a different kettle of fish.

Similarly to the case of calcium atoms, chloride ( $^{35}\text{Cl}$  and  $^{37}\text{Cl}$ ) NMR spectroscopy remains a potential route to identify the presence of chloride ions in a cement sample [Cano2002]. The technique relies on the detection of energy transitions of nuclei (with a non zero nuclear spin) as a response to electromagnetic radiation. In theory, it is possible to determine chloride concentration with it. In the context of tracking diffusing species, in situ NMR is best. However, given the limited power of the magnets (up to 1T) in embedded NMR devices and the volume constraint on the sample size, Yun et al. conclude that in situ NMR is not practical [Yun2004]. The alternative would be to conduct an inside-out procedure by irradiating a sufficiently concentrated sample over a long enough period of time to be able to compute averages and, hence, extract an exploitable signal.

## ii) Theoretical

In continuity with the theoretical perspectives on the EDL study, explicit ion methods can also bring insight on the mechanisms of ionic diffusion, although great care should be taken in the choice of the system of interest. An example of a bad set-up would be the simulation of ions diffusing in large pores where the solution is quasi-uniform and no sizable surface effects are in action. On the other hand, ionic diffusion in pores of 1 or 2 nm width can be interesting to address with Molecular dynamics or Brownian dynamics. Such techniques can also be a power tool to study cycles of ionic adsorption/desorption and quantify the residency time of the different species at the surface of cement hydrates. However, the atomic-scale validation of such models with experiments remains one of the inherent pitfalls of this methodology.

Yet, it still remains that the majority of experimental measurements lead to macroscopic diffusion coefficients that enclose all of the micro structural, chemical and physical processes within the material. It therefore follows that the upscaling of microscopic models is the way toward experimental validation. In this regard, Hassanizadeh and Gray have developed since 1979 a rigorous averaging procedure to derive macroscopic multiphase transport equations from microscopic balance laws for mass, momentum, energy, and entropy [Hass1979]. The homogenization procedure relied, in fact, on the existence of a representative element of volume REV (and a representative element area REA), although not explicitly developed. As a matter of fact, the construction of a mesoscopic REV that describes the heterogeneities within cementitious materials through a representative length range is one of the challenges that still lie ahead. The difficulty being that the characteristic sizes of interest cover a wide range of scales from gel pores (~3nm) or portlandite crystals (~10 $\mu$ m) up to aggregates (~1cm). So far, the existing studies that aim to compute macroscopic effective diffusion coefficients rely, for the most part, on descriptive models where macroscopic transport equations are derived from intuitively adjusted single-phase relations i.e. typically Fick's law [Yang2019] and Poisson-Nernst-Planck equations [Samson2007, Hosok2011, Elak2012].

## III. Closing words

In definitive, the use of atomic-scale simulation methods allowed a better understanding of surface effects at the C-S-H/solution interface. The electrical double layer (EDL) was proved to have a non-negligible influence on both the adsorption mechanisms and the diffusion properties of ions, especially in gel pores of few nanometers size. And while the most recent advances on the modelling of C-S-H surfaces will allow the development of more realistic EDL models, experimental validation of the full panoply of existing theoretical results remains, without question, the most urgent matter.



## IV. References

- [Bryce2010] Bryce, David L. "Calcium binding environments probed by  $^{43}\text{Ca}$  NMR spectroscopy." *Dalton Transactions* 39.37 (2010): 8593-8602.
- [Casar2022] Z. Casar, K. Scrivener, P. Bowen, A. Kunhi Mohamed, Towards a representative model of the calcium silicate hydrate surface (2022, in preparation)
- [Cano2002] De J Cano, F., et al. "Magnetic resonance imaging of  $^1\text{H}$ ,  $^{23}\text{Na}$ , and  $^{35}\text{Cl}$  penetration in Portland cement mortar." *Cement and concrete research* 32.7 (2002): 1067-1070.
- [Duque2022] E. Duque-Redondo, P.A. Bonnaud, H. Manzano, A comprehensive review of C-S-H empirical and computational models, their applications, and practical aspects, *Cement and Concrete Research*. 156 (2022) 106784.
- [DeWeerd2015] De Weerd, Klaartje, et al. "Impact of the associated cation on chloride binding of Portland cement paste." *Cement and Concrete Research* 68 (2015): 196-202.
- [DeWeerd2014] De Weerd, Klaartje, Harald Justnes, and Mette R. Geiker. "Changes in the phase assemblage of concrete exposed to sea water." *Cement and Concrete Composites* 47 (2014): 53-63.
- [Elak2012] Elakneswaran, Yogarajah, and Tetsuya ISHIDA. "Development Of A Physical And Geochemical Model For Long-Term Performance Of Cementitious Materials." (2012).
- [Georget2021] Georget, Fabien, William Wilson, and Karen L. Scrivener. "edxia: Microstructure characterisation from quantified SEM-EDS hypermaps." *Cement and Concrete Research* 141 (2021): 106327.
- [Hosok2011] Hosokawa, Yoshifumi, et al. "Development of a multi-species mass transport model for concrete with account to thermodynamic phase equilibriums." *Materials and Structures* 44.9 (2011): 1577-1592.
- [Hass1979] Hassanizadeh, Majid, and William G. Gray. "General conservation equations for multi-phase systems: 1. Averaging procedure." *Advances in water resources* 2 (1979): 131-144.
- [Kumar2017] Kumar, Abhishek, et al. "The atomic-level structure of cementitious calcium silicate hydrate." *The Journal of Physical Chemistry C* 121.32 (2017): 17188-17196.
- [Kroutil2015] Kroutil, O., et al. "Computer simulations of quartz (101)–water interface over a range of pH values." *The Journal of Physical Chemistry C* 119.17 (2015): 9274-9286.
- [Ker2005] Kerisit, Sebastien, et al. "Atomistic simulation of charged iron oxyhydroxide surfaces in contact with aqueous solution." *Chemical communications* 24 (2005): 3027-3029.
- [Moh2022] A. Kunhi Mohamed, S.A. Weckwerth, R.K. Mishra, H. Heinz, R.J. Flatt, Molecular modeling of chemical admixtures; opportunities and challenges, *Cement and Concrete Research*. 156 (2022) 106783.
- [Machner2018] Machner, Alisa, et al. "Chloride-binding capacity of hydrotalcite in cement pastes containing dolomite and metakaolin." *Cement and Concrete Research* 107 (2018): 163-181.

[Maraghechi2018] Maraghechi, Hamed, et al. "Performance of Limestone Calcined Clay Cement (LC3) with various kaolinite contents with respect to chloride transport." *Materials and structures* 51.5 (2018): 1-17.

[Ricci2013] Ricci, Maria, et al. "Direct visualization of single ions in the Stern layer of calcite." *Langmuir* 29.7 (2013): 2207-2216.

[Sui2019] Sui, Shiyu, et al. "Quantification methods for chloride binding in Portland cement and limestone systems." *Cement and Concrete Research* 125 (2019): 105864.

[Samson2007] Samson, E., and J. Marchand. "Modeling the transport of ions in unsaturated cement-based materials." *Computers & Structures* 85.23-24 (2007): 1740-1756.

[Teo2012] Teo, Boon K. EXAFS: basic principles and data analysis. Vol. 9. Springer Science & Business Media, 2012.

[Valavi2022] Valavi, Masood, et al. "Molecular dynamic simulations of cementitious systems using a newly developed force field suite ERICA FF." *Cement and Concrete Research* 154 (2022): 106712.

[Wilson2022] Wilson, William, et al. "Insights on chemical and physical chloride binding in blended cement pastes." *Cement and Concrete Research* 156 (2022): 106747.

[Yang2019] Yang, Yuankai, et al. "Multiscale modeling of ion diffusion in cement paste: electrical double layer effects." *Cement and Concrete Composites* 96 (2019): 55-65.

[Yun2004] Yun, Haebum, et al. "Detection of free chloride in concrete by NMR." *Cement and concrete research* 34.3 (2004): 379-390.





# Khalil Daniel Ferjaoui



## Personal data

Born June 3, 1991

## Nationality

French/Tunisian

## Phone

+41 77 223 99 53

## Email

khalilferjaoui@yahoo.fr

## Address

Avenue des Toises 14,  
1005 Lausanne,  
Suisse

## Languages

**Arabic/French:** Bilingual,

**English:** Fluent,

**Spanish:** Good command,

**Japanese:** Working knowledge

## Programming languages & Simulation softwares

Fortran 90, C, C++, Python,  
Matlab, Latex, ANSYS Fluent,  
Abaqus, OpenFOAM,  
FreeFem++, Paraview,  
LAMMPS, COMSOL...

## Coursework & Theoretical background

**Applied mathematics** Statistical methods for management, Probability theory, Numerical methods, Optimization mathematics...

### Mechanics & Materials

Composite materials, Crystal growth, Turbomachinery, Fluid mechanics, Damage and fracture mechanics...

**Basic knowledge in finance & economics**

## Personal profile

Highly talented engineer with extensive knowledge in Materials Science and Applied Mathematics in various fields. Hardworking and constantly eager to learn.

## Education

2018–2022	<b>Doctoral degree (Ph.D)</b> <i>Majoring in Materials Science &amp; Applied Physics</i>	EPFL, Lausanne, Switzerland
2017–2018	<b>Master of Science (MSc) in Multiscale &amp; Multiphysics Modeling of Materials &amp; Structures</b> <i>Majoring in Materials Science &amp; Structural Mechanics</i>	Ecole Polytechnique (X), Paris, France
2016–2017	<b>MSc in Fundamental Mechanics &amp; Applications</b> <i>Double Degree with the Master of Engineering</i>	University of Bordeaux, France
2013–2017	<b>Master of Engineering (MEng/Engineer's degree) in Applied Mathematics &amp; Mechanical Engineering</b> <i>Majoring in Fluid Mechanics &amp; Energetics</i>	Polytechnic Institute of Bordeaux, France
2010–2013	<b>3-year intensive undergraduate program preparing for the competitive entrance examinations to French top-level "Grandes Écoles"</b> <i>Main subjects: Mathematics, physics, chemistry and philosophy.</i>	IPEST, Tunis

## Projects & Professional experience

Oct2018-Sep2022	<b>Doctoral assistant</b> <i>PhD thesis under the supervision of Prof. Karen Scrivener</i>	Swiss Federal Institute of Technology in Lausanne (EPFL), Switzerland
	<ul style="list-style-type: none"> <li>Assistant duties i.e. teaching undergraduate and graduate students.</li> <li>Research work: Development of a new physical model to explain the mechanisms of ionic transport in the microscopic porous network within cement-based materials.</li> </ul>	
Feb-Sep 2018	<b>Industrial internship III (Master's thesis for MSc)</b> <i>Composites engineer</i>	Safran Tech, Paris, France
	<ul style="list-style-type: none"> <li>Implementation (Python) of a code for predicting the elasticity properties of 3D woven composites</li> <li>Implementation (C++) of a Fast Fourier Transform method to cross validate the first approach.</li> </ul>	
May-Sep 2017	<b>Industrial internship II (Master's thesis for MEng)</b> <i>Submarine navigation systems engineer</i>	Thales Underwater Systems, France
	<ul style="list-style-type: none"> <li>Implemented and verified a ray-tracing algorithm to describe the propagation of acoustic waves under water.</li> <li>Developed a consistent code to predict the diffraction phenomenon in the high frequency band.</li> </ul>	
Feb-April 2017	<b>Industrial internship I</b> <i>Plasma physics engineer</i>	Sparc Industries Sarl, Ellange, Luxembourg
	<ul style="list-style-type: none"> <li>Developed an algorithm based on classical Fast Multipole Methods in order to reduce the computational time of the simulation code.</li> <li>Implemented the algorithm and developed test cases (typical plasma instabilities) to verify it.</li> <li>Relevant industrial applications: neutron generators, plasma propulsion technology...</li> </ul>	
Sep2016-Jan2017	<b>Part-time CFD scientist</b> <i>Study of the impact of turbulence on hydro-kinetic turbine farms</i>	CNRS, Bordeaux, France
	<ul style="list-style-type: none"> <li>Characterization of turbulence phenomena through benchmark experiments.</li> <li>Simulation (ANSYS/OpenFOAM) of the effect of turbulence on the wake of turbines.</li> </ul>	

## Interests & Activities

- Volunteer work in POUR UN SOURIRE D'ENFANT (PSE), a charitable association which aims to help underprivileged children and school dropouts in Cambodia (particularly ragpickers' children from Phnom Penh city dump) [Set up exhibition to promote the cause]
- Tennis, swimming, biking...